

Journal of Mechanics of Materials and Structures

Volume 14, No. 5

December 2019



JOURNAL OF MECHANICS OF MATERIALS AND STRUCTURES

msp.org/jomms

Founded by Charles R. Steele and Marie-Louise Steele

EDITORIAL BOARD

ADAIR R. AGUIAR	University of São Paulo at São Carlos, Brazil
KATIA BERTOLDI	Harvard University, USA
DAVIDE BIGONI	University of Trento, Italy
MAENGHYO CHO	Seoul National University, Korea
HUILING DUAN	Beijing University
YIBIN FU	Keele University, UK
IWONA JASIUK	University of Illinois at Urbana-Champaign, USA
DENNIS KOCHMANN	ETH Zurich
MITSUTOSHI KURODA	Yamagata University, Japan
CHEE W. LIM	City University of Hong Kong
ZISHUN LIU	Xi'an Jiaotong University, China
THOMAS J. PENCE	Michigan State University, USA
GIANNI ROYER-CARFAGNI	Università degli studi di Parma, Italy
DAVID STEIGMANN	University of California at Berkeley, USA
PAUL STEINMANN	Friedrich-Alexander-Universität Erlangen-Nürnberg, Germany
KENJIRO TERADA	Tohoku University, Japan

ADVISORY BOARD

J. P. CARTER	University of Sydney, Australia
D. H. HODGES	Georgia Institute of Technology, USA
J. HUTCHINSON	Harvard University, USA
D. PAMPLONA	Universidade Católica do Rio de Janeiro, Brazil
M. B. RUBIN	Technion, Haifa, Israel

PRODUCTION production@msp.org

SILVIO LEVY Scientific Editor


Cover photo: Mando Gomez, www.mandolux.com

See msp.org/jomms for submission guidelines.

JoMMS (ISSN 1559-3959) at Mathematical Sciences Publishers, 798 Evans Hall #6840, c/o University of California, Berkeley, CA 94720-3840, is published in 10 issues a year. The subscription price for 2019 is US \$635/year for the electronic version, and \$795/year (+\$60, if shipping outside the US) for print and electronic. Subscriptions, requests for back issues, and changes of address should be sent to MSP.

JoMMS peer-review and production is managed by EditFlow® from Mathematical Sciences Publishers.

PUBLISHED BY

 **mathematical sciences publishers**
nonprofit scientific publishing

<http://msp.org/>

© 2019 Mathematical Sciences Publishers

PREFACE

MAURIZIO ANGELILLO AND SANTIAGO HUERTA FERNÁNDEZ

The theory of arches and masonry vaults originated at the end of the seventeenth century: Robert Hooke had the brilliant intuition to analyse arches as inverted hanging chains and this allowed the analysis to be incorporated within the science of statics. In France, La Hire published at the beginning of the eighteenth century the first article on the collapse of arches, intending to calculate their thrust. Both the equilibrium and collapse approaches were developed further during the eighteenth century. Since the beginning of the nineteenth century, large masonry bridges have been calculated almost routinely using either of the two approaches. In the middle of that century, the diffusion of the concept of lines of thrust was a crucial step in advancing the analysis of arches and masonry vaults, as it allowed one to understand both collapse and equilibrium.

However, this coincided with a pronounced decline in the interest in the theory of masonry construction. The second half of the nineteenth century concentrated on the development of elastic theory, which is more suited to wrought iron and steel structures. The notion took hold that masonry arches, too, should be calculated as an elastic continuum, contradicting both common sense (masonry is essentially discrete at the macroscale) and the observed collapse of arches. This was a huge step backwards in the understanding of arches and vaults; however, from a practical point of view, engineers and architects continued to use equilibrium graphical methods.

By 1900 the theory of masonry structures had stagnated and articles on masonry structures practically disappeared from specialized journals. The so-called Modern Architecture of Bauhaus dramatically broke with the millenary tradition of vaulted construction: arches and vaults were considered old-fashioned and largely disappeared from architecture (though they were still being built; traditions do not die suddenly). Towards the 1930s the increase in the weight of road vehicles made it necessary to reconsider the safety of many old masonry bridges. Nineteenth-century tests on voussoir arches were repeated and it was noted that the appearance of cracks substantially modified the results of elastic analysis. In the 1960s photoelastic methods and, above all, the appearance of computers, which could handle linear elastic equations easily, revived interest in the use of elastic models of masonry structures, ignoring the evidence of century-old voussoir arch tests and the cracked state of actual masonry structures.

It was within this confusing framework that the figure of Professor Jacques Heyman of Cambridge emerged, almost miraculously. Having contributed decisively to the final development of the plastic calculation of steel frames within Baker's Cambridge team, he realised that the whole field of masonry structures could be included within the wider field of limit analysis if the material met certain conditions: high compressive strength, no tensile strength and a construction which precludes sliding. Precisely these conditions were the hypotheses used in the calculation of masonry arches throughout the nineteenth

century. In his paper “The stone skeleton”, published in 1966, Professor Heyman took this crucial step, rigorously explaining the theory and applying it to the Gothic structure. In the following five decades he has continued to improve the understanding of masonry construction, combining popularization with specialized articles on the most important structural types such as bridge arches, cross and fan vaults, domes, towers and spires, rose windows, and stairs, not only explaining their structural behaviour, but also giving, for the first time, a rational interpretation of their cracks and movements, inherent in this type of constructions.

It would be difficult to imagine the current field of masonry structures without Professor Heyman’s seminal contributions. It was he who first realized that the main corollary of the Safe Theorem is the equilibrium approach. Indeed, far from having to make adventurous hypotheses about boundary conditions (essentially ephemeral), Professor Heyman has shown that masonry buildings can be analysed simply by looking for that equilibrium solution, among the infinitely many possible, that respects the compressive nature of the material — its yield condition.

Thus, after 100 years it turns out that the so-called old theory of vaults, used throughout the nineteenth century, was proved to be valid within the more general framework of modern limit analysis. This explains why the calculations made by nineteenth-century engineers on large masonry bridges were essentially correct. So too were equilibrium analyses on masonry vaulted buildings carried out by some architects and engineers in the late nineteenthth and early twentiethth centuries (Planat, Wittmann, Mohrmann). Finally, Gaudí’s genius led him to use the equilibrium approach to generate his complex structures using funicular models.

The work by Professor Heyman over the last fifty years allows us not only to analyse masonry structures, but also to understand the complete framework of the evolution of these constructions that go back more than 6000 years in the Near East. Certainly, as he pointed out, limit analysis leads to geometric statements: the safety of a masonry structure depends essentially on its shape, regardless of size. The old structural rules that have come down to us are indeed geometric, and collect and synthesize the critical experience of the great master builders.

We want this issue of the *Journal of Mechanics of Materials and Structures* to stand in recognition and tribute to the work of Professor Jacques Heyman, which has helped and continues to help us understand masonry structures, illuminating this wide structural field that forms the core of our monumental heritage.

MAURIZIO ANGELILLO: mangelillo@unisa.it

Dipartimento di Ingegneria Civile, Università degli Studi di Salerno, Fisciano, Italy

SANTIAGO HUERTA FERNÁNDEZ: santiago.huerta@upm.es

Escuela Técnica Superior de Arquitectura de Madrid (ETSAM), and Instituto Juan de Herrera, Madrid, Spain

STUDYING THE DOME OF PISA CATHEDRAL VIA A MODERN REINTERPRETATION OF DURAND-CLAYE'S METHOD

DANILO AITA, RICCARDO BARSOTTI AND STEFANO BENNATI

The dome of the Pisa cathedral is a masonry structure of great interest for many aspects related to history, architecture, building techniques as well as geometry and mechanical behaviour. This Romanesque dome presents a peculiar shape, with an oval base and a pointed profile. Scaffolding has recently been erected in order to perform the restoration operations in preparation for the 900th anniversary of the cathedral's dedication. Thanks to the cooperation of the *Opera della Primaziale Pisana*, this has provided a unique opportunity to carry out a research project aimed at an overall analysis of the dome, including its shape, building details, material properties and the state of preservation of the intrados and extrados surfaces. The present contribution, part of the aforementioned research project, focuses on a modern translation of Durand-Claye's method in order to perform a preliminary study of the mechanical response of the dome. The results obtained can provide an estimate of the geometrical safety factor for the dome under vertical loads. In terms of conventional limit thickness the results suggest that the Pisa dome is a safe structure.

1. Introduction

The present paper represents one of the first outcomes of a multidisciplinary research project that has taken advantage of recent restoration works being carried out on the cathedral in preparation for the 900th anniversary of its dedication (1118). With the cooperation of the *Opera della Primaziale Pisana*, this privileged circumstance has allowed for thorough examination of the dome, which involved its building details, material properties and state of preservation.

The study of the dome's structural response has been performed by means of both analytical and numerical models. Although the study is still currently in progress, a first set of results has already been obtained regarding the effects of the vertical dead loads (a first account of some preliminary results is given in [Bennati et al. 2018]).

The present contribution focuses on a structural assessment of the Pisa cathedral dome made based on an interesting historical method for structural analysis, the *stability area method* of the renowned French scholar Durand-Claye [1867; 1880]. Originally designed for masonry arches, the method was extended (1880) to domes of revolution by subdividing the idealized dome into several lunes by means of meridian planes; each lune is then considered as an independent arch of varying width.

In fact we propose a reinterpretation and enhancement of this method, with the aim of assessing the stability of the Pisa dome. As already proposed by the authors in some previous works on masonry arches [Aita et al. 2015; 2016], the stress distribution in the masonry is considered to be nonlinear, both

Keywords: masonry dome, Pisa cathedral, limit analysis, Durand-Claye's method.

in tension and compression. Furthermore, kinematic compatibility issues at collapse, as well as the influence of hoop forces are addressed [Aita et al. 2017a].

The method has been suitably adapted to the problem at hand: a dome with a peculiar elliptical plan. The solution is pursued by means of an expressly developed, in-house algorithm implemented in Mathematica, which allows for determining statically admissible solutions and defining the dome's level of safety.

2. Durand-Claye's method for assessing the stability of domes of revolution

2.1. A brief reference to studies on masonry domes. In order to set the work of Durand-Claye within its historical context, it seems worthwhile to briefly recall the main stages of the research conducted on the structural behavior of masonry domes. The first issue regarding to masonry domes was the search for their optimal shape. Early eighteenth-century contributions on the stability of masonry domes extended to domes the results that had already been obtained for the hanging chain problem [Poleni 1748; Bouguer 1734; Bossut 1774; 1778], by showing that in order to attain equilibrium, the meridian must have the same shape as the curve representing the funicular of the loads corresponding to a slice of dome. Hoop forces are thus disregarded.

This approach was subsequently further extended in [Mascheroni 1785] and [Venturoli 1833]. (Some remarks on the historical evolution of these methods are made in [Aita et al. 2017a].) In all of these studies, the masonry dome is divided into lunes (arches of variable width) by meridian planes: if the meridian profile is shaped according to the hanging chain defined by the load conditions, the assumption of zero hoop forces — usually considered different from zero in the context of membrane theory — is justified.

Among the 19th century contributions, the method of stability areas, originally introduced by Durand-Claye [1867; 1880] for masonry arches is central for our purposes. Other contributions in the same century attempted to account for hoop forces, such as [Lamé and Clapeyron 1823; Navier 1839, pp. 155–157; Lévy 1888, pp. 42–52]. In particular, Lévy observed that hoop stresses are compressive in the upper part of the dome, specifically above a meridian point named the *point neutre*, which Lévy determined. Hoop stresses would instead become tensile in the lower part of the dome, under the aforementioned point, and are disregarded, since tensile stresses are considered inadmissible. For our purposes, other interesting methods were aimed at translating the membrane stress solution through graphical statics (Eddy's and Wolfe's procedures [Eddy 1877; Wolfe 1921]). It is interesting to observe that membrane theory allows for hoop forces to be considered so as to determine statically admissible solutions. However, it is unable to determine the actual solution, unless constitutive relations are considered.

In the 20th century assessment methods were introduced and developed based on the new discoveries of structural mechanics and advanced numerical techniques. Without pretending to be exhaustive, we cite the contributions based on linear and nonlinear FEMs, discrete element codes, 3D thrust network analysis, and several other computational procedures [Block and Ochsendorf 2007; Block and Lachauer 2014; D'Ayala and Tomasoni 2011; Simon and Bagi 2016; Varma and Ghosh 2016; Tempesta et al. 2015b; Beatini et al. 2018]. By way of example, in [Tempesta et al. 2015b] the structural analysis of polygonal masonry domes is performed by means of a numerical procedure, according to which the dome is modeled as a discrete system of rigid blocks linked through elastic mortar layers, able to describe

the actual behaviour of the material. Another interesting analysis is presented in [Beatini et al. 2018], where the *Project Chrono* software has been employed to show the role of friction on the stability of masonry domes, which are envisioned as composed of blocks in dry contact. The analysis highlights the impact of the bond pattern and the blocks' aspect ratio on their capacity to equilibrate the hoop stress. With reference to these complex models, it seems worth noting that some require knowing a large number of mechanical and geometrical parameters, which are generally uncertain and difficult to determine experimentally.

Because of these operating problems, some authors have revisited simple historical models. In [Heyman 1977; Oppenheim et al. 1989] it is assumed that the dome is composed of a finite number of adjacent lunes. Equilibrium is guaranteed as long as the thrust line lies inside the dome meridian profile. The thrust line does not necessarily have to be coincident with the middle surface, as instead assumed within classical membrane theory. These authors carry out the equilibrium analysis by considering the single “arches” constituting the dome and determining the collapse condition in terms of the minimum dome thickness.

More recent contributions [Bacigalupo et al. 2015; Pavlovic et al. 2016] also adopt the same approach by imposing equilibrium on each dome lune. Furthermore, some graphical methods for assessing dome stability have been reevaluated. For example, the historical contributions [Lévy 1888; Eddy 1877; Wolfe 1921] have been reexamined in the light of numerical calculations to obtain the admissible thrust lines [Rapallini and Tempesta 1997; Lau 2006; Zessin et al. 2010; Tempesta et al. 2015a]. Other works, such as [Foraboschi 2014], underline the fundamental role of geometry, as well as the importance of considering the architectural design of the time in conducting any structural analysis. Some interesting recent contributions focus on oval domes, such as that of the Pisa cathedral. Santiago Huerta [2007] illustrates the origin and application of the oval shape in historical architecture, and addresses the mechanics response of oval domes by using the Rankine's theorem. Simon and Bagi [2016] aim at finding the minimum thickness of oval domes loaded by their own weight, by simulating numerically their collapse mechanisms by means of the discrete element code 3DEC. Finally, Beatini et al. [2018] studied the collapse of oval domes, adopting a nonsmooth contact dynamic approach.

Our contribution falls within that context. Its aim is to discover the application potential of an interesting historical method, namely the Durand-Claye method, which turns out to be quite able to provide effective working tools for structural analysis, as will be explained in the following sections.

2.2. A revised version of Durand-Claye's method for masonry domes. As already recalled, Durand-Claye extends his stability area method — originally conceived for masonry arches — in order to assess the equilibrium of domes of revolution [Durand-Claye 1880]. In particular, the method illustrated in [Durand-Claye 1867] for masonry arches can also be applied to each single lune composing a dome by determining the stability area under the hypotheses of limited compressive and tensile strength.

As described by one of the authors in [Foce and Aita 2003], Durand-Claye's original method examines the equilibrium of a symmetric arch, by considering an ideal voussoir comprised between the crown joint c_0d_0 and the generic joint cd . The stability area allows for identifying all the admissible crown thrusts with respect to equilibrium and masonry strength [Durand-Claye 1867]. In particular, Durand-Claye assumes a nil tensile strength, and finite values for the compressive strength and friction coefficient. It is worthy to point out that, when the compressive strength is infinite and the tensile strength is nil, the

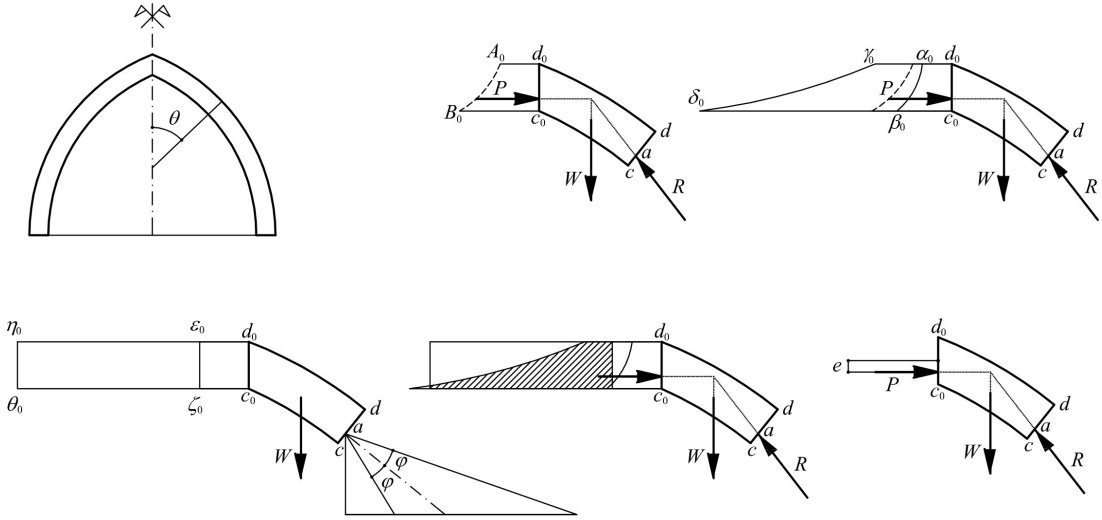


Figure 1. Equilibrium conditions according to the Durand-Claye method.

stability area obtained by Durand-Claye is an effective representation of Coulomb's [1776] method of *maxima and minima*.

The original formulation proposed by Durand-Claye consists in a graphical construction. He considers a symmetric arch (Figure 1, top left) and examines the ideal voussoir comprised between the crown joint c_0d_0 , and a generic joint cd (Figure 1, top middle). He assumes that the line of action of the resultant R that makes equilibrium to the horizontal thrust, P , and the weight W of the voussoir passes through the point a of cd . By varying the application point of the crown thrust, P , from c_0 to d_0 , whereas point a is fixed, the statically admissible thrusts will then be measured by horizontal segments drawn from the crown joint c_0d_0 to line A_0B_0 ; for a coinciding with c and d , the two lines $\alpha_0\beta_0$ and $\gamma_0\delta_0$ are similarly obtained (Figure 1, top right), so that the area $\alpha_0\beta_0\gamma_0\delta_0$, contains the extremes of the segments measuring the admissible thrusts compatible with the rotational equilibrium of the voussoir. In order to prevent sliding along cd , it is sufficient to draw at point a the friction cone, defined by the friction angle φ (Figure 1, bottom left). If the weight W is ideally shifted at point a , the *minimum* and *maximum* horizontal thrusts, i.e. the thrusts values which make the resultant of internal actions coincide with the boundaries of the friction cone, can be determined by considering the triangle of forces plotted in Figure 1 (bottom left) starting from point a . Hence, the extremes of the segments representing admissible thrusts at the crown section will lie between the two vertical lines $\varepsilon_0\zeta_0$ and $\eta_0\theta_0$.

To assure both the voussoir rotational and translational equilibrium, the extremes of admissible thrusts must be comprised within the intersection of the area $\alpha_0\beta_0\gamma_0\delta_0$ with the area $\varepsilon_0\zeta_0\eta_0\theta_0$ comprised between two vertical lines, i.e. within the dashed area in Figure 1 (bottom middle). By repeating this procedure for each joint, Durand-Claye finds the area within which the extremes of the statically admissible thrusts must be included. Thus, each point within the stability area corresponds to a statically admissible *line of thrust*, under the assumptions above. When such an area shrinks to a point (or a segment) the arch attains a limit equilibrium condition, i.e., there is only one admissible value left for the crown thrust.

The main innovation of Durand-Claye's method, as pointed out in [Aita et al. 2015; 2016; Foce

and Aita 2003], concerns the introduction of finite values for the compressive (and shear) strength. By denoting as e the eccentricity of the crown thrust, P , with respect to the centre of the crown section (Figure 1, bottom right), the area of stability is obtained by considering the region formed by all the points of coordinates (P, e) that fulfil the equilibrium equations of any arch portion, as well as the limitations imposed by the masonry bounded compressive and tensile strength. For the sake of brevity, the description of this final step of the procedure is here omitted; the interested reader is referred, for example, to [Foce and Aita 2003] or some previous works by the authors, where a modern formulation of Durand-Claye's method is used for determining the collapse modes of symmetric masonry arches of different shape [Aita et al. 2015; 2016; 2019a]. In those contributions, the graphical constructions proposed by Durand-Claye are translated in terms of numerical operations on internal forces.

We recall that in the present paper we assume infinite compressive strength and an infinite friction coefficient: for this reason, issues concerning the strength of the material are not considered.

According to Durand-Claye's method when infinite friction is assumed, whenever the stability area reduces to a single point, the arch is in a limit condition and a kinematically admissible mechanism is triggered in the arch. Durand-Claye, in his contribution published in 1880, points out that his method, originally conceived for masonry arches, can be suitably modified to assess the stability of domes of revolution. Durand-Claye starts his reasoning by considering the single lunes composing the dome (Figure 2).

With reference to Figure 2 (left), drawn from the original [Durand-Claye 1880], he considers a lune comprised between two meridional planes forming a small angle, $d\theta$ (Figure 2, right). Then, he examines the equilibrium of the voussoir comprised between segments $\alpha\beta$, ab , after expressing its weight by means of Guldin's theorem. The resultant reaction force acting on the arch joint ab (Figure 2, left) is obtained by imposing the equilibrium of the lune upper portion. Furthermore, the crosssectional bending moment and shear capacities are determined as functions of the masonry compressive and tensile strengths and friction coefficient along the joints.

As observed in [Aita et al. 2017a; 2019a; 2019b], the extension of Durand-Claye's method to domes presents some critical issues.

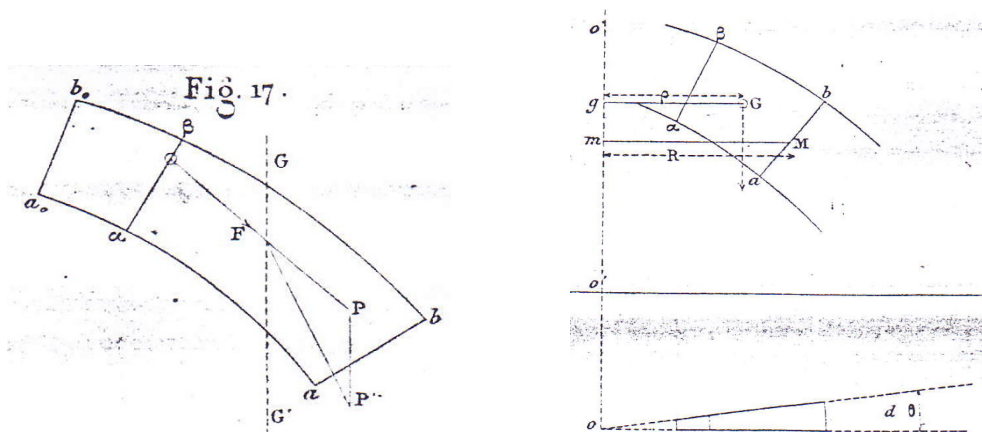


Figure 2. The extension of Durand-Claye's method to the equilibrium of a single lune. Taken from [Durand-Claye 1880].

A first caution concerns the assumption of limited compressive strength: under that assumption the crown thrust would vanish, since the crown’s width is nil (see [Figure 2](#), right). A second remark regards the procedure adopted by Durand-Claye. By reasoning in terms of equilibrium of a single lune, the limit condition identified by the vanishing of the stability area might not correspond to a collapse condition in some cases, i.e., when a kinematically admissible collapse mechanism for the entire dome cannot be determined. A third *caveat* regards the analysis of hoop forces proposed by Durand-Claye. He considers only the hoop forces acting within the *anneau supérieur* (the upper part of the dome). However, he assumes that their effect would always be counterproductive by observing that they produce a further reduction of the stability area, since they cannot exceed the limit imposed by the finite compressive strength. As is evident, this approach does not take into consideration the well-known beneficial effects that compressive hoop forces have on system stability, as will be clarified in the following.

Our reinterpretation of Durand-Claye’s method aims at assessing the stability of domes by translating the complex graphical construction into a suitable set of equations in terms of the internal forces, namely: the axial force, N , and bending moment, M . Furthermore, the method has been reedited in order to adequately address the abovementioned issues.

This remainder of the section provides some remarks on Durand-Claye’s method for the particular case in which an infinite friction coefficient is assumed.

Let us consider a portion of a dome of revolution having the profile shown in [Figure 3](#) (left); it is comprised between two meridian planes forming a “small” angle ζ . A pointed profile with constant thickness, resembling that of the Pisa dome, has been chosen for the example. The meaning of the symbols is as follows: R is the radius of the circular line of axis, β the crown angle, related to the inclination of the line of axis at the crown section, h the constant thickness of the dome profile in the radial direction, l the intrados span, θ the inclination of a generic joint with respect to the vertical axis; moreover, P is the crown thrust, and e its eccentricity with respect to the crown joint’s center of gravity.

Firstly, the stability area ([Figure 3](#), right) is determined for a single lune by assuming nil hoop stresses, according to the procedure illustrated in [\[Aita et al. 2017a\]](#). As in [\[Aita et al. 2015; 2016\]](#), Durand-Claye’s method is extended here to domes by accounting for a nonlinear stress distribution in both tension and compression.

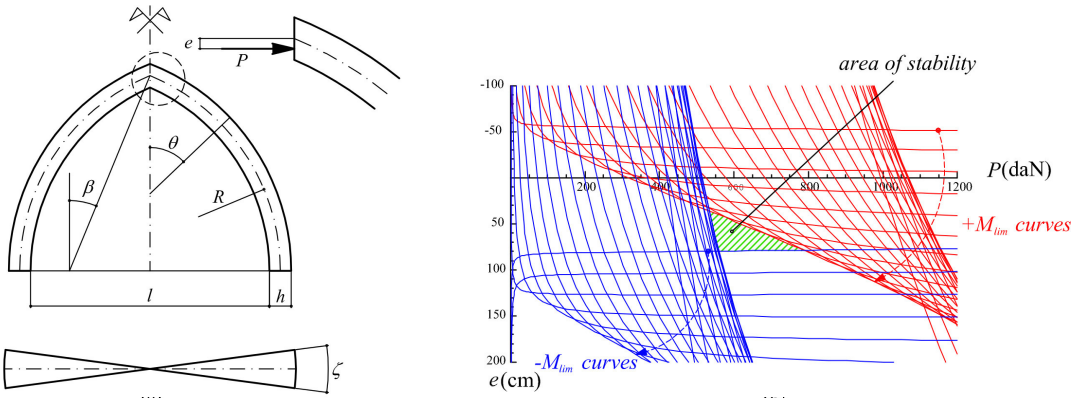


Figure 3. Left: a pointed dome profile. Right: the area of stability associated with a dome’s lune.

Without going into detail (the interested reader is referred to [Aita et al. 2017a]), it is enough to recall that a first set of limitations for the crown thrust arises from the bounded bending moment capacity at the cross-sectional level. By indicating with P and e the crown thrust and its eccentricity with respect to the crown joint's center of gravity, respectively, equilibrium conditions regarding the portion between the crown and any given joint θ along the arch enable obtaining the formal expressions for the axial force, $N(P, \theta)$, and bending moment, $M(P, e, \theta)$, for any θ .

At each joint, the bending moment is limited in absolute value by a limit threshold, M_{lim} , which depends on the local value of the axial force N and masonry's bounded compressive and tensile strengths, σ_c and σ_t , as well. This limit bending moment corresponds to a birectangular distribution of stresses along the joint. In the case of nil tensile strength and infinite compressive strength, as assumed in the following applications, this limit value is given by $M_{\text{lim}} = |Nh/2|$, corresponding to the well-known assumptions proposed in [Coulomb 1776] and revisited in [Heyman 1966]. A second set of limitations would follow from the bounded shear capacity at the cross-sectional level. However, these are not taken into consideration herein, as the friction coefficient is assumed to be infinite.

The curves of the (P, e) plane defined implicitly by equations $|M(P, e, \theta)| - M_{\text{lim}}(P, \theta) = 0$, for θ kept constant, correspond to the locus of points where the bending moment reaches its limit value—whether it be positive or negative. Figure 1 (top middle) shows a plot for each joint θ of the red and blue curves corresponding to the attainment of a positive or negative limit bending moment, denoted respectively as $-M_{\text{lim}}$ and $+M_{\text{lim}}$ curves. In the (P, e) plane, the stability area (the green hatched area in Figure 3, right), bounded by the aforementioned limit curves, is defined as the locus of the points (P, e) corresponding to statically admissible solutions under the hypothesis of nil hoop forces, i.e. for the single lune.

The following describes the reinterpretation of the classical Durand-Claye stability area method developed by the authors in order to account for the presence of hoop forces.

Let us choose the dome thickness, h , as a significant parameter in order to define a limit condition. Firstly note that, if all interaction between adjacent lunes is disregarded, by decreasing h , the stability area for each lune would reduce progressively to a single point in the (P, e) plane. Thus, the corresponding values of crown thrust and eccentricity define a collapse condition for the lune itself, since this point would correspond to an equilibrated solution as well as a kinematically admissible mechanism, which could develop according to one of the two modes shown in Figure 4 [Aita et al. 2015; 2016]. As observed

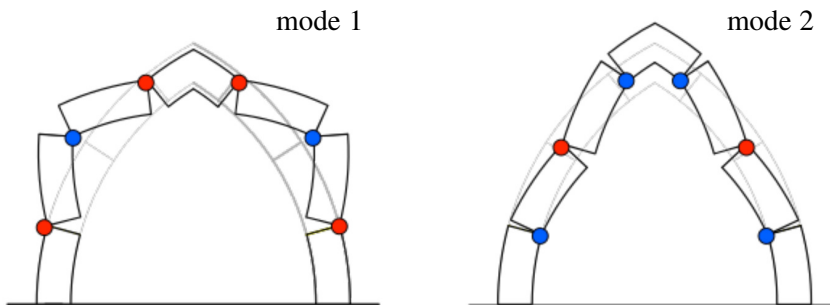


Figure 4. Rotational collapse. Left: mode 1, kinematically admissible for the entire dome. Right: mode 2, not admissible for the entire dome.

in [Heyman 1977], although each lune is considered independently, the collapse mechanism must be a kinematically admissible mechanism for the dome considered as a whole. In this case, only mode 1 is admissible: a central region near the crown of the dome merely descends vertically, while adjacent lunes move apart in the region comprised between the two red hinges (Figure 4, left). On the other hand it is an easy matter to conclude that collapse mode 2 cannot be considered a kinematically compatible mechanism, as it would require some interpenetration between adjacent lunes. In this case, the lateral surfaces of each lune, in particular their portions comprised between the two blue hinges (Figure 4, right) act as constraints, by preventing motion towards inside.

For the reasons reported above, a first significant modification to Durand-Claye's original method is to be made: searching for the limit dome thickness value, h_{lim} , under the assumption that only collapse mode 1 can occur [Heyman 1977; Oppenheim et al. 1989]. To this end, an iterative method has been expressly developed by means of the Mathematica software package. Moreover, as will be explained in more detail in Section 3.2, a second crucial modification to the original Durand-Claye method will be required regarding the action of hoop forces.

3. The case study: the Pisa cathedral dome

The dome of the Pisa cathedral can be dated back as early as the 12th century. It has an elliptical plan and a pointed profile (Figure 5). It is extremely interesting in that it represents quite an original solution, from an architectural as well as a structural point of view [Aita et al. 2017b; Sanpaolesi 1959].

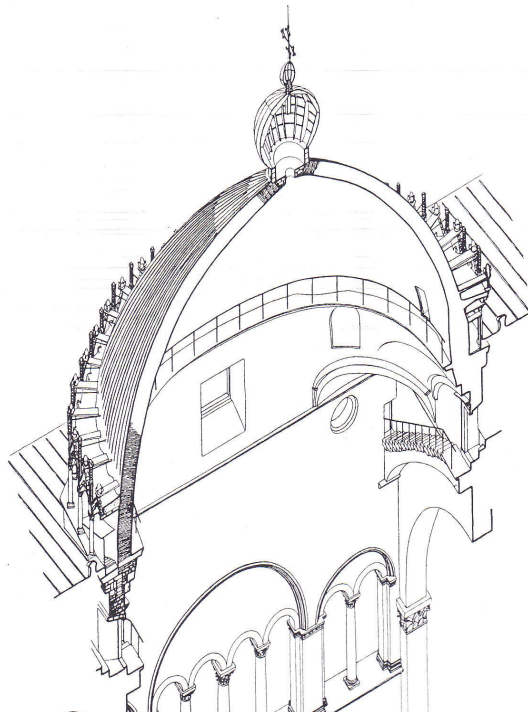


Figure 5. Axonometric view from the survey promoted by the *Istituto di Restauro dei Monumenti* (Florence) [Università di Firenze. Istituto di restauro dei monumenti 1970].

The first issue addressed as preliminary to the structural analysis was to define regular surfaces that allow for a sufficiently simple analytical representation, while at the same time being able to closely approximate the actual shape of the dome intrados and extrados. The results yielded by a geometrical survey of the intrados surface have shown that the meridian sections are approximately circular arcs, and that the oval horizontal sections are well described by ellipses [Aita et al. 2017b]. Hence, the analytical expression for the regular surface chosen to fit the intrados points coordinates was built under the assumption that each horizontal section was an ellipse, while the two vertical sections along the major and minor axes were pointed circular arcs.

The structural analysis of the dome has been performed through formulation of the semianalytical model sketched out in Section 2.2, which will be described in more detail in Sections 3.1 and 3.2. A basic input for this model consists of the representation of the ideal surfaces describing the intrados and extrados geometry, which can be obtained by appropriately processing the output of the survey of the dome (some results of which are reported in [Bennati et al. 2018] and [Aita et al. 2017b]). For the purposes of this study, the analytical representation of the intrados surface proposed in [Barsi 2017] have been taken as a starting point. More in detail, as described in [Bennati et al. 2018; Aita et al. 2017b; Barsi 2017], starting from the laser scanner survey, a postprocessing procedure has been adopted, that yields the dome's intrados and extrados horizontal sections in CAD format from which a representative subset of points has been selected. The coordinates of these points have been used as input data to find the analytically determined best approximating surfaces, described by relatively simple expressions in terms of a few parameters. The search for the parameters' optimal values has been performed by means of a simplified automatic procedure, which makes use of a minimization routine in Mathematica. The results provided by the survey allow for concluding that a fully adequate representation of the extrados surface can be obtained by assuming a conventional, constant dome thickness, h , in the radial direction.

3.1. A first assessment of the dome's stability. Stability of the Pisa cathedral oval plan dome is addressed through Rankine's theorem of transformation of structures [Rankine 1958; Gross 1913]. In brief, the theorem states that if a masonry structure is in equilibrium, that is, if at least one thrust surface is fully contained within the masonry, an affine projection of the structure will also be in equilibrium, and the new thrust surface will be the affine projection of the original. As pointed out in [Huerta 2010], this theorem can be applied to any masonry structure, provided that its compressive strength and friction coefficient are unbounded.

By taking into account the aforementioned theorem, the degree of safety exhibited by the Pisa cathedral dome has been assessed by studying the stability of two ideal domes of revolution whose profiles coincide with those of the actual dome that lie in the two vertical meridian planes passing respectively through the major and minor axes of its elliptical plan (these are the two symmetry planes of the actual dome).

Figure 6 (top left) shows the first dome profile, namely the one in the meridian plane containing the major axis. It presents a crown angle $\beta = 0.405$ rad, and an intrados span $l = 16.30$ m. The second dome under examination, corresponding to the profile along the minor axis, presents a crown angle $\beta = 0.550$ rad, and an intrados span $l = 14$ m. A small amplitude of the lunes ($\zeta = 1^\circ$) and a constant thickness, $h = 0.60$ m, in the radial direction have been considered for both domes of revolution.

In the numerical application, we have assumed an infinite friction coefficient, nil tensile strength, infinite compressive strength, and a specific weight $\gamma = 20$ kN/m³. In passing, note that very similar

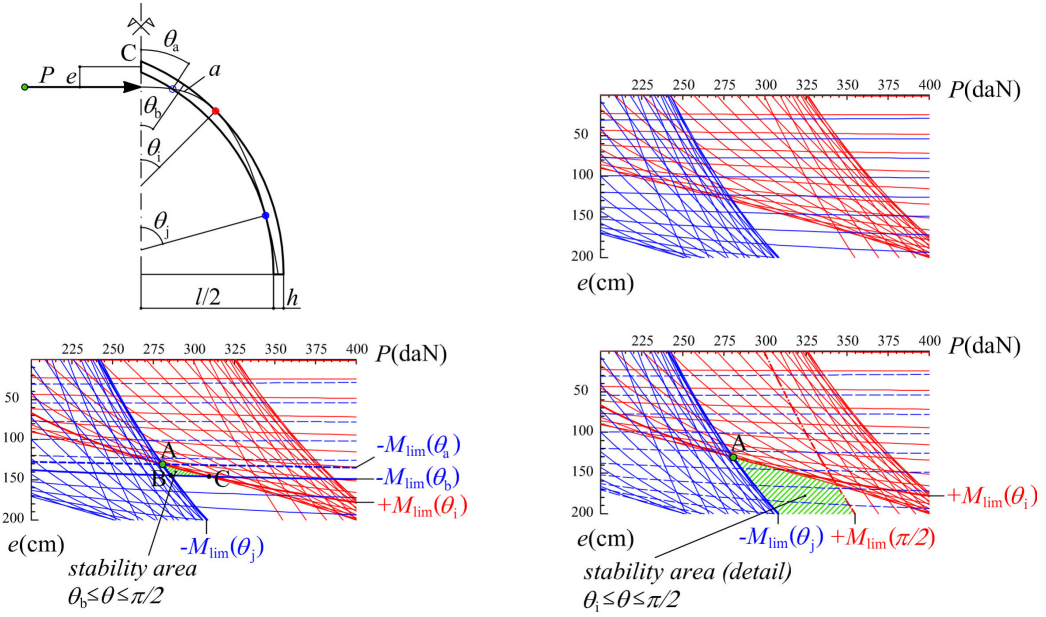


Figure 6. The meridian profile of the Pisa cathedral dome (top left); the limit curves $-M_{\text{lim}}$ and $+M_{\text{lim}}$ in the (P, e) plane, when all (top right) or a selected subset (bottom) of joints are considered.

results would have been obtained by assuming a limited compressive strength for masonry, since this has only a weak influence on the mechanical behaviour of domes subjected to their own weight alone, as the one considered here. In a forthcoming study, the actual masonry mechanical properties will be more accurately taken into account.

As a first step, our analysis begins by assuming that each lune that ideally constitutes the dome can be considered as an independent arch, for which the curves $-M_{\text{lim}}$ and $+M_{\text{lim}}$ in the (P, e) plane are plotted. The problem is solved by means of an expressly developed, in-house algorithm implemented in Mathematica. The limit curves are drawn for a finite number of joints in the radial direction, obtained by subdividing the intrados profile into 60 equal parts. The results thus obtained show that no point in the (P, e) plane could correspond to a statically admissible solution for such a lune (in other terms, the stability area is the empty set, Figure 6, top right). The minimum thickness — corresponding to a unique, statically admissible solution for the lune — would be equal to 1.20 m, which would be twice its actual value. However, what is more important is that at that thickness the lune would undergo collapse according to mode 2 (Figure 4, right), which, as pointed out in the preceding section, is unphysical for the entire dome, since it would require some material interpenetration, as explained in Section 2.2.

Such a clearly unacceptable result shows that it is necessary to account for some distribution of hoop forces to properly assess the dome's stability. To this end, we proceed to the second step of the analysis.

In this stage, the stability area method is effectively modified so as to check for lune stability under the restriction that only collapse mode 1 can occur. Accordingly, we admit the presence of hoop forces in the upper part of the dome only.

The search for a statically admissible solution for the lune is then performed by splitting the problem in two: first, a statically admissible solution is determined for the lower part of the lune, where no hoop forces are allowed, and then static admissibility is restored in the upper part by adding a suitable set of hoop forces.

As per the problem regarding the lune lower part, only a selected subset is considered in the (P, e) plane of all the limit curves that would be required by the standard Durand-Claye's method. This is to say, when the stability area for the single lune turns out to be the empty set, as in the present case (Figure 6, top right), the analysis is performed by progressively disregarding the $\pm M_{\text{lim}}$ curves corresponding to the joints near the crown. The procedure enables finding the inclination $\theta = \theta_a$ (Figure 6, top left), in such a way that the stability area related to the joints $\theta_a \leq \theta \leq \pi/2$ is a single point (point A in Figure 6, bottom left). Note that this limit condition would correspond to a hinge at the intrados of joint θ_a and the activation of collapse mode 2 for the lune portion between this joint and the springing (Figure 4, right).

The coordinates (P_A, e_A) of point A are determined by means of an expressly developed procedure, which operates on the intersection points (P, e) between a suitable set of $+M_{\text{lim}}$ and $-M_{\text{lim}}$ curves. Furthermore, the two joints θ_i and θ_j also are determined. For the case at hand, the coordinates of point A are $P_A = 2.8 \text{ kN}$, $e_A = 1.302 \text{ m}$, while the two joints where a limit condition is attained are $\theta_i = 45.84^\circ$ (positive limit bending moment) and $\theta_j = 74.54^\circ$ (negative limit bending moment). It is worth observing that the corresponding thrust line (Figure 6, top left) touches the arch extrados and intrados at the same joints θ_i and θ_j . However, in the upper portion of the lune (above joint θ_a) the thrust line exits from the intrados.

After determining point A, as well as joints θ_i and θ_j , an extended stability area is found by limiting the analysis to the arch portion that extends from the joint at inclination θ_i to the springing ($\theta = \pi/2$), in order to check if a collapse mechanism corresponding to mode 1 can occur. This stability area is shown in Figure 6 (bottom right) for the dome under examination (the green hatched area): the dashed blue $-M_{\text{lim}}$ curves corresponding to the joints above θ_i are excluded from the analysis. In the present case, the area is extended. Hence, an infinite number of statically admissible solutions become available for the lune portion in the range $\theta_i \leq \theta \leq \pi/2$, and the actual value of h is larger than that allowing for activation of a type 1 collapse mechanism.

By progressively decreasing the value of the thickness, h , a limit value, h^* , can be found, so as to shrink this new stability area back to a single point again. With reference to Figure 6 (bottom right), in the limit case in which the dash-dot red $+M_{\text{lim}}$ curve corresponding to $\theta = \pi/2$ passes through point A, three hinges are formed, consistent with collapse mode 1. Thus, the limit value h^* is compatible with a mode 1 collapse mechanism that is kinematically admissible for the entire dome.

The procedure described above assures that, although the set of internal forces is statically admissible for the bottom part of the lune (defined by $\theta_i \leq \theta \leq \pi/2$), static admissibility is not verified in the upper portion. Some hoop forces are then needed above joint θ_i to obtain fully statically admissible solutions for the entire dome, as will be described in the following section.

3.2. Assessment of the dome's stability in the presence of hoop forces. In order to find statically admissible solutions for the entire lune, the action of hoop forces in the upper part of the dome will now be accounted for. Hoop forces have been introduced in many contributions, both historical and recent (by way of example, see [Lévy 1888; Eddy 1877; Wolfe 1921; Lau 2006; Zessin et al. 2010]). Roughly

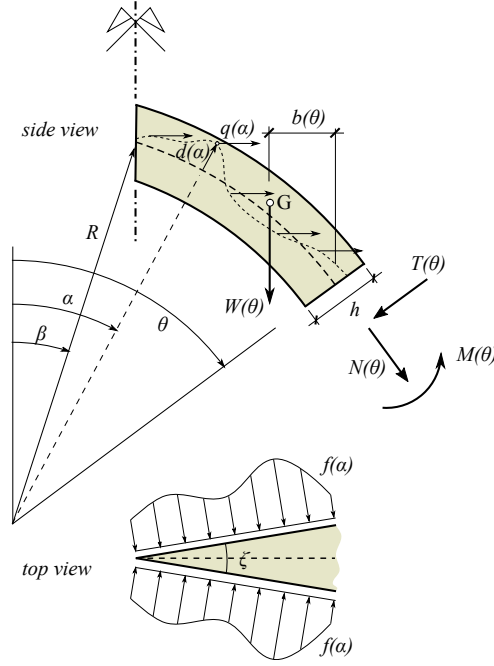


Figure 7. The hoop forces per unit length along the meridian that are exerted on both sides of the lune.

speaking, the presence of hoop forces may be interpreted, as far as lune equilibrium is concerned, as an additional loading term. As schematically represented in Figure 5, the hoop forces per unit length along the meridian, $f(\alpha)$, that are exerted on both sides of the lune result in the horizontal distributed load $q(\alpha)$, possibly acting at a distance $d(\alpha)$ from the middle surface. This additional loading term changes the shape of the thrust line and possibly brings it within the dome thickness.

In order to illustrate the procedure developed to assess dome stability, it turns out to be useful to start by writing the simple, explicit expressions for the internal forces along the lune. With reference to Figure 7, the equilibrium of the lune upper portion, between the crown and any generic joint at inclination θ , is considered. Simple calculations yield

$$N(\theta) = -W(\theta) \sin \theta - \int_{\beta}^{\theta} q(\alpha) R \cos \theta \, d\alpha,$$

$$M(\theta) = -b(\theta)W(\theta) + \int_{\beta}^{\theta} q(\alpha)[(R + d(\alpha)) \cos \alpha - R \cos \theta] R \, d\alpha,$$

where $q(\alpha) = 2f(\alpha) \sin(\zeta/2)$ is the horizontal distributed load due to hoop forces, $W(\theta)$ is the weight of the portion above θ , and b is the distance between its center of gravity, G , and the centroid of the end joint, measured along the horizontal.

In order to assure that the lune is in equilibrium and the internal forces are statically admissible, a suitable distribution $q(\alpha)$, $d(\alpha)$ has to be found so that $N(\theta) \leq 0$ and $|M(\theta)| \leq M_{\text{lim}}$ at any joint.

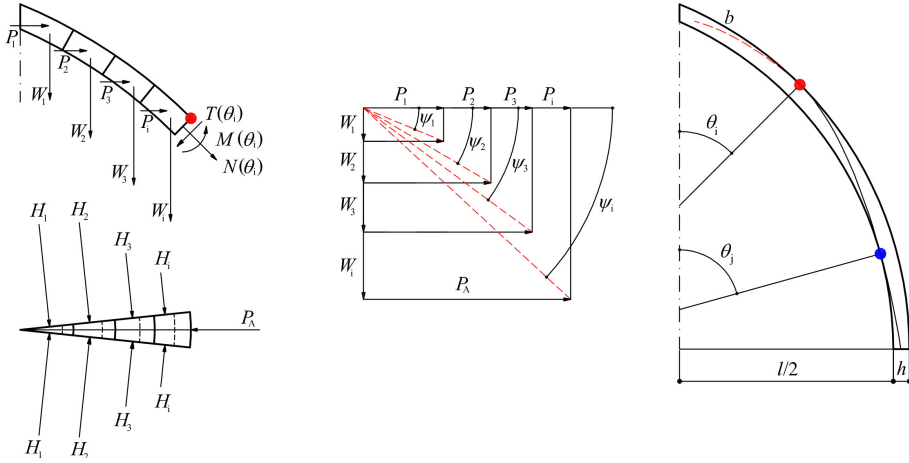


Figure 8. The influence of hoop forces on the portion of the dome's lune above joint θ_1 .

Let us reconsider the thrust line a (Figure 6, top left) corresponding to point A of the stability area plotted in Figure 6 (bottom right). As already observed, in the absence of hoop forces, the internal forces would not be statically admissible within the part of the dome's lune above joint θ_a . Hence, we look for some suitable values for the horizontal load q distributed along the upper part of the lune, that is, above joint θ_1 , where the positive limit bending moment is attained (see the red hinge in Figure 6, top left). The problem is solved numerically by subdividing this portion into a finite number of voussoirs and by approximating q with a set of concentrated forces (Figure 8). The admissibility conditions, $N(\theta) \leq 0$ and $|M(\theta)| \leq M_{\text{lim}}$, are enforced only at the joints separating adjacent voussoirs. Moreover, we add the two end conditions

$$M(\theta_1) = M_{\text{lim}}, \quad \int_{\beta}^{\theta_1} q(\alpha) R d\alpha = P_A, \quad (1)$$

to ensure continuity of the internal forces between the upper and lower parts of the lune.

This problem is easily seen to have multiple solutions; generally, there are infinitely many distributions of q that yield statically admissible internal forces. For our purposes, it is enough to determine one among these solutions.

The lune upper portion, above joint θ_1 , is subdivided into a finite number of voussoirs (in Figure 8, left, for example, four have been plotted). The weights W_1, W_2, \dots, W_i of each voussoir act, respectively, at the corresponding centers of gravity. A set of pairs of hoop forces, H_1, H_2, \dots, H_i , act on the lateral surfaces of the voussoirs. The resultants of each pair of hoop forces are, respectively, the horizontal forces P_1, P_2, \dots, P_i .

The equilibrium of each portion of the lune above joint θ_1 imposes that the resultant's direction at each joint θ_k be given by the angle ψ_k , namely $\tan \psi_k = (W_1 + W_2 + \dots + W_k) / (P_1 + P_2 + \dots + P_k)$ (Figure 8, middle). The internal forces N and M can be easily written for each joint θ_k . At joint θ_1 the two end conditions (1) are imposed, since N and M are known.

In this way, by assigning a set of arbitrary values to both the horizontal forces P_1, P_2, \dots, P_i and the coordinates of their application points, the corresponding thrust line can be found by calculating the

ratio M/N at each joint. Via a trial-and-error process many (in principle, an infinite number of) different statically admissible internal force distributions can be found for the portion of the dome above joint θ_1 , each corresponding to a different thrust surface. Thus, the thrust line a plotted in Figure 6 (top left) can be moved to within the dome thickness (by way of example, line b in Figure 8 (right) represents one such admissible thrust surface).

Via this procedure, statically admissible solutions are determined for each of the two theoretical revolution domes described in Section 3.1, whose profiles correspond to those along the vertical planes containing the major and minor axis of the actual elliptical plan, respectively. This first result suggests that the dome of Pisa cathedral can be considered to be a safe structure.

3.3. A safety factor for the Pisa cathedral dome. In order to define a geometrical safety factor for the dome of the Pisa cathedral, let us consider once again the two theoretical domes of revolution derived from the actual one (see Section 3.1). By decreasing the value of thickness h , while keeping the intrados profile fixed, the procedure described in sections 2.2 and 3.1 allows for determining the limit thicknesses. In particular, for decreasing h , we check the extension of the stability area for the lune lower part (the hatched green area in Figure 6, bottom right), and we look for the thickness that reduces the stability area to a single point on the (P, e) plane. The limit thicknesses, $h_1^* = 29.8$ cm for the first dome, and $h_2^* = 24.5$ cm for the second one, have been determined in this way. When the thickness is set equal to $h_1^* = 29.8$ cm, at least one statically admissible internal forces distribution can be determined for the lower part of both the lunes under consideration. Moreover, by applying the method described in the preceding section, it can be verified that suitable hoop force distributions are found, each corresponding to statically admissible internal forces within the upper part of the lunes, as well. Hence, the ratio $\nu = h/h_{\text{lim}} = 2$, where $h_{\text{lim}} = h_1^*$, can be taken as an estimate of a geometric safety factor for the dome under its own weight. In this case, by assuming the same notation as in Section 3.1, the limit condition — compatible with a kinematically admissible mechanism — occurs when $P = 1.54$ kN, $e = 1.731$ m. The limit bending moment is attained at three joints: $\theta_1 = 50.26^\circ$ (positive limit bending moment), $\theta_j = 74.54^\circ$ (negative limit bending moment), and $\theta_k = 90^\circ$ (positive bending moment).

As already observed at the beginning of Section 3.1, the results obtained for the two domes of revolution considered in this section could be reinterpreted within the framework of Rankine's theorem of transformation of structures [Rankine 1958; Gross 1913], recalled at the beginning of Section 3.1.

For our purposes, the affine transformation to consider is that which maps the middle surface of the larger of the two ideal domes of revolution to that of the actual Pisa cathedral dome. The dome thusly obtained would be of the same shape as the actual one, though its thickness would be slightly variable. In particular, along the major axis of the elliptical plan, the thickness of the projected dome will coincide with that of the actual one, while along the minor axis, the new thickness will be a bit smaller, equal to $60 \times 0.86 = 52$ cm. The projected dome, whose safety factor is still equal to two, would be wholly contained within the actual one, thus suggesting that the dome of Pisa cathedral is a safe masonry structure.

A last remark concerns the role of friction. Since in the present analysis sliding was disregarded, i.e., an infinite friction coefficient was assumed, it is interesting to get a first estimate of the minimum friction coefficient, μ , able to prevent sliding. More precisely, by considering the circular plan dome of limit thickness, $h_{\text{lim}} = h_1^*$ examined above, the ratio $|T/N|$ has been determined between the shear force, T ,

and the axial force, N , acting at each joint. In the lower part of the dome where hoop forces are set to zero, $\theta_1 \leq \theta \leq \theta_k$, $|T/N|$ is easily calculated. Its maximum value is equal to 0.1714 and it is attained at the springing ($\theta = 90^\circ$). In the upper part of the dome, hoop forces are present and an infinite number of different statically admissible distributions of internal forces are allowed at collapse. By considering one of these statically admissible solutions (obtained via a trial and error process, analogous to that reported in Figure 8 and omitted here for the sake of brevity), the maximum value of $|T/N|$ results equal to 0.1723 and it is attained at the joint $\theta = 25.97^\circ$. Hence, if a friction coefficient $\mu > 0.1723$ is assumed, sliding is prevented and only pure rotational collapse modes can occur. This value of μ is low compared the ones likely to be observed in the actual masonry. It is worth observing that the result just obtained concerning the friction coefficient is strictly valid for the circular-plan dome of limit thickness whose intrados surface is circumscribed to the actual one. However, since the ratio between the minor and major axis of the actual elliptic-plan dome is equal to 0.86, not too far from unity, and since the minimum friction coefficient required to prevent sliding is very low, it is reasonable to assume that sliding can be disregarded in the actual dome too.

Further insights on these issues will be provided in a forthcoming paper.

4. Concluding remarks

The present contribution is part of a multidisciplinary research project aimed at studying the structural behaviour of the dome of the Pisa cathedral. In particular, it reports on a preliminary study of the dome's mechanical response by means of a modern translation of Durand-Claye's method.

With reference to domes of revolution, the original Durand-Claye's is suitably modified in order to account for the interaction between the dome's lunes, in terms of kinematic compatibility and hoop force transmission.

The peculiar elliptical plan of the dome of the Pisa cathedral makes it necessary to further modify the method in order to apply it to the present case study. Some first considerations on this issue are advanced by evaluating the stability of two theoretical domes of revolution obtained by considering the profile of the actual dome.

The method allows for determining statically admissible solutions for the two theoretical domes of revolution derived from the Pisa cathedral dome, as well as the limit thickness for both. By considering the ratio between the actual and the limit thicknesses, an estimate of the geometric safety factor for the dome under its own weight has been determined. It turns out to be far larger than the unity, thus suggesting, as expected, that an ample safety factor may be assumed for the dome of the Pisa cathedral under permanent loads.

References

- [Aita et al. 2015] D. Aita, R. Barsotti, and S. Bennati, "Notes on limit and nonlinear elastic analyses of masonry arches", pp. 237–264 in *Masonry structures: between mechanics and architecture*, edited by D. Aita et al., Birkhäuser, Basel, 2015.
- [Aita et al. 2016] D. Aita, R. Barsotti, and S. Bennati, "Influence of the wall shape on the collapse of arch-wall systems", in *Structures and architecture: beyond their limits*, edited by P. J. S. Cruz, 2016.
- [Aita et al. 2017a] D. Aita, R. Barsotti, and S. Bennati, "A modern reinterpretation of Durand-Claye's method for the study of equilibrium conditions of masonry domes", pp. 1459–1471 in *Proceedings of the XXIII Conference of the Italian Association of Theoretical and Applied Mechanics (AIMETA)* (Salerno, Italy), edited by L. Ascione et al., 2017.

- [Aita et al. 2017b] D. Aita, R. Barsotti, S. Bennati, G. Caroti, and A. Piemonte, “[3-dimensional geometric survey and structural modelling of the dome of Pisa cathedral](#)”, *ISPRS Arch.* **XLII-2/W3** (2017), 39–46.
- [Aita et al. 2019a] D. Aita, R. Barsotti, and S. Bennati, “Looking at the collapse modes of circular and pointed masonry arches through the lens of Durand-Claye’s stability area method”, *Arch. Appl. Mech.* (2019), 1–18.
- [Aita et al. 2019b] D. Aita, R. Barsotti, and S. Bennati, “A parametric study of masonry domes equilibrium via a revisitation of the Durand-Claye method”, in *7th International Conference on Computational Methods in Structural Dynamics and Earthquake Engineering* (Crete, Greece), edited by M. Papadrakakis and M. Fragiadakis, 2019.
- [Bacigalupo et al. 2015] A. Bacigalupo, A. Brencich, and L. Gambarotta, “On the statics of the dome of the basilica of S. Maria Assunta in Carignano, Genoa”, pp. 101–126 in *Masonry structures: between mechanics and architecture*, edited by D. Aita et al., Birkhäuser, Basel, 2015.
- [Barsi 2017] F. Barsi, *Equilibrio di cupole ogivali in muratura a base ovale: il caso studio della cupola del duomo di Pisa*, Master’s Degree thesis, University of Pisa, 2017.
- [Beatini et al. 2018] V. Beatini, G. Royer-Carfagni, and A. Tasora, “[The role of frictional contact of constituent blocks on the stability of masonry domes](#)”, *Proc. Royal Soc. A* **474**:2209 (2018), 20170740.
- [Bennati et al. 2018] S. Bennati, D. Aita, R. Barsotti, G. Caroti, G. Chellini, A. Piemonte, F. Barsi, and C. Traverso, “Survey, experimental tests and mechanical modeling of the dome of Pisa cathedral: a multidisciplinary research”, in *Proceedings of the 10th IMC — 10th International Masonry Conference* (Milan, Italy), edited by G. Milani et al., 2018.
- [Block and Lachauer 2014] P. Block and L. Lachauer, “[Three-dimensional funicular analysis of masonry vaults](#)”, *Mech. Res. Commun.* **56** (2014), 53–60.
- [Block and Ochsendorf 2007] P. Block and J. Ochsendorf, “[Thrust network analysis: a new methodology for three-dimensional equilibrium](#)”, *J. IASS* **48**:155 (2007), 167–173.
- [Bossut 1774] C. Bossut, “Recherches sur l’équilibre des voûtes”, *Mem. Ac. Roy. Des Sc.* (1774), 534–566.
- [Bossut 1778] C. Bossut, “Nouvelles recherches sur l’équilibre des voûtes en dôme”, *Mem. Ac. Roy. Des Sc.* (1778), 587–596.
- [Bouguer 1734] P. Bouguer, “Sur les lignes courbes qui sont propres à former les voûtes en dôme”, *Mem. Ac. Roy. Des Sc.* (1734), 149–166.
- [Coulomb 1776] C. Coulomb, “Essai sur une application de règles de maximis et minimis à quelques problèmes de Statique, relatifs à l’Architecture”, pp. 343–382 in *Mémoires de Mathématique et de Physique présentés à l’Académie Royale des Sciences*, vol. 17, 1776.
- [D’Ayala and Tomasoni 2011] D. F. D’Ayala and E. Tomasoni, “[Three-dimensional analysis of masonry vaults using limit state analysis with finite friction](#)”, *Int. J. Archit. Herit.* **5**:2 (2011), 140–171.
- [Durand-Claye 1867] A. Durand-Claye, “Note sur la vérification de la stabilité des voûtes en maçonnerie et sur l’emploi des courbes de pression”, *Ann. des Ponts et Chaussées* **13** (1867), 63–93.
- [Durand-Claye 1880] A. Durand-Claye, “Vérification de la stabilité des voûtes et des arcs: applications aux voûtes sphériques”, *Annales des Ponts et Chaussées* **19**:I sem. (1880), 416–440.
- [Eddy 1877] H. T. Eddy, *New constructions in graphical statics*, D. Van Nostrand, New York, 1877.
- [Foce and Aita 2003] F. Foce and D. Aita, “The masonry arch between ‘limit’ and ‘elastic’ analysis: a critical re-examination of Durand-Claye’s method”, pp. 895–908 in *Proceedings of the first international congress on construction history* (Madrid), vol. II, 2003.
- [Foraboschi 2014] P. Foraboschi, “[Resisting system and failure modes of masonry domes](#)”, *Eng. Fail. Anal.* **44** (2014), 315–337.
- [Gross 1913] J. Gross, *Die Beziehung zweier einander räumlich affiner Gewölbe in statischer Hinsicht*, Ph.D. thesis, München, Technischen Hochschule, 1913.
- [Heyman 1966] J. Heyman, “[The stone skeleton](#)”, *Int. J. Solids Struct.* **2**:2 (1966), 249–279.
- [Heyman 1977] J. Heyman, *Equilibrium of shell structures*, Oxford University Press, 1977.
- [Huerta 2007] S. Huerta, “Oval domes: history, geometry and mechanics”, *NNJ* **9**:2 (2007), 211–248.

- [Huerta 2010] F. S. Huerta, “Designing by geometry: Rankine’s theorems of transformation of structures”, pp. 262–285 in *Geometría y proporción en las estructuras: ensayos en honor de Ricardo Aroca*, edited by P. Cassinello et al., Lampreave, 2010.
- [Lamé and Clapeyron 1823] M. G. Lamé and E. Clapeyron, “Mémoire sur la stabilité des voûtes”, *Annales des Mines* **VIII** (1823), 789–836.
- [Lau 2006] W. W. Lau, *Equilibrium analysis of masonry domes*, MSc dissertation, Massachusetts Institute of Technology, 2006.
- [Lévy 1888] M. Lévy, *La statique graphique et ses applications aux constructions*, Gauthier-Villars, Paris, 1888.
- [Mascheroni 1785] L. Mascheroni, *Nuove ricerche sull’equilibrio delle volte*, Francesco Locatelli, Bergamo, 1785.
- [Navier 1839] C. L. M. H. Navier, *Résumé des leçons données à l’École des Ponts et Chaussées sur l’application de la mécanique à l’établissement des constructions et des machines*, Bruxelles, 1839.
- [Oppenheim et al. 1989] I. J. Oppenheim, D. J. Gunaratnam, and R. H. Allen, “Limit state analysis of masonry domes”, *J. Struct. Eng. (ASCE)* **115**:4 (1989), 868–882.
- [Pavlovic et al. 2016] M. Pavlovic, E. Reccia, and A. Cecchi, “A procedure to investigate the collapse behavior of masonry domes: some meaningful cases”, *Int. J. Archit. Herit.* **10**:1 (2016), 67–83.
- [Poleni 1748] G. Poleni, *Memorie istoriche della Gran Cupola del Tempio Vaticano*, Stamperia del Seminario, Padova, 1748.
- [Rankine 1958] W. J. M. Rankine, *A manual of applied mechanics*, Griffin, London, 1958.
- [Rapallini and Tempesta 1997] M. Rapallini and G. Tempesta, “Limit analysis of masonry domes”, in *Computer methods in structural masonry-4: proceedings of the fourth international symposium on computer methods in structural masonry* (Florence, Italy), edited by G. N. Pande et al., Taylor & Francis, 1997.
- [Sanpaolesi 1959] P. Sanpaolesi, “Il restauro delle strutture della cupola della Cattedrale di Pisa”, *Bollettino d’Arte* **XLIV**:III (1959), 199–230.
- [Simon and Bagi 2016] J. Simon and K. Bagi, “Discrete element analysis of the minimum thickness of oval masonry domes”, *Int. J. Archit. Herit.* **10**:4 (2016), 457–475.
- [Tempesta et al. 2015a] G. Tempesta, M. Paradiso, S. Galassi, and E. Pieroni, “Maurice Lévy’s original contribution to the analysis of masonry domes”, *Domes and Cupolas* **2**:2 (2015).
- [Tempesta et al. 2015b] G. Tempesta, M. Paradiso, S. Galassi, and E. Pieroni, “The Structural analysis of polygonal masonry domes: the case of Brunelleschi’s dome in Florence”, *Domes and Cupolas* **2**:2 (2015).
- [Università di Firenze. Istituto di restauro dei monumenti 1970] Università di Firenze. Istituto di restauro dei monumenti, *Il Duomo di Pisa, rilievo a cura dell’Istituto di Restauro dei monumenti*, Nistri-Lischi, 1970.
- [Varma and Ghosh 2016] M. N. Varma and S. Ghosh, “Finite element thrust line analysis of axisymmetric masonry domes”, *IJMRI* **1**:1 (2016).
- [Venturoli 1833] G. Venturoli, *Elementi di meccanica*, 5th ed., Napoli, 1833.
- [Wolfe 1921] W. S. Wolfe, *Graphical analysis: a text book on graphic statics*, McGraw-Hill, New York, 1921.
- [Zessin et al. 2010] J. Zessin, W. Lau, and J. Ochsendorf, “Equilibrium of cracked masonry domes”, *Proc. Inst. Civ. Eng. Eng. Comput. Mech.* **163**:3 (2010), 135–145.

Received 16 Jun 2018. Revised 4 Apr 2019. Accepted 12 Apr 2019.

DANIILA AITA: danila.aita@unipi.it

Department of Civil and Industrial Engineering, University of Pisa, Largo L. Lazzarino 2, 56122 Pisa, Italy

RICCARDO BARSOTTI: riccardo.barsotti@unipi.it

Department of Civil and Industrial Engineering, University of Pisa, Largo L. Lazzarino 2, 56122 Pisa, Italy

STEFANO BENNATI: s.bennati@ing.unipi.it

Department of Civil and Industrial Engineering, University of Pisa, Largo L. Lazzarino 2, 56122 Pisa, Italy

EXPERIMENTAL AND NUMERICAL STUDY OF THE DYNAMIC BEHAVIOUR OF MASONRY CIRCULAR ARCHES WITH NON-NEGLIGIBLE TENSILE CAPACITY

ALEJANDRA ALBUERNE, ATHANASIOS PAPPAS, MARTIN WILLIAMS AND DINA D'AYALA

Continuous arches and vaults made of cohesive materials with low but nonzero tensile strength, such as Roman concrete, are a common feature in historic and monumental structures, many of them sited in earthquake-prone regions. The effect of tension capacity on the dynamic behaviour of masonry vaulted structures has scarcely been studied. We describe a series of shaking table tests on model-scale, continuous circular arches of 1m span, with the aims of assessing the effect of tensile capacity on mechanism formation, evaluating the structures' lateral acceleration capacity and comparing their performance to that of voussoir arches. While tested arches fail by forming a four-link mechanism like the no-tension voussoir arch, significant differences in behaviour between continuous and voussoir arches are observed, including: differences in hinge positions; higher accelerations required to initiate rocking; cracking of material required to form hinges; inability of hinges, once formed, to close and move to a different location (travelling hinges). Conventional limit analysis, whose basis includes an assumption of zero tensile strength, is a suitable analytical tool for voussoir arches, but is shown to be inaccurate when applied to arches having a modest tensile capacity. The experimental observations are modelled using nonlinear finite elements Abaqus/Explicit dynamic analysis algorithm, from commercial software Abaqus 2017. By applying the concrete damage plasticity numerical material law, good agreement is obtained between the tests and the numerical predictions, supporting the formation of collapse mechanisms that significantly differ from the mechanisms observed for no-tension arches. Finally, the numerical model is upscaled to study full-size arches with a span of 4m, obtaining results that align with the experimental observations and do not agree with observations and models for the no-tension voussoir arch, evidencing the need to account for tensile capacity of vaulted structures when assessing their dynamic capacity.

1. Introduction

Modern analysis of masonry structures under the framework of plastic theory was established in the second half of the 20th century [Kooharian 1952; Heyman 1966]. It treats masonry as rigid and embraces the three classic axioms stated in the 18th century by Couplet [1729]: infinite compressive strength, zero tensile strength, and no sliding. Under these premises, the only possible failure for a masonry structure is through the formation of a kinematically admissible mechanism by developing rotational hinges. Such mechanism depends purely on geometry and loading conditions, including self-weight.

The axioms that support this theory are simplifications of the material properties that respond to observations of masonry failure over time. They are, however, open to question. As early as 1806, Monasterio explored the possibility of sliding failure in mechanism formation [Albuerne and Huerta

Keywords: arches, shaking table tests, dynamic analysis, Roman concrete, dynamics of masonry.

2010]. Later, Livesley [1978] formulated limit analysis for 2D block structures accounting for frictional forces on the interfaces. Livesley [1992] extended this analysis to 3D arches introducing Coulomb friction at the block interfaces. Casapulla and D'Ayala [2001] incorporated nonsymmetric loading in order to establish when sliding failure becomes a limiting factor.

The axiom of “zero tensile strength” is commonly redefined as “zero tensile strength at the joints” [Boothby 2001], recognising that masonry blocks do resist tensile stresses and hinges tend to open at the joints, where the mortar is typically weaker, may have experienced decay or may not be present. Under this assumption, hinges are free to form at any joint in the structure. There are, however, numerous masonry constructions that present a level of tensile strength at joints exerting a resistance against separation of masonry blocks. An important category of vaulted structures exhibiting some tensile strength is ancient Roman construction made of Roman concrete, as exemplified by the remains of the Basilica of Maxentius in Rome [Giavarini 2005; Albuerne and Williams 2017].

The failure of vaulted structures with a moderate capacity to withstand tensile forces has received limited attention in the literature. While zero tensile strength may be a safe assumption for structures under static loads [Heyman 1966], its safety for structures subject to dynamic loading has not been demonstrated.

Smars [2000; 2008] explored the applicability of limit analysis to vaulted structures that feature both some tensile strength and finite friction and proposes the existence for certain structures of a "potentially stable" domain in addition to the classic stable and unstable domains.

Ramaglia et al. [2016] explored the problem applied to barrel vaults subject to dynamic lateral loading and proposed accounting for tensile strength in limit analysis by applying an expansion of the boundaries of permissible positions of the line of thrust. This simplified model does not account for the quasi-brittle nature of typical masonry materials. These materials experience an immediate drop in strength post crack initiation that leads to a redistribution of stresses after every crack forms. As a result, in the general cases the maximum moment capacity is not experienced simultaneously at all hinges.

This paper explores the effect that moderate tensile strength has on the failure of vaulted masonry structures subject to dynamic loading. The paper describes novel shaking table tests on cohesive, continuous arches made of quasi-brittle material and subject to cyclic base motion, comparing their performance to that of zero-tension voussoir arches. It further presents the results of a fully dynamic computational analysis using nonlinear finite elements (NLFE) carried out to understand the experimental findings regarding the formation of the first hinge through the opening of a crack.

2. Dynamic behaviour of the voussoir circular arch

The study of the no-tension voussoir or dry-joint arch is an insightful step towards understanding the behaviour of vaulted masonry structures. It has been explored in the literature as a fundamental element of masonry vaulted systems, with a particular focus on the constant-thickness circular arch, as related in this section. The circular arch has a simple geometry that can be easily constructed using similar voussoirs, be these cut stones or bricks. This arch has been used repeatedly throughout the history of construction in buildings, gates or bridges. It often features fill on the extrados, in particular in bridges, which can have a significant impact on its structural behaviour, as explored by Pulatsu et al. [2019]. Addressing the arch by itself, without including the effect of fill and isolating it from the performance of abutment

systems, is a significant step in exploring the mechanical performance of masonry structures, as it does not introduce additional complexities [Heyman 1969] and thus the findings are easier to interpret. The study of the circular arch by itself is primarily a theoretical question that contributes towards understanding the capacity of masonry vaulted structures.

The stability of simple arches has been examined for centuries (see [Huerta 2004] for a detailed account). From the formulation of plastic theory for masonry by Heyman [1966], limit analysis has been applied to examine simple circular arches in 2D under the three fundamental axioms (see, e.g., [Heyman 1969; Ochsendorf 2002; Makris and Alexakis 2013]), as well as considering possible sliding failure (e.g., [Livesley 1978]). The problem has been studied in 3D in works such as [Smars 2000; Casapulla and D'Ayala 2001], exploring the effect of finite Coulomb friction and eccentric loading, concluding that friction is the limiting parameter in a range of not uncommon occasions.

The behaviour of the voussoir arch under seismic lateral loads has been explored more rarely. Static-equivalent approaches aimed at identifying the minimum horizontal load required to initiate a mechanism in a circular arch when acting in combination with gravity loads have been explored in works such as [Otto 1983; Oppenheim 1992; Clemente 1998; Ochsendorf 2002; Alexakis and Makris 2014]. Most studies of this problem employ energy formulations to determine the point of mechanism formation.

Shaking table tests to explore the dynamic behaviour of voussoir arches have been reported in [2007; 2010; 2013; 2017]. A nonsymmetric four-hinge mechanism, hereon referred to as 4-link mechanism, has been observed to form (see Figure 1), with hinge D systematically opening on the extrados at one of the supports and hinge B opening near the crown. The phenomenon of travelling hinges is normally observed, with hinges shifting from one joint to the next as the motion progresses.

The dynamic behavior of arches has been studied analytically. Oppenheim [1992] developed an analytical model for the behaviour of the arch 4-link mechanism during the first half-cycle of a cyclic base motion, before the first impact of the rocking motion occurs. The model was extended in [2007] to include behaviour after impact, presuming that the mirror mechanism will open as rocking reverses.

Different computational approaches have been applied to modelling the dynamic response of voussoir arches. Discrete element modelling (DEM) has been frequently adopted as the most effective computational framework for modelling discontinuities and capturing the mechanics of loose block structures [Lemos 2007]. DEM has been applied to study the dynamics of no-tension voussoir arches subject to base motion (see, e.g., [Lemos 2001; Alexakis and Makris 2016], obtaining good agreement between

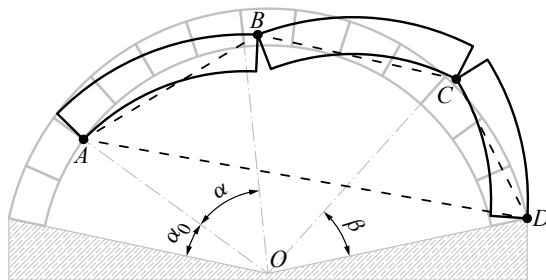


Figure 1. Typical four-link mechanism failure for zero-tension voussoir arch.

modelling and experimental results (see, e.g., [DeJong et al. 2008; Albuerne et al. 2013]). The development of (NLFEM) has enabled the application of finite element modelling (FEM) to the problem of collapse of dry-joint masonry structure. See Section 4.1 for a brief review of the literature.

In spite of the deep interest of the dynamic performance of the dry-joint voussoir arch, in many vaulted structures the material exhibits some bond between the blocks. As a result, hinges are not “free” to open at any joint in the structure and must be the result of fracture of the material. In the following sections, the behaviour of vaults with (low) tensile strength is explored.

3. Experimental tests on circular arches with non-negligible tensile strength

Semicircular continuous arches were subject to cyclic base motion on a shaking table, testing samples to increasing load until cracking and subsequent collapse occurred. This section summarises the construction and testing procedure.

3.1. Geometry of arch specimens. Specimens were semicircular arches (angle of embrace of 180°), with parallel intrados and extrados, and internal span of 900 mm; see Figure 2, left. Three thicknesses were tested: $t = 62$ mm (giving $t/r_m = 0.13$), $t = 67$ mm ($t/r_m = 0.14$) and $t = 72$ mm ($t/r_m = 0.15$).

3.2. Material of arch specimens. Arches were made of a quasi-brittle mortar having natural hydraulic lime (NHL 5.0) as binder and washed sharp sand (average particle size of 1.2 mm) as aggregate. This material aimed to replicate the behaviour of moderately cohesive masonry in the fashion of Roman concrete. The tensile strength was kept as low as practically possible for handleability considerations. The average ratio of lime, sand and water by volume was 1 : 3.2 : 0.88, with small variations in water content to achieve desirable workability of the mix.

The material properties were characterised through a testing campaign of three-point bending tests on pre-notched samples, 300 mm long and 50 × 50 mm in cross-section. A series of 35 control samples with lime-sand volume ratio of 1 : 3.2 were tested (see Figure 11 for a summary of results). As a quasi-brittle material, mortar exhibits a progressive drop in strength with increased deformation beyond the point of maximum load [Karihaloo and Huang 1991], as shown in the typical test result in Figure 2, right. The exact form is dependent on mix details and on the internal microstructure, including the number, size and

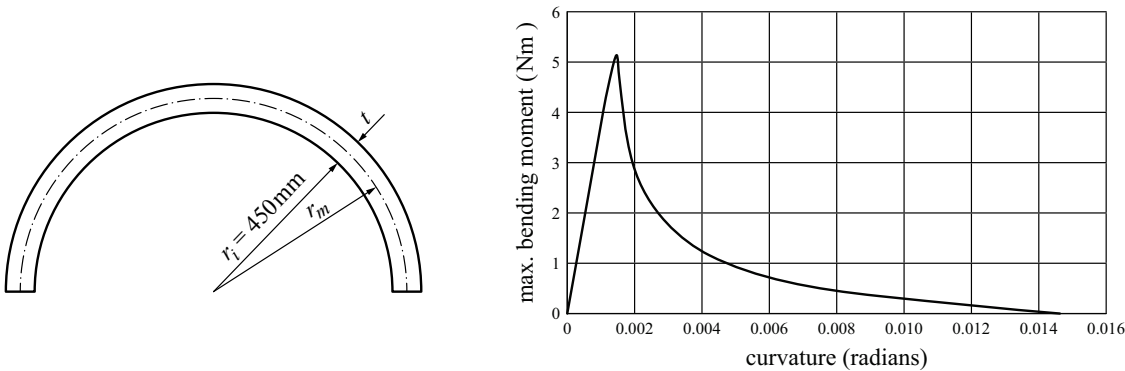


Figure 2. Left: semicircular arch geometry. Right: corrected moment-rotation curve for a three-point-bending test of lime mortar used in test specimen construction.

Lime mortar: 1 : 3.2 : 0.88 volume ratio (lime:sand:water)

compressive strength = 1.65 MPa tensile strength = 0.426 MPa (S.D. 0.108) density = 18.7 kN/m³

Hadrian's Villa: Vaults of *Sala a tre essedre* [Giavarini et al. 2006]

compressive strength = 4.5 MPa tensile strength = 0.77 MPa density = 17.7 kN/m³
compressive strength = 5.87 MPa tensile strength = 0.88 MPa density = 17.7 kN/m³

Table 1. Material properties of mortar used in experiments compared with available strength tests performed on original Roman concrete samples.

distribution of internal pores and cracks [Shah and Ouyang 1994]. Inherent variability in the values of peak load and curve shape between different samples of the same material has been observed, resulting in a variability of tensile strength f_t and fracture energy G_f , consistent with other tests on modern concrete, also a quasi-brittle material, and reproductions of ancient Roman mortar [Samuelli Ferretti 2000; Brune 2010]. The mean material properties of the mortar mix were: density 1870 kg/m³, compressive strength 1.65 MPa, tensile strength 0.426 MPa (SD: 0.108 or 25.3%) and fracture energy 7.85 Nm/m² (SD: 2.67 or 34.0%). The tensile strength is obtained as the peak tensile strength experienced by the test sample, calculated using the maximum bending moment recorded in the bending moment vs curvature plot for each three-point bending test. The fracture energy is obtained by computing the area under the bending moment vs curvature curve, introducing the corrections given by [Planas and Elices 1985; Rodriguez del Viso 2008]. The standard deviation values reflect the inherent variability of the material properties.

Based on scaling theory, the scaling relationship can be obtained by considering a vertical cantilever of density ρ , length L , and cross-sectional depth d , subject to an inertial lateral acceleration a [Albuerné 2016]. The ratio of fracture stress f_f to maximum bending stress f_b is given by

$$\frac{f_f}{f_b} = \frac{f_f d}{3L^2 \rho a}.$$

This ratio should be preserved in the test specimen. Using '*' to represent the quantities in the test specimen compared to the unstarred real prototype values, we have

$$\frac{f_f d}{3L^2 \rho a} = \frac{f_f^* d^*}{3L^{*2} \rho^* a^*}.$$

Given that linear dimensions will scale the same and that accelerations scale at unity (to preserve similitude of stresses due to gravity and lateral acceleration), the resulting scaling relationship for these model arches is given by

$$\frac{f_t^2}{f_t} = \frac{\rho^*}{\rho} \cdot \frac{L^*}{L}.$$

Taking Roman concrete as a reference material, we obtain that the density ratio is approximately equal to unity while the tensile strength of the real material as tested by Giavarini et al. [2006] is 2 to 3 times higher than the characteristic value for the lime mortar (Table 1). This results in the test specimen being representative of real Roman concrete arches with a span twice as long, which is approximately 2 m.



Figure 3. Support conditions for arch samples on shaking table with rubber padded metal brackets on both intrados and extrados to prevent sliding, while a degree of rotation can be expected.

3.3. Test procedure. Tests were performed on a uniaxial shaking table in the Oxford Structural Dynamics Laboratory (University of Oxford), comprising a 1 m square platform running on horizontal linear bearings. It is driven by a single 10 kN Instron servo-hydraulic actuator that can apply unidirectional displacement amplitudes up to ± 75 mm. Arches were simply supported on the table, with sliding prevented by padded brackets placed on both sides of the supports (Figure 3). These support conditions could be representative of arches and vaults supported on metal brackets or beams, such as is sometimes encountered in 19th and early 20th timber vaults. In the case of masonry vaults with continuity down the supports, such as Roman concrete structures, these support conditions represent a singular theoretical case in which cracks exist at the base of the arch. While real structures are commonly cracked, the typical crack pattern for a circular arch comprises three cracks, with a crack at midspan and a crack at each support. The present setup without the midspan crack is nonetheless an interesting case to analyse as the degree of static indeterminacy is reduced to 1, which simplifies the study.

While elastic response spectra are not appropriate for identifying the seismic response of highly inelastic structures [Douglas et al. 2015] pulse-type excitations representing the principal impulse of an earthquake wave have been found to be appropriate simplifications of near-source ground motions for appraisal of rocking structures [DeJong and Ochsendorf 2010; Makris and Roussos 2000; Campillo et al. 1989]. Given their continuous derivatives, sine pulses were chosen, in agreement with [Zhang and Makris 2001; Gaetani et al. 2017]. To prevent large acceleration spikes at the start and end of the test, ramped attack and decay cycles were added as shown in Figure 4 [Williams et al. 2012].

Because tests involved large motions, fracture and collapse, particle image velocimetry (PIV) was used to track the motion of the specimens. GeoPIV software by White et al. [2003] is based on high-density-image and single-exposure multi-frame PIV and is designed to be applied to conventional (non-rectified) digital images. A speckle pattern was applied to the front face of each arch to facilitate accurate tracking and a reference static grid was introduced to provide scale (see Figure 5). A black-and-white high-speed camera was used, recording 250 fps (time step 4 ms) at a resolution of 1024×512 pixels. Further details of the PIV implementation can be found in [2015].

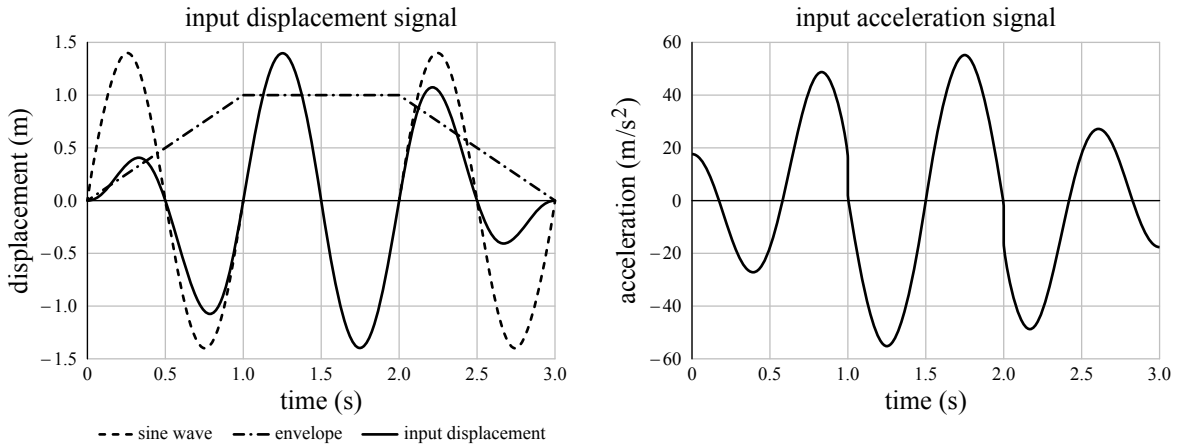


Figure 4. Input displacement signal (left) and corresponding input acceleration (right). Scaled to the appropriate amplitude and frequency at time of testing. Note discontinuities in gradient of acceleration signal, resulting from the second derivative of the envelope applied to displacement signal.

Differences were observed between the ideal input motion (Figure 4) and the motion observed by the tested arches (Figure 5). These are caused by the shaking table controller, which rectifies the actuator motion to correct the displacement. The parameters of the controller were adjusted to prioritise a smooth acceleration wave.

3.4. Experimental results. The arches were tested under pulses of increasing amplitude and/or frequency until accelerations that generated crack formation and subsequent collapse were reached. In this section the main observed failure mechanism is described and the acceleration levels required to cause failure are presented. The differences in behaviour between continuous arches and discrete voussoir arches are highlighted.

The mode of failure of the tested arches is by forming a four-link mechanism, as illustrated in Figure 5. This shows snapshots of arch deformation showing how deformations vary with time, the corresponding mechanism diagrams and the displacement and acceleration time signal. The time signal plots present the displacement and acceleration recorded for the top centre section of the arch (in bold) and the command signal sent to the table (lighter dashed line). As expected, the signals diverge significantly as the arch collapses, after around 0.5 s. Imperfect actuator control results in the introduction of a higher frequency component in the motion, most clearly visible in the acceleration plot. The numbering i–iv below refers to the photos in Figure 5.

- i–ii As the acceleration reaches a peak, hinges open in positions *B* (crack opening on the intrados) and *C* (crack opening on the extrados). Together with the hinges at the two supports, a four-hinge mechanism is formed. Close examination of high-speed camera images reveals that the crack that forms hinge *B* becomes visible before that for hinge *C*.
- iii–iv The arch may then either directly collapse, toppling in the direction of the acceleration that generated the mechanism, or (more often) rock to collapse in the following half cycle, its motion having

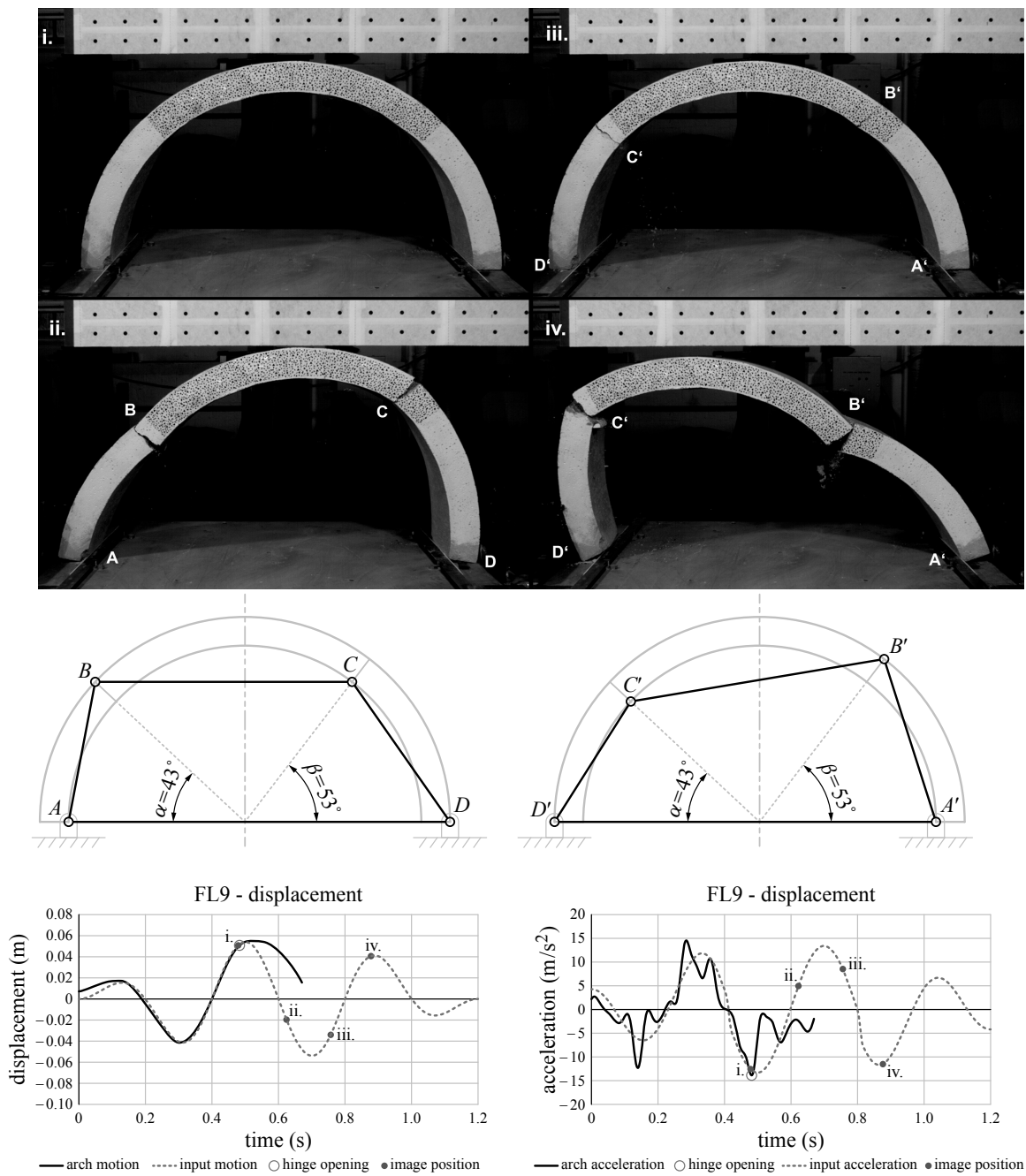


Figure 5. Hinge formation and collapse of tested arch by forming a four-link mechanism (test specimen FL9). The photos at the top illustrate the steps in the collapse; the diagrams in the middle row show the initial four-link mechanism and subsequent reversed mechanism; the bottom row plots the displacement and acceleration at the centre of the arch, showing the position of images i–iv and the formation of cracks. The first image, labeled i, is taken an instant before cracks form at positions B and C, seen in image ii.

test	t/r_m	acceleration at hinge formation	hinge position (angle from base)	
			Hinge B	Hinge C
FL1+	0.13	1.12 g	52°	55°
FL2	0.13	1.00 g	57°	49°
FL3	0.13	1.07 g	52°	59°
FL4*	0.13	1.05 g	62°	52°
FL5	0.14	1.44 g	67°	61°
FL7	0.14	1.21 g	61°	41°
FL8+	0.15	1.42 g	51°	54°
FL9	0.15	1.42 g	43°	53°
FL10	0.15	1.49 g	53°	44°
FL11	0.15	0.91 g	51°	41°

Table 2. Summary of results for tests showing four-hinge mechanism. See Figure 1 for the definition of hinges B and C, and Figure 6 for Test FL9. Entries marked † experienced direct collapse without rocking; those marked * returned to equilibrium after rocking.

reversed. In a small number of tests, the arch rocked repeatedly, returning to its equilibrium position at the end of the test.

Table 2 summarises the ten tests failing by mobilisation of a four-link mechanism. The horizontal acceleration at onset of the mechanism (crack formation) and the hinge positions are provided. There is a degree of variability in acceleration at the onset of cracking that is understood to be directly related to the variability of the material discussed in Section 3.1. The standard deviation in acceleration at hinge formation corresponds to 4.1% for $t/r_m = 0.13$; 8.7% for $t/r_m = 0.14$; and 17.8% for $t/r_m = 0.15$, all smaller than the standard deviation for the material properties f_t and G_f .

Hinge positions for the tested arches are illustrated in Figure 6. Hinges A and D open at the supports, where there is no resistance to rotation. Hinges B and C open on either side of the centreline of the arch, at significantly similar distance. This is different from the minimum horizontal acceleration mechanism

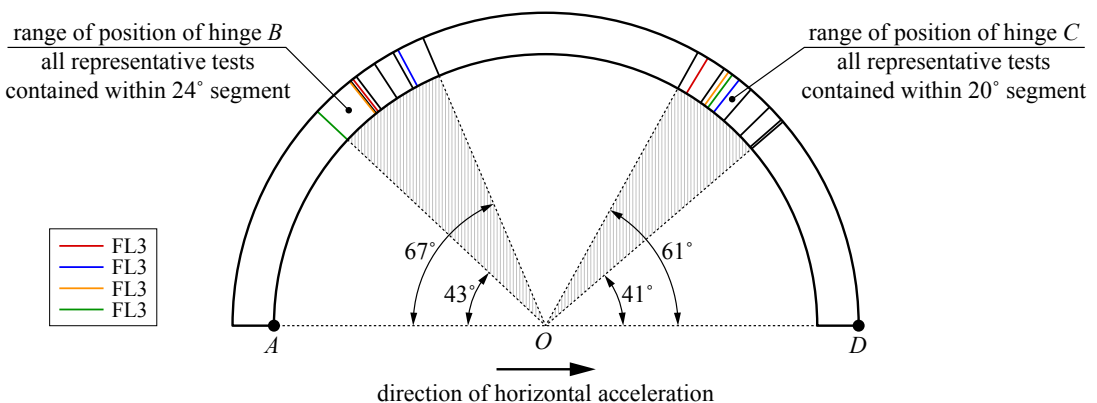


Figure 6. Summary of hinge positions for tests forming a 4-link mechanism.

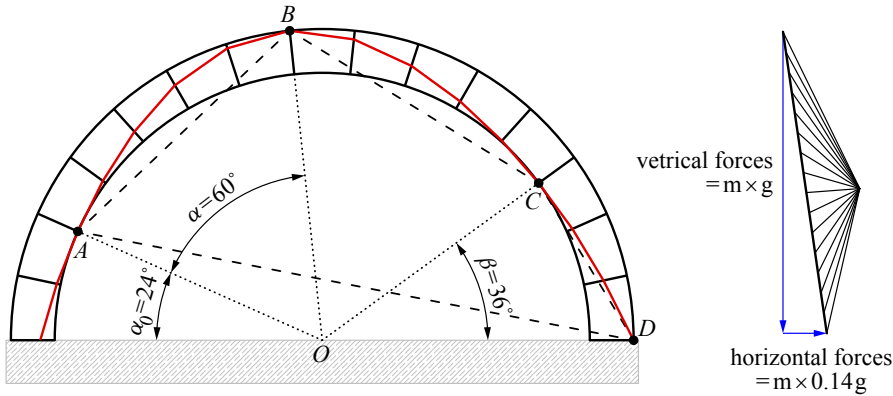


Figure 7. Minimum-acceleration 4-link collapse mechanism for a discretized zero-tension voussoir arch with $t/r_m = 0.15$ and 15 voussoirs, computed by static-equivalent limit analysis: in red, thrust-line; in blue, acting static-equivalent forces as part of the corresponding polygon of forces.

obtained for the zero-tension voussoir arch, shown in Figure 7 for the same $t/r = 0.15$, discretized into 15 equal voussoirs. This mechanism is calculated using limit analysis for the voussoir arch subject to gravity and inertial loads caused by the minimum lateral acceleration required to mobilise a mechanism [Ochsendorf 2002], applying the method of graphic statics. DeJong and Ochsendorf [2010] observed the limit analysis mechanism to match that observed in experimental dynamic tests.

The position of hinges B and C also presents variability between tests. The observed location of each of these hinges lies within a bracket of approximately 20° . This variation is exemplified in the difference between tests FL8 and FL9, identified in colour in Figure 6. While the acceleration at crack formation for these two tests is very close, the position of the hinges is visibly different. Hinge C opens almost at the same place, while hinge B is shifted by 8° , resulting in different angle BOC (75° for FL8 and 84° for FL9). Another example is found in comparing tests FL3 and FL4, also experiencing cracking at similar levels of lateral acceleration. In this case, the angle BOC is similar in both tests (69° for FL3 and 66° for FL4), but is shifted by 10° towards hinge D .

These differences in position are linked to the aforementioned variability of the material, together with the dynamic nature of the loading. The random distribution of the microstructure of the material can lead to the existence of points along the arch where crack initiation is more likely. The distribution of internal stresses within the arch is constantly changing throughout the shaking table test, with the position of maximum stresses shifting along the arch.

Shaking table tests have been performed on voussoir arches with similar span and $t/r_m = 0.15$, applying the same form of base motion [Albuerne et al. 2013]. Voussoir arches also rocked and collapsed by forming four-link mechanisms, but there are significant differences in behaviour with quasi-brittle arches:

In quasi-brittle arches two of the four hinges open at the supports (A and D) as a result of the finite tensile strength along the arch, while in voussoir arches these hinges are free to form at other points, as observed in shaking table tests.

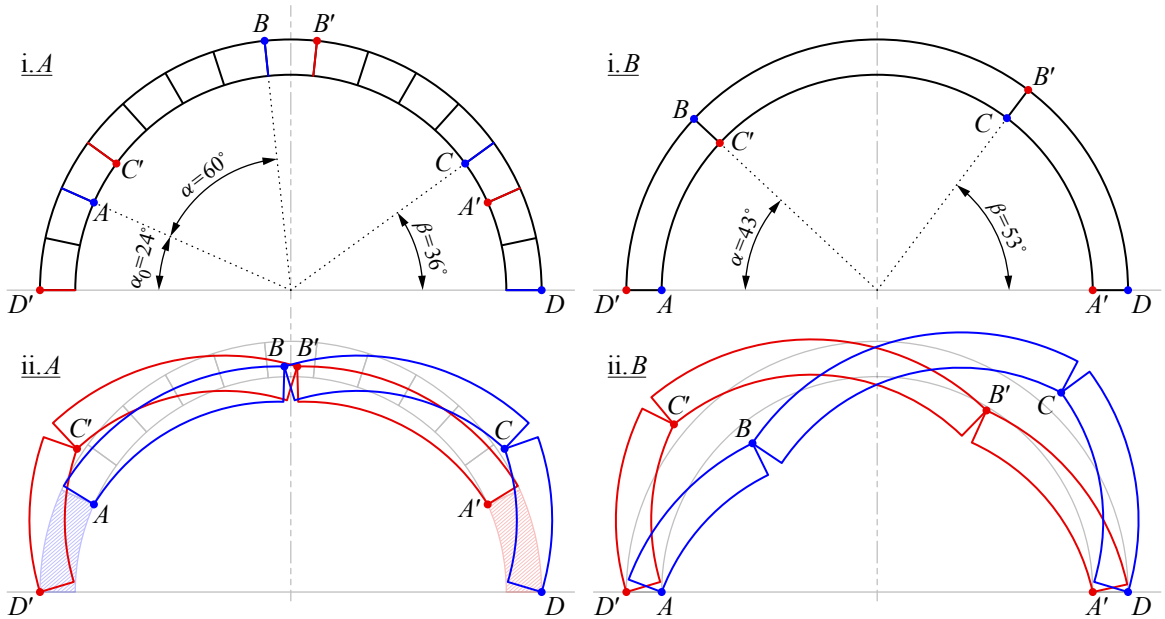


Figure 8. Comparison of failure mechanism between voussoir (A) and quasi-brittle (B) arches, for $t/r_m = 0.15$: initial mechanism (in blue) and reverse mechanism (in red). Voussoir arch mechanism based on static-equivalent limit analysis (Figure 7).

When the voussoir arch rocks, the mirror mechanism tends to form when motion reverses, which requires different joints to open when motion reverses (see Figure 8). On the contrary, in quasi-brittle arches, exactly the same cracks serve as joints when the motion reverses, resulting in two different mechanisms forming, depending the direction of the rocking.

The travelling hinge phenomenon is observed in voussoir arches, while this is not present in quasi-brittle arches.

Figure 8 also illustrates the difference in location of the “internal” hinges B and C between voussoir and quasi-brittle arches.

4. Nonlinear finite element models of undamaged arches

4.1. Description of the finite element model. The numerical model is developed with the finite element (FE) commercial software Abaqus 2017 [Abaqus 2017]. The Abaqus/Explicit dynamic analysis algorithm is used which applies a consistent, large-displacement theory that allows large rotations and large deformations. The explicit algorithm marches a numerical solution forward through time in small time increments without solving a coupled system of equations at each increment nor forming a global stiffness matrix, which often becomes ill-conditioned under extensive material damage. This makes it a stable and computationally efficient algorithm for analysing highly nonlinear and transient dynamic behaviours [Abaqus 2017; Karapitta et al. 2011]. The numerical modelling presented in this work follows the continuum mechanics approach, broadly used for quasi-brittle materials such as unreinforced concrete, adobe and masonry [Lourenço et al. 2007; Pela 2008; Roca et al. 2010; Tarque et al. 2014].

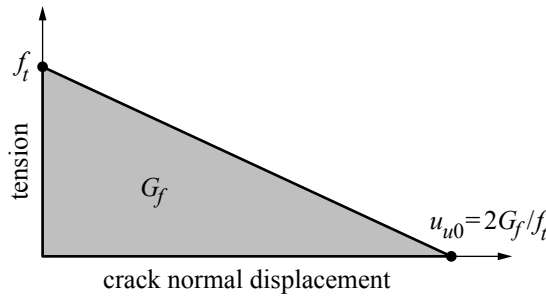


Figure 9. Linear tension softening; where u_{u0} is the crack normal displacement at which complete loss of tensile strength takes place.

A two-dimensional model of the concrete arch and the steel base is created. Structured mesh with the four-node reduced integration plane stress elements CPS4R is used. The mesh size varies between 9.5 and 11 mm. Using reduced integration elements and having multiple elements across the thickness helps avoiding shear locking and hourglass phenomena which can affect slender structures under bending load [Belytschko et al. 1984; Zienkiewicz et al. 1971]. The steel base is modelled with linear elastic properties whereas the concrete damage plasticity (CDP) smeared-crack model is used for the mortar arch. In this material law, the stress-strain curves of the material are treated separately for tension and compression. CDP has been based on the on Lee1998, Lubliner1989 and has been widely used in analysis of historic structure made of quasi-brittle materials such as roman concrete [Ivancic et al. 2014] and masonry with a degree of cohesion [Humberto et al. 2013; Milani and Valente 2015; Silva et al. 2017].

Regarding the properties of the CDP model, the concrete dilation angle ψ is taken as $= 30^\circ$ and the parameter K as 0.666. The compressive strength of the concrete is taken as 10 MPa. Since in the experimental campaign the concrete arch is observed to break due to tensile stresses, the stress-strain curve for tension is the most influential parameter of the CDP model. Linear tension softening (see Figure 9) is adopted for the post-peak stress-strain branch of the tension curve [Abaqus 2017; Hillerborg et al. 1976]. The softening branch of the curve is calculated from the tensile fracture energy (G_f). According to this law, when the maximum principal stress exceeds the tensile strength (f_t), a crack is formed in the plane orthogonal to the direction of principal tensile stress. Various combinations of f_t and G_f , based on the material characterisation of the tested arches, are considered for the numerical analysis (see Figure 11).

The base motion is applied as horizontal displacements on the steel base of the FE model, whereas the steel base is fixed in the vertical direction. A sufficiently small time-step of 0.0001s is used for the discretisation of the input motion. The contact surfaces between the arch and the steel base are governed by Coulomb friction law with an assumed friction angle equal to 12° ($\mu = 0.2$) and zero cohesion, based on qualitative observations of low friction during experimentation. A lateral gap of around 0.5 mm is introduced between the arch and the intrados and extrados brackets that are modelled as part of the steel base. This gap is modelled to represent the irregularities present at arch supports in the experimental configuration that led to small amounts of relative displacement between the arch specimen and the shaking table. The support configuration in the FE model also allows rocking at the supports similar to the structural behaviour manifested during the shaking table tests.

The model investigates the development of the failure pattern and specifically the formation of the first crack. There are two limitations for using the model for prediction of formation of second crack and, moreover, for prediction of collapse. One limitation is the characterization of crack growth in the experimental material, lime mortar: the material law used has been developed for concrete, which, in spite of similarly being a quasi-brittle material, has a different internal macro- and microstructure to that of lime mortar. As such, there may be differences in the rate of growth of a crack between the two materials that could have a significant impact on the formation of subsequent cracks under dynamic loading. The second limitation is the fact that, once a crack is fully developed, the FE code is unable to treat that crack as a new dry-contact surface. This affects the way the crack responds to large displacements, which can be of significance in a shaking table test of the nature of those being modelled. As a result, the details of the formation of the second and any subsequent cracks will not be examined closely.

4.2. Modelling the formation of the first crack.

FEM analysis of tested arch model. The nonlinear FE model is tested and calibrated against experimental test FL9, the details of which, including arch motion and geometry of failure mechanism, are given in Figure 5 and Table 2. The input motion applied to the model is that experienced by the arch on the shaking table test, amplified until failure of the model is observed. The lime mortar batch used for the fabrication of this arch, with lime-sand-water ratio of 1:3.2:0.88, is characterised by a single three-point bending test, yielding a value of tensile strength f_t of 0.516 MPa and fracture energy G_f of 8.645 Nm/m². These values fall comfortably within the range of material tests results obtained for the mortar. Because a single sample was tested, the characteristic (mean) values obtained for the material are used in the FE model ($f_t = 0.426$ MPa; $G_f = 7.85$ Nm/m²).

Figure 10 summarises the results obtained from the FE analysis. The overall shape of the failure mechanism matches that observed in the experiment in that hinges A and D form at the supports, with the first hinge forming by cracking the material.

The FE model is aimed at predicting the formation of the first crack, where agreement between analysis model and experiment is very close. The first crack forms hinge B, with the crack initiating on the intrados at an acceleration peak of the input motion. The model predicts the formation of the crack at an angle of 44° from the closest support (hinge A), which compares well with the experimental result of 43°. The model overpredicts the acceleration at which the crack forms by approximately 23%, with the first crack forming at a base acceleration of 1.75 *g* while in the shaking table test the crack opened when the arch experienced an acceleration of 1.42 *g*.

The analysis is repeated for the material parameters obtained for the FL9 batch sample given above, obtaining a very similar result. Cracking acceleration is 1.74 *g* and hinge B forms at an angle of 40° from hinge A.

There are two factors that can explain the overprediction in acceleration at failure. The first is the existence of imperfections and irregularities in the physical sample subject to experimental testing. The second is the fact that the material properties are characterised by a single material sample, while it has been observed that there is an inherent variability in the properties of the material and this sample could have overestimated the characteristic strength of the mortar batch.

Parametric variations of tensile strength f_t and fracture energy G_f . A parametric study of the behaviour of the circular arch under base motion varying the tensile capacity of the material is carried out in order

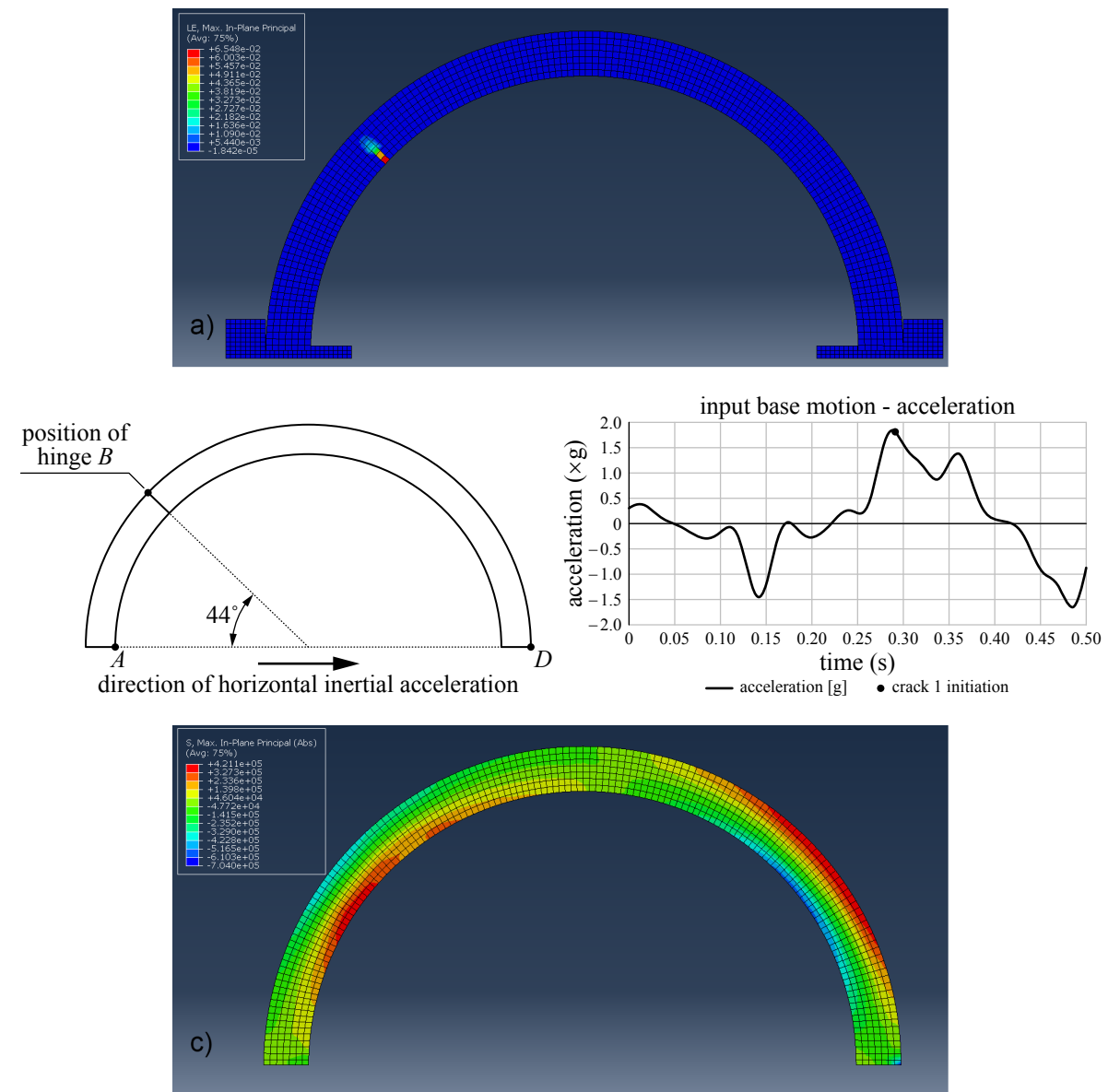


Figure 10. Nonlinear FE results for model of tested arch FL9. Top: numerical model of the arch, showing the formation of the first crack. Middle: position of formation of the first crack (left) and input motion, indicating the time of formation of first crack (right). Bottom: stress distribution at the initiation of first crack.

to explore how the tensile capacity affects the response of a masonry material under dynamic loads. The tensile capacity is defined by two parameters, the tensile strength f_t and the fracture energy G_f , both of which are required for defining the material law used in the model, CDP.

The three-point bending tests carried out to characterise the material evidenced a correlation between tensile strength and fracture energy (Figure 11). A parametric variation of tensile strength is proposed,

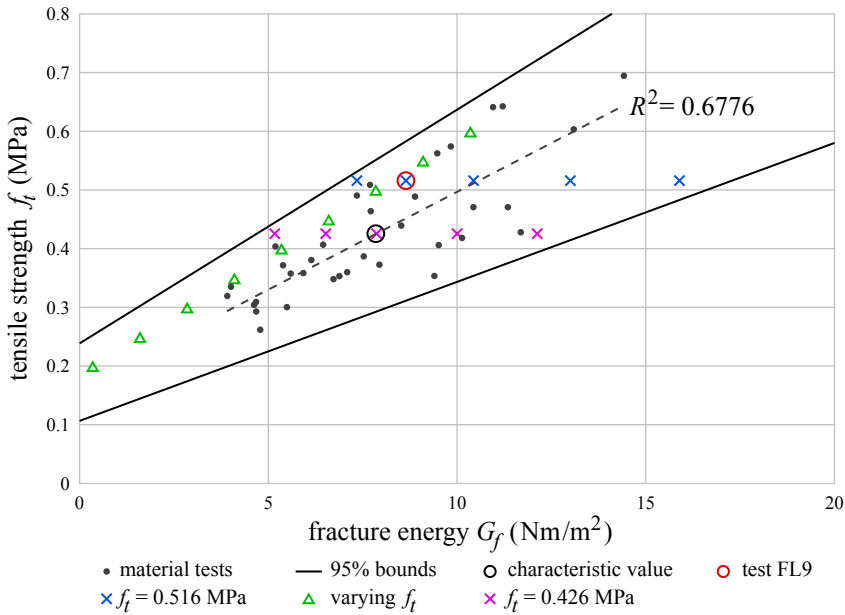


Figure 11. Lime mortar material tensile strength f_t vs. fracture energy G_f , presenting material characterisation test results (in black) and values adopted for FE analysis (in colour).

adjusting the fracture energy using a linear correlation as shown in Figure 11. In addition, the effect of the fracture energy in the model is studied by considering two series of variation of fracture energy at constant tensile strength: 1) $f_{t1} = 0.516$ MPa, the tensile strength for the tested arch FL9; and 2) $f_{tk} = 0.426$ MPa, the lime mortar characteristic strength. The tested series are also shown in Figure 11.

The results of the variation of tensile strength with adjusted fracture energy according to a linear relationship are summarised on Figure 12, where the horizontal acceleration at crack initiation is plotted against the tensile strength. A linear variation can be seen in the lower section of the curve, while a plateau in horizontal acceleration at crack formation is reached as the tensile strength increases.

The dynamic nature of the load results in a constantly changing stress distribution. The peak tensile stress continuously shifts along the arch as the ratio between vertical and horizontal inertial loads changes. In the presence of horizontal acceleration, the stress distribution is asymmetric, with the point of maximum sagging bending shifting from midspan to the windward side of the arch for the given verse of the applied acceleration.

A point of maximum hogging bending appears, displaced from the midspan in the opposite direction. Sagging bending generates tensile stresses on the intrados, i.e., leading to hinging about the extrados. This hinge, which corresponds to hinge B (Figure 10) is the first one to materialise in the analysis, as was seen for FL9, with the first crack initiating on the intrados of the arch, displaced from the midspan of the arch. This behaviour agrees very well with the observations from experimental tests. In the analyses, all first cracks were contained in a small arch segment ranging from 43° to 58° from hinge A (Figure 12). The position of the crack appears to depend on the tensile capacity of the material. For lower capacities,

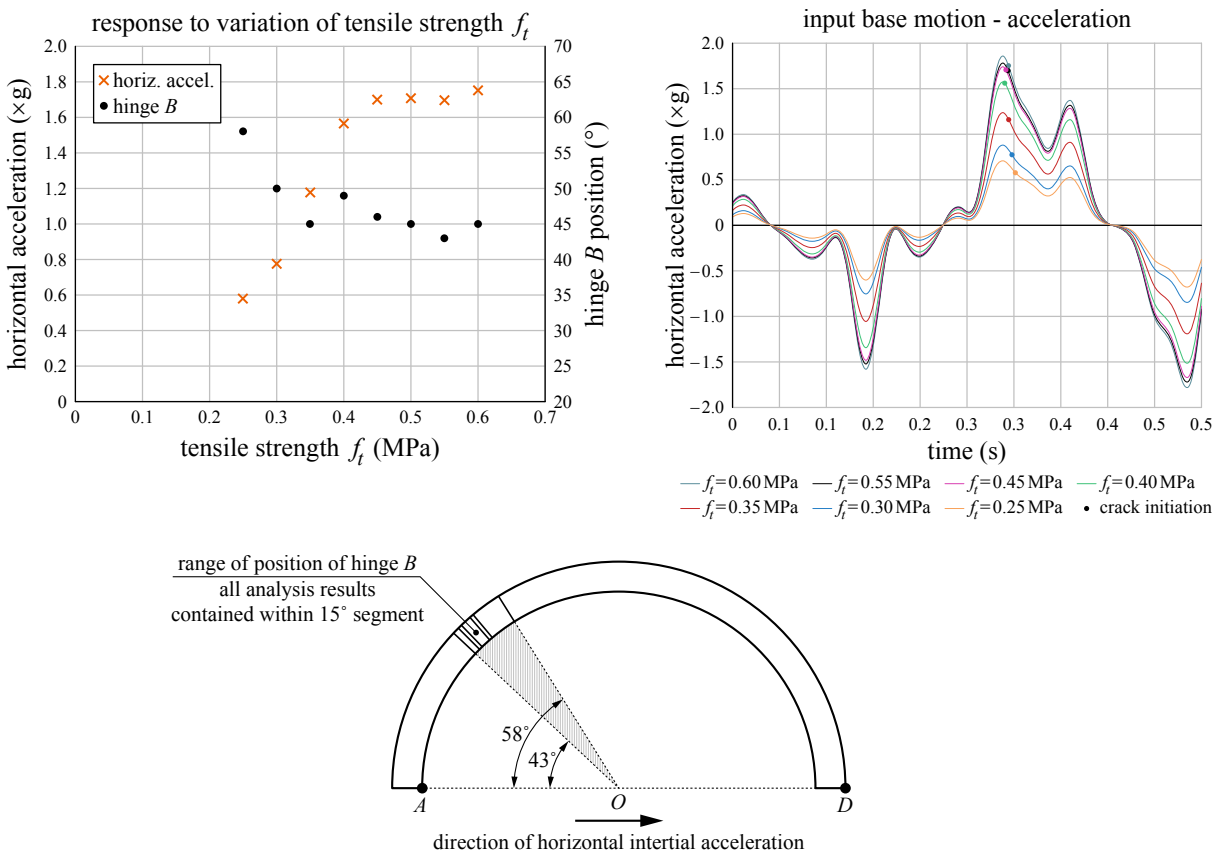


Figure 12. Summary of nonlinear FE models of failure of continuous arches for variation in tensile strength f_t . Top left: horizontal acceleration at initiation of first crack vs. tensile strength f_t . Top right: input motion at failure for selected values of tensile strength f_t , giving the point of initiation of the first crack. Bottom: position of first cracks, corresponding to hinge B in all cases.

hinge B forms further from the support and closer to the value of the AOB angle for zero tensile capacity (Figure 7). This angle reduces as the tensile capacity increases, stabilising around 45° for the larger capacity values analysed.

In the experimental tests the position of hinge B was recorded to fall within an arch segment ranging from 43° to 67° from hinge A (Figure 6). This bigger spread in experimental tests can be explained by the possible existence of material imperfections that can result on weak points where cracks can more readily form.

The results of the parametric variations of fracture energy for constant tensile strength are presented in Figure 13. The values of fracture energy are evenly spread within the 95% bounds of the material characterisation tests (see Figure 11). The results evidence a strong dependence of crack formation on

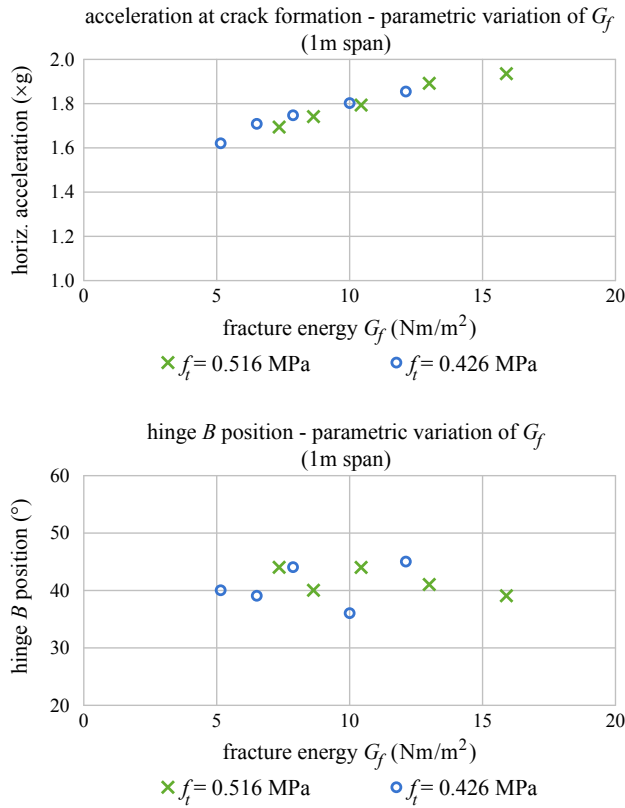


Figure 13. Summary of nonlinear FE models of failure of continuous arches for variation in fracture energy G_f : Top: Horizontal acceleration at initiation of first crack vs. fracture energy G_f ; bottom: Hinge B position vs. fracture energy G_f .

fracture energy, highlighting the importance of this parameter in the behaviour of masonry with non-negligible tensile capacity. The position of the crack, however, does not show a strong correlation with fracture energy variation, suggesting that position may be more strongly related to the tensile strength.

4.3. Simplified static-equivalent analysis of precracked arches. When the first crack opens in the mortar arch, there is a sudden drop in strength at the cross section of the crack and internal stresses experience an immediate redistribution. Furthermore, the formation of this first crack generates a 3-pinned arch. In this condition the arch can be simplified as a statically determinate 1D structure that can be analysed using equilibrium equations only (Figure 14).

This simplified model is used for predicting the position of the second and final crack, the crack that becomes the fourth hinge in the arch and turns it into a mechanism.

The formation of the final crack has been computed for all arches subject to shaking table tests given in Table 1. The first crack is treated as a hinge and the simplified structural model is subject to the inertial loads resulting from gravity and from the lateral acceleration that has generated the first crack. Under these loads, the point of maximum tensile stress is taken as the estimate of the position where the final crack will form. The predicted position is given in Figure 15.

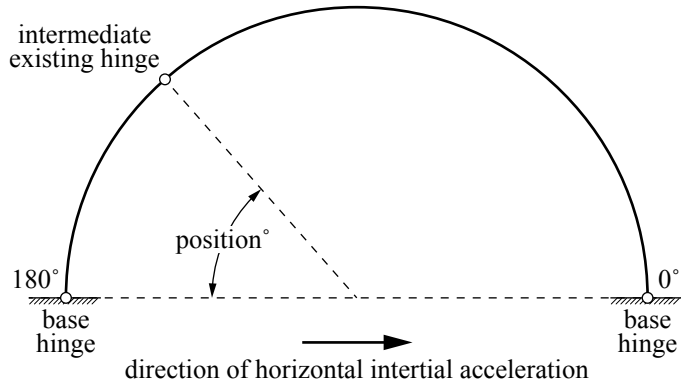


Figure 14. Simplified structural model of 3-pinned arch for the analysis of the cracked arch to estimate the position of the formation of the second and final crack.

These results evidence that the simplified 1D statically-determinate model is appropriate for predicting the formation of the fourth hinge in the structure, with 50% of predictions lying within 5° of the experimental observations and 80% of predictions being within 10° of the experiments.

4.4. Modelling the behaviour of full-size arches. It has been shown that the FE model can reliably simulate the results of the experimental tests of specimens, which are scaled representation of prototypes 2-3 times larger (Section 3.2). With the intention of better understanding how real masonry structures behave under seismic loading, a second FE model is created to represent full-size structures and to capture more realistic characteristics.

The size of the model is increased to 4m in order to represent 4m span real arches. The tensile strength of the material is increased to $f_t = 0.820$ MPa, the average value of existing experimental results for Roman concrete in the literature (Table 1), representative of real full-size structures. The fracture energy for this tensile strength is computed to be $G_f = 16.25$ Nm/m², in accordance with the correlation established from the material data in Figure 11. The contact properties between the arch and the base are also modified to replace the laboratory conditions of an arch resting on a smooth metal plate. The coulomb friction coefficient μ is raised from 0.2 to 0.7, a value that falls in the range of results for experimental characterization of masonry joints [Vasconcelos et al. 2008; Jafari et al. 2017].

Failure occurs at a base horizontal acceleration of 0.73 g. The failure pattern observed in the full-size arch model is similar to that of the scale model, with the first crack opening at 58° from hinge A at the support (Figure 16, top), which lies within the range of crack formation positions observed experimentally and agrees with the trend observed numerically for the specimen arches, with larger angles for proportionately lower tensile capacities (Figure 12). A small degree of sliding of the arch with respect to the supporting base occurs as a result of the discontinuity at the support, as observed in the scaled arches. Increasing the coefficient of friction to assimilate masonry joints reduces the sliding velocity of the large arches, thus introducing a difference in dynamic behaviour with respect to the analysis of scaled arches. This results in differences in the instant of crack formation observed in the acceleration signal (Figure 16, bottom).

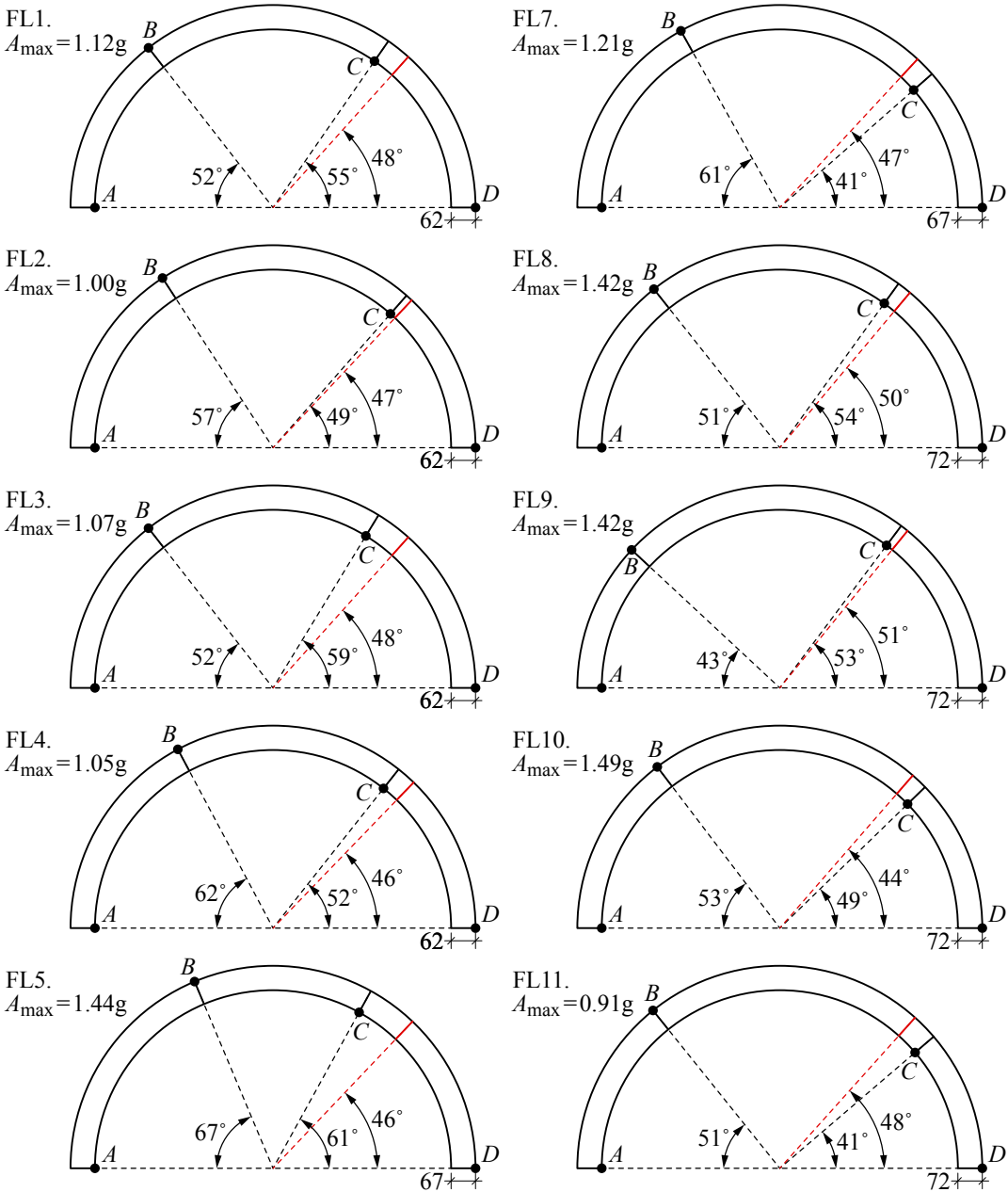


Figure 15. Predicted position for the formation of second and final crack (in red) for the arches subject to shaking table tests based on the simplified 3-pinned arch model, compared to the observed crack position (in black).

Applying the simplified analysis for precracked (3-pinned) arches described above, the second crack and final hinge (hinge C) opens at 45° from hinge D at the support. This final mechanism differs significantly from the mechanism for the zero-tension similar arch given in Figure 7.

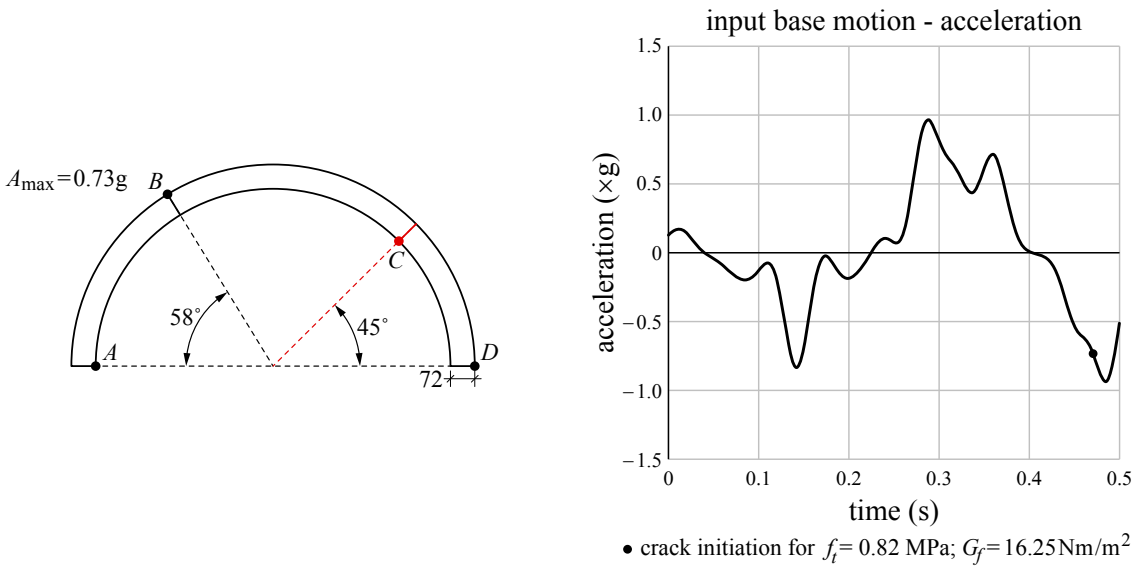


Figure 16. Summary of results of analysis of 4m span FE model, tensile strength $f_t = 0.820 \text{ MPa}$ and fracture energy $G = 16.25 \text{ Nm/m}^2$. Left: position of first crack corresponding to hinge B as predicted numerically and position of final crack corresponding to hinge C predicted analytically based on 3-pinned arch model. Right: input motion at failure giving the point of initiation of the first crack.

This model supports the relevance of the experimental observations that the presence of low tensile capacity in masonry arches has a significant impact in the structural response to dynamic horizontal loading, resulting in the formation of a mechanism that is different to that of a zero-tension arch and that requires the formation of hinges through fracture of the material.

5. Conclusions

The seismic stability of continuous, quasi-brittle arches with a small but non-negligible tensile strength is a subject of great importance in the preservation of historic structures in earthquake-prone regions. Examples include arches, vaults and domes built in Roman concrete, or built with cohesive mortar, such as timbered vaulting.

Shaking table tests have been performed on quasi-brittle semicircular arches made of lime mortar (hydraulic lime-to-sand volume ratio of 1:3.2) with 1m span to explore the behaviour of masonry arches with non-negligible tensile strength. The lime mortar, which presents a variability in material strength that is typical of quasi-brittle materials, has been characterised to have a tensile strength $f_t = 0.426 \text{ MPa}$ (SD: 25.3%) and a fracture energy $G_f = 7.85 \text{ Nm/m}^2$ (SD: 34.0%). Based on available material tests of samples taken from real existing structures, these experimental arches are representative of real Roman concrete arches 2-to-3 times larger, that is, with a span between 2m and 3m, according to the scaling relationship that the scaling of the tensile strength must be equal to the scaling of the linear dimensions.

Results show clear and consistent patterns of behaviour of these arches that evidence significant effect of the tensile capacity. Arches fail by forming a collapse mechanism and present a degree of variation of failure acceleration (acceleration at formation of first hinge), with SD up to 17.8%, and hinge position that are nonetheless within the inherent variation of the material.

Compared to the geometrically similar no-tension voussoir arch, the tested arches fail at larger peak horizontal accelerations and, while they fail through the formation of a four-link mechanism like the no-tension arch, the position of the hinges is different. Instead of the strongly nonsymmetric mechanism of the nontension arch, in the tested arches the extreme hinges A and D open always at the supports and the intermediate hinges B and C open at cracks located closer to mirror-symmetry about the middle axis (though not perfectly symmetric). Furthermore, failure occurs by the opening of only four hinges fixed in location (two at the supports and two at internal cracks), without the phenomenon of travelling hinges observed consistently in lateral failure of voussoir arches under dynamic loading.

Nonlinear FE analysis is used for modelling the failure of the tested arches and determine the level of horizontal acceleration necessary for causing cracking and to estimate the position of the first crack. Abaqus/Explicit dynamic analysis algorithm, from commercial software Abaqus 2017 is used for this analysis, modelling the arch with the concrete damage plasticity numerical material law. Tested arch FL9 is modelled to calibrate the model, obtaining good correlation of the crack position while the failure acceleration is overestimated by roughly 20%, which is explained as an effect of lack of imperfections in the numerical model. CDP material law requires the input of both the tensile strength f_t and the fracture energy G_f of the material, which present a degree of variability characteristic of quasi-brittle materials. Parametric variations of both properties evidence a strong dependence of the failure acceleration on either parameter. The position of the first crack (hinge B), however, is less clearly affected with the first crack opening consistently in the same 15° portion of the arch. A trend between hinge B position and material tensile strength is observed, showing hinge B to form closer to hinge A for higher tensile strengths. The position of the second and final crack is predicted with reasonable agreement by performing a quasi-static analysis of a 3-pin arch simplified model.

A second similar model of a full-size arch with a span of 4m is created to model the behaviour of real arches. The tensile strength is taken as the average of existing experimental tests on real Roman concrete samples and the fracture energy is computed according to the relationship established for the material tests performed on the quasi-brittle lime mortar used in shaking table tests. The failure pattern is similar to that observed in shaking table tests and computed in the scale model, with the first crack opening in the same range of position, at a lower acceleration that is consistent with the increase in size-to-tensile strength ratio.

These novel experiments evidence the effect that low but non-negligible tensile capacity has on the mechanism behaviour of vaulted masonry structures subject to dynamic loading, and the proposed analysis is an initial approximation to modelling this effect. Further experimentation on larger test specimens with proportionately lower tensile capacity would be an insightful next step to continue investigating this behaviour and bound the type of materials and constructions where consideration of tensile capacity in the presence of dynamic loads is necessary.

References

- [Abaqus 2017] “Abaqus documentation - version 2017 Golden”, Providence, RI, 2017.
- [Albuerne 2016] A. Albuerne, *Seismic collapse of vaulted structures: unreinforced quasi-brittle materials and the case study of the Basilica of Maxentius in Rome*, D. Phil. thesis, University of Oxford, 2016.
- [Albuerne and Huerta 2010] A. Albuerne and S. Huerta, “Coulomb’s Theory of arches in Spain ca. 1800: the manuscript of Joaquín Monasterio”, in *ARCH '10* (Fuzhou, 2010), 2010.
- [Albuerne and Williams 2015] A. Albuerne and M. S. Williams, “Monitoring the seismic performance of arch models using particle image velocimetry”, in *SECED Conference 2015* (Cambridge), 2015.
- [Albuerne and Williams 2017] A. Albuerne and M. S. Williams, “Structural appraisal of a Roman concrete vaulted monument: The Basilica of Maxentius”, *Int. J. Archit. Herit.* **11**:7 (2017), 901–912.
- [Albuerne et al. 2013] A. Albuerne, M. S. Williams, and V. Lawson, “Prediction of the failure mechanism of arches and vaults under base motion using DEM based on the NCSD method”, *Wiadomosci Konserw.* **34** (2013), 41–47.
- [Alexakis and Makris 2014] H. Alexakis and N. Makris, “Limit equilibrium analysis and the minimum thickness of circular masonry arches to withstand lateral inertial loading”, *Arch. Appl. Mech.* **84** (2014), 757–772.
- [Alexakis and Makris 2016] H. Alexakis and N. Makris, “Validation of the discrete element method for the limit stability analysis of masonry arches”, in *Computational modeling of masonry structures using the discrete element method*, edited by V. Sarhosis et al., IGI Global, Hershey, PA, 2016.
- [Belytschko et al. 1984] T. Belytschko, J. S. J. Ong, W. K. Liu, and J. M. Kennedy, “Hourglass control in linear and non-linear problems”, *Comput. Methods Appl. Mech. Eng.* **43** (1984), 251–276.
- [Boothby 2001] T. E. Boothby, “Analysis of masonry arches and vaults”, *Prog. Struct. Eng. Mater.* **3** (2001), 246–256.
- [Brune 2010] P. F. Brune, *The mechanics of imperial Roman concrete and the structural design of vaulted monuments*, Ph.D. thesis, University of Rochester, Rochester, NY, 2010.
- [Campillo et al. 1989] M. Campillo, J. C. Gariel, K. Aki, and F. J. Sanchez-Sesma, “Destructive strong ground motion in Mexico City: source, path and site effects during the great 1985 Michoacán earthquake”, *Bulletin Seismol. Soc. Amer.* **79** (1989), 1718–735.
- [Casapulla and D’Ayala 2001] C. Casapulla and D. D’Ayala, “Lower bound approach to the limit analysis of 3D vaulted block masonry structures”, in *Computer methods in structural masonry: Proc. 5th Intern. Symp.* (Rome, 2001), edited by T. G. Hughes and G. N. Pande, Computers & Geotechnics Limited, Swansea, UK, 2001.
- [Clemente 1998] P. Clemente, “Introduction to dynamics of stone arches”, *Earthq. Eng. Struct. D* **27** (1998), 513–522.
- [Couplet 1729] P. Couplet, “De la poussée des voûtes”, *Hist. Acad. Royale des Sciences Paris* (1729), 79–117 and 117–141.
- [De Lorenzis et al. 2007] L. De Lorenzis, M. J. DeJong, and J. A. Ochsendorf, “Failure of masonry arches under impulse base motion”, *Earthq. Eng. Struct. D* **36** (2007), 2119–2136.
- [DeJong and Ochsendorf 2010] M. J. DeJong and J. A. Ochsendorf, “Dynamics of in-plane arch rocking: an energy approach”, *Proc. Instn Civ. Engrs. Engng. Comp. Mech.* **163** (2010), 179–186.
- [DeJong et al. 2008] M. J. DeJong, L. De Lorenzis, S. Adams, and J. A. Ochsendorf, “Rocking stability of masonry arches in seismic regions”, *Earthq. Spectra* **24** (2008), 847–865.
- [Douglas et al. 2015] J. Douglas, D. M. Seyedi, T. Ulrich, H. Modaressi, E. Foerster, K. Pitilakis, D. Pitilakis, A. Karatzetizou, G. Gazetas, E. Garini, and M. Loli, “Evaluation of seismic hazard for the assessment of historical elements at risk: description of input and selection of intensity measures”, *Bull. Earthq. Eng.* **13** (2015), 49–65.
- [Gaetani et al. 2017] A. Gaetani, P. Lourenço, G. Monti, and M. Moroni, “Shaking table tests and numerical analyses on a scaled dry-joint arch undergoing windowed sine pulses”, *Bull. Earthq. Eng.* **15** (2017), 4939–4961.
- [Giavarini 2005] C. Giavarini, *The Basilica of Maxentius: the monument, its materials, construction, and stability*, “L’Erma” di Bretschneider, Rome, 2005.
- [Giavarini et al. 2006] C. Giavarini, A. Samuelli Ferretti, and M. L. Santarelli, “Mechanical characteristics of Roman “opus caementicium””, in *Fracture and failure of natural building stones* (Athens), edited by S. K. Kourkoulis, Springer, 2006.
- [Heyman 1966] J. Heyman, “The stone skeleton”, *Int. J. Solids Struct.* **2**:2 (1966), 249–279.

- [Heyman 1969] J. Heyman, “The safety of masonry arches”, *Int. J. Mech. Sci.* **11**:4 (1969), 363–385.
- [Hillerborg et al. 1976] A. Hillerborg, M. Modéer, and P. E. Petersson, “Analysis of crack formation and crack growth in concrete by means of fracture mechanics and finite elements”, *Cem. Concr. Res.* **6**:6 (1976), 773–781.
- [Huerta 2004] S. Huerta, *Arcos, bóvedas y cúpulas: geometría y equilibrio en el cálculo tradicional de estructuras de fábrica*, Instituto Juan de Herrera, Madrid, 2004.
- [Humberto et al. 2013] V. Humberto, N. Tarque, D. Silveira, G. Camata, B. Lobo, M. Blondet, and A. Costa, “Structural behaviour and retrofitting of adobe masonry buildings”, pp. 37–75 in *Structural rehabilitation of old buildings*, edited by A. In Costa et al., Springer, Berlin, 2013.
- [Ivancic et al. 2014] S. Ivancic, P. Brune, and R. Perucchio, “Concrete damage plasticity model for ancient roman pozzolanic concrete”, in *Ninth International Masonry Conference - IMC*, 2014.
- [Jafari et al. 2017] S. Jafari, J. G. Rots, R. Esposito, and F. Messali, “Characterizing the material properties of dutch unreinforced masonry”, *Procedia Eng.* **193** (2017), 250–257.
- [Karapitta et al. 2011] L. Karapitta, H. Mouzakis, and P. Carydis, “Explicit finite-element analysis for the in-plane cyclic behaviour of unreinforced masonry structures”, *Earthq. Eng. Struct. D* **401** (2011), 175–193.
- [Karihaloo and Huang 1991] B. L. Karihaloo and X. Huang, “Tensile response of quasi-brittle materials”, *Pure Appl. Geophys.* **137** (1991), 461–487.
- [Kooharian 1952] A. Kooharian, “Limit analysis of voussoir (segmental) and concrete arches”, *J. Am. Concrete Inst.* **49**:12 (1952), 317–328.
- [Lemos 2001] J. V. Lemos, “Modelling the behaviour of a stone masonry arch structure under cyclic loads”, in *Computer methods in structural masonry: Proc. 5th Intern. Symp.* (Rome, 2001), edited by T. G. Hughes and G. N. Pande, Computers & Geotechnics Limited, Swansea, UK, 2001.
- [Lemos 2007] J. V. Lemos, “Discrete element modeling of masonry structures”, *Int. J. Archit. Herit.* **1**:2 (2007), 190–213.
- [Livesley 1978] R. K. Livesley, “Limit analysis of structures formed from rigid blocks”, *Int. J. Numer. Meth. Eng.* **12** (1978), 1853–1871.
- [Livesley 1992] R. K. Livesley, “A computational model for the limit analysis of three-dimensional masonry structures”, *Mechanica* **27** (1992), 161–172.
- [Lourenço et al. 2007] P. B. Lourenço, G. Milani, A. Tralli, and A. Zucchini, “Analysis of masonry structures: review of and recent trends of homogenisation techniques”, *Can. J. Civil Eng.* **34** (2007), 1443–1457.
- [Makris and Alexakis 2013] N. Makris and H. Alexakis, “The effect of stereotomy on the shape of the thrust-line and the minimum thickness of semi-circular masonry arches”, *Arch. Appl. Mech.* **83** (2013), 1511–1533.
- [Makris and Roussos 2000] N. Makris and Y. S. Roussos, “Rocking response of rigid blocks under near-source ground motions”, *Géotechnique* **50** (2000), 243–262.
- [Milani and Valente 2015] G. Milani and M. Valente, “Failure analysis of seven masonry churches severely damaged during the 2012 Emilia-Romagna (Italy) earthquake: Non-linear dynamic analyses vs conventional static approaches”, *Eng. Fail. Anal.* **54** (2015), 13–56.
- [Ochsendorf 2002] J. Ochsendorf, *Collapse of masonry structures*, Ph.D. thesis, University of Cambridge, 2002.
- [Oppenheim 1992] I. J. Oppenheim, “The masonry arch as a four-link mechanism under base motion”, *Earthquake Engng Struct. Dyn.* **21** (1992), 1005–1017.
- [Otto 1983] F. Otto, “Der Bogen, Teil 3: Eine Arbeit des Instituts für leichte Flächentragwerke”, *Arcus* **1983** (1983), 199–207.
- [Pela 2008] L. Pela, *Continuum damage model for nonlinear analysis of masonry structures*, Ph.D. thesis, Università degli Studi di Ferrara, 2008.
- [Planas and Elices 1985] J. Planas and M. Elices, “Fractura del hormigón en regimen no lineal: intentos para medir la energía de fractura G_f ”, *Informes de la Construcción* **37** (1985), 35–52.
- [Pulatsu et al. 2019] B. Pulatsu, E. Erdogmus, and P. B. Lourenço, “Simulation of masonry arch bridges using 3D discrete element modeling”, in *Structural analysis of historical constructions*, edited by R. Aguilar et al., RILEM **18**, Springer, Cham, 2019.

- [Ramaglia et al. 2016] G. Ramaglia, G. P. Lignola, and A. Prota, “Collapse analysis of slender masonry barrel vaults”, *Eng. Struct.* **117** (2016), 86–100.
- [Roca et al. 2010] P. Roca, M. Cervera, G. Gariup, and L. Pelà, “Structural analysis of masonry historical constructions: classical and advanced approaches”, *Arch. Comput. Methods Eng.* **17**:3 (2010), 299–325.
- [Samuelli Ferretti 2000] A. Samuelli Ferretti, “Opus caementicium, the Roman concrete”, in *Domus Aurea and Basilica of Maxentius: stress analysis and safety* (Madrid), vol. 12th Int. Conf. on Brick/Block Masonry, 2000.
- [Shah and Ouyang 1994] S. P. Shah and C. Ouyang, “Fracture mechanics for failure of concrete”, *Ann. Rev. Mater. Sci.* **24** (1994), 293–320.
- [Silva et al. 2017] L. C. Silva, P. B. Lourenço, and G. Milani, “Nonlinear discrete homogenized model for out-of-plane loaded masonry walls”, *J. Struct. Eng.* **143**:9 (2017).
- [Smars 2000] P. Smars, *Etudes sur la stabilité des arcs et voûtes, confrontation des méthodes de l’analyse limite aux voûtes gothiques en Brabant*, Ph.D. thesis, K. U. Leuven, 2000.
- [Smars 2008] P. Smars, “Influence of friction and tensile resistance on the stability of masonry arches”, in *Structural analysis of historic construction*, edited by D. D’Ayala and E. Fodde, Taylor & Francis, London, 2008.
- [Tarque et al. 2014] N. Tarque, G. Camata, E. Spacone, H. Varum, and M. Blondet, “Nonlinear dynamic analysis of a full-scale unreinforced adobe model”, *Earthquake Spectra* **30**:4 (2014), 1643–1661.
- [Vasconcelos et al. 2008] G. Vasconcelos, P. B. Lourenço, and D. Oliveira, “Experimental shear behaviour of stone masonry joints”, in *Structural analysis of historic construction*, edited by D. D’Ayala and E. Fodde, Taylor & Francis, London, 2008.
- [Rodriguez del Viso 2008] J. Rodriguez del Viso, *Comportamiento mecánico en fractura del hormigón de alta resistencia y su variación con la velocidad de sollicitación*, Escuela de Ingenieros de Caminos, Canales y Puertos de Ciudad Real, Universidad de Castilla–La Mancha, Ciudad Real, 2008.
- [White et al. 2003] D. J. White, W. A. Take, and M. D. Bolton, “Soil deformation measurement using particle image velocimetry (PIV) and photogrammetry”, *Geotechnique* **53** (2003), 619–631.
- [Williams et al. 2012] M. S. Williams, A. Albuerne, V. Lawson, and F. Yip, “Model scale shaking table tests on masonry barrel and cross vaults”, in *15th World Conf. on Earthquake Engng.* (Lisbon), 2012.
- [Zhang and Makris 2001] J. Zhang and N. Makris, “Rocking response of free-standing blocks under cycloidal pulses”, *J. Eng. Mech.* **127**:5 (2001), 473–483.
- [Zienkiewicz et al. 1971] O. C. Zienkiewicz, R. L. Taylor, and J. M. Too, “Reduced integration technique in general analysis of plates and shells”, *Int. J. Numer. Methods Eng.* **3** (1971), 275–290.

Received 19 Dec 2018. Revised 24 Apr 2019. Accepted 30 May 2019.

ALEJANDRA ALBUERNE: a.albuerne@ucl.ac.uk

Institute for Sustainable Heritage, Bartlett School of Environment, Energy and Resources, University College London, Central House, 14 Upper Woburn Place, London, WC1H 0NN, United Kingdom

ATHANASIOS PAPPAS: a.pappas@ucl.ac.uk

Department of Civil, Environmental and Geomatic Engineering, University College London, London, WC1E 6BT, United Kingdom

MARTIN WILLIAMS: martin.williams@eng.ox.ac.uk

Department of Engineering Science, University of Oxford, Oxford, OX1 3PJ, United Kingdom

DINA D’AYALA: d.dayala@ucl.ac.uk

Department of Civil, Environmental and Geomatic Engineering, University College London, London, WC1E 6BT, United Kingdom

INFLUENCE OF GEOMETRY ON SEISMIC CAPACITY OF CIRCULAR BUTTRESSED ARCHES

GIUSEPPE BRANDONISIO AND ANTONELLO DE LUCA

The effect of geometry on the seismic capacity of masonry buttressed arches with circular shape is addressed in this paper. In particular, in the contest of the limit analysis approach for masonry structures, a numerical procedure developed by the authors in previous studies is here used to perform an extensive parametric analysis of 320 circular buttressed arches, obtained by varying the geometrical configuration, namely the angle of embrace, the arch thickness and the buttress aspect ratio. The aim of the parametric analysis is studying the effect of both arch configuration (angle of embrace and arch thickness) and buttress geometry (height and width) on the horizontal strength of buttressed arches. To this end, the results of this study are presented in terms of collapse multiplier and failure mechanism aimed to provide reference values to be used for straightforward assessment of the horizontal strength of arched masonry structures, and for checking the results of more complex structural analyses performed by using “advanced” structural engineering software.

1. Introduction

A masonry arch is a construction, usually curved, that spans an opening. It is generally built by placing wedge-shaped blocks (the so-called voussoirs) having their narrower ends toward the opening on temporary centering. Arches vary in shape, from those that have little or no curvature to those that are acutely pointed. These structures are very common in historical masonry buildings, as in the cases of triumphal arches in churches, as colonnades at the base of buildings or in internal patios. Traditionally, the determination of suitable structural dimensions of arches has been carried out by experience in the early ages, and in the modern era through the application of equilibrium principles such as thrust lines. More recently, the availability of the newly developed limit analysis (LA) and elasticity theory has provided more refined tools for analysis and verification of masonry arched structures. The first one, in the approach originally proposed by Kooharian [1952] in his milestone paper for the voussoir arches and then formalized and adapted to unreinforced masonry arches by Heyman [1966] in his seminal paper, is considered particularly appealing. Actually, it requires no material characterization, relying only on the activation of kinematic mechanisms, due to the formation of a sufficient number of nondissipative rotational hinges, and on simple variationally written equilibrium equations.

The possibility of using the LA approach, in the form of kinematic theorem, for the seismic analysis of arched structures is also allowed by Italian Technical Codes [NTC 2008; 2018; CM 2009; Linee guida dei Beni Culturali 2010], that point out the importance of the right selection of the collapse mechanisms that can be activated. To this end, the set of potential failure mechanisms can be a priori selected, thanks to the deep knowledge of the collapse modes collected during the post-earthquake reconnaissance activity

Keywords: masonry buttressed arch, limit analysis, collapse mechanism, seismic capacity, nonlinear programming.

of the past decades by scholars (see [Russo 1918; Doglioni et al. 1994; Decanini et al. 2004; Lagomarsino and Podestà 2004; D’Ayala and Pagnoni 2011; Dizhur et al. 2011; Lagomarsino 2012; Sorrentino et al. 2013; Brandonisio et al. 2013], among others).

In this contest, the collapse behavior of typical URM elements of churches has been studied by the authors in the last 15 years by using the kinematic approach of LA. The aim in this study was to provide simplified closed form expressions for evaluating the horizontal load multiplier of URM masonry arches [De Luca et al. 2004; Brandonisio et al. 2017a; 2017b] and façades [Giordano et al. 2007; Lucibello et al. 2013; Brandonisio et al. 2015].

The LA approach is used to provide simplified “closed form” expressions of the horizontal collapse multiplier, also taking into account the contribution of steel tie rods (see [Brandonisio et al. 2015] for details). The proposed formulations have been used for performing an extensive parametric analysis, with the aim of studying the effect of both geometry and vertical/horizontal loading distributions on the portal horizontal strength. Furthermore, the influence of the steel tie rods has been addressed in order to understand their effectiveness on the portal seismic capacity.

A numerical procedure based on the application of LA approach combined with the nonlinear programming (NLP) technique is proposed in [Brandonisio et al. 2017a] for the assessment of circular buttressed arches loaded by horizontal forces. The automatic procedure is also validated through the comparison with numerical and experimental data retrieved from the literature. The validation result shows the reliability of the proposed procedure both in terms of activated collapsed mode and of actual horizontal load multiplier λ .

The reliability of the proposed procedure has been also assessed in [Brandonisio et al. 2017b] through the comparison with the real response of two triumphal arches of the Santa Maria delle Grazie church in Navelli (AQ) during the 2009 L’Aquila earthquake. The comparison has shown a good agreement in terms of failure mechanism, of hinges positions and of horizontal capacity, showing the reliability of the numerical procedure.

In this paper the numerical procedure is used to perform an wide parametric analysis of 320 circular buttressed arches. The aim was to grasp the influence of the buttressed arch geometry on its horizontal strength by varying the geometrical configuration, i.e., angle of embrace, arch thickness and buttress aspect ratio.

2. The masonry buttressed arches

Figure 1 shows a schematic representation of circular buttressed arch with the indication of the main parameters that allows for defining its geometry, namely: the inner radius (R), the clear span (L), the arch thickness (t), the centre height (h_O), the angle of embrace (2ω), the buttress height (h), the buttress width (B), the global width (D) and the global height (H).

Therefore, the geometry of buttressed arch can be parameterized by adopting appropriate geometrical ratios (appointed as fundamental ratios in the following), that are the arch thickness over radius ratio (t/R), the buttress width over radius ratio (B/R) and the buttress height over radius (h/R). In Figure 1 are also depicted the loads acting on the structure, consisting of gravity loads (W) and horizontal actions that increase proportionally to the vertical forces through a horizontal loading multiplier λ .

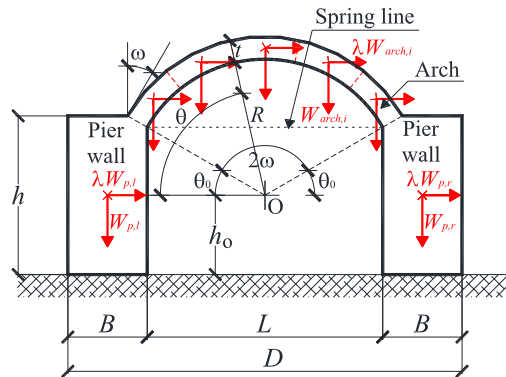


Figure 1. Masonry buttressed arch: geometry and loads.

The geometrical dimensions of arches have been established by the experience of ancient builders, on the bases of theory of proportions under the assumption that the static of arches under gravity loads is governed uniquely by their geometry. Therefore, several rules of thumb were used to establish the more appropriate arch geometry, the minimum thickness and the minimum buttress thickness.

With reference to the circular arch shape, the current paper aims to investigate on the seismic capacity of buttressed arches designed according to empirical rules of art. The rules are based on the theory of proportions used in the past for the stability of arched structures under gravity loads (see also [Milani 1923; Benvenuto 1981; 1991; Brandonisio and De Luca 2019]).

3. Limit analysis of buttressed arches under horizontal loading through nonlinear programming

A brief description of the numerical procedure proposed by the authors in [Brandonisio et al. 2017a] for the seismic assessment of circular buttressed arches is provided in this section.

The procedure is based on the application of the kinematic theorem of limit analysis approach coupled with the use of NLP technique, and it can be schematized in the following steps:

- (1) identification and analysis of all the potential failure mechanisms that can be activated for the buttressed arch. These mechanisms can be defined on the basis of similar structures damaged during the past earthquakes, or based on the existing crack patterns;
- (2) calculation of horizontal load multiplier λ that causes the activation of each considered collapse mechanism under the well-known Heyman's assumptions on the masonry material (null tensile strength; infinite compression strength; sliding of a stone or of a part of the structure upon another cannot occur);
- (3) evaluation of actual horizontal load multiplier λ as the minimum among the ones calculated for the considered collapse mechanisms.

Concerning the potential failure mechanisms that can be significant for a buttressed arch under seismic actions (step 1), on the basis of considerations provided in [Como 2013] and [Brandonisio et al. 2017a], three failure modes are considered:

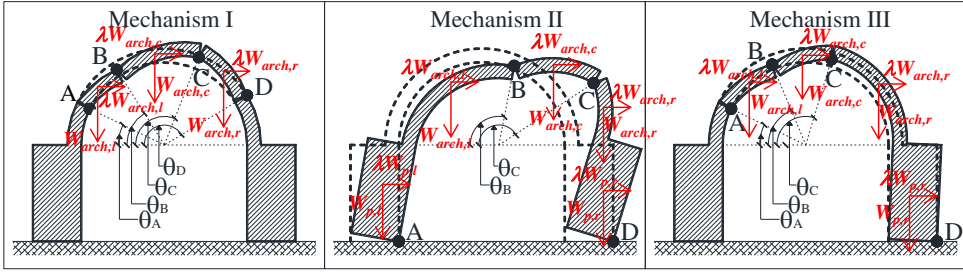


Figure 2. Considered collapse mechanisms: arch mechanism (mech. I, left), global mechanism (mech. II, center), and mixed mechanism (mech. III, right).

- (1) arch mechanism (Figure 2, left), also appointed as mechanism I, characterized by the activation of four hinges A, B, C, and D within the development of the arch, whose locations are identified through the angles θ_A , θ_B , θ_C and θ_D , measured with respect to the horizontal line;
- (2) global mechanism (Figure 2, center), also appointed as mechanism II, that considers the rocking of the two piers about two hinges A and D at the pier basis and two hinges B and C within the arch, whose positions are defined by the angles θ_B and θ_C , respectively;
- (3) mixed mechanism (Figure 2, right), also appointed as mechanism III, having one hinge D at the base of the pier on the opposite side of the horizontal force and three hinges A, B and C within the development of the arch, whose positions are identified by the angles θ_A , θ_B and θ_C , respectively.

For each selected collapse mechanisms of Figure 2 (step 2), the horizontal load multiplier can be evaluated by using the kinematic theorem of LA through the application of the principle of virtual works that allows for writing

$$\lambda^j = \frac{W_{p,l} \cdot v_{p,r} + \sum_{i=l,r,l} [W_{arch,i}(\vartheta_k) \cdot v_{arch,i}(\sin(\vartheta_k), \cos(\vartheta_k))] + W_{p,r} \cdot v_{p,r}}{W_{p,l} \cdot u_{p,r} + \sum_{i=l,r,l} [W_{arch,i}(\vartheta_k) \cdot u_{arch,i}(\sin(\vartheta_k), \cos(\vartheta_k))] + W_{p,r} \cdot u_{p,r}}, \quad (1)$$

where λ^j is the horizontal load multiplier, given by the ratio between the horizontal load (F^j) that activates the corresponding mechanism j ($j = \text{I, II, III}$) and the total vertical load ($W_{\text{tot}} = W_{p,l} + W_{\text{arch}} + W_{p,r}$); $W_{p,l}$ and $W_{p,r}$ are the self-weight of left and right buttress, respectively; $W_{arch,i}$ ($i = l, c, r$) is the self-weight of three rigid parts of the arch ($l = \text{left}$, $c = \text{central}$, $r = \text{right}$) involved in the collapse mechanism that are identified by the angles θ_i ($i = A, B, C, D$) that define the position of the hinges in the arch (therefore, the weight of the whole arch is: $W_{\text{arch}} = W_{arch,l} + W_{arch,c} + W_{arch,r}$); $v_{p,i}$ and $u_{p,i}$ ($i = l, r$) are the vertical and horizontal displacements of the centroid of the pier walls ($l = \text{left}$, $r = \text{right}$); $v_{arch,i}$ and $u_{arch,i}$ ($i = l, c, r$) are the vertical and horizontal displacements of the centroid of the three parts of the arch ($l = \text{left}$, $c = \text{central}$, $r = \text{right}$) involved in the collapse mechanism.

The expressions for evaluating the weights and the displacement components of the rigid bodies involved in the kinematical chains are reported in [Brandonisio et al. 2017a].

Finally (step 3), the actual horizontal load multiplier λ is evaluated as the minimum value among the three multipliers λ^I , λ^{II} , λ^{III} that have to be calculated according to the equation (1):

$$\lambda = \min \begin{cases} \lambda_{\min}^I = \min[\lambda^I(\vartheta_A, \vartheta_B, \vartheta_C, \vartheta_D)] \\ \lambda_{\min}^{II} = \min[\lambda^{II}(\vartheta_B, \vartheta_C)] \\ \lambda_{\min}^{III} = \min[\lambda^{III}(\vartheta_A, \vartheta_B, \vartheta_C)], \end{cases} \quad (2)$$

To this end, nonlinear optimization techniques, based on the Generalized Reduced Gradient (GRG) code as implemented in [Lasdon et al. 1978], is used since the parameters involved in (1) for the evaluation of the horizontal load multipliers λ^j have nonlinear relationship with the hinge locations. In fact, as specified in [Brandonisio et al. 2017a], the weights $W_{\text{arch},l}$, $W_{\text{arch},c}$, $W_{\text{arch},r}$ are function of the angles θ_k and the components of displacements of the rigid blocks formed in the arch vary with $\sin \theta_k$ and $\cos \theta_k$, where $j = I, II, III$ and $k = A, B, C, D$.

Therefore, the application of nonlinear optimization problem to the three failure mechanisms of Figure 2, allows for obtaining the position of the hinges in the arch, through the value of the angles θ_A , θ_B , θ_C and θ_D (nonnegative unknown variables) that minimizes the objective function $\lambda^j = \lambda^j(\theta_A, \theta_B, \theta_C, \theta_D)$ given by (1).

The constraint conditions that define the nonlinear optimization problem (i.e., the boundary conditions that the unknown variables θ_i ($i = A, B, C, D$) have to satisfy for each failure mechanism of Figure 2) are imposed by assuming that the first hinge in the arch can occur at a minimum inclination of $\theta_0 = \pi/2 - \omega$ with respect to the springing line (i.e., $\theta_{A,\min} = \theta_0$ for the mechanisms I and III; $\theta_{B,\min} = \theta_0$ for the mechanism II), while the last hinge was considered with a maximum inclination of $\pi - \theta_0$ with respect to the springing line (i.e., $\theta_{D,\min} = \pi - \theta_0$ for the mechanism I; $\theta_{C,\min} = \pi - \theta_0$ for the mechanisms II and III).

4. Parametric analysis of circular buttressed arches: description of 320 case studies, activated collapse mechanisms and seismic capacity

4.1. Description of 320 case studies. The numerical procedure illustrated in the previous section for evaluating the seismic capacity of masonry buttressed arches is herein parametrically applied on 320 case studies obtained by varying the main geometrical parameters that define the arch configuration.

In detail, the analyzed buttressed arches have been obtained by varying the following geometrical parameters:

- angle of embrace 2ω , according to four configurations of the arch depression, i.e., $2\omega = 90^\circ, 120^\circ, 150^\circ, 180^\circ$;
- arch thickness t , variable in the range: $t/R = 0.10, 0.20, 0.30, 0.40$;
- buttress height h , variable between one and four times the inner radius of the arch R , i.e., $h/R = 1.00, 2.00, 3.00, 4.00$;
- buttress width B , variable between 38% and 125% of the arch R , namely: $B/R = 0.38, 0.50, 0.75, 1.00, 1.25$.

As underlined in [Brandonisio and De Luca 2019], the stepwise variability of the fundamental ratios used in the parametric analysis allows for covering the geometry of masonry arches built according to the rules of thumb.

The combination of the values fixed for the fundamental ratios allows for obtaining 320 different geometries, whose seismic analyses give us a proper understanding of the effect of geometry on the horizontal strength of buttressed arches. In order to better explain this concept, Figure 3 shows an abacus with the geometry of some analyzed structures; the red arrows underline the influence of the investigated parameters, namely: (i) the angle of embrace 2ω , whose effect can be appreciated by looking at the horizontal red arrow provided at the bottom of the figure that goes from depressed arches on the left side (corresponding to $2\omega = 90^\circ$) to semicircular arches on the right side (corresponding to $2\omega = 180^\circ$); (ii) the arch thickness t/R , whose influence can be studied, for a fixed value of the angle of embrace 2ω , by looking at the horizontal red arrows at the top of Figure 3; (iii) the buttress slenderness, that varies with the h/R ratio, as outlined by the vertical short arrows; (iv) the buttress width, represented by the B/R ratio, whose influence is remarked by the vertical arrow provided on the left side of the abacus of Figure 3.

The geometrical representation of the 320 examined buttressed arches is provided in figures 4 and 5 that have been divided in macrorows, each two corresponding to a fixed value of the arch thickness t/R , and in four macrocolumns, each column corresponding to a fixed value of the buttress width B/R . Every framework defined by a couple of t/R and B/R ratios has been again subdivided into 16 squares corresponding to the four fixed values of angle of embrace 2ω and to the four fixed values of the h/R ratio.

Depending on the arch thickness-to-radius ratio, the overall view of the 320 buttressed arches in figures 4 and 5 allows for classifying the arches in: (i) thin arches, when $t/R = 0.10$ (see the left side of Figure 4); (ii) arches with medium thickness, namely $t/R = 0.20$ and $t/R = 0.30$, as depicted on the right side of Figure 4 and on the left side of Figure 5, respectively; and (iii) thick arches, when $t/R = 0.40$ (see the right side of Figure 5). This classification in thin, medium and thick arches will be useful in the next subsections for discussing the results of parametric analysis in terms of activated collapse mechanism and of seismic capacity.

4.2. Prevailing collapse mechanisms. Figure 6 shows a synoptic framework of the activated collapse mechanisms resulting from the parametric analysis. By looking at the figure it is possible to understand when one failure mechanism prevails on another depending on the buttressed arch geometry.

According to the format used in figures 4 and 5, Figure 6 is composed by four frames, each one corresponding to a value of the arch thickness t/R . Every frame is divided in four columns corresponding to the investigated values of angle of embrace 2ω , and in five macrorows, each two corresponding to a fixed value of the buttress width B/R , that in turn are subdivided in four lines associated to the stepwise variability of the h/R ratio. The arched structures collapsed according to the arch mechanism have been depicted by using a grey square appointed with the Roman numeral “I” to indicate the mechanism I; similarly, the global and the mixed failure modes have been plotted with green and white squares appointed with the Roman numeral “II” and “III” to mean the activation of the mechanism II or of the mechanism III, respectively.

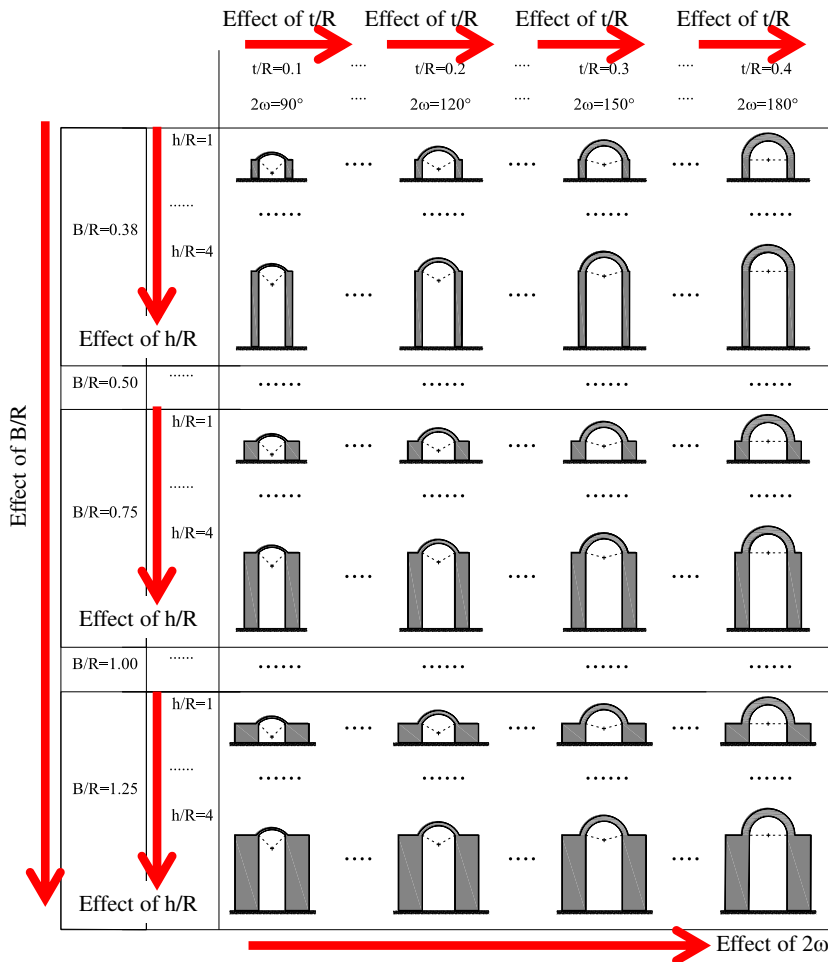


Figure 3. Analyzed geometric parameters of buttressed arches: effect of fundamental ratios h/R , B/R , t/R and 2ω .

From the synoptic framework (Figure 6), it can be observed that the prevailing failure modes are the mixed (or mech. III) and, in minor recurrence, the arch mechanisms (or mech. I). In fact, the global mechanism II occurs only in two semicircular buttressed arches with $t/R = 0.40$ and $h/R = 1$.

The mixed mechanism is always activated in presence of depressed arches (i.e., $2\omega = 90^\circ$), and it generally prevails in presence of buttressed arches characterized by angle of embrace equal to $2\omega = 150^\circ$ and $2\omega = 120^\circ$.

On the contrary, the arch mechanism I prevails in presence of semicircular buttressed arches ($2\omega = 180^\circ$), as well as in the cases for arches with medium thickness and stocky buttresses, when the angle of embrace is equal to $2\omega = 150^\circ$ and $2\omega = 120^\circ$.

Finally, from the synoptic framework of Figure 6 it can be observed that semicircular buttressed arches with thin thickness (i.e., $t/R = 0.10$) have no lateral capacity because the arch thickness is not able to contain the thrust line modified by the presence of horizontal forces.



Figure 4. Geometry of analyzed buttressed arches: thin arch thickness, $t/R = 0.10$ (left column) and medium arch thickness, $t/R = 0.20$ (right column).

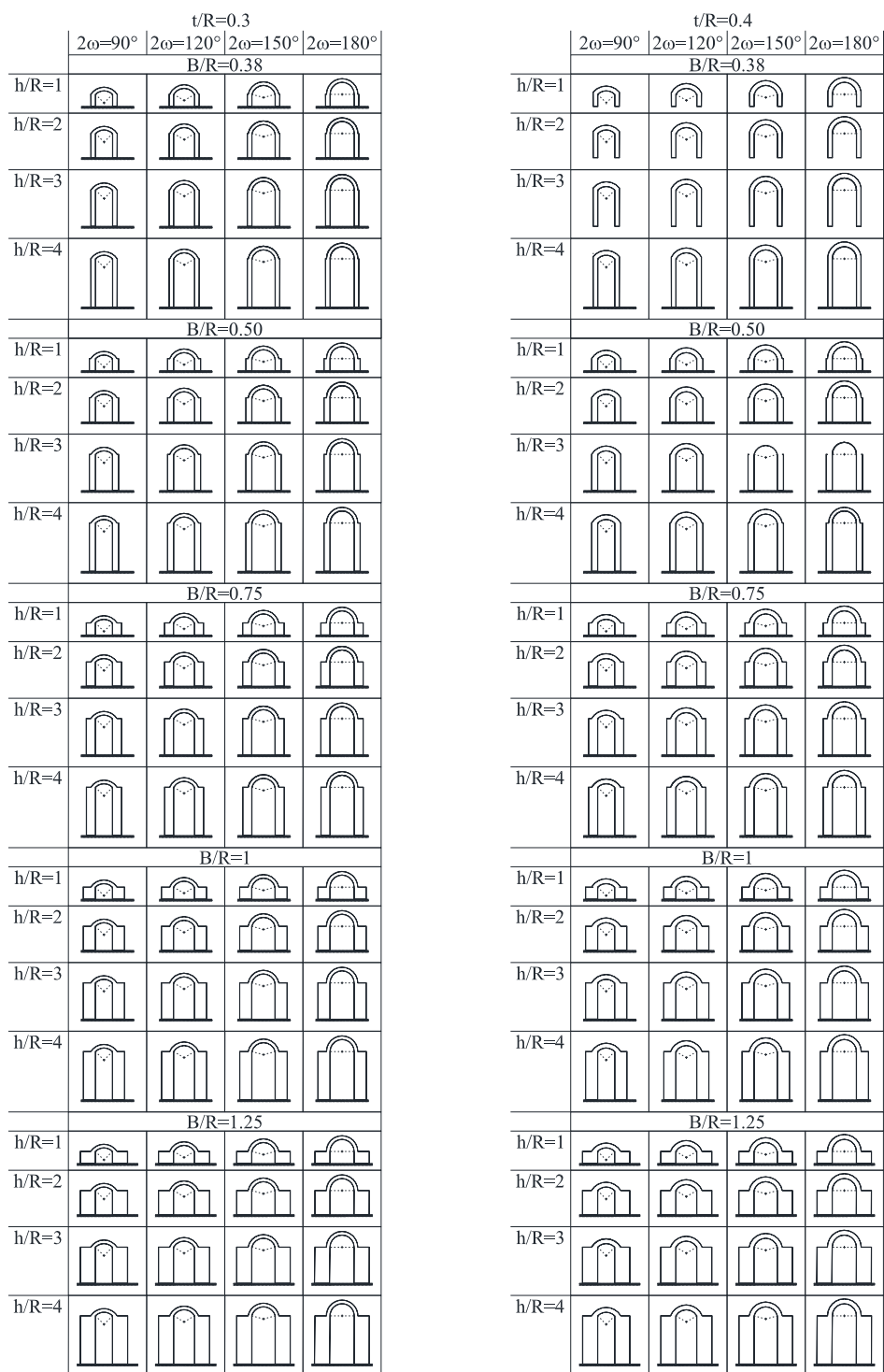


Figure 5. Geometry of analyzed buttressed arches: medium arch thickness, $t/R = 0.30$ (left column) and thick arch thickness, $t/R = 0.40$ (right column).

		t/R=0.10 (Thin arch thickness)				t/R=0.20 (Medium arch thickness)			
		2ω=90°	2ω=120°	2ω=150°	2ω=180°	2ω=90°	2ω=120°	2ω=150°	2ω=180°
B/R=0.38	h/R=1	III	III	III	No horizontal capacity	III	III	III	I
	h/R=2	III	III	III		III	III	III	I
	h/R=3	III	III	III		III	III	III	I
	h/R=4	III	III	III		III	III	III	I
B/R=0.5	h/R=1	III	III	III		III	III	III	I
	h/R=2	III	III	III		III	III	III	I
	h/R=3	III	III	III		III	III	III	I
	h/R=4	III	III	III		III	III	III	I
B/R=0.75	h/R=1	III	III	I		III	III	III	I
	h/R=2	III	III	I		III	III	III	I
	h/R=3	III	III	I		III	III	III	I
	h/R=4	III	III	I		III	III	III	I
B/R=1	h/R=1	III	I	I		III	III	I	I
	h/R=2	III	I	I		III	III	I	I
	h/R=3	III	III	I		III	III	III	I
	h/R=4	III	III	I		III	III	III	I
B/R=1.25	h/R=1	III	I	I		III	I	I	I
	h/R=2	III	I	I		III	I	I	I
	h/R=3	III	I	I		III	III	I	I
	h/R=4	III	I	I		III	III	I	I

		t/R=0.30 (Medium arch thickness)				t/R=0.40 (Thick arch thickness)			
		2ω=90°	2ω=120°	2ω=150°	2ω=180°	2ω=90°	2ω=120°	2ω=150°	2ω=180°
B/R=0.38	h/R=1	III	III	III	I	III	III	III	III
	h/R=2	III	III	III	III	III	III	III	III
	h/R=3	III	III	III	III	III	III	III	III
	h/R=4	III	III	III	III	III	III	III	III
B/R=0.5	h/R=1	III	III	III	I	III	III	III	I
	h/R=2	III	III	III	I	III	III	III	III
	h/R=3	III	III	III	I	III	III	III	III
	h/R=4	III	III	III	III	III	III	III	III
B/R=0.75	h/R=1	III	III	III	I	III	III	III	II
	h/R=2	III	III	III	I	III	III	III	I
	h/R=3	III	III	III	I	III	III	III	I
	h/R=4	III	III	III	I	III	III	III	I
B/R=1	h/R=1	III	III	I	I	III	III	III	II
	h/R=2	III	III	I	I	III	III	III	I
	h/R=3	III	III	III	I	III	III	III	I
	h/R=4	III	III	III	I	III	III	III	I
B/R=1.25	h/R=1	III	III	I	I	III	III	III	I
	h/R=2	III	III	I	I	III	III	III	I
	h/R=3	III	III	I	I	III	III	III	I
	h/R=4	III	III	I	I	III	III	III	I

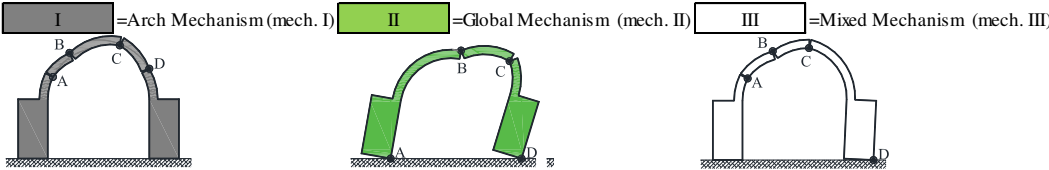


Figure 6. Activated collapse mechanisms.

4.3. Seismic capacity. The results of the parametric analysis are summarised in figures 7 and 8 in terms of horizontal load multiplier λ and angle of embrace 2ω curves. In detail, the diagrams of Figure 7 (left column) refer to the thin arch thickness ($t/R = 0.10$), the diagrams of Figure 7 (right column) and of Figure 8 (left column) refer to medium arch thickness (i.e., $t/R = 0.20$ and $t/R = 0.30$, respectively), while the diagrams of Figure 8 (right column) are related to the arches with thick thickness ($t/R = 0.40$).

The five diagrams of each column refer to the fixed values of the B/R ratio, namely $B/R = 0.38, 0.50, 0.75, 1.00, 1.25$, while the four curves plotted in each diagram correspond to the investigated values of the h/R ratio (i.e., $h/R = 1, 2, 3, 4$).

The overall vision of the diagrams of figures 7 and 8 allows for observing a different trend of the $\lambda(2\omega, h/R)$ curves, depending on the t/R ratio. In fact, in presence of thin arches ($t/R = 0.10$) the $\lambda(2\omega, h/R)$ curves of Figure 7 (left column) have a decreasing trend with the angle of embrace. Otherwise, in presence of medium arch thickness the diagrams of Figure 7 (right column) and of Figure 8 (left column) have a subhorizontal trend and the four curves corresponding to stocky buttresses ($B/R < 0.75$) are superimposed because the horizontal strengths of these case studies are slightly afflicted by the h/R ratio. Finally, in the cases of thick arch thickness ($t/R = 0.40$), the curves of Figure 8 (right column) show an increasing trend with 2ω .

Concerning the seismic capacity of buttressed arches with thin thickness ($t/R = 0.10$), by looking at the diagrams of Figure 7 (left column) it can be firstly observed that the depressed arches have larger horizontal capacities, while the semicircular ones have no horizontal strength. It can be also observed that the $\lambda(2\omega, h/R)$ curves are horizontal in the depressed arches, and show decreasing evolution with the angle of embrace, where the curves are overlapped due to activation of the arch mechanism that is not affected by the t/R parameter. Furthermore, it can be noted that the horizontal load multiplier is less than $\lambda = 20\%$ in presence of angle of embrace $2\omega \geq 150^\circ$, while the lateral strength increases up to $\lambda = 40\%$ to 60% in the cases of depressed buttressed arches.

Regarding the arched structures with medium thickness ($t/R = 0.20$ and $t/R = 0.30$), as already observed, the curves have a prevailing horizontal evolution because the lateral capacity is not affected by the angle of embrace. The unique exception is provided by semicircular arches with buttresses characterized by $t/R = 0.20$, $B/R \geq 1$ and $h/R \leq 2$ (see Figure 7, right column, fourth and fifth row), where the $\lambda(2\omega, h/R)$ curves show a decreasing trend induced by the activation of the arch mechanism. Concerning the values of horizontal load multipliers observed in the cases of medium arch thickness, the lateral strength varies with no influence of the h/R ratio up to $\lambda = 10\%$ when $B/R \leq 0.5$, and in the range $\lambda = 10\%$ to 20% when $B/R = 0.75$; in the cases of buttresses with $B/R \geq 1$, the load multiplier ranges between $\lambda = 20\%$ and $\lambda = 40\%$ and the curves show that the horizontal capacity decreases up to half when the buttress height goes from $h/R = 1$ to $h/R = 4$.

The results obtained from the parametric analysis performed on the structures with thick arch thickness (Figure 8, right column) allows for observation that the horizontal capacity of the buttressed arches characterized by $B/R \leq 0.5$ is low, being less than $\lambda = 10\%$ independently by the angle of embrace 2ω and by the h/R ratio. In the cases of buttress with $B/R \geq 0.75$, it can be noted that the horizontal load multiplier of depressed arches (i.e., $2\omega = 90^\circ$ and $2\omega = 120^\circ$) ranging from $\lambda \cong 10\%$ to $\lambda \cong 25\%$, regardless of 2ω and h/R parameters; on the contrary, when $2\omega \geq 150^\circ$, the $\lambda(2\omega, h/R)$ curves show an increasing trend and differentiating among them to take into account the value of the h/R ratio, and the horizontal load multiplier λ rising from $\lambda = 20\%$ to $\lambda = 50\%$ passing from $h/R = 4$ to $h/R = 1$.

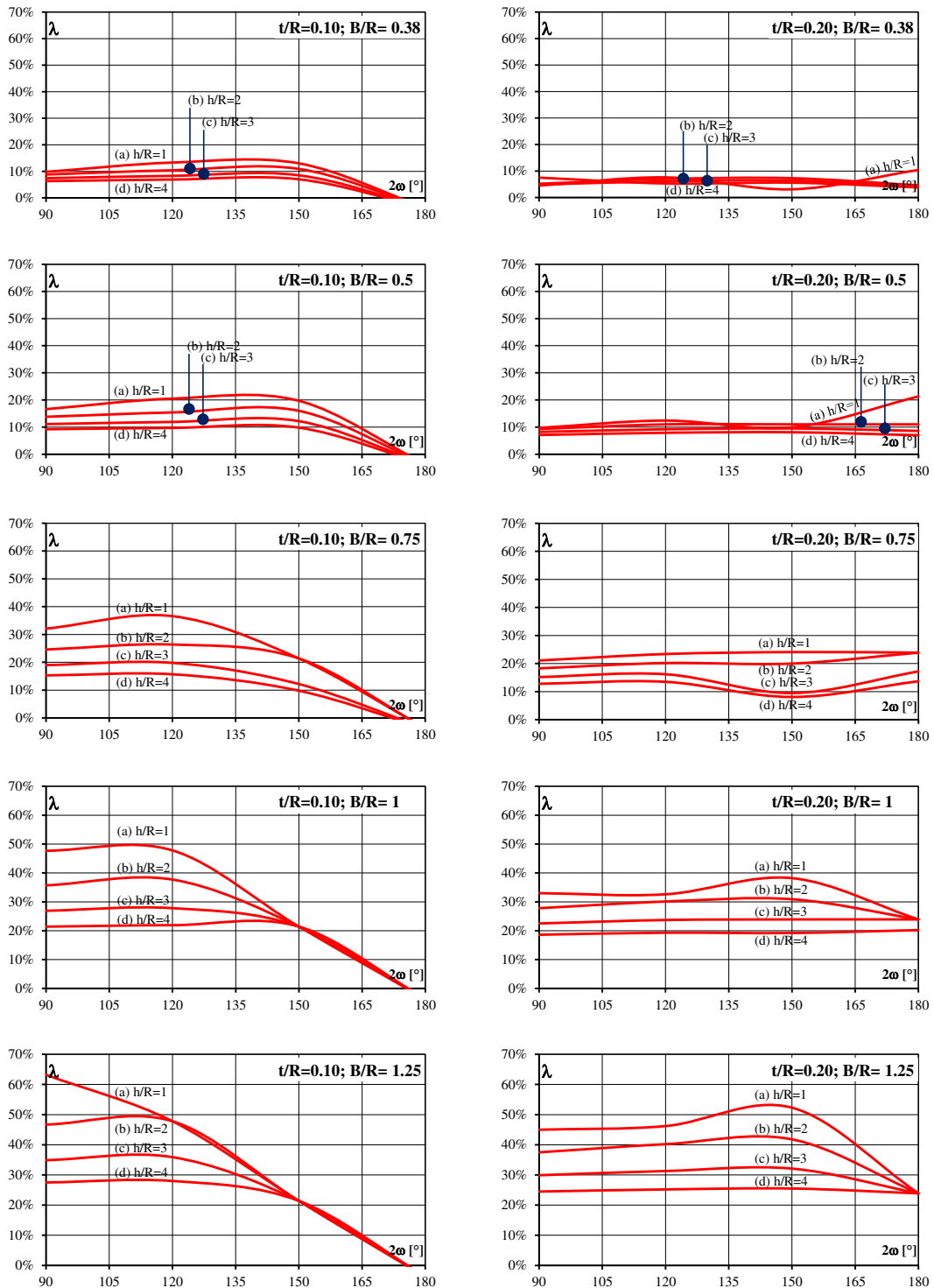


Figure 7. Effect of angle of embrace (2ω) on horizontal capacity λ of thin arch thickness ($t/R = 0.10$, left column) and medium arch thickness ($t/R = 0.20$, right column).

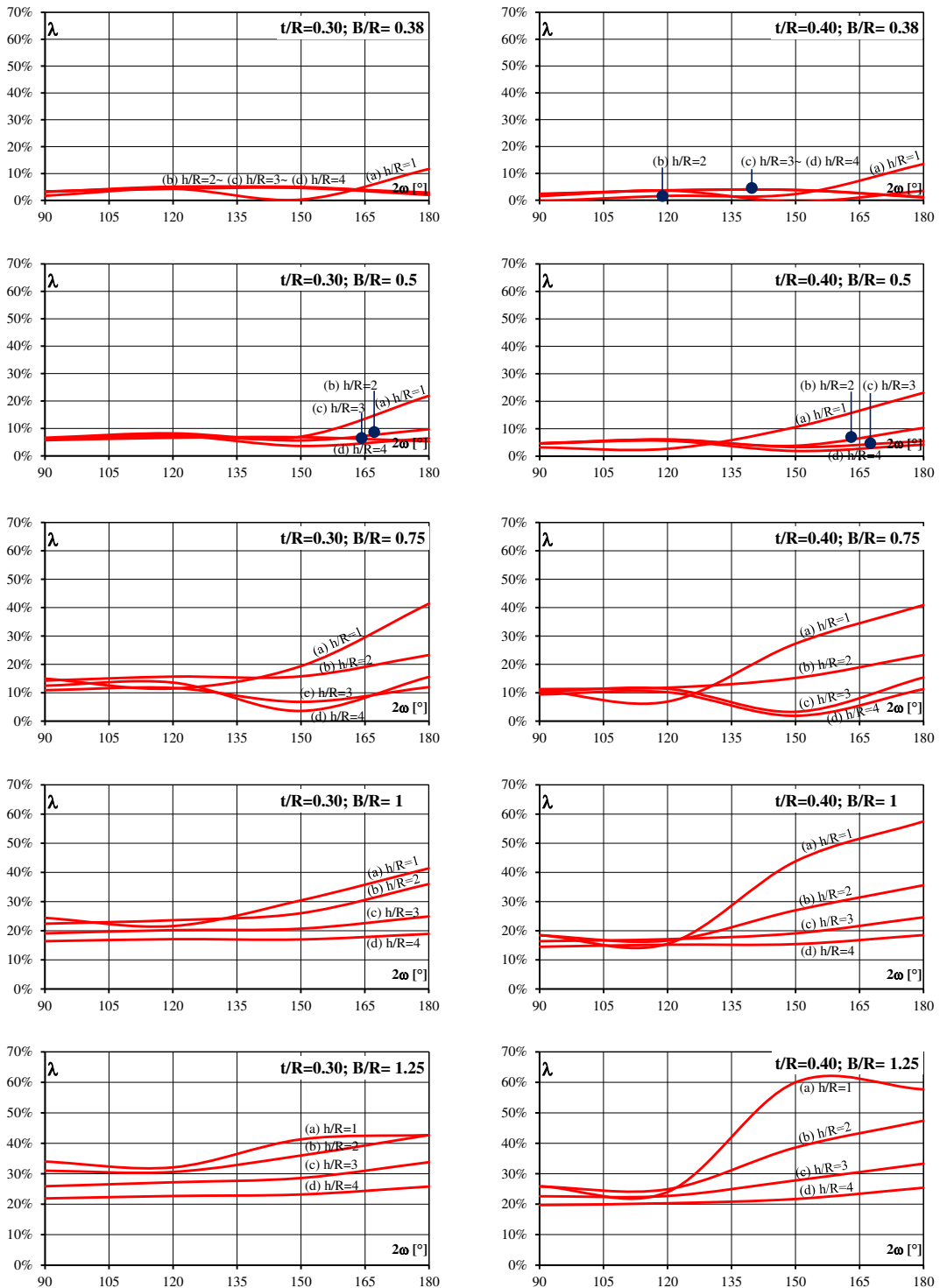


Figure 8. Effect of angle of embrace (2ω) on horizontal capacity λ of medium arch thickness ($t/R = 0.30$, left column) and thick arch thickness ($t/R = 0.40$, right column).

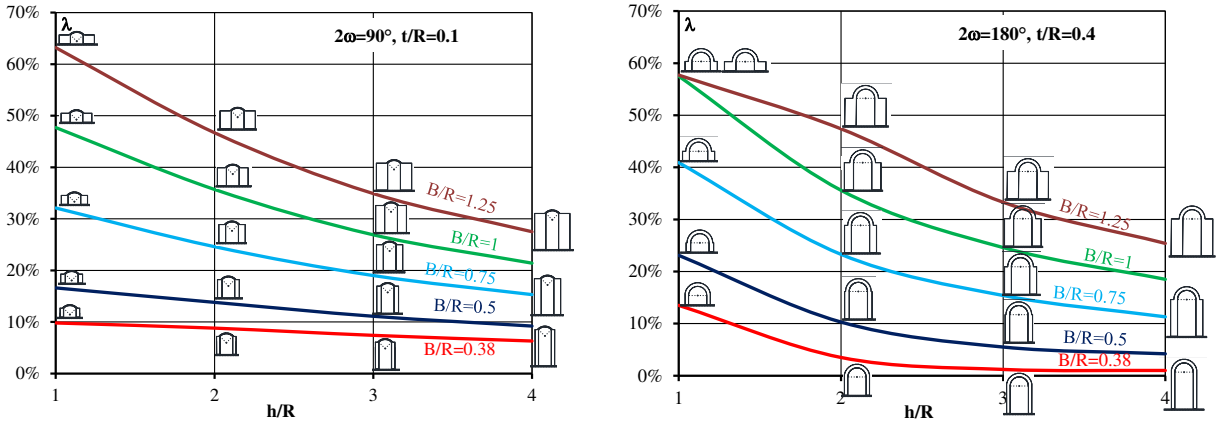


Figure 9. Effect of buttress geometry on the horizontal strength of depressed thin arches (left) and on semicircular thick arches (right).

The effect of geometry on the seismic capacity of analyzed buttressed arches can be also established by revising the numerical results according to the format of Figure 9, where the horizontal load multiplier λ has been plotted as a function of the h/R ratio for the extreme geometrical configuration, namely for depressed arches with thin thickness (i.e., $2\omega = 90^\circ$, $t/R = 0.10$ in Figure 9, left) and for semicircular arches with thick thickness (i.e., $2\omega = 180^\circ$, $t/R = 0.40$ in Figure 9, right).

Five curves have been plotted in each diagram of Figure 9, each one corresponding to the five investigated values of B/R . The related geometrical representation of the buttressed arches has been also provided in Figure 9 with the aim of correlating the horizontal capacity with the geometric shape of the examined structures.

Both the diagrams show that the lateral strength λ of buttressed arches decreases from the stockier to the slender buttresses, with higher gradient for semicircular arches that are more sensible to the buttress geometry, i.e., to the h/R and B/R ratios, respect to the depressed arches.

These considerations can be extended to all examined case studies by observing the diagrams of Figure 10 that have been plotted by using the same format of Figure 9. In particular, each column in Figure 10 refers to the investigated values of angle of embrace (2ω), while each row concerns to the selected values of nondimensional arch thickness t/R .

Regarding the buttressed arches with small arch thickness, by looking at the diagrams at the top row of Figure 10 corresponding to $t/R = 0.10$, it can be noted how depressed arches ($2\omega = 90^\circ$) have lateral capacity higher than the ones of arched structures with intermediate angles of embrace, namely $2\omega = 120^\circ$ and $2\omega = 150^\circ$, while semicircular arches have no horizontal capacity, as already observed.

Concerning the horizontal capacity of buttressed arches with medium thickness (i.e., $t/R = 0.20$ and $t/R = 0.20$), from the second and third rows of Figure 10 it can be observed that the horizontal load multiplier is less affected by the angle of embrace.

On the contrary, in presence of thick arch thickness (see bottom row in Figure 10), it can be noted that the horizontal capacity increases with angle of embrace, showing a more strong dependence by the buttress shape, i.e., by the h/R and B/R ratios in presence of arches characterised by $2\omega = 150^\circ$ and $2\omega = 180^\circ$.

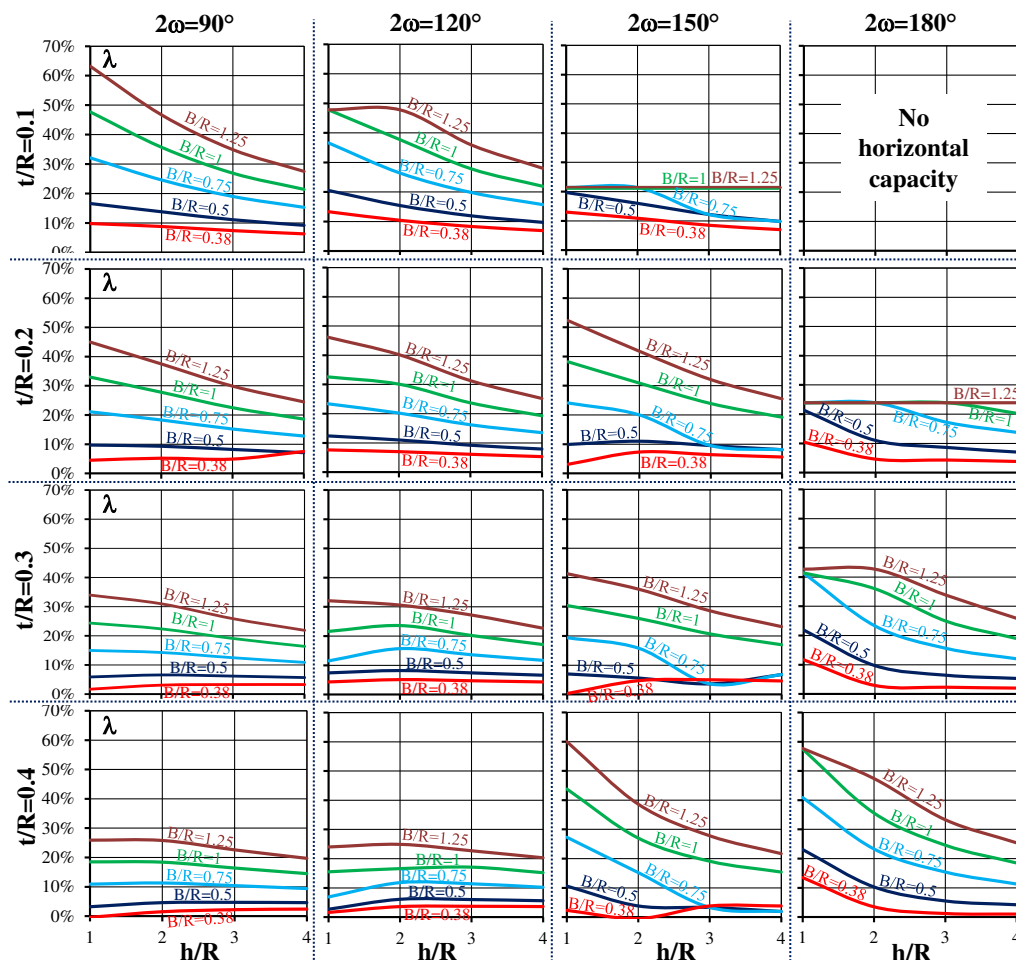


Figure 10. Effect of buttress geometry on the horizontal strength of 320 examined arches.

Finally, it can be observed that the collapse multiplier λ of depressed arches (namely, $2\omega = 90^\circ$, left column in Figure 10) strongly decreases with the t/R ratio, is no longer influenced by the t/R ratio for arches with angles of embrace $2\omega = 120^\circ$ and $2\omega = 150^\circ$, while, in a different way, the horizontal strength λ of semicircular arches increases greatly with the arch thickness, reaching very high values in presence of thick arch and stocky buttresses, namely $\lambda = 40\%$ to 60% .

5. Conclusions

In this paper, the effect of geometry on the seismic capacity of masonry buttressed circular arches has been studied in the framework of the limit analysis approach for masonry structures.

The numerical procedure developed by the authors in [Brandonisio et al. 2017a] has been used to perform an extensive parametric analysis of 320 circular buttressed arches, obtained by varying the fundamental ratios that define the arches from a geometrical point of view, namely the angle of embrace (2ω), the arch thickness (t/R) and the buttress height (t/R) and width (B/R).

The results of parametric analysis allowed for establishing that the prevailing failure mechanisms is the “mixed” one, while the “arch” mechanism generally occurs in presence of semicircular arches and of arches characterised by $2\omega = 150^\circ$ and $B/R \geq 1$. The “global” mechanism is activated only in two cases of semicircular arches with thick arch thickness ($t/R = 0.4$) and stocky buttresses.

Concerning the seismic capacity, the numerical analyses discussed in the paper suggests that the horizontal load multiplier λ is very sensitive in presence of depressed and semicircular arch shape (i.e., $2\omega = 90^\circ$ and $2\omega = 180^\circ$), while the intermediate configurations of angle of embrace (i.e., $2\omega = 120^\circ$ and $2\omega = 150^\circ$) seem to be less influenced by the values of fundamental geometrical ratios.

In particular, the horizontal capacity of depressed arches ($2\omega = 90^\circ$) with thin arch thickness ($t/R = 0.1$), ranging between $\lambda = 10\%$ and $\lambda = 60\%$, is generally 1.5 times to 2 times greater than the capacity of arched structures with both intermediate arch thickness (variable from $\lambda = 5\%$ to $\lambda = 40\%$) and thick arch thickness (variable between $\lambda = 5\%$ and $\lambda = 25\%$).

On the contrary, the semicircular arches with the minimum allowable arch thickness (that is $t/R = 0.1$), have no horizontal capacity, that increases in presence of medium thickness, reaching maximum values of seismic capacity equal to $\lambda = 30\%$ to 40% . On the contrary, semicircular buttressed arches with thick arch thickness have higher lateral capacity, with horizontal load multipliers that reach values of $\lambda = 40\%$ to 50% in presence of stocky buttresses (i.e., when $h/R \leq 2$ and $B/R \geq 1$).

Finally, buttressed arches with angles of embrace $2\omega = 120^\circ$ and $2\omega = 150^\circ$ show intermediate values of seismic capacity, which generally ranges from $\lambda = 5\%$ to $\lambda = 40\%$ depending on the buttress geometry.

The authors emphasize the usefulness of the results of parametric analysis provided in this paper, as simple tool for analysts and designers to make a fast evaluation of the seismic capacity of buttressed arches as well as for checking the results of more complex numerical analysis.

Acknowledgment

This research has been supported by ReLUIS — Research Project 2018 “Rete di Laboratori Universitari Ingegneria Sismica”, in the context of the activities of Task Masonry Structures.

References

- [Benvenuto 1981] E. Benvenuto, *La scienza delle costruzioni e il suo sviluppo storico*, Sansoni, Firenze, 1981.
- [Benvenuto 1991] E. Benvenuto, *An introduction to the history of structural mechanics — part II: vaulted structures and elastic systems*, Springer, New York, 1991.
- [Brandonisio and De Luca 2019] G. Brandonisio and A. De Luca, “Statics of buttressed masonry arches in light of traditional design rules”, in *AIMETA 2019 — XXIV conference of the Italian Association of Theoretical and Applied Mechanics* (Rome, Italy), 2019.
- [Brandonisio et al. 2013] G. Brandonisio, G. Lucibello, and E. M. A. De Luca, “Damage and performance evaluation of masonry churches in the 2009 L’Aquila earthquake”, *Eng. Fail. Anal.* **34** (2013), 693–714.
- [Brandonisio et al. 2015] G. Brandonisio, E. Mele, and A. De Luca, “Closed form solution for predicting the horizontal capacity of masonry portal frames through limit analysis and comparison with experimental test results”, *Eng. Fail. Anal.* **55** (2015), 246–270.
- [Brandonisio et al. 2017a] G. Brandonisio, E. Mele, and A. De Luca, “Limit analysis of masonry circular buttressed arches under horizontal loads”, *Meccanica (Milano)* **52**:11-12 (2017), 2547–2565.
- [Brandonisio et al. 2017b] G. Brandonisio, E. Mele, and A. De Luca, “Seismic capacity of URM buttressed arches”, pp. 1555–1569 in *Proc. of AIMETA 2017 XXIII conference — the Italian Association of Theoretical and Applied Mechanics*, 2017.

- [CM 2009] CM, *Istruzioni per l'applicazione delle "Norme tecniche per le costruzioni"*, 2009.
- [Como 2013] M. Como, *Statics of historic masonry constructions*, Springer, Berlin Heidelberg, 2013.
- [D'Ayala and Pagnoni 2011] D. F. D'Ayala and S. Pagnoni, "Assessment and analysis of damage in L'Aquila historic city centre after 6th April 2009", *Bull. Earthq. Eng.* **9**:1 (2011), 81–104.
- [De Luca et al. 2004] A. De Luca, A. Giordano, and E. Mele, "A simplified procedure for assessing the seismic capacity of masonry arches", *Eng. Struct.* **26**:13 (2004), 1915–1929.
- [Decanini et al. 2004] L. Decanini, A. De Sortis, A. Goretti, R. Langenbach, F. Mollaioli, and A. Rasulo, "Performance of masonry buildings during the 2002 Piedritise, Italy, Earthquake", *Earthq. Spectra* **20**:S1 (2004), S191–S220.
- [Dizhur et al. 2011] D. Dizhur, J. Ingham, L. Moon, M. Griffith, A. Schultz, I. Senaldi, G. Magenes, J. Dickie, S. Lissel, J. Centano, C. Ventura, J. Leite, and P. Lourenco, "Performance of masonry buildings and churches in the 22 February 2011 Christchurch earthquake", *Bull. New Zealand Soc. Earthq. Eng.* **44**:4 (2011), 279–296.
- [Doglioni et al. 1994] F. Doglioni, A. Moretti, and V. Petrini, *Le chiese e il terremoto. Dalla vulnerabilità constatata nel terremoto del Friuli al miglioramento antisismico nel restauro*, Lint Editoriale, Trieste, 1994.
- [Giordano et al. 2007] A. Giordano, A. De Luca, E. Mele, and A. Romano, "A simple formula for predicting the horizontal capacity of masonry portal frames", *Eng. Struct.* **29**:9 (2007), 2109–2123.
- [Heyman 1966] J. Heyman, "The stone skeleton", *Int. J. Solids Struct.* **2**:2 (1966), 249–279.
- [Kooharian 1952] A. Kooharian, "Limit analysis of voussoir (segmental) and concrete arches", *ACI J.* **49**:12 (1952), 317–328.
- [Lagomarsino 2012] S. Lagomarsino, "Damage assessment of churches after L'Aquila earthquake (2009)", *Bull. Earthq. Eng.* **10**:1 (2012), 73–92.
- [Lagomarsino and Podestà 2004] S. Lagomarsino and S. Podestà, "Seismic vulnerability of ancient churches: II. Statistical analysis of surveyed data and methods for risk analysis", *Earthq. Spectra* **20**:2 (2004), 395–412.
- [Lasdon et al. 1978] L. S. Lasdon, A. D. Waren, A. Jain, and M. Ratner, "Design and testing of a generalized reduced gradient code for nonlinear programming", *ACM Trans. Math. Softw.* **4**:1 (1978), 34–50.
- [Linee guida dei Beni Culturali 2010] Linee guida dei Beni Culturali, "Linee Guida per la valutazione e riduzione del rischio sismico di patrimonio culturale con riferimento alle Norme tecniche per le costruzioni di cui al D.M. 14/01/2008", 2010.
- [Lucibello et al. 2013] G. Lucibello, G. Brandonisio, E. Mele, and A. De Luca, "Seismic damage and performance of Palazzo Centi after L'Aquila earthquake: a paradigmatic case study of effectiveness of mechanical steel ties", *Eng. Fail. Anal.* **34** (2013), 407–430.
- [Milani 1923] G. B. Milani, *L'Ossatura murale — parte II: L'Estetica*, S. Lattes & C. Editori, 1923.
- [NTC 2008] NTC, *Norme Tecniche per le costruzioni*, 2008. S.O. n. 30, G. U. n. 29.
- [NTC 2018] NTC, *Norme Tecniche per le costruzioni*, 2018. S.O. n. 8, G. U. n. 42.
- [Russo 1918] C. Russo, *Trattato sulle lesioni dei fabbricati*, Unione Tipografico-Editrice Torinese, Torino, 1918.
- [Sorrentino et al. 2013] L. Sorrentino, L. Liberatore, L. D. Decanini, and D. Liberatore, "The performance of churches in the 2012 Emilia earthquakes", *Bull. Earthq. Eng.* **12**:5 (2013), 2299–2331.

Received 8 Jun 2018. Revised 14 May 2019. Accepted 19 Aug 2019.

GIUSEPPE BRANDONISIO: giuseppe.brandonisio@unina.it

Department of Structures for Engineering and Architecture (Di.St.), University of Naples "Federico II", P.le Tecchio, 80, 80125 Naples, Italy

ANTONELLO DE LUCA: antonio.deluca@unina.it

Department of Structures for Engineering and Architecture (Di.St.), University of Naples "Federico II", P.le Tecchio, 80, 80125 Naples, Italy

FAILURE PATTERN PREDICTION IN MASONRY

GIANMARCO DE FELICE AND MARIALAURA MALENA

The structural assessment of masonry remains an open challenge due to its intrinsic nonhomogeneous nonisotropic and nonlinear behavior. Aiming at providing a tool for structural applications, this paper presents the formulation and implementation in a FE code of a simple constitutive model to describe the behavior of masonry walls regarded as elastoplastic homogenized anisotropic plates. The model is based on few geometrical and mechanical parameters that can be easily detected from masonry typology. Nonetheless, it can capture the essential features of the structural behavior of ancient masonry, i.e., the failure in traction and the anisotropic behavior deriving from the joints layout. The model succeeded in predicting the failure mechanism and load carrying capacity under different boundary and loading conditions, including soil settlement and seismic loading. Its validation is finally carried out for some selected case studies.

1. Introduction

The response of ancient masonry structures under foundation settlements or seismic events is usually affected by local failure modes which typically involve both in-plane and out-of-plane collapse mechanisms. The prediction of the failure patterns associated with these mechanisms can be carried out using different analysis and modelling approaches [de Felice et al. 2017]. When numerical analysis is adopted, an adequate constitutive law for the masonry is requested. Considering the uncertainties that typically affect the detection of the structural properties of historical constructions, numerical models suitable for analyses should be as simple as possible and based on few mechanical parameters. In the meantime, the model should be able to describe some essential features of masonry behavior, such as: the ability to capture the failure in traction, the inclusion of the anisotropic behavior, at least in terms of failure condition, and the capability to reproduce the failure pattern under different boundary and loading conditions.

A considerable number of nonlinear models have been developed for masonry, aiming at capturing the essential no-tensile strength under traction [Angelillo 1993; Angelillo et al. 2010], according to the well-known Heyman hypothesis [Heyman 1966], or the complex interaction between masonry units, resulting in an overall anisotropic behavior [Page 1978; de Buhan and de Felice 1997; Sacco 2009; Zucchini and Lourenço 2002; Massart et al. 2005; Sab 2003; Stefanou et al. 2015; Amorosi et al. 2012; 2014; Roselli et al. 2018]. More complex three-dimensional models have been proposed in the framework of either continuum [Milani et al. 2006a; 2007], or discrete limit analysis [Livesley 1978; Portioli et al. 2014], or resorting to a discrete macroelements approach [Calió et al. 2012].

Keywords: masonry, FE model, failure pattern, plastic strain, settlement, earthquake loads.

In this work, an elastic perfectly-plastic plate model able to describe the nonlinear behavior of masonry walls subject to both in-plane and out-of-plane loads is proposed. The model is an extension of a previous formulation in which only the in-plane behavior was considered [de Felice et al. 2010].

The proposed model represents the masonry wall as an elastoplastic homogenized Love–Kichhoff plate, with associated flow-rule. The macroscopic elastic properties are obtained through a micro mechanical approach, while the strength domain is assumed to coincide with the one defined in [Sab 2003; Sab et al. 2007], derived by a homogenization procedure on a thin periodic heterogeneous plate made of 3D infinitely resistant blocks connected by Mohr–Coulomb interfaces.

In the present case, the cohesive contribution of the mortar joints is practically neglected. This hypothesis, widely used in modelling masonry after Heyman’s contribution, seems appropriate for old structures, since the joints have experienced loss of mortar or degradation of its mechanical properties, due to environmental ageing conditions. Accordingly, the old masonry structure becomes similar to a dry joints masonry structure. On the other hand, material crushing under compression is neglected as well, since masonry units are supposed having infinite compressive strength. This hypothesis, in agreement with Heyman’s assumptions, appears justified for the problems at hand (soil settlement and earthquake loads in low-rise buildings), for which material crushing does not occur since the compressive stress remains much lower than the material strength. It should be pointed out that the no-tensile and infinite compression hypotheses do not yield to the well known no-tension model since the model, according to the homogenization approach, includes a pseudo tensile strength in the horizontal direction deriving from the interlocking of masonry blocks and the presence of friction at the interfaces.

The model has been implemented in the Finite Element code Abaqus in the context of perfect plasticity theory, aiming at carrying out path-following nonlinear analyses of masonry structures under various loading and boundary conditions. If on the one hand, a path-following analysis requires a computation cost higher than the limit analysis, on the other hand, it provides the whole equilibrium path under external loads that, for instance, can be used for the seismic assessment through pushover analysis [Acito et al. 2016]. It is worth noting that, according to experimental evidences [Lourenço and Ramos 2004], material behavior of masonry constituents is not perfectly plastic, but generally exhibit a softening behavior both in compression, once crushing is attained, and in traction, once the tensile strength is reached. However, in the present case, as both, joint cohesion and crushing in compression, are neglected, there is no reason to include the softening behavior, that would induce computational problems of mesh dependence and difficulties in convergence. The hypothesis of associated plastic flow-rule does not completely reflect the behavior of masonry since, especially in presence of high compressive stresses, sliding in mortar joints occur without dilatancy. This hypothesis could represent a serious drawback for the case of masonry constructions having boundary conditions constraining the joint dilatation. Hence, in general terms, the proposed model provides only an upper bound prediction of the failure load, that should be prudently adopted. However, as usually masonry walls are simply subjected to self-weight, for current problems, the hypothesis of associated flow-rule does not significantly affect the prediction of failure load. Moreover, the hypothesis is straightforward to apply the Haar–Karman’s principle in the solution procedure.

A further drawback of the proposed model is that, since a Love–Kirchhoff plate is adopted, the shear deformation and the possible disaggregation of the wall in out-of-plane bending are neglected. Both these phenomena that may occur in thick walls, are therefore disregarded, since the model more accurately describes the behavior of thin walls. In fact, according to [Cecchi et al. 2007] there are no meaningful

differences between the Love–Kirchhoff model and the Reissner–Mindlin model when thin walls are considered.

This model has been also adopted in a previous work of Malena et al. [2019], where a comparison with the results of limit analysis of structures made of rigid blocks is presented in the way to highlight the weakness and the potentiality of continuous versus discrete formulations.

In the first section, the model is formulated in terms of elastic properties, strength conditions and elastic-plastic constitutive law. Then, in Section 2, the results of numerical simulations of masonry walls under foundation settlements are presented and compared with the outcomes of a more accurate discrete model [Malena et al. 2019; Portioli and Cascini 2016]. Finally, in Section 3, the numerical simulations of a prototype consisting of three U-shaped connected walls subjected to horizontal loads are presented and compared with experimental outcomes presented in [Restrepo Vélez et al. 2014], to assess the capability of the model to predict the failure patterns resulting from seismic action.

2. Masonry model

Let us consider the masonry wall in Figure 1, made of parallelepiped blocks having thickness h , height a and length b , arranged in a regular pattern and bonded with mortar joints. Mortar joints are viewed as interfaces forming a regular network of two sets of orthogonal planes: horizontal bed joints (parallel to the Ox_1x_3 plane) are continuous, while vertical head joints (parallel to the Ox_2x_3 plane) are discontinuous, as a result of the running bond pattern.

If the dimensions of the blocks are small when compared with the sizes of the wall L , H , and if the actions are characterized by a wavelength much larger than the size of the blocks, according to [Caillerie 1984], the masonry wall can be represented as a homogenized continuum Love–Kirchhoff plate. In this case, the masonry wall occupies the domain $\Omega \times]-h/2; h/2[$ (Figure 1), where Ω is its middle plane and h the corresponding out-of-plane thickness.

2A. Macroscopic elastic properties. The elastic properties of masonry may be derived from the properties of its constituents according to the homogenization theory for periodic media, through the resolution of a boundary value problem on the unit cell with periodicity conditions. By adopting reasonable simplifications on the geometry of the unit cell, a closed form solution is available. In most contributions

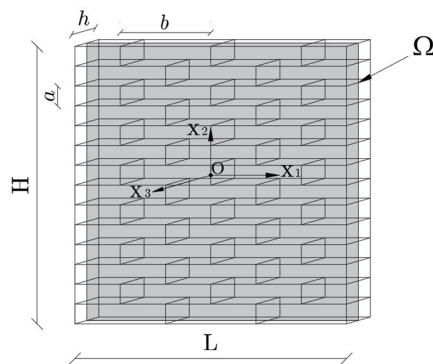


Figure 1. Block structure.

in the literature, only the in-plane behavior of masonry was investigated: in [de Felice 1995] the elastic macroscopic properties have been deduced under condition that the blocks behave as rigid bodies and the joints are simply interfaces that control the deformability of the assembly; in [de Felice 2001; Cecchi and Sab 2002] the contribution in deformation provided by the blocks has been accounted for, assuming a constant strain field; in [Milani et al. 2006b] an affine displacement field has been assumed in both, the blocks and the joints, taking into account the finite thickness of these latter. Whenever addressed, the out-of-plane behavior refers either to the shear deformation of masonry bulk, [Zucchini and Lourenço 2002; Pande et al. 1989; Pietruszczak and Niu 1992], or to the joint contribution to bending [Cecchi and Sab 2002; Mistler et al. 2007; Taliercio 2016].

In this work, according to [Mistler et al. 2007], the orthotropic equivalent elastic properties of masonry are based on the following macroscopic parameters: the Young's moduli in the horizontal and vertical directions E_1 and E_2 , the Poisson ratios ν_{12} , ν_{21} and the shear modulus G_{12} , which are based on mechanical and geometrical properties of the constituents as shown hereafter. Let us define the vector $\mathbf{t} = (\mathbf{N}, \mathbf{M})$ collecting, for the homogenized plate, the macroscopic in-plane (membrane) forces $\mathbf{N} = N_{\alpha\beta}$ and out-of-plane bending moments $\mathbf{M} = M_{\alpha\beta}$, and the vector $\boldsymbol{\varepsilon} = (\mathbf{E}, \boldsymbol{\chi})$ collecting the corresponding in-plane strain $\mathbf{E} = E_{\alpha\beta}$ and out-of-plane curvature $\boldsymbol{\chi} = \chi_{\alpha\beta}$, for $\alpha, \beta = 1, 2$. The flexibility matrix \mathbf{A} relating the membrane strains and curvatures to the membrane forces and bending moments is given by

$$\begin{pmatrix} E_{11} \\ E_{22} \\ 2E_{12} \\ \chi_{11} \\ \chi_{22} \\ 2\chi_{12} \end{pmatrix} = \begin{pmatrix} 1/hE_1 & -\nu_{12}/hE_1 & 0 & 0 & 0 & 0 \\ -\nu_{21}/hE_2 & 1/hE_2 & 0 & 0 & 0 & 0 \\ 0 & 0 & 1/hG_{12} & 0 & 0 & 0 \\ 0 & 0 & 0 & 12/h^3E_1 & -12\nu_{12}/h^3E_1 & 0 \\ 0 & 0 & 0 & -12\nu_{21}/h^3E_2 & 12/h^3E_2 & 0 \\ 0 & 0 & 0 & 0 & 0 & 12/h^3G_{12} \end{pmatrix} \begin{pmatrix} N_{11} \\ N_{22} \\ N_{12} \\ M_{11} \\ M_{22} \\ M_{12} \end{pmatrix}. \quad (2-1)$$

The coefficients in (2-1), as shown in the previous work [de Felice et al. 2010], depend on the elastic properties of blocks (λ'_b, μ_b) and joints (K_n, K_t) and on the dimensions of the blocks (a, b) as

$$\frac{1}{E_1} = \frac{4a}{4abK_n + b^2K_t} + \frac{1}{4\mu_b} + \frac{1}{4(\lambda'_b + \mu_b)}, \quad (2-2)$$

$$\frac{1}{E_2} = \frac{1}{aK_n} + \frac{1}{4\mu_b} + \frac{1}{4(\lambda'_b + \mu_b)}, \quad (2-3)$$

$$\frac{1}{G} = \frac{1}{aK_t} + \frac{4a}{b^2K_n + 4abK_t} + \frac{1}{\mu_b}, \quad (2-4)$$

$$\frac{\nu_{12}}{E_1} = \frac{\nu_{21}}{E_2} = \frac{\lambda'_b}{4\mu_b(\lambda'_b + \mu_b)}. \quad (2-5)$$

As pointed out in [Mistler et al. 2007], the out-of-plane constants in (2-1) should be different from the in-plane ones, but the approximation introduced when considering the in-plane constants is reasonable.

2B. Macroscopic strength condition. A homogenization procedure for determining the overall yield strength properties of a thin periodic heterogeneous plate was proposed in [Sab 2003; Sab et al. 2007], and applied to masonry walls made of 3D infinitely resistant blocks connected by Mohr–Coulomb interfaces. The procedure provides a smooth representation of the piecewise kinematics of block masonry through

an average strain field. According to these works, the macroscopic strength domain $G_{\mathbf{t}}$ can be written as

$$G_{\mathbf{t}} := \{\mathbf{t} \mid f^i(\mathbf{t}) \leq 0, \quad \forall i \in [1, \dots, m]\}, \quad (2-6)$$

where $f^i(\mathbf{t})$ are m independent planes intersecting in a nonsmooth way:

$$f^i(\mathbf{t}) := \mathbf{n}^i : \mathbf{t} - c^i, \quad i \in [1, \dots, m]. \quad (2-7)$$

and the vector $\mathbf{n}^i := \partial f^i / \partial \mathbf{t}$ collects the normal to the yield surfaces.

The yield surface comprises $m = 8$ planes which can be written in terms of stress components in the Ox_1x_2 plane as

$$\begin{aligned} f^1 &:= \mu N_{11} + \operatorname{tg}(\phi) N_{22} + (1 + \operatorname{tg}(\phi)\mu) N_{12} - h \left(c + \frac{c\mu}{\operatorname{tg}(\phi)} \right) \leq 0, \\ f^2 &:= \mu N_{11} + \operatorname{tg}(\phi) N_{22} - (1 + \operatorname{tg}(\phi)\mu) N_{12} - h \left(c - \frac{c\mu}{\operatorname{tg}(\phi)} \right) \leq 0, \\ f^3 &:= N_{22} + \frac{1}{\operatorname{tg}(\phi) N_{12}} - \frac{hc}{\operatorname{tg}(\phi)} \leq 0, \\ f^4 &:= N_{22} - \frac{1}{\operatorname{tg}(\phi) N_{12}} - \frac{hc}{\operatorname{tg}(\phi)} \leq 0, \\ f^5 &:= N_{22} + \frac{2}{h} M_{22} - \frac{hc}{\operatorname{tg}(\phi)} \leq 0, \\ f^6 &:= N_{22} - \frac{2}{h} M_{22} - \frac{hc}{\operatorname{tg}(\phi)} \leq 0, \\ f^7 &:= (p + q) N_{22} + \frac{2}{h} M_{11} - \frac{2}{h} (q - p) M_{22} - \frac{h(p + q)c}{\operatorname{tg}(\phi)} \leq 0, \\ f^8 &:= (p + q) N_{22} - \frac{2}{h} M_{11} - \frac{2}{h} (q - p) M_{22} - \frac{h(p + q)c}{\operatorname{tg}(\phi)} \leq 0, \end{aligned} \quad (2-8)$$

where $p = (\operatorname{tg}(\phi)/\mu) \cdot (b/4h)$ and $q = (\operatorname{tg}(\phi)/\mu) \sqrt{1 + (b/4h)^2}$. The macroscopic strength condition explicitly depends on the aspect ratio $\mu = 2a/b$ of the blocks, the friction angle ϕ and the cohesion c of the joints. This latter is included into the formulation and, generally, provided with a very small value, to ensure convergence of the numerical simulations. The strength condition is anisotropic as a consequence of the arrangement of the blocks within the assembly and is unbounded in the direction of compression, according to the hypothesis of infinite crushing strength. As expected, the four planes defining the in-plane strength condition correspond to the macroscopic strength domain obtained in [de Buhan and de Felice 1997].

2C. Macroscopic elastoplastic constitutive law. Aiming at building up a constitutive law, let us assume that masonry behaves as an elastic-perfectly plastic homogenized medium with associated flow-rule, having the elastic properties defined in Section 2A and the elastic domain coinciding with the macroscopic strength condition given by (2-6). The model is thus formulated in the framework of infinitesimal multisurface rate-independent elastoplasticity. The total strain $\boldsymbol{\varepsilon}$ is decomposed additively in an elastic

(reversible) part $\boldsymbol{\varepsilon}^e$ and a plastic (irreversible) part $\boldsymbol{\varepsilon}^p$:

$$\boldsymbol{\varepsilon} = \boldsymbol{\varepsilon}^e + \boldsymbol{\varepsilon}^p. \quad (2-9)$$

By (2-9), the stress-strain relationship can be written as

$$\boldsymbol{t} = \boldsymbol{C} : (\boldsymbol{\varepsilon} - \boldsymbol{\varepsilon}^p), \quad (2-10)$$

where $\boldsymbol{C} = \boldsymbol{A}^{-1}$ is the elastic stiffness tensor equal to the inverse of the flexibility matrix defined in (2-1).

The previously defined macroscopic strength domain given by equations (2-6)–(2-8) is assumed to coincide with the elastic domain $E_{\boldsymbol{t}}$:

$$E_{\boldsymbol{t}} \equiv G_{\boldsymbol{t}} = \{\boldsymbol{t} \mid f^i(\boldsymbol{t}) := \boldsymbol{n}^i : \boldsymbol{t} - \boldsymbol{c}^i \leq 0, \quad \forall i \in [1, \dots, m]\}. \quad (2-11)$$

Accordingly, the boundary of the domain is given by

$$\partial E_{\boldsymbol{t}} := \{\boldsymbol{t} \mid f^i(\boldsymbol{t}) := \boldsymbol{n}^i : \boldsymbol{t} - \boldsymbol{c}^i, \quad \forall i \in [1, \dots, m]\}. \quad (2-12)$$

The evolution of plastic strain $\boldsymbol{\varepsilon}^p$ is controlled by the associated flow-rule expressed as proposed in [Koiter 1960]:

$$\dot{\boldsymbol{\varepsilon}}^p := \sum_{i=1}^m \dot{\gamma}^i \frac{\partial f^i(\boldsymbol{t})}{\partial \boldsymbol{t}}, \quad (2-13)$$

where $\dot{\gamma}^i$ are the m plastic multipliers, subjected to the Kuhn–Tucker conditions for $i \in [1, \dots, m]$:

$$\dot{\gamma}^i \geq 0, \quad f^i(\boldsymbol{t}) \leq 0, \quad \dot{\gamma}^i f^i(\boldsymbol{t}) \equiv 0, \quad (2-14)$$

and to the consistency condition $\dot{\gamma}^i f^i(\boldsymbol{t}) \equiv 0$.

Equations (2-9)–(2-13) define the constitutive behavior of the material but in order to be used inside the FEM framework, they have to be integrated (see [Simo et al. 1988] for details), obtaining the following equations in terms of finite increments:

$$\boldsymbol{t}_{n+1} = \boldsymbol{C} : (\boldsymbol{\varepsilon}_{n+1} - \boldsymbol{\varepsilon}_{n+1}^p), \quad (2-15)$$

$$\boldsymbol{\varepsilon}_{n+1}^p = \boldsymbol{\varepsilon}_n^p + \sum_{i=1}^m \Delta \gamma_{n+1}^i \frac{\partial f^i(\boldsymbol{t}_{n+1})}{\partial \boldsymbol{t}_{n+1}}, \quad (2-16)$$

where $n + 1$ denotes the new solutions $\{\boldsymbol{t}_{n+1}, \boldsymbol{\varepsilon}_{n+1}^p\}$ to be determined with respect to the known state $\{\boldsymbol{t}_n, \boldsymbol{\varepsilon}_n^p\}$ and the assigned total strain $\{\boldsymbol{\varepsilon}_{n+1}\}$. The Kuhn–Tucker conditions in discrete form are expressed as

$$\Delta \gamma_{n+1}^i \geq 0, \quad f^i(\boldsymbol{t}_{n+1}) \leq 0, \quad \Delta \gamma_{n+1}^i f^i(\boldsymbol{t}_{n+1}) = 0, \quad \text{for } i \in [1, \dots, m]. \quad (2-17)$$

As pointed out in [Simo et al. 1988], the solution of the system of equations (2-15)–(2-17), according to the Haar–Karman’s principle, coincides with the following minimization problem:

$$\begin{cases} \text{minimize:} & \Pi_{HK}[\Delta \boldsymbol{t}_{n+1}] = \frac{1}{2}(\Delta \boldsymbol{t}_{n+1} : \boldsymbol{C}^{-1} : \Delta \boldsymbol{t}_{n+1}), \\ \text{subject to:} & f^i(\Delta \boldsymbol{t}_{n+1}) := -\boldsymbol{n}^i : \Delta \boldsymbol{t}_{n+1} - b_{n+1}^i \geq 0, \quad \text{for } i \in [1, \dots, m]. \end{cases} \quad (2-18)$$

Here $\Delta \mathbf{t} := \mathbf{t} - \mathbf{t}_E$, where \mathbf{t}_E the elastic predictor related to the strain increment through the elastic matrix \mathbf{C} , while $\mathbf{b}^i := \mathbf{c}^i - \mathbf{n}^i : \mathbf{t}_E$.

Equation (2-18) represents a standard strictly convex quadratic programming problem expressed in the so-called primal form, where $\Delta \mathbf{t}_{n+1}$ are the primal variables and the plastic multipliers $\Delta \gamma_{n+1}$ the dual ones. The approach adopted here for its solution, called dual active set method, was originally proposed in [Goldfarb and Idnani 1983] and then adopted in [Malena and Casciaro 2008] to solve a shakedown structural problem.

3. Cracking due to settlement

In this section, the failure pattern in the masonry structure due to ground surface differential settlement is investigated referring to both, a bidimensional façade and a tridimensional building. As suggested in [Portioli and Cascini 2016] and [Mastrodicasa 1993], the foundation settlement is simulated by substituting a part of the foundation by a movable rigid block, connected to the masonry above by a no-tension frictional interface allowing for the possible detachment. By imposing a downward vertical displacement to the movable rigid block, the masonry structure experiences a progressive reduction of the reaction at the basis, up to a limit value corresponding to the self-weight of the portion of the wall involved in the settlement (Figure 4). The resulting failure pattern of masonry is then represented by the plastic strain fields provided by the analyses (Figures 2 and 3). The choice of such a rough simulation of settlement has the advantage of reproducing the same boundary conditions of the well-known experiments carried in [Mastrodicasa 1993] allowing for a direct comparison with them.

3A. Plane wall. The first considered masonry wall has a length of 10 m, height of 5 m and a thickness of 0.5 m, while the blocks have a length of 0.5 m, height of 0.25 m and thickness of 0.5 m. The friction coefficient and the unit volume weight are set equal to 0.5 kN/m³ and 18.0 kN/m³, respectively.

Two different settlement configurations were adopted (Figure 2), with a portion of the foundation undergoing a downward displacement having a length of 2 m (short settlement) and 5 m (long settlement).

The vertical reaction at the base of the movable block prior to the application of the settlement is equal to 90.0 kN and 225.0 kN for the two walls, respectively. At failure, the base reactions become equal to 27.8 kN and 152.9 kN (see Figure 4), with a reduction of about 70% and 45%, respectively. The failure patterns are shown in Figure 2 in terms of plastic strain depicted over the deformed configuration of the wall.

The predicted failure patterns are in agreement with the experimental ones presented in [Mastrodicasa 1993]: in both cases the inelastic strain is localised over a diagonal band originating at the boundary between the movable block and the fixed foundation, with an inclination that depends on the aspect ratio of the blocks. In the case of the short settlement (Figure 2, left), the inelastic deformed band terminates on the lateral edge of the wall, while, in case of the long settlement (Figure 2, right), terminates on the top of the wall, with a larger portion of the wall mobilized by the settlement and a corresponding lower decrease in the vertical reaction.

3B. Wall with openings. The second masonry wall taken into account has the same geometry as the previous one, but is provided with three orders of openings spanning $1 \times 1 \text{ m}^2$ (Figure 3). The end settlement 1.5 m long, and the central settlement 5 m long were analyzed. As expected, the presence of

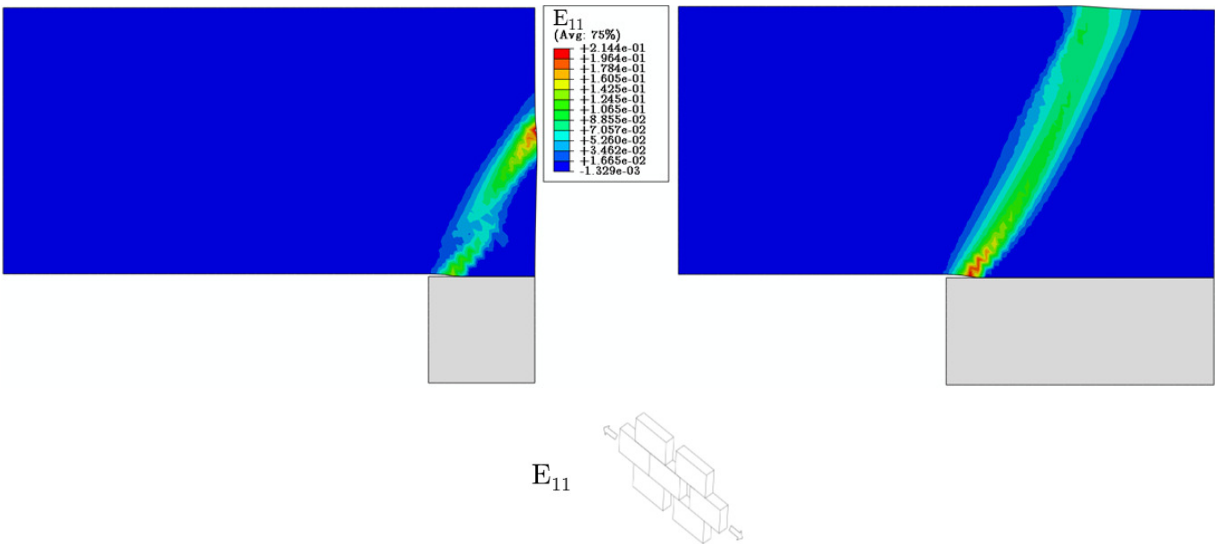


Figure 2. Plastic strain distributions at failure: short (left) and long settlement for plane wall (right).

openings introduces discontinuities that affect the strain pattern at failure. The inelastic strains always originate at the boundaries of the portion of the foundation that displaces downwards, but end to localize in the masonry strips over the openings (Figure 3). Clearly, the inelastic strain pattern depend on how the lintels are modelled. In both cases the displacement of the wall can be described as a rigid body vertical translation of the pier lying over the movable foundation. The relative displacement of the pier with the rest of the structure is then accommodated through the inelastic strain concentrating over the horizontal masonry strips between the openings adjacent to the pier.

The base reaction versus the vertical support displacement is plotted in Figure 4 (right): almost no reduction is obtained in the case of the end settlement, since the subsidence of the pier does not involve a significant redistribution of the load towards the adjacent masonry.

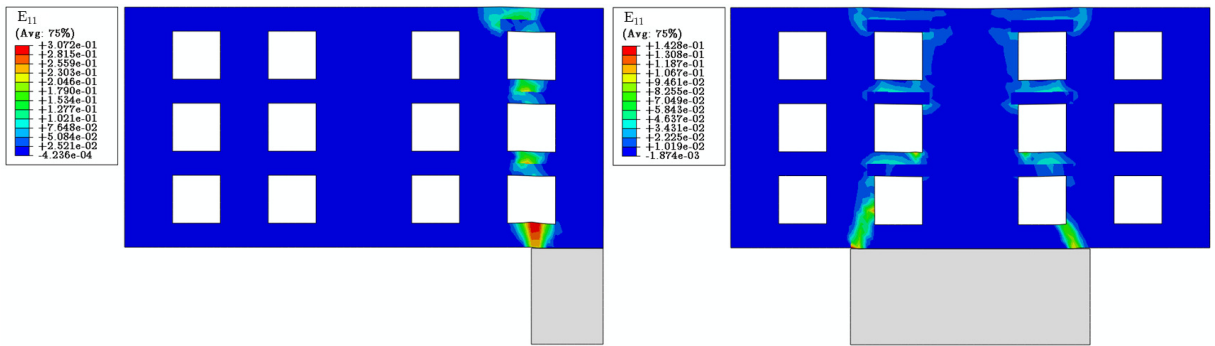


Figure 3. Plastic strain distributions at failure: end settlement for wall with openings (left) and central settlement for wall with openings (right).

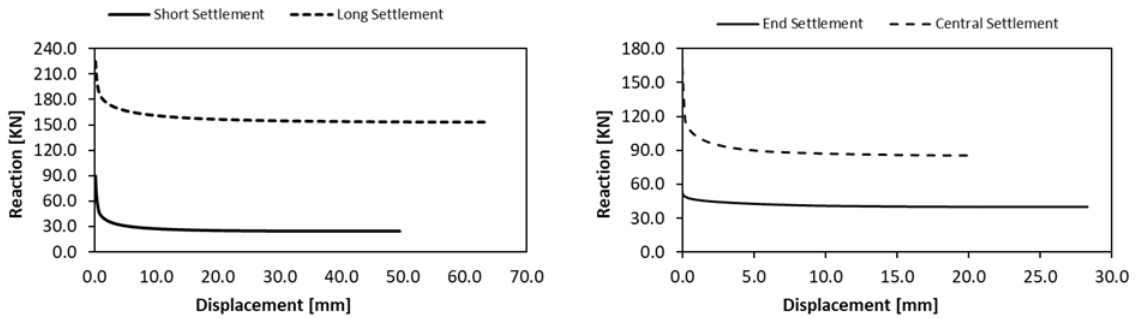


Figure 4. Base reaction versus vertical support displacement for full wall (left) and wall with openings (right).

3C. 3D building. Aiming at testing the capability of the proposed model to catch the three dimensional behavior, a small two-story masonry building is considered made of four connected walls. The considered 3D building (Figure 5) is the same as the one proposed in [Portioli and Cascini 2016]. The front façade includes two doors at the ground floor and two windows at the first floor having timber lintels above the openings. The size of a single brick is $80 \text{ mm} \times 40 \text{ mm} \times 30 \text{ mm}$ (length, height, thickness). The friction coefficient is set equal to 0.5, while the unit weights of masonry and timber are equal to 26.8 kN/m^3 and 6.0 kN/m^3 , respectively.

The settlement was imposed through the application of a vertical downward displacement at the right corner of the building, including the central wall of the façade between the openings and half of the lateral wall (see Figure 5, left). The inelastic strain field, as depicted in Figure 5 (right), results in a good agreement with the corresponding analysis on the discrete masonry assembly shown in [Portioli and Cascini 2016], demonstrating the capability of the proposed model to provide a reliable prediction of the expected failure mode. The vertical reaction at the base of the movable support decreases from 1.027 kN, before the settlement, up to 0.659 kN when the plastic flow occurs.

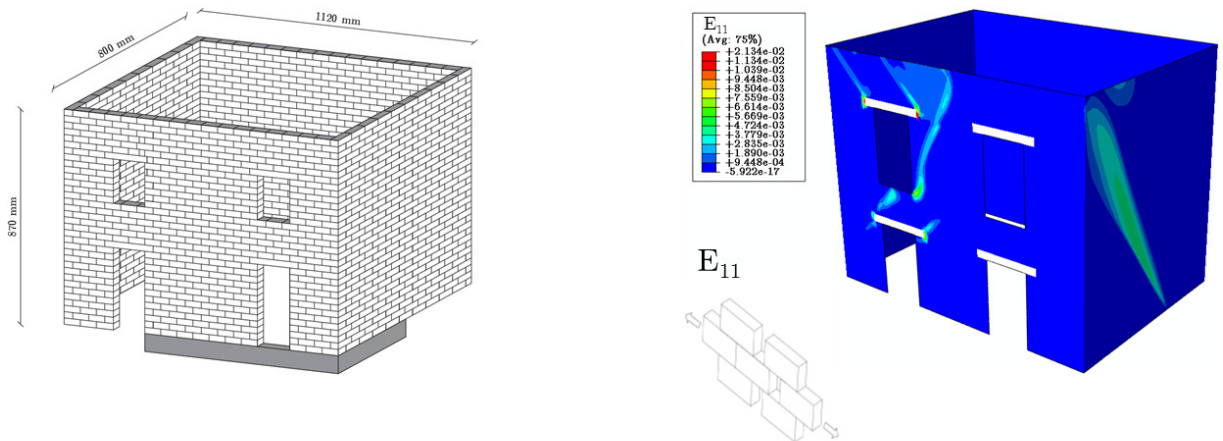


Figure 5. 3D building subject to foundation settlement: geometrical characteristics (left) and plastic strain distribution at failure (right).

4. Cracking due to earthquake

This section aims at assessing the capability of the model in providing a prediction of the expected failure modes of masonry buildings under earthquake loading. To this end, as frequently proposed in the literature, the earthquake load is simply represented by horizontal body forces increasing up to the attainment of the failure mechanism. Some preliminary benchmark are carried out, aiming at describing how the model behaves under out-of-plane loads, and then some more complex geometries are investigated and the results compared to the tilting tests carried out in [Restrepo Vélez et al. 2014] on 1 : 5 scale on dry-stone masonry.

4A. Preliminary benchmarks. The first benchmark, originally proposed in [Cecchi et al. 2007], consists of a rectangular panel subjected to self-weight and to increasing horizontal out-of-plane distributed load. The wall has a length of 3 m, height 3 m and a thickness of 30 cm. It is simply supported at the base and restrained at the top against out-of-plane displacement. The blocks are 20 cm \times 10 cm \times 30 cm. The unit weight of masonry is equal to 20 kN/m³, while the friction coefficient and the cohesion in the joints are equal to 0.471 N/mm² and 0.1 N/mm², respectively.

The results of the analysis are provided in Figure 6 in terms of plastic strain component χ_{22} , corresponding to the curvature along the vertical direction, and in terms of vertical displacement u_2 . The horizontal load at failure is equal to 1.421 N/cm², while the plastic hinge develops at 184 cm from the ground. The solution shows the uplift of the wall, as a consequence of the fact that the horizontal plastic hinge does not arise in the middle-plane but on the external surface, as it actually occurs in masonry walls. The results are well in accordance with those provided in [Cecchi et al. 2007].

As a second benchmark, two masonry panels experimentally tested in [Southcombe et al. 1995; Chong et al. 1994] have been numerically simulated. The panels, having dimensions 5625 mm \times 2465 mm \times 102.5 mm, were loaded by air-bags up to failure with increasing uniform lateral pressure. They are fully clamped at the base and free on the top, while both lateral edges are simply supported, as shown in Figure 7 (second row).

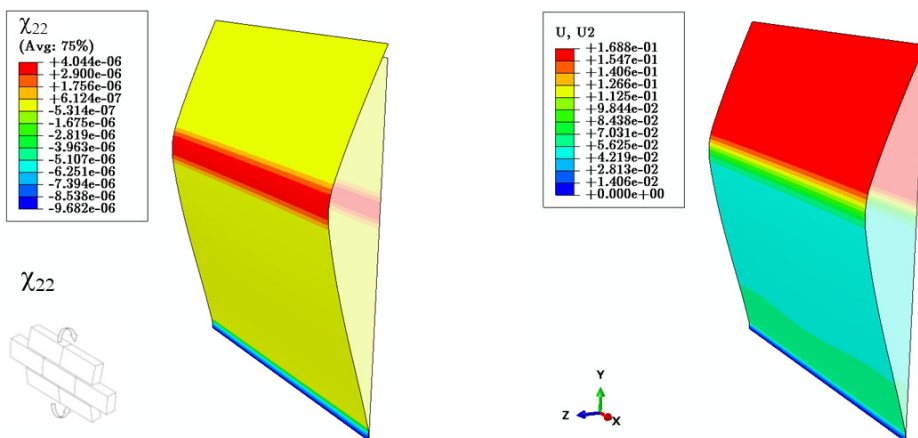


Figure 6. Plastic strain distribution (left) and vertical displacement (right) at failure.

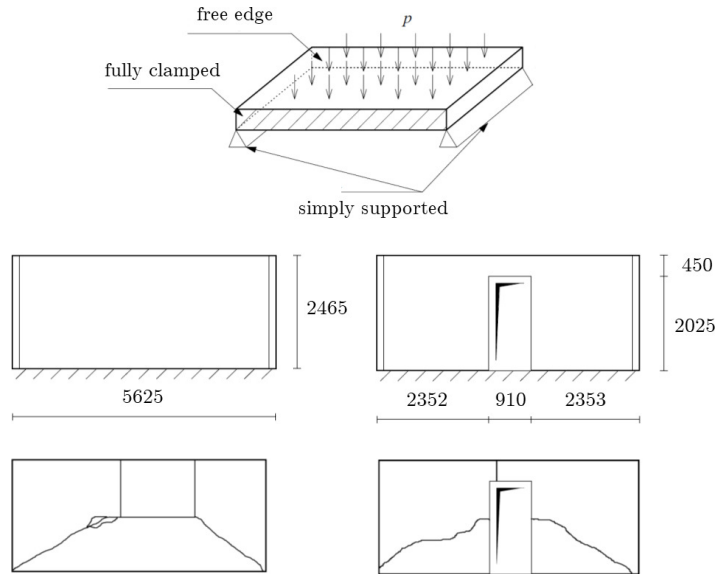


Figure 7. Masonry panels experimentally tested in [Southcombe et al. 1995; Chong et al. 1994]: geometry (second row) and failure patters (third row).

Each panel consists of solid clay bricks having dimensions $215 \text{ mm} \times 65 \text{ mm} \times 102.5 \text{ mm}$, and mortar joints with thickness 10 mm . The pressure at failure provided by the experiments is equal to 2.8 kN/m^2 and 2.2 kN/m^2 for the plane wall (SB01 test) and for the wall with the opening (SB04 test), respectively. The numerical simulations have been carried out assuming a cohesion equal to 0.32 MPa and a friction angle equal to 36° . The pressure at failure provided by the model is equal to 2.71 kN/m^2 and 2.49 kN/m^2 for the SB01 and SB04 tests, respectively. The plastic strain component χ_{11} , corresponding to the curvature along the horizontal direction, is represented in Figure 8, showing a reasonable matching with the experimental crack pattern (Figure 7, third row).

4B. Tilting tests. In this section, the capability of the model in reproducing the failure mechanisms obtained in the experimental campaign carried out in [Restrepo Vélez et al. 2014] are described. The experimental campaign consists in $1 : 5$ scale dry-stone masonry walls built over a tilting table and tested up to failure. Each prototype was first built under the self-weight and then brought up to failure by tilting the table. The horizontal collapse multiplier is simply the tangent of the table tilt angle causing the collapse. The walls are made of dry-stone bricks, with specific weight 26.8 kN/m^3 and dimensions of $30 \text{ mm} \times 80 \text{ mm} \times 40 \text{ mm}$. The friction coefficient ranges from 0.67 to 0.77 , as shown in [Restrepo Vélez et al. 2014]. Several configurations were tested, consisting in three U-shaped walls made of an out-of-plane loaded wall constrained at both lateral edges by in-plane loaded walls, having different length and vertical loading at the top. The numerical simulations are carried out by reproducing the same geometry, assuming a friction coefficient of 0.7 and neglecting the cohesion, while the load condition is enforced by constraining the walls at their base, activating the self-weight and then applying increasing horizontal body forces, up to failure, while recording the horizontal collapse multiplier λ_c equal to the ratio between horizontal and vertical body forces.

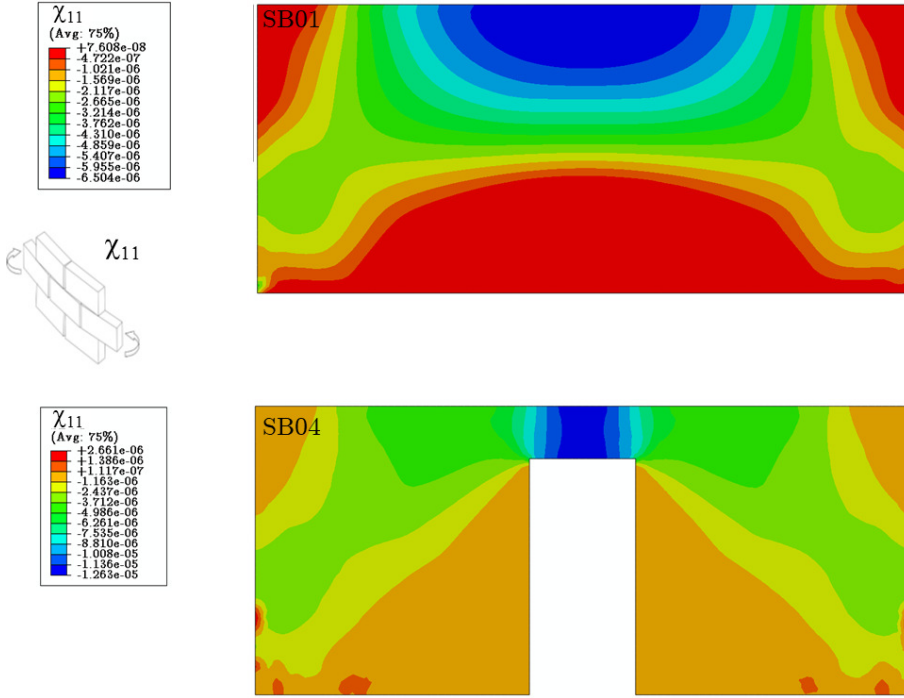


Figure 8. Plastic strain distributions at failure for tests SB01 (top) and SB04 (bottom).

4B.1. U-shaped walls loaded inward. The first experimental test named S1 [Restrepo Vélez et al. 2014] consists of a wall with a length of 11 bricks and a height of 21 bricks, loaded inward and restrained by two lateral side walls having the same height and a length of 4 bricks (Figure 9, top). The test was repeated three times, providing an average value of the collapse multiplier equal to 0.241, while the numerical prediction is equal to 0.284 with an overestimate of about 18%. The predicted versus experimental failure modes are compared in Figure 9, resulting in a good reproduction of the failure pattern, with the inelastic strain component χ_{11} corresponding to the opening of the head joints in the upper central portion of the main wall and at the corner with the side walls.

4B.2. U-shaped walls loaded outward. The three experimental tests S7, S10 and S20 are similar to the previous S1 test but with the front wall loaded outwards. The three specimens have the same height of 21 bricks but differ in the length of the walls: the specimen S7 has the out-of-plane loaded front wall made of 8 bricks and the side walls of 7 bricks; the specimen S10 has the front wall made of 12 bricks and the side walls of 10 bricks; the specimen S20 has the front wall made of 14 bricks and the side walls of 10 bricks, with a further central transversal wall similar to the side walls (see the figures 10 (top), 11 (top) and 12 (top)). The experimental collapse horizontal multipliers are equal to 0.291, 0.231 and 0.285, while those predicted by the model are equal to 0.287, 0.241 and 0.262 for test S7, S10 and S20, respectively, with a discrepancy of about -1% , $+7\%$ and -8% .

The failure modes depend on the length-to-height ratio of the front wall: for shorter wall length the failure is driven by the in-plane diagonal cracking of the side walls, while for greater wall length the failure is controlled by out-of-plane bending of the front wall. Both inelastic phenomena are correctly

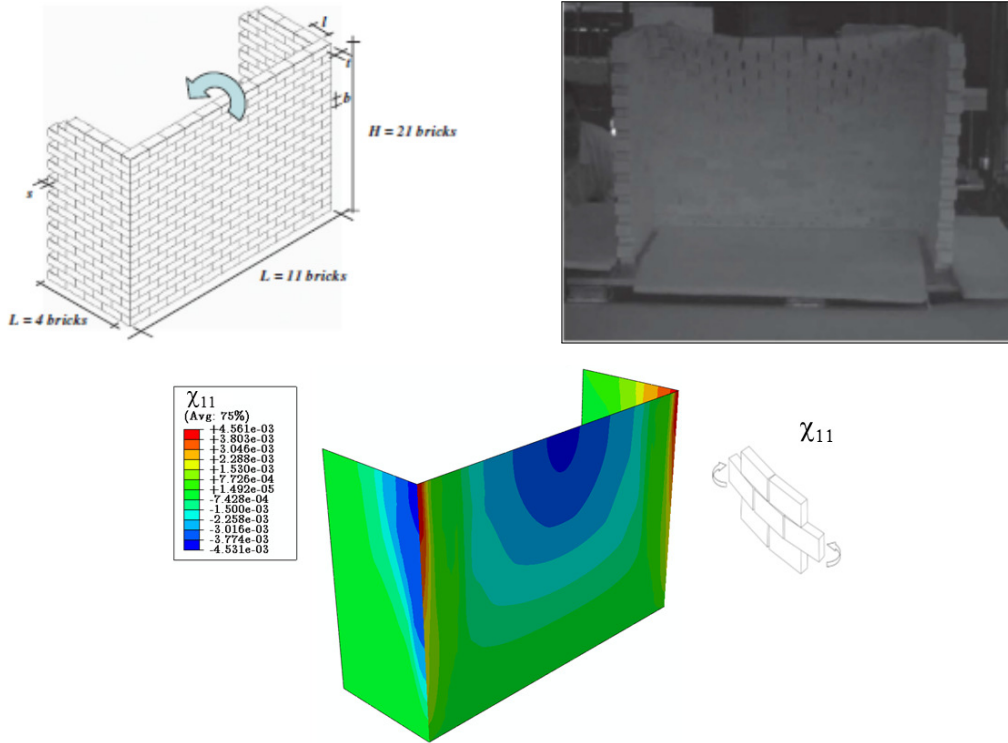


Figure 9. Test S1: experimental ($\lambda_{\text{exp}} = 0.241$) [Restrepo Vélez et al. 2014] (top) versus numerical results ($\lambda = 0.284$) (bottom).

simulated by the numerical analyses as shown by the plastic strain field represented in figures 10, 11 and 12, resulting in a good agreement with experimental results. More precisely, in test S7, failure is reached through overturning of the upper part of the front wall, with a horizontal hinge forming at about half of its height, while the side walls display opening of the head joints and sliding of the bricks. Both phenomena are nicely simulated by the inelastic strain components χ_{22} related to curvature in the vertical direction and E_{11} , related to the opening of the head joints, as shown in Figure 10. In test S10, the out-of-plane displacement of the front wall is accompanied by a more pronounced bending deformation, with the χ_{11} inelastic curvature localised at the upper central portion of the front wall (Figure 11). In test S20, the failure pattern displays a mixed failure mode including both, overturning and out-of-plane bending, associated with in-plane diagonal cracking in the transversal walls, especially in the central one (Figure 12).

4B.3. Effect of vertical load. The Specimens S32 and S41 were tested to study the effect of overburden forces and restrains coming from floor joists (figures 13, top and 14, top). The specimen S32 consists in a simple wall with a length of 14 bricks and height of 21 bricks restrained at the top by means of the floor joists which also apply a vertical load on the wall of about 181 N.

The specimen S41 consists in three U-shaped walls with a height of 21 bricks, comprising two side walls with a length of 8 brick and a front wall with a length of 10 bricks restrained at the top, as in the previous case, and subjected to a vertical load of about 115 N (Figure 14, top).

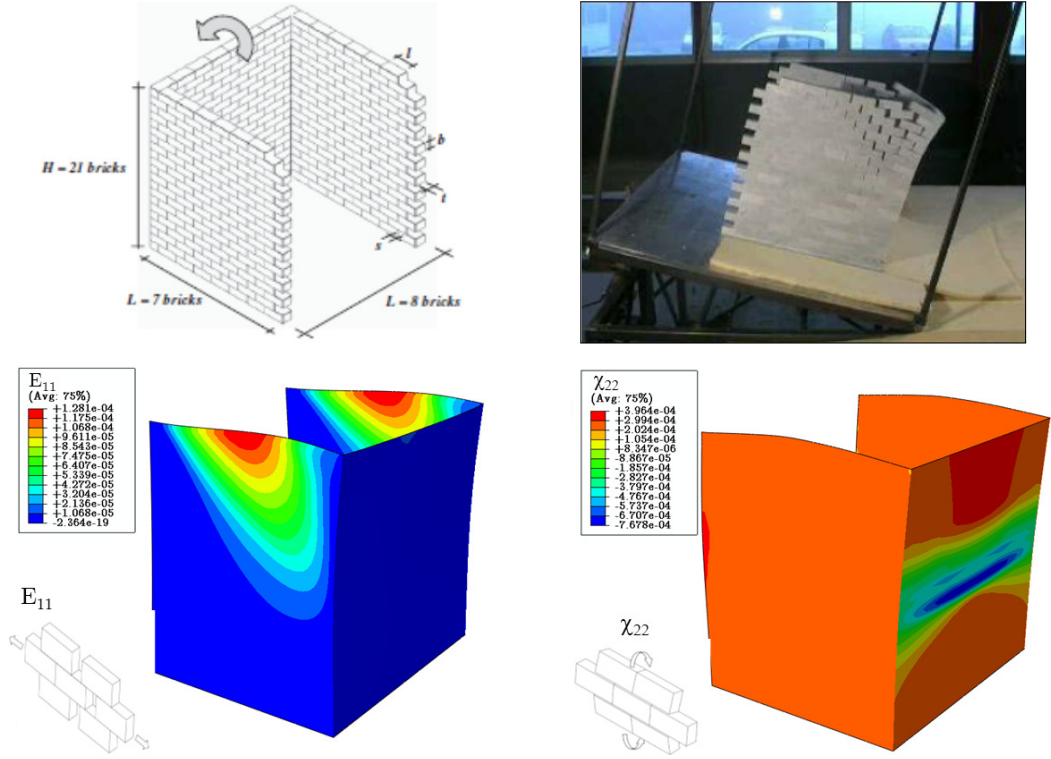


Figure 10. Test S7: experimental ($\lambda_{\text{exp}} = 0.291$) [Restrepo Vélez et al. 2014] (top) versus numerical results ($\lambda = 0.287$) (bottom).

The collapse multipliers resulting from the experiments are equal to 0.293 and 0.423, while the numerical predictions are equal to 0.285 and 0.413, for tests S32 and S41, respectively, with a slight underestimate of about 3% for both the simulations.

For the test S32, the failure pattern consists in the vertical bending around two horizontal hinges forming at the base and at about 3/4 of the height of the wall. The numerical results (see Figure 13) provide a strong concentration of the inelastic curvature χ_{22} that matches perfectly to the flexural opening in the bed joints at the intermediate hinge.

Numerical and experimental results for test S41 are compared in Figure 14. The failure pattern on the front wall is similar to the previous case, but the hinge is much higher, at about 80% of the height of the wall. On the lateral side walls the bricks slide and the vertical joints open along a diagonal crack that is well represented by the inelastic strain component E_{11} resulting from the numerical simulations.

4B.4. 3D Building. As a final benchmark, the test S42 was simulated by numerical analysis, aiming at reproducing the behavior of a two-story 3D building. The geometry of the specimen consists in a masonry cell made of four connected walls with a height of 42 bricks and a length of 10 and 13 bricks. Two opposite walls are provided with four openings each. The collapse multiplier measured in the laboratory was equal to 0.236, while the numerical prediction is equal to 0.226, with a slight underestimate of about 4%.

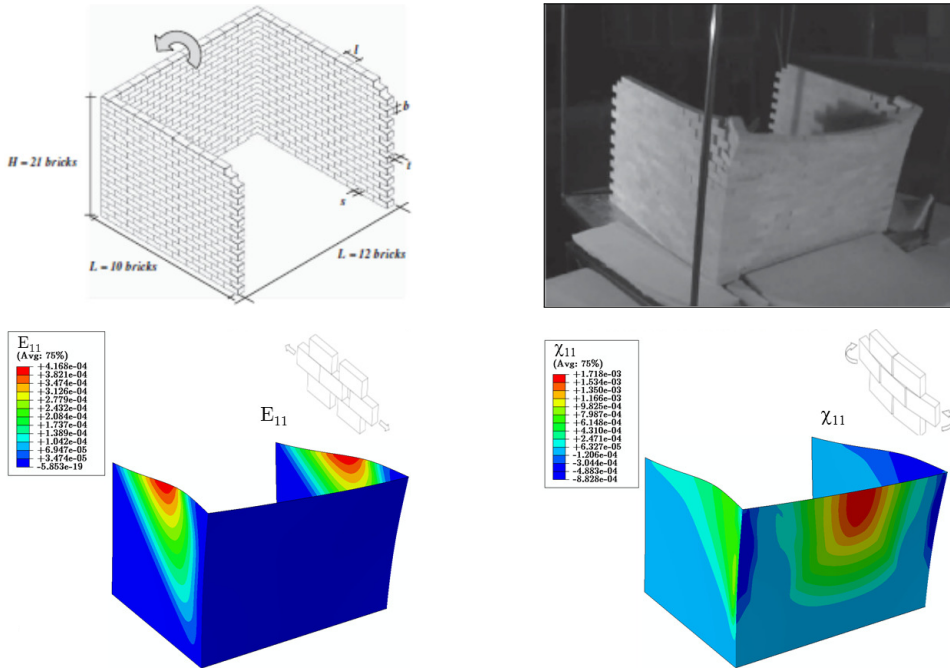


Figure 11. Test S10: experimental ($\lambda_{\text{exp}} = 0.231$) [Restrepo Vélez et al. 2014] (top) versus numerical results ($\lambda = 0.241$) (bottom).

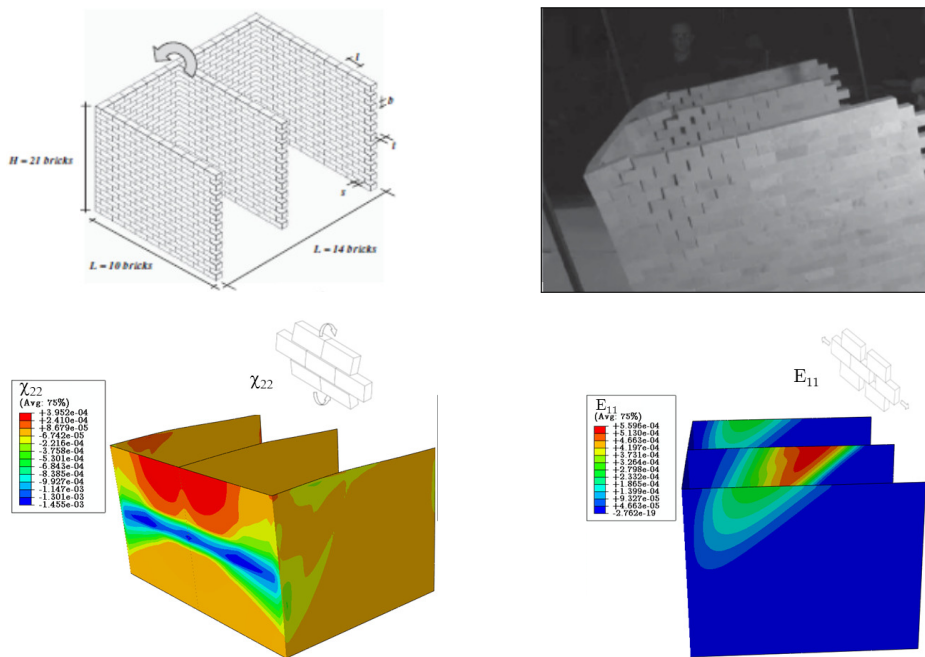


Figure 12. Test S20: experimental ($\lambda_{\text{exp}} = 0.285$) [Restrepo Vélez et al. 2014] (top) versus numerical results ($\lambda = 0.262$) (bottom).

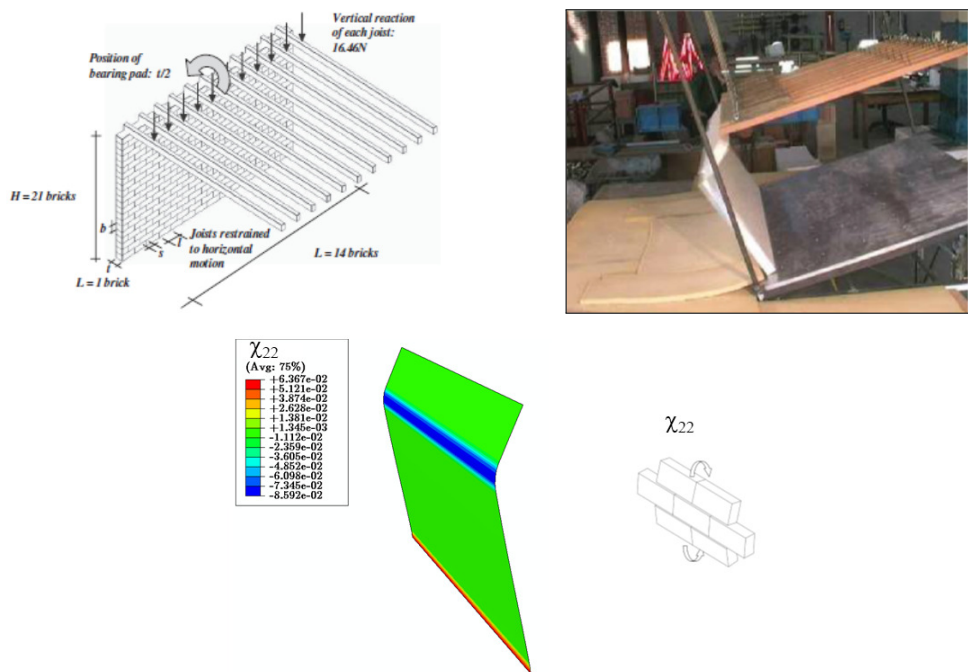


Figure 13. Test S32: experimental ($\lambda_{\text{exp}} = 0.293$) [Restrepo Vélez et al. 2014] (top) versus numerical results ($\lambda = 0.285$) (bottom).

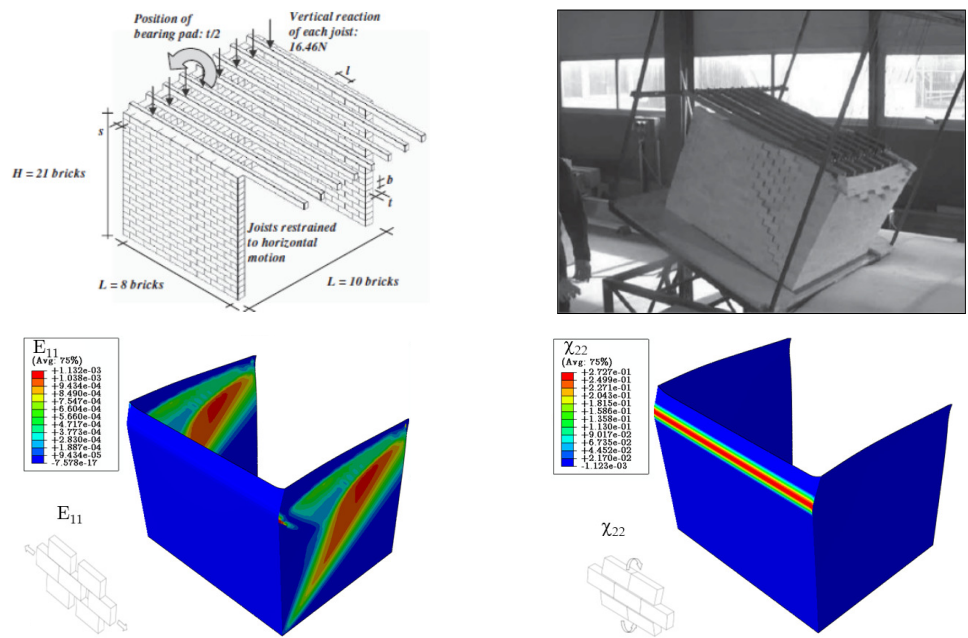


Figure 14. Test S41: experimental ($\lambda_{\text{exp}} = 0.423$) [Restrepo Vélez et al. 2014] (top) versus numerical results ($\lambda = 0.413$) (bottom).

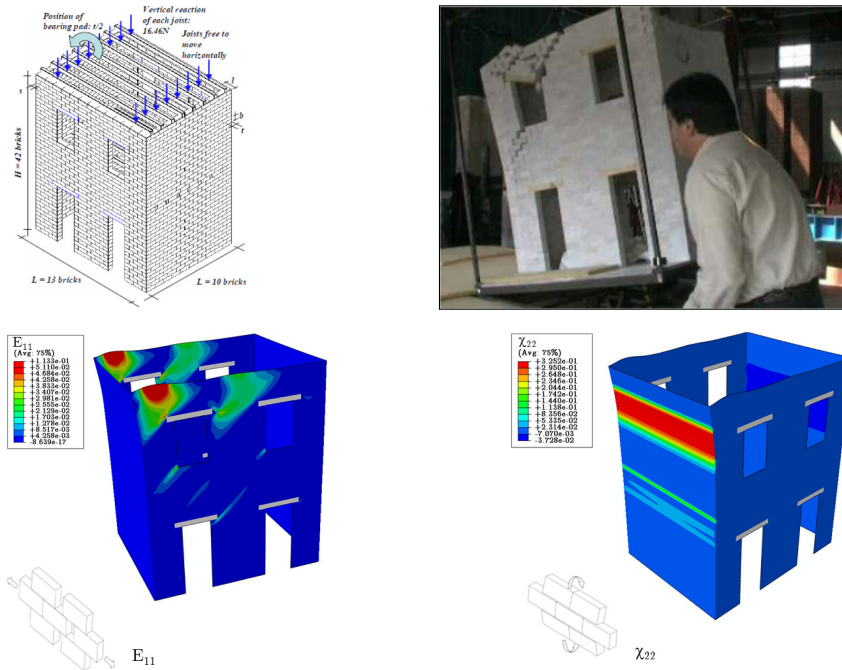


Figure 15. Test S42: experimental ($\lambda_{\text{exp}} = 0.236$) [Restrepo Vélez et al. 2014] (top) versus numerical results ($\lambda = 0.226$) (bottom).

The failure pattern concentrates at the left upper top of the specimen, close to the opening, with the appearance of a diagonal crack originating at the lower left corner and at the upper right corner of the lateral opening (Figure 15). Once again, the crack pattern provided by the experiments is well reproduced by the inelastic strain field predicted by the numerical analyses. Referring to Figure 15 (bottom), the horizontal strain component E_{11} tends to localise in accordance with the opening of the head joints in the in-plane loaded walls, while the vertical curvature χ_{22} , reproduces the horizontal hinges corresponding to the overturning of the upper part of the out-of-plane loaded walls.

As a summary of the tests under horizontal loading, it is worth noting that the numerical outcomes of the tests controlled by the in-plane behavior (i.e., S7, S22, S32, S41 and S42) match quite well the experimental results in terms of failure load. Conversely, the numerical outcomes for tests S1 and S10 are affected by a larger discrepancy. The difference can be ascribed to the simplicity of the model adopted for the definition of the strength domain [Sab 2003], which overestimate the load multiplier when torsional behavior is involved.

5. Conclusion

A continuous finite element model for the nonlinear analysis of ancient masonry buildings is developed, implemented in a finite element code and applied to the assessment of masonry buildings subjected either to foundation settlements or to lateral seismic loads. The model is validated by comparison with the experimental results in terms of failure pattern and ultimate live load. The comparison shows the ability of the model in predicting the failure pattern with different loading and boundary conditions.

Accordingly, the expected collapse mechanism is a result of the analysis and does not have to be a-priori defined, as suggested by current assessment procedures. The model is based on few parameters, namely a mechanical parameter consisting in the friction coefficient of the joints and a geometrical parameter consisting in the aspect ratio of the blocks, that can be easily evaluated in existing masonry structures. It should be noticed that more refined models are available in the literature that are based on advanced constitutive laws including softening, cracking and describing more accurately the nonlinear mechanical behavior of masonry. However, the use of such models generally requires many data input, which are often hardly available in current practice and a strong computational effort for application to real structures. In this perspective, the nonlinear model presented in this study might represent a good compromise in terms of accuracy of the results, available input data, and computational cost. For this reason, the proposed numerical approach represents a promising tool for the analysis of historic masonry buildings under foundation settlements or earthquake loads.

Acknowledgements

The present work was supported by the research grant SiCura 2018-2020 funded by the Regione Lazio and by the research grant DPC-ReLUIIS 2019-2021 funded by the Italian Civil Protection Department.

References

- [Acito et al. 2016] M. Acito, C. Chesi, G. Milani, and S. Torri, “Collapse analysis of the clock and fortified towers of Finale Emilia, Italy, after the 2012 Emilia Romagna seismic sequence: lesson learned and reconstruction hypotheses”, *Constr. Build. Mater.* **115** (2016), 193–213.
- [Amorosi et al. 2012] A. Amorosi, D. Boldini, G. de Felice, and M. Malena, “Tunnelling-induced deformation on a masonry structure: a numerical approach”, pp. 353–359 in *Geotechnical aspects of underground construction in soft ground* (Rome, 2011), edited by G. Viggiani, Taylor & Francis, London, 2012.
- [Amorosi et al. 2014] A. Amorosi, D. Boldini, G. de Felice, M. Malena, and M. Sebastianelli, “Tunnelling-induced deformation and damage on historical masonry structures”, *Géotechnique* **64**:2 (2014), 118–130.
- [Angelillo 1993] M. Angelillo, “Constitutive relations for no-tension materials”, *Meccanica (Milano)* **28**:3 (1993), 195–202.
- [Angelillo et al. 2010] M. Angelillo, L. Cardamone, and A. Fortunato, “A numerical model for masonry-like structures”, *J. Mech. Mater. Struct.* **5**:4 (2010), 583–615.
- [de Buhan and de Felice 1997] P. de Buhan and G. de Felice, “A homogenization approach to the ultimate strength of brick masonry”, *J. Mech. Phys. Solids* **45**:7 (1997), 1085–1104.
- [Caillerie 1984] D. Caillerie, “Thin elastic and periodic plates”, *Math. Methods Appl. Sci.* **6**:2 (1984), 159–191.
- [Calió et al. 2012] I. Calió, M. Marletta, and B. Pantó, “A new discrete element model for the evaluation of the seismic behaviour of unreinforced masonry buildings”, *Eng. Struct.* **40** (2012), 327–338.
- [Cecchi and Sab 2002] A. Cecchi and K. Sab, “A multi-parameter homogenization study for modeling elastic masonry”, *Eur. J. Mech. A Solids* **21**:2 (2002), 249–268.
- [Cecchi et al. 2007] A. Cecchi, G. Milani, and A. Tralli, “A Reissner–Mindlin limit analysis model for out-of-plane loaded running bond masonry walls”, *Int. J. Solids Struct.* **44**:5 (2007), 1438–1460.
- [Chong et al. 1994] V. L. Chong, C. Southcombe, and I. M. May, “The behaviour of laterally loaded masonry panels with openings”, pp. 178–182 in *Masonry* (London, 1992), edited by H. W. H. West, Proc. British Masonry Soc. **6**, Brit. Masonry Soc., Stoke-on-Trent, UK, 1994.
- [de Felice 1995] G. de Felice, “Détermination des coefficients d’élasticité de la maçonnerie par une méthode d’homogénéisation”, pp. 393–396 in *Actes du 12ème Congrès Français de Mécanique, I* (Strasbourg, 1995), Assoc. Univ. Mécanique, Strasbourg, 1995.

- [de Felice 2001] G. de Felice, “Overall elastic properties of brickwork via homogenization”, pp. 411–418 in *Structural engineering, mechanics, and computation, I* (Cape Town, 2001), edited by A. Zingoni, Elsevier, 2001.
- [de Felice et al. 2010] G. de Felice, A. Amorosi, and M. Malena, “Elasto-plastic analysis of block structures through a homogenization method”, *Int. J. Numer. Anal. Methods Geomech.* **34**:3 (2010), 221–247.
- [de Felice et al. 2017] G. de Felice, S. de Santis, P. B. Lourenço, and N. Mendes, “Methods and challenges for the seismic assessment of historic masonry structures”, *Int. J. Archit. Herit.* **11**:1 (2017), 143–160.
- [Goldfarb and Idnani 1983] D. Goldfarb and A. Idnani, “A numerically stable dual method for solving strictly convex quadratic programs”, *Math. Program.* **27**:1 (1983), 1–33.
- [Heyman 1966] J. Heyman, “The stone skeleton”, *Int. J. Solids Struct.* **2**:2 (1966), 249–279.
- [Koiter 1960] W. T. Koiter, “General theorems for elastic-plastic solids”, pp. 165–221 in *Progress in solid mechanics*, edited by I. N. Sneddon and R. Hill, North-Holland, Amsterdam, 1960.
- [Livesley 1978] R. K. Livesley, “Limit analysis of structures formed from rigid blocks”, *Int. J. Numer. Methods Eng.* **12**:12 (1978), 1853–1871.
- [Lourenço and Ramos 2004] P. B. Lourenço and L. F. Ramos, “Characterization of cyclic behavior of dry masonry joints”, *J. Struct. Eng. (ASCE)* **130**:5 (2004), 779–786.
- [Malena and Casciaro 2008] M. Malena and R. Casciaro, “Finite element shakedown analysis of reinforced concrete 3D frames”, *Comput. Struct.* **86**:11-12 (2008), 1176–1188.
- [Malena et al. 2019] M. Malena, F. Portioli, R. Gagliardo, G. Tomaselli, L. Cascini, and G. de Felice, “Collapse mechanism analysis of historic masonry structures subjected to lateral loads: a comparison between continuous and discrete models”, *Comput. Struct.* **220** (2019), 14–31.
- [Massart et al. 2005] T. J. Massart, R. H. J. Peerlings, M. G. D. Geers, and S. Gottcheiner, “Mesoscopic modeling of failure in brick masonry accounting for three-dimensional effects”, *Eng. Fract. Mech.* **72**:8 (2005), 1238–1253.
- [Mastrodicasa 1993] S. Mastrodicasa, *Dissesti statici delle strutture edilizie*, 9th ed., Hoepli, Milan, 1993.
- [Milani et al. 2006a] G. Milani, P. B. Lourenço, and A. Tralli, “Homomogenised limit analysis of masonry walls, I: Failure surfaces”, *Comput. Struct.* **84**:3-4 (2006), 166–180.
- [Milani et al. 2006b] G. Milani, P. B. Lourenço, and A. Tralli, “Homomogenised limit analysis of masonry walls, II: Structural examples”, *Comput. Struct.* **84**:3-4 (2006), 181–195.
- [Milani et al. 2007] G. Milani, P. B. Lourenço, and A. Tralli, “3D homogenized limit analysis of masonry buildings under horizontal loads”, *Eng. Struct.* **29**:11 (2007), 3134–3148.
- [Mistler et al. 2007] M. Mistler, A. Anthoine, and C. Butenweg, “In-plane and out-of-plane homogenisation of masonry”, *Comput. Struct.* **85**:17-18 (2007), 1321–1330.
- [Page 1978] A. W. Page, “Finite element model for masonry”, *J. Struct. Div. (ASCE)* **104**:8 (1978), 1267–1285.
- [Pande et al. 1989] G. N. Pande, J. X. Liang, and J. Middleton, “Equivalent elastic moduli for brick masonry”, *Comput. Geotech.* **8**:3 (1989), 243–265.
- [Pietruszczak and Niu 1992] S. Pietruszczak and X. Niu, “A mathematical description of macroscopic behaviour of brick masonry”, *Int. J. Solids Struct.* **29**:5 (1992), 531–546.
- [Portioli and Cascini 2016] F. Portioli and L. Cascini, “Assessment of masonry structures subjected to foundation settlements using rigid block limit analysis”, *Eng. Struct.* **113** (2016), 347–361.
- [Portioli et al. 2014] F. Portioli, C. Casapulla, M. Gilbert, and L. Cascini, “Limit analysis of 3D masonry block structures with non-associative frictional joints using cone programming”, *Comput. Struct.* **143** (2014), 108–121.
- [Restrepo Vélez et al. 2014] L. F. Restrepo Vélez, G. Magenes, and M. C. Griffith, “Dry stone masonry walls in bending, I: Static tests”, *Int. J. Archit. Herit.* **8**:1 (2014), 1–28.
- [Roselli et al. 2018] I. Roselli, M. Malena, M. Mongelli, N. Cavalagli, M. Giofrè, G. De Canio, and G. de Felice, “Health assessment and ambient vibration testing of the ‘Ponte delle Torri’ of Spoleto during the 2016-2017 Central Italy seismic sequence”, *J. Civ. Struct. Health Monit.* **8**:2 (2018), 199–216.
- [Sab 2003] K. Sab, “Yield design of thin periodic plates by a homogenization technique and an application to masonry walls”, *C. R. Mécanique* **331**:9 (2003), 641–646.

- [Sab et al. 2007] K. Sab, J. Dallot, and A. Cecchi, “[Determination of the overall yield strength domain of out-of-plane loaded brick masonry](#)”, *Int. J. Multiscale Comput. Eng.* **5**:2 (2007), 83–92.
- [Sacco 2009] E. Sacco, “[A nonlinear homogenization procedure for periodic masonry](#)”, *Eur. J. Mech. A Solids* **28**:2 (2009), 209–222.
- [Simo et al. 1988] J. C. Simo, J. G. Kennedy, and S. Govindjee, “[Nonsmooth multisurface plasticity and viscoplasticity: loading/unloading conditions and numerical algorithms](#)”, *Int. J. Numer. Methods Eng.* **26**:10 (1988), 2161–2185.
- [Southcombe et al. 1995] C. Southcombe, I. M. May, and V. L. Chong, “[The behaviour of brickwork panels with openings under lateral load](#)”, pp. 105–110 in *Masonry*, edited by H. W. H. West, Proc. British Masonry Soc. **7**, Brit. Masonry Soc., Stoke-on-Trent, UK, 1995.
- [Stefanou et al. 2015] I. Stefanou, K. Sab, and J.-V. Heck, “[Three dimensional homogenization of masonry structures with building blocks of finite strength: a closed form strength domain](#)”, *Int. J. Solids Struct.* **54** (2015), 258–270.
- [Taliercio 2016] A. Taliercio, “[Closed-form expressions for the macroscopic flexural rigidity coefficients of periodic brickwork](#)”, *Mech. Res. Commun.* **72** (2016), 24–32.
- [Zucchini and Lourenço 2002] A. Zucchini and P. B. Lourenço, “[A micro-mechanical model for the homogenisation of masonry](#)”, *Int. J. Solids Struct.* **39**:12 (2002), 3233–3255.

Received 26 Nov 2018. Revised 16 Sep 2019. Accepted 28 Sep 2019.

GIANMARCO DE FELICE: defelice@uniroma3.it

Department of Engineering, Roma Tre University, via Vito Volterra 62, 00146 Rome, Italy

MARIALAURA MALENA: marialaura.malena@uniroma3.it

Department of Engineering, Roma Tre University, via Vito Volterra 62, 00146 Rome, Italy

ENERGY BASED FRACTURE IDENTIFICATION IN MASONRY STRUCTURES: THE CASE STUDY OF THE CHURCH OF “PIETÀ DEI TURCHINI”

ANTONINO IANNUZZO

The present work deals with the identification of fractures in “old” masonry structures modelled by extending the Heyman model to continua, particularly to 2D structures composed of normal rigid no-tension material, and subjected to given loads and settlements. The equilibrium problem is formulated as an energy minimum search and two numerical methods for approximating the solution are adopted, namely the PRD method and the C^0 method. By using the PRD method, the energy is minimized within the set of piecewise rigid displacements (PRD), whilst with the second one, the search of the minimum is restricted to continuous (C^0) displacement fields. A case study, regarding the church of “Pietà dei Turchini” (an XVII century church located in Naples), is here presented to illustrate how an admissible class of kinematical data (i.e., foundation displacements) associated to a given crack pattern can be identified by using an iterative procedure. Firstly, the analysis is conducted through the PRD method and secondly, the C^0 method is used to assess the quality of the first solution, and to make comparisons between these two approaches showing pro and contra of both methods.

1. Introduction

The first to propose the application of limit analysis (LA) to voussoir arches was Kooharian [1952]. Some years later, Heyman [1966] laid a theoretical basis for the application of LA to generic masonry structures through the clear and rigorous formulation of three basic material restrictions: (i) masonry has no tensile strength, (ii) masonry has infinite compressive strength, (iii) sliding does not occur.

In his work, Heyman studied in deep the arch and extended the analysis to a wide range of masonry structures, with particular reference to Gothic cathedrals and their peculiar structural elements.

The three assumptions of Heyman, on one hand, constitute the necessary ingredients for the application of the two basic theorems of LA to masonry structures (see [Heyman 1998; Huerta 2006; 2008; Kurrer 2008]), and on the other hand give also a mathematical base to the equilibrium approach taken from the study of Hooke [1676] and Gregory [1695] and used by many scientists in the past centuries, such as Couplet [1729; 1730], Danyzy [1732/1778], Poleni [1748], Le Seur et al. [1742], Coulomb [1776], Barlow and Yvon de Villarceau [Yvon Villarceau 1853; 1854].

The present paper deals with the application of Heyman’s theory to a real masonry structure, and in particular, is concerned with the identification of the cracks appearing in the walls of the church of “Pietà dei Turchini” in Naples. The material composing the structure is modelled as normal rigid no-tension (NRNT). The NRNT material is rigid in compression, but extensional deformations, regular or singular, are allowed at zero energy price.

Keywords: masonry, unilateral materials, settlements, piecewise rigid displacements, continuous displacements, concentrated and smeared cracks.

For discussion and applications of limit analysis to masonry-like structures the reader can refer to [Livesley 1978; Castellano 1988; Como 1992; Di Pasquale 1984; Giuffrè 1991; Angelillo 1993; 2014; 2019; Bagi 2014; Block et al. 2006; Block and Lachauer 2013; 2014; Block 2009; Del Piero 1998; Ochsendorf 2006; Sacco 2014; Angelillo et al. 2014; 2018; Brandonisio et al. 2015; 2017; Cennamo et al. 2018; Gesualdo et al. 2017; Fortunato et al. 2018; Fraddosio et al. 2019; Marmo and Rosati 2017; Marmo et al. 2018; Shin et al. 2016; Portioli et al. 2014; Romano and Romano 1979; Van Mele et al. 2012; Zuccaro et al. 2017].

Since in NRNT structures extensional deformation could appear as either diffuse (smeared cracks) or concentrated (macroscopic cracks), and there is any reason to prefer one type of fractures upon the others, on an energy ground, the crack pattern of the church is identified on adopting two different numerical strategies, namely the PRD and C^0 methods (for more examples the reader can refer to [Iannuzzo 2017; Iannuzzo et al. 2018b; 2018c]). With both methods, the solution of the boundary value problem (BVP) is searched by adopting a displacement approach, and by restricting to small displacement fields, it reduces to the search of the minimum of a linear functional, namely the total potential energy (TPE). With the PRD method, the search of the solution of the BVP is performed within the set of piecewise rigid displacements: the strain admits only a singular part, represented by line Dirac deltas, and it is concentrated along the skeleton of the mesh, that is along the element interfaces; the C^0 method, instead, approximates the solution within the set of continuous displacements and then the strain admits only a regular part. The two methods represent two different numerical strategies to implement numerically Heyman's material restrictions to continua.

2. Material restrictions, BVP and the energy criterion for NRNT materials

NRNT materials. The Heyman's constraints ((i), (ii), (iii)) can be extended to 2D continua on introducing suitable unilateral material restrictions on stress and strain. A 2D masonry structure is modelled as a continuum occupying the region Ω of the Euclidean space \mathbb{R}^2 . Restricting to small strain and displacement fields, we denote \mathbf{T} the stress inside Ω , \mathbf{u} the displacement of material points \mathbf{x} belonging to Ω and \mathbf{E} the infinitesimal strain adopted as the strain measure.

The so-called normal rigid no-tension (NRNT) material is defined by the following three restrictions:

$$\mathbf{T} \in \text{Sym}^-, \quad \mathbf{E} \in \text{Sym}^+, \quad \mathbf{T} \cdot \mathbf{E} = 0, \quad (1)$$

where Sym^- , Sym^+ are the mutually polar cones (see Figure 1) of negative and positive semidefinite symmetric tensors.

The restrictions (1) are equivalent to the so-called *normality conditions*:

$$\mathbf{T} \in \text{Sym}^-, \quad (\mathbf{T} - \mathbf{T}^*) \cdot \mathbf{E} \geq 0, \quad \forall \mathbf{T}^* \in \text{Sym}^-, \quad (2)$$

and to the *dual normality conditions*:

$$\mathbf{E} \in \text{Sym}^+, \quad (\mathbf{E} - \mathbf{E}^*) \cdot \mathbf{T} \geq 0, \quad \forall \mathbf{E}^* \in \text{Sym}^+. \quad (3)$$

The restrictions defining the NRNT material are then the essential ingredients for the application of the theorems of LA (see [Kooharian 1952; Giaquinta and Giusti 1985; Livesley 1978; Fortunato et al. 2014; 2016; Milani 2011; Angelillo et al. 2010; Addessi and Sacco 2018]).

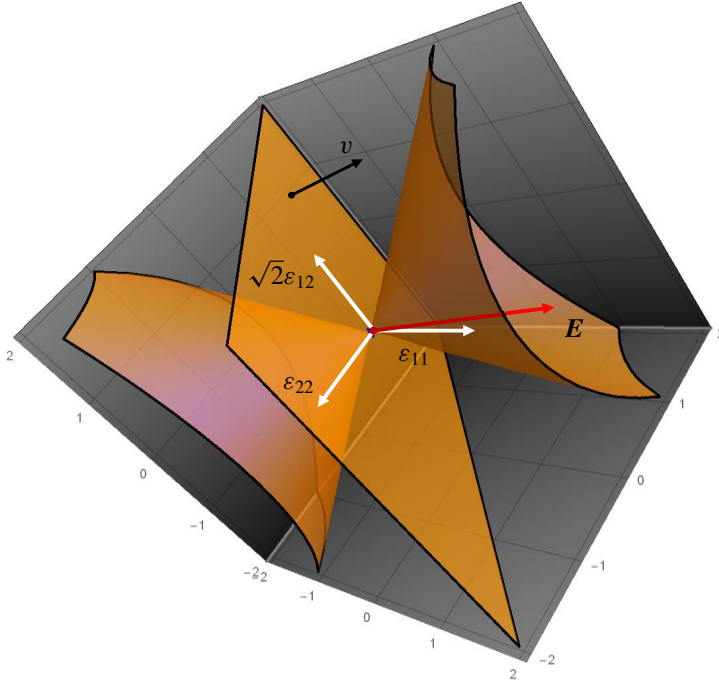


Figure 1. A three-dimensional geometrical representation of relation (1)² in the space $(\varepsilon_{11}, \varepsilon_{22}, \sqrt{2}\varepsilon_{12})$: the cone $C : \det \mathbf{E} \geq 0$ and the plane $\pi : \text{tr} \mathbf{E} = 0$. A generic tensor $\mathbf{E} \in \text{Sym}^+$ is represented. For the symbols adopted the reader can refer to (31) and (32), and to the subsequent paragraph.

The boundary value problem. The equilibrium of a 2D masonry structure, modelled as a continuum composed of NRNT material and subject to given loads and settlements, can be formulated as a Boundary Value Problem (BVP) in the following form: “find a displacement field \mathbf{u} and the corresponding strain \mathbf{E} , and a stress field \mathbf{T} such that

$$\mathbf{E} = \frac{1}{2}(\nabla \mathbf{u} + \nabla \mathbf{u}^T), \quad \mathbf{E} \in \text{Sym}^+, \quad \mathbf{u} = \bar{\mathbf{u}} \text{ on } \partial\Omega_D, \quad (4)$$

$$\text{div} \mathbf{T} + \mathbf{b} = 0, \quad \mathbf{T} \in \text{Sym}^-, \quad \mathbf{T} \mathbf{n} = \bar{\mathbf{s}} \text{ on } \partial\Omega_N, \quad (5)$$

$$\mathbf{T} \cdot \mathbf{E} = 0, \quad (6)$$

where \mathbf{n} is the unit outward normal to the boundary $\partial\Omega$, $\bar{\mathbf{u}}$ are the boundary displacements on the constrained part $\partial\Omega_D$ and $\bar{\mathbf{s}}$ are the given tractions on the loaded part $\partial\Omega_N$ (see [Angelillo and Fortunato 2004]).

Concentrated strain and stress. For NRNT materials, it has been shown (see [Giaquinta and Giusti 1985; Šilhavý 2014]) that the strain and stress are bounded measures and can be decomposed into the sum of two parts:

$$\mathbf{E} = \mathbf{E}^r + \mathbf{E}^s, \quad \mathbf{T} = \mathbf{T}^r + \mathbf{T}^s, \quad (7)$$

where $(\cdot)^r$ is the regular part (i.e., absolutely continuous with respect to the area measure) and $(\cdot)^s$ is the singular part.

A nonzero singular part of the strain or of the stress corresponds to the possibility of admitting discontinuities of the displacement vector or of the stress vector across certain curves. For a more detailed review about jump discontinuities of stress or of displacement for masonry-like material, the reader can refer to [Angelillo et al. 2016].

Displacement approach. A solution of the BVP through the *displacement approach* consists in the search of a displacement field $\mathbf{u} \in \mathcal{K}$ for which there exists a stress field $\mathbf{T} \in \mathcal{H}$ such that $\mathbf{T} \cdot \mathbf{E}(\mathbf{u}) = 0$, where \mathcal{K} and \mathcal{H} are the sets of kinematically admissible displacements and statically admissible stresses, defined as

$$\mathcal{K} = \{\mathbf{u} \in S / \mathbf{E} = \frac{1}{2}(\nabla \mathbf{u} + \nabla \mathbf{u}^T) \in \text{Sym}^+ \quad \text{and} \quad \mathbf{u} = \bar{\mathbf{u}} \text{ on } \partial\Omega_D\}, \quad (8)$$

$$\mathcal{H} = \{\mathbf{T} \in S' / \text{div} \mathbf{T} + \mathbf{b} = 0, \quad \mathbf{T} \in \text{Sym}^-, \quad \mathbf{T} \mathbf{n} = \bar{\mathbf{s}} \text{ on } \partial\Omega_N\}, \quad (9)$$

where S, S' are two suitable functional spaces (see [Angelillo and Rosso 1995; Chambolle et al. 2007]). It is worth noting that, by adopting a displacement approach, the functional space S defines the set where the solution has to be found: in particular, as shown in what follows, the two numerical approximations, namely PRD and C^0 methods, work on two different subsets of the starting set \mathcal{S} .

Energy criterion. The energy $\mathcal{P}(\mathbf{u})$ for brittle materials is the sum of the potential energy of the applied loads and of the elastic and interface ones, with this latter necessary to activate a crack system on a set of internal surfaces (see [Gesualdo et al. 2018; Monaco et al. 2014; Angelillo et al. 2012; Gesualdo and Monaco 2015]). For Heyman's material the total potential energy is just the potential energy of the external loads [De Serio et al. 2018], namely

$$\mathcal{P}(\mathbf{u}) = - \int_{\partial\Omega_N} \bar{\mathbf{s}} \cdot \mathbf{u} \, ds - \int_{\Omega} \mathbf{b} \cdot \mathbf{u} \, da. \quad (10)$$

The search of a solution of the BVP through a displacement approach could be got by looking for the minimizer \mathbf{u}° of $\mathcal{P}(\mathbf{u})$ as in [Iannuzzo 2017], namely

$$\mathcal{P}(\mathbf{u}^\circ) = \min_{\mathbf{u} \in \mathcal{K}} \mathcal{P}(\mathbf{u}) \quad \text{with } \mathbf{u} \in \mathcal{K}. \quad (11)$$

It is worth noticing that the existence of a minimizer \mathbf{u}° guarantees also the equilibrium of the loads imposed on the structure.

3. The search for an approximate solution in two different subsets of \mathcal{K} : PR and C^0 methods

In this section, two possible approximations of the solution of the BVP, are introduced, namely the PRD method and the C^0 method. These approximations are obtained by restricting the search of the minimizer to two suitable subsets of the set \mathcal{K} . With the PRD method, the energy is minimized in the set $\mathcal{S}_{\text{PRD}} \subset \mathcal{S}$ of piecewise rigid displacements, whilst with the C^0 method the search of the minimum is restricted to the space of continuous displacements $C^0 \subset \mathcal{S}$.

3.1. PRD method. The first approximated solution of problem (11) is obtained by restricting the search of the minimum to the subset $\mathcal{S}_{\text{PRD}} \subset \mathcal{S}$ of piecewise rigid displacements, and then the set of kinematically admissible displacements becomes

$$\mathcal{H}_{\text{PRD}} = \{\mathbf{u} \in \mathcal{S}_{\text{PRD}} / \mathbf{E} \in \text{Sym}^+ \quad \text{and} \quad \mathbf{u} = \bar{\mathbf{u}} \text{ on } \partial\Omega_D\} \subset \mathcal{H}, \quad (12)$$

where \mathcal{H}_{PRD} is an infinite-dimensional space and can be discretized by considering a proper finite subset, namely $\mathcal{H}_{\text{PRD}}^M$, generated by a finite polygonal partition of the whole domain Ω :

$$(\Omega_i)_{i \in \{1, 2, \dots, M\}}. \quad (13)$$

The minimizer $\mathbf{u}_{\text{PRD}}^0 \in \mathcal{H}_{\text{PRD}}^M$ of the total potential energy, namely

$$\mathcal{P}(\mathbf{u}_{\text{PRD}}^0) = \min_{\mathbf{u} \in \mathcal{H}_{\text{PRD}}^M} \mathcal{P}(\mathbf{u}), \quad (14)$$

constitutes an approximation of the solution \mathbf{u}^0 of the exact problem (11), in the subset $\mathcal{H}_{\text{PRD}}^M$ and, in this sense, represents the approximate solution of the BVP obtained by using the PRD method. The numerical way used to solve the discretized problem (14) under NRNT restrictions is briefly described in what follows.

The boundary $\partial\Omega_i$ of the generic (convex) polygon Ω_i is composed of straight segments (from here on called *interfaces*) of length ℓ and whose extremities are denoted generically 0 and 1. Each segment is associated with a unit normal \mathbf{n} and a tangent vector \mathbf{t} . Since the number of elements of the partition (13) is M , a generic piecewise rigid displacement $\mathbf{u} \in \mathcal{H}_{\text{PRD}}^M$ can be expressed through a vector \mathbf{U} of $3M$ components representing the $3M$ rigid body parameters of translation and rotation of each element. Then, the set $\mathcal{H}_{\text{PRD}}^M$ is in one-to-one correspondence with the set $\mathbb{K}_{\text{PRD}}^M$ generated by $\mathbf{U} \in \mathbb{R}^{3M}$.

For piecewise rigid displacements, the strain \mathbf{E} coincides with its singular part \mathbf{E}^s concentrated along the interfaces and can be written as

$$\mathbf{E} = v \delta(\Gamma) \mathbf{n} \otimes \mathbf{n} + \frac{1}{2} w \delta(\Gamma) (\mathbf{t} \otimes \mathbf{n} + \mathbf{n} \otimes \mathbf{t}), \quad (15)$$

where v , w are the normal and tangential components of the displacement jump across the interface Γ . The displacement jump is modelled through the use of the Dirac delta function $\delta(\Gamma)$ having Γ as support. Relation (15) represents the most general form of the strain tensor in the subset $\mathcal{H}_{\text{PRD}}^M$. Nevertheless, by taking into account the normality conditions (2) or equivalently the Heyman's restrictions (1), it is deduced that on each interface among blocks a condition of unilateral contact with no sliding must be enforced, that is

$$v = [\mathbf{u}] \cdot \mathbf{n} \geq 0, \quad (16)$$

$$w = [\mathbf{u}] \cdot \mathbf{t} = 0, \quad (17)$$

where $[\mathbf{u}]$ represents the displacement jump on the interfaces. On allowing for internal eigenstrains along the interfaces the above conditions transform into the following nonhomogeneous relations:

$$v = [\mathbf{u}] \cdot \mathbf{n} \geq \Delta_n, \quad (18)$$

$$w = [\mathbf{u}] \cdot \mathbf{t} = \Delta_t, \quad (19)$$

Δ_n , Δ_t being given distortions. Due to conditions (16), (17) the strain must reduce to the following form:

$$\mathbf{E} = v \delta(\Gamma) \mathbf{n} \otimes \mathbf{n}. \quad (20)$$

By calling N the number of the interfaces, and $v(0)$, $v(1)$, $w(0)$, $w(1)$ the normal and tangential components of the relative displacements of the ends 0, 1 of any interface, restrictions [(18), (19)] are equivalent to the $2N$ inequalities

$$v(0) \geq \Delta_n^0, \quad v(1) \geq \Delta_n^1, \quad (21)$$

and to the $2N$ equalities

$$w(0) = \Delta_t, \quad w(1) = \Delta_t. \quad (22)$$

Transforming identities (22) into double inequalities, restrictions (21), (22) can be expressed in terms of \mathbf{U} . In a matrix form (see [Iannuzzo et al. 2018a]) these inequalities can be written as

$$\mathbf{A}\mathbf{U} \geq \Delta. \quad (23)$$

Finally, the minimum problem (14) which approximates the minimum problem (11) can be transformed into

$$\mathcal{P}(\mathbf{U}^0) = \min_{\mathbf{U} \in \mathbb{K}_{\text{PRD}}^M} \mathcal{P}(\mathbf{U}), \quad (24)$$

where $\mathbb{K}_{\text{PRD}}^M$ is the set

$$\mathbb{K}_{\text{PRD}}^M = \{\mathbf{U} \in \mathbb{R}^{3M} / \mathbf{A}\mathbf{U} \geq \Delta\}. \quad (25)$$

Problem (24) is a standard linear finite-dimensional minimization problem, since the function $\mathcal{P}(\mathbf{U})$ is a linear function of the $3M$ vector \mathbf{U} , and all the constraints are represented by linear relations (25). It is worth noticing that problem (24) transforms the original minimization problem (11) for a continuum, into a minimization problem for a structure composed of rigid parts subject to unilateral contact conditions along the interfaces. There exist many numerical methods to obtain the solution of this minimum problem; in particular, for large problems, the solution can be searched with the interior-point algorithm (see [Mehrotra 1992; Dantzig 1963]).

3.2. \mathbf{C}^0 method. A second approximation of the solution of problem (11) is obtained considering the subset \mathbf{C}^0 (see [Iannuzzo et al. 2018c]) of \mathcal{S} formed by continuous displacement fields, and then the set of kinematically admissible displacements becomes

$$\mathcal{H}_{\mathbf{C}^0} = \{\mathbf{u} \in \mathbf{C}^0 / \mathbf{E} \in \text{Sym}^+ \quad \text{and} \quad \mathbf{u} = \bar{\mathbf{u}} \text{ on } \partial\Omega_D\} \subset \mathcal{H}, \quad (26)$$

where $\mathcal{H}_{\mathbf{C}^0}$ is an infinite-dimensional space and can be discretized by considering a finite partition of the domain Ω :

$$(\Omega_i)_{i \in \{1, 2, \dots, M\}}, \quad (27)$$

where each element Ω_i is associated with a suitable Finite Element-like (FE) shape function. By calling N the total number of nodes of the FE mesh associated with the partition (27), we denote $\mathcal{H}_{\mathbf{C}^0}^M$ the subset

of \mathcal{H}_{C^0} generated by this discretization. The approximated solution in $\mathcal{H}_{C^0}^M$ of the BVP obtained by applying the energy criterion, is the minimizer $\mathbf{u}_{C^0}^0$ of the total potential energy, namely

$$\mathcal{P}(\mathbf{u}_{C^0}^0) = \min_{\mathbf{u} \in \mathcal{H}_{C^0}^M} \mathcal{P}(\mathbf{u}). \quad (28)$$

The minimizer $\mathbf{u}_{C^0}^0$ represents the solution of the BVP with the C^0 method. The approach adopted with the C^0 method, to implement the material restrictions and to preserve the linearity of the problem, is briefly illustrated below.

Since it is assumed that FE mesh associated to the partition (27) is based on the hypothesis of continuity of the displacement fields at the nodes, the strain (7)¹ admits only a regular part. The NRNT material restrictions have, then, to be enforced on the strain arising inside the elements: with the C^0 method the interfaces, i.e., the boundary edges between two finite adjacent elements, play a minor role.

The displacement field \mathbf{u} generated by the chosen FE mesh is a function of the N nodes and then is in a one to one correspondence with the nodal vector $\mathbf{U} \in \mathbb{R}^{2N}$ collecting the displacement components of the N nodes of the mesh. By recalling definition (1) the latent strain \mathbf{E} has to belong to the positive semidefinite cone

$$\mathbf{E} \in \text{Sym}^+. \quad (29)$$

This restriction, for 2D problems, is equivalent to the two following inequalities:

$$\text{tr} \mathbf{E} \geq 0, \quad \det \mathbf{E} \geq 0, \quad (30)$$

and in a fixed Cartesian reference in which the strain can be represented as

$$\mathbf{E} = \begin{bmatrix} \varepsilon_{11} & \varepsilon_{12} \\ \varepsilon_{21} & \varepsilon_{22} \end{bmatrix}, \quad (31)$$

conditions (30) can be written in terms of Cartesian components, as

$$\varepsilon_{11} \varepsilon_{22} - \varepsilon_{12}^2 \geq 0, \quad \varepsilon_{11} + \varepsilon_{22} \geq 0, \quad (32)$$

which represent restrictions on the displacement \mathbf{u} being $\mathbf{E} = \text{Sym} \nabla \mathbf{u}$. Geometrically, the nonlinear relation (32)¹ defines a double cone in the space Sym whilst condition (32)² selects one of the two parts of this cone (see Figure 1). With the aim of preserving the linearity of the problem, relation (32)¹ is approximated through a plane envelope (see Figure 2) and then restriction $\mathbf{E} \in \text{Sym}^+$ is enforced, in all points of the mesh, by restricting \mathbf{E} to belong to the envelope of a finite number of tangent planes (Figure 2). Therefore, all the material restrictions are enforced by writing linear inequalities in all the nodes and can be expressed as functions of the unknown nodal displacements \mathbf{U} . Then, also in this case these inequalities can be compactly expressed in a matrix form (for more details see [Iannuzzo 2017; Iannuzzo et al. 2018c]):

$$\mathbf{A} \mathbf{U} \geq 0. \quad (33)$$

Finally, with the proposed FE approximation, the minimum problem (28) can be approximated by the following discretized minimum problem:

$$\mathcal{P}(\mathbf{U}^0) = \min_{\mathbf{U} \in \mathbb{K}_{C^0}^M} \mathcal{P}(\mathbf{U}), \quad (34)$$

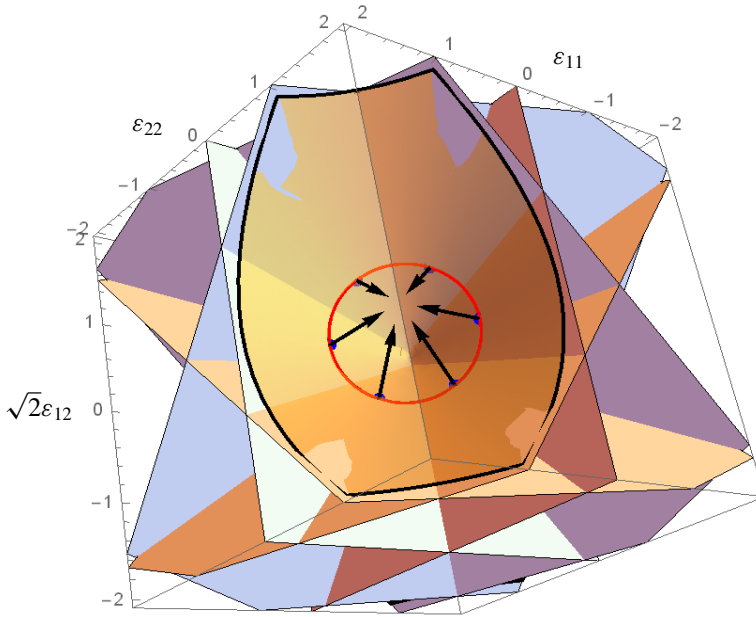


Figure 2. An envelope formed by six tangent planes and the surface gradient vectors at the tangent points are represented. The condition $\mathbf{E} \in \text{Sym}^+$ is discretized and written as a system of inequalities by using these gradient vectors.

where $\mathbb{K}_{C^0}^M$ is the set

$$\mathbb{K}_{C^0}^M = \{\mathbf{U} \in \mathbb{R}^{2N} / \mathbf{A}\mathbf{U} \geq 0\}. \quad (35)$$

Like the previous problem (24), problem (34) is a standard linear finite-dimensional minimization problem since $\mathcal{P}(\mathbf{U})$ is a linear functional of the $2N$ parameters of nodal displacements collected in \mathbf{U} whilst all the constraints (35) are represented by linear inequalities.

4. The church of “Pietà dei Turchini”

The two proposed numerical methods, that is PRD and C^0 methods, are now applied to a real case, namely the church of “Santa Maria Incoronatella della Pietà dei Turchini”, an XVII century building located in Via Medina in Naples. During its life, a diffuse crack pattern due to foundation displacements interested this church. The fractures, detected before the recent restoration works, are depicted in Figure 3. This crack pattern was essentially the effect of a piecewise rigid body mechanism through which the masonry structure responded to the ground displacements.

The main aim is to use both methods for finding the foundation displacements producing the observed crack pattern. This case study was already analysed in [Iannuzzo et al. 2018a] by using the PRD method, but here a developed version has been used.

A second aim of present paper, beyond testing this developed version of PRD method, is to simulate the same problem with the C^0 method to compare these two numerical approximations and to find if and

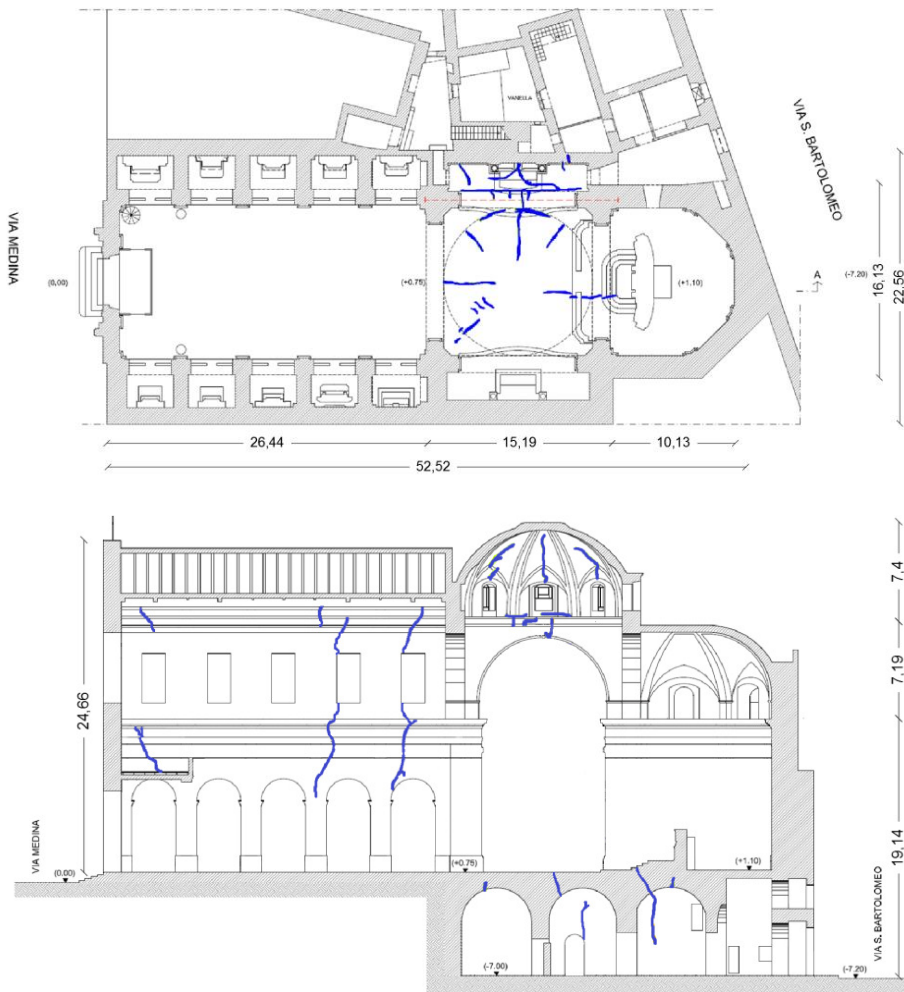


Figure 3. Plan (top) and section A-A' (bottom) of the church showing the crack pattern.

how is possible to relate this two methods to get information about the best discretization that one can choose with the PRD method.

It is to be pointed out that though the crack pattern was fully manifested and consistent, the size of the rigid body movements produced by the given settlements remained everywhere small with respect to the overall size of the structure. Therefore, we can consider that the equilibrium state of the structure is not sensibly affected by these displacements, and a linearized kinematic analysis can be adopted.

The problem studied concerns the left wall of the central nave including the big arch of the transept and the left lateral wall of the apse (see Figure 3, bottom), treated as a plane case. The external loads acting on the structure are the mass density ($\rho = 1800 \text{ kg/m}^3$) and uniformly distributed tractions, applied along external and internal lines, and representing the load exerted by secondary structures (see Figure 4).

In what follows the plane wall reported in Figure 4 is analysed by using both PRD and C^0 methods. Preliminarily the analysis is conducted by applying the PRD method and after some iterations, the

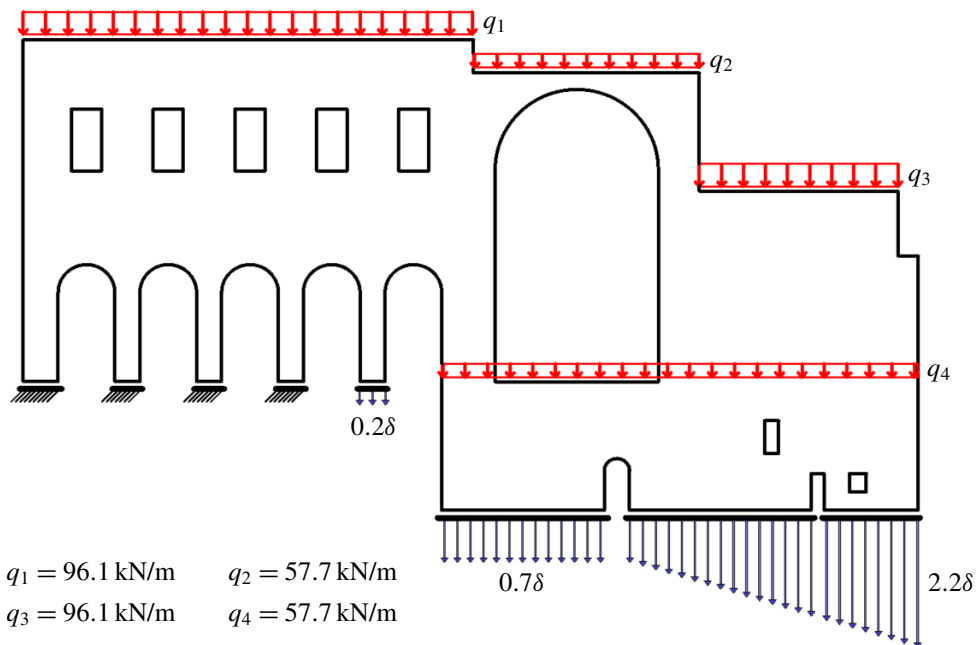


Figure 4. Structural scheme of the left wall of the central nave of the church. Distributed tractions due to the secondary structures and their values. Profile of the foundation displacements.

optimal profile of foundation displacements (depicted in Figure 4) has been found. In both cases the profile of foundation displacements has been used as boundary condition. The two numerical methods, implemented in Mathematica®, consist of the following main steps:

- (1) definition of the structural geometry and of its discretization;
- (2) characterization of the displacement field with support in the given discretization;
- (3) characterization of the potential energy as a linear functional of the displacement parameters;
- (4) definition of the internal and external constraints;
- (5) numerical solution of the problem with a linear programming routine;
- (6) postprocessing (evaluation of the displacement and strains corresponding to the solution).

4.1. Analysis through the PRD method. In Figure 5 the discretization adopted to implement the PRD method is shown. This real case was already analysed with the PRD method in [Iannuzzo et al. 2018a]. In this reference the structural scheme was discretized by using quadrilateral elements having only potential horizontal and vertical crack lines. In the present work, we redo the analysis by adopting a much richer mesh. Particularly, the discretization has been refined by adopting different kinds of polygonal rigid elements: starting from triangular elements going to hexagonal elements. Then, the discretization has been further cut by using diagonal lines in order to allow many potential diagonal cracks but at the same time without making any preferential choice.

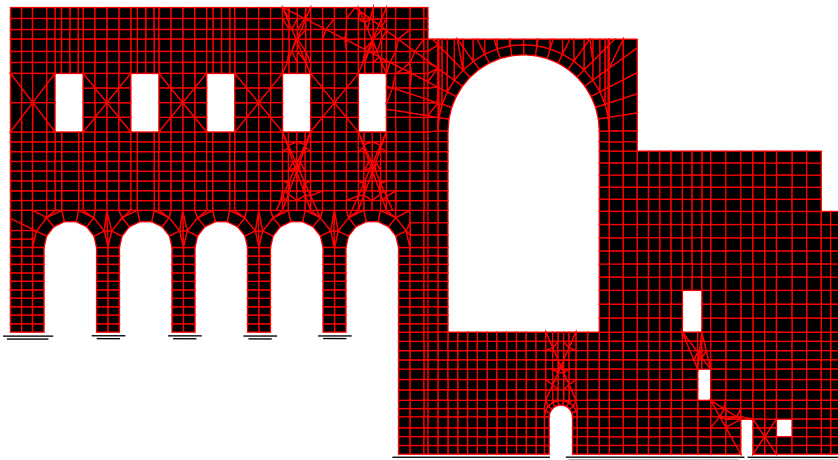


Figure 5. The rigid block discretization used with the PRD method: 2301 rigid polygonal elements are used.

The analysis is performed on a mesh of 2301 (rigid) polygonal elements (see Figure 5) and by considering the effect of the self-weight and of the external line loads shown in Figure 4. The total number of interfaces is 4650, of which 4068 are internal while the remaining 582 are external. Homogeneous conditions (16) and (17) have to be written for each internal interface, whilst boundary conditions, expressing the foundation settlements, have to be written at all external constrained interfaces.

The total number of unknowns is 6903; the number of restrictions (equalities and inequalities) is 16465. The solution of the minimum problem (24) was obtained with the interior point method in 57 s (with an Intel® Core™ i7-6700HQ) and, shown graphically in Figure 6.

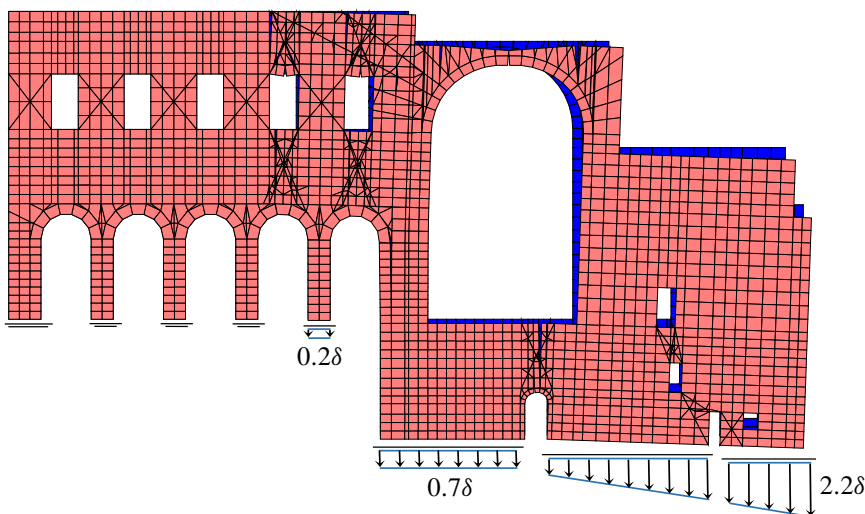


Figure 6. Displacement of the blocks corresponding to the solution of the minimum problem (11) obtained with the PRD method.

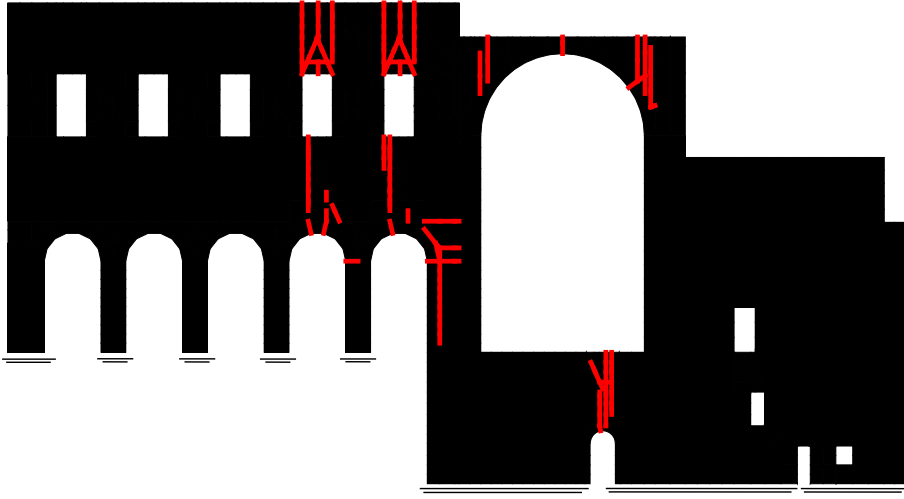


Figure 7. The internal interfaces on which there is a jump displacement are depicted with a red thick line.

In [Figure 7](#) the internal interfaces on which there is a nonzero jump of the displacement field (that is the absolute values of the jump above a numerical threshold $10^{-2}\delta$) are underlined with a red thick line. The collection of such red lines gives a rough picture of the fracture pattern. The phenomenological observation that masonry structures, when subjected to settlements, exhibit a rigid macroblock mechanism, is perfectly caught by the numerical solution produced by the PRD method: the cracks (displacement jumps) concentrate on a selected set of a small number of interfaces and a *rigid macroblock partition* of the structural domain form.

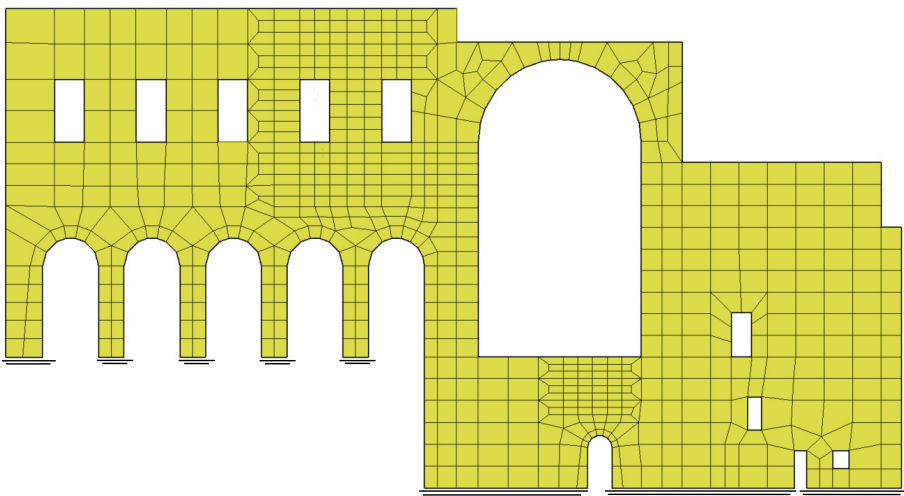


Figure 8. Plane section of [Figure 3](#) (bottom) is here discretized into 677 square second-order Lagrangian elements.

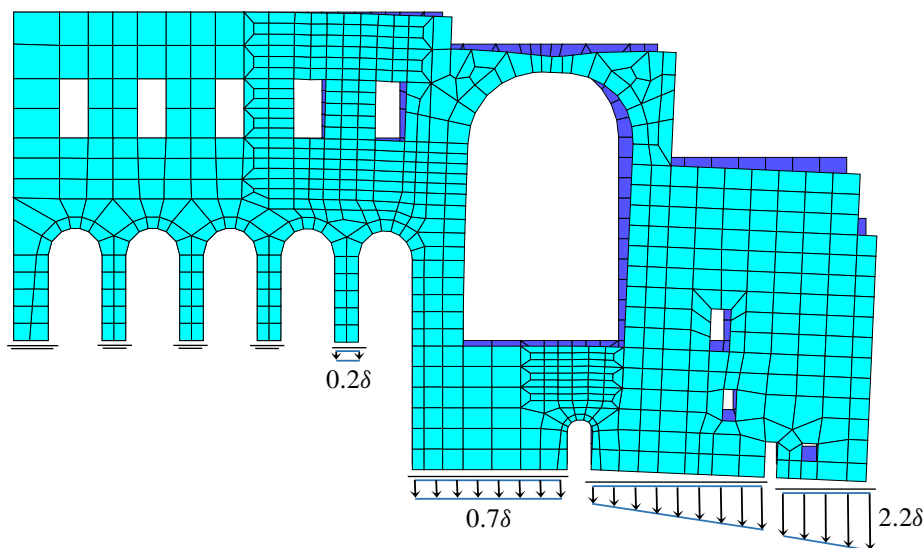


Figure 9. Displacement corresponding to the solution of the minimum problem (11) obtained with the C^0 method.

4.2. Analysis through the C^0 method. The lateral section of Figure 3 (bottom) is here analysed with the C^0 method. The structure composed of NRNT material is discretized into 677 nine-node square elements (see [Bathe and Wilson 1976]). The external loads reported in Figure 4 and the self-weight applied at the centroid of each quadrilateral elements are considered.

The solution of the minimum problem (34), obtained with the interior point method in 300 s (with an Intel® Core™ i7-6700HQ) is shown graphically in Figure 9.

In this case, since the strain is purely regular (no singular strains are allowed), the strain is smeared and an indication of possible fractures is associated with zones where the displacement exhibits large gradients. In order to highlight such regions, the strain associated to the solution of the minimum problem (34) is graphically represented. A map of the regions over which the measure of \mathbf{E} , namely $|\mathbf{E}|^2 = \text{tr}(\mathbf{E}\mathbf{E}^T)$, is nonzero is reported in Figure 10. From Figure 11, where a contour plot of $|\mathbf{E}|^2$ by using 200 level lines is reported. It can be observed that such fractures tend to nucleate in the neighbourhood of some lines. The remaining part of the domain is almost undeformed being characterized by strains whose norm is close to zero.

5. Comparison between PRD and C^0 methods

The safety assessment of masonry structures interested by a crack pattern and then, the understanding of causes producing these effects, is one of the key issues in practical applications to real constructions. Several times, if we are not facing problems due to horizontal actions, the causes are represented by foundation displacements. However, these displacements cannot affect the stability of a structure and, therefore, they cannot drive the structure to the collapse as long as they are “small” in a certain sense. In fact, accommodating small changes of the external environment (in this case the kinematical data that is the foundation displacements) through a stable rigid macroblock partition of the structural domain is the

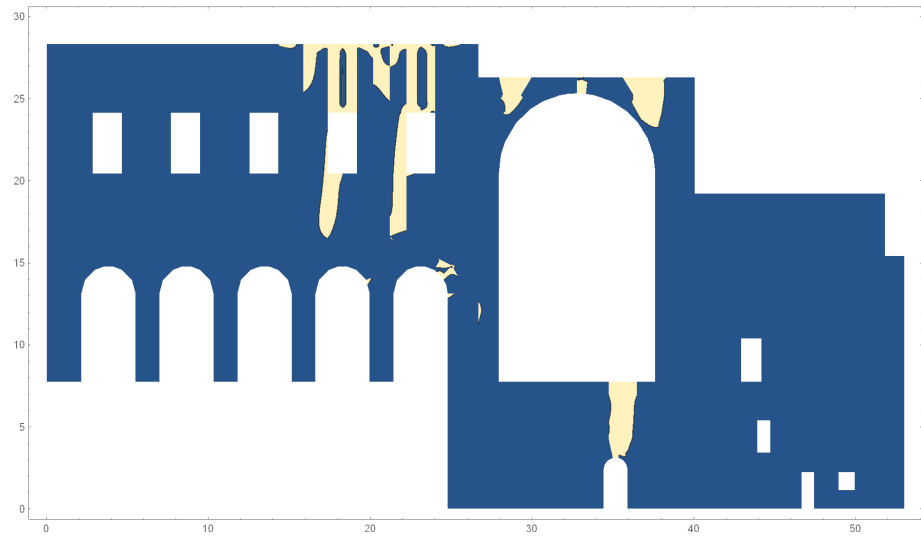


Figure 10. A map of the areas on which the norm of the strain E , namely $|E|^2 = \text{tr}(EE^T)$, is greater than zero is reported: the remaining part of the domain, i.e., blue areas, is characterized by strains whose norm is close to zero.

peculiar behaviour of a masonry structure. Nevertheless, if the foundation displacements can increase, assessing if the structure is still stable in a new configuration and then evaluate its displacement capacity is the consequent concern. Anyway, behind both these two issues, there is, in a certain way, the same question: how to detect the rigid macroblock partition exhibited by a structure when it is subjected

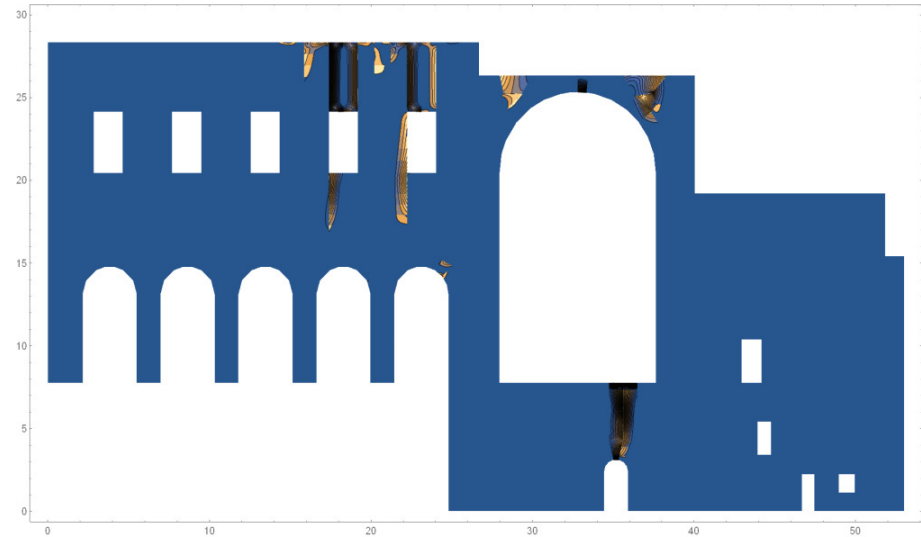


Figure 11. Contour plot of the strain field by using 200 contour level lines: fractures are concentrated along certain lines.

to foundation displacements? Because of the intrinsic unilateral behaviour of a masonry structure, the answer is not trivial and, so far, no computational tools, at least for generic structures, has been developed for this aim.

To tackle this problem, and then for setting up a numerical model able to detect the rigid macroblock nucleation, it is reasonable to work with small displacements since the goal is to define a partition on the initial configuration. If the size of the displacements is small related to the overall size of the structure, the error made in considering small displacements rather than finite ones is small and, one can also relate the size of the openings (cracks) to the foundation displacements.

Both the methods here presented, PRD and C^0 methods, have been developed to answer this question and are based on the small displacements assumption that also allows to make the optimization problem linear and then to solve it in a few seconds. As a consequence of this fast calculation speed, particularly for the PRD method, these are suitable tools for solving an inverse problem, since many trials in an iterative procedure have to be performed for individuating the optimal profile of foundation displacements giving the best qualitative fit with the actual crack pattern. In the case of small settlements, as stated before, a reasonable estimation of their size can be achieved by relating them with the width of the cracks.

One of the main issues addressed in this paper was the definition of the partition adopted with the PRD method. In fact, it is intuitively clear that the solution obtained with the PRD method depends on the initial partition much more than the one got with C^0 method. For instance, in [Iannuzzo et al. 2018a] it has been shown a shortcoming of the PRD method: the solution cannot converge to a concentrated crack whose support is not parallel to the skeleton of the mesh, that is, jump discontinuities along zigzag lines are not kinematically admissible. The C^0 method does not suffer from this defect, and though more cumbersome from the numerical point of view, can converge to cracks whose support is not parallel to the interfaces of the elements.

On the contrary, as shown with many benchmark cases in [Iannuzzo et al. 2018a], if an “optimal” discretization of the domain is suggested by the stereotomy of the real structure (e.g., arched structures), the results of the PRD method are impressive when compared to analytical ones.

However, in this case study no information about an opportune discretization into rigid blocks is available, and the partition adopted with both methods has been driven by the detected crack pattern in the sense that, as one can see from figures 5 and 9, the mesh is much more refined on areas interested by the cracks. Whilst for the C^0 method (see Figure 9) this was done only for reducing the computational time, for the PRD method the need of taking into account also diagonal cracks was the main concern. In fact, by looking at Figure 5 it is possible to see that many potential crack lines have been added in areas where the mesh has been refined, but without doing any preferential choice on them.

In Figure 12, the overlap of the solutions got with the two methods is reported and a perfect concordance of the displacements obtained with the two methods can be observed.

In Figure 13 the concentrated cracks obtained with the PRD method and the smeared cracks obtained with the C^0 method are compared. From this figure, again a good concordance between fractures obtained with these two methods is detected. Furthermore, the solution got with C^0 method, even if it is based on continuous functions, concentrates smeared cracks in small areas returning an approximate partition of the whole structure into rigid blocks, confirming the validity of the PRD approach.

In this respect, it is to point out that the appearance of piecewise rigid mechanisms (producing concentrated strains) rather than continuous mechanisms (entailing diffuse strains), is often due, in real

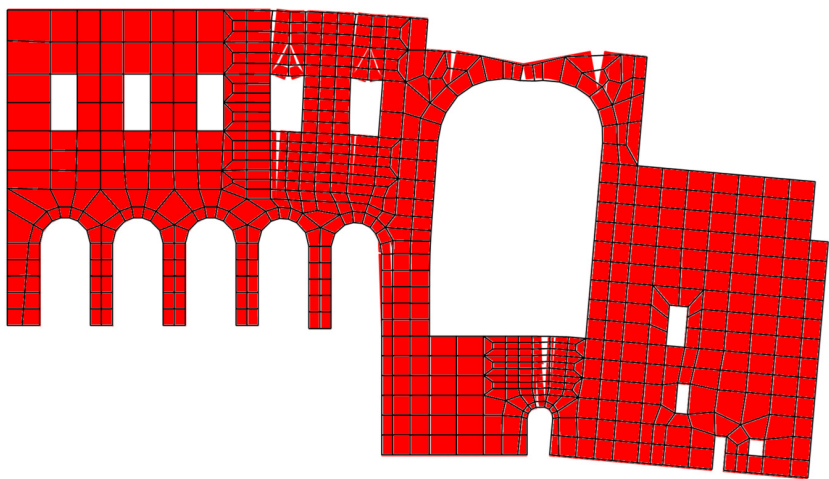


Figure 12. Overlapping of the solutions obtained with the two methods: in the background in red the solution with the PRD method is represented, whilst the black skeleton mesh represents the solution reached with the C^0 method.

structures, to mechanical characteristics, such as cohesion, toughness and finite friction, which are not accounted by the NRNT model.

This perfect concordance among the solutions in terms of both displacements and fractures, gives a hint about a further potential use of C^0 method: if no information on the discretization for PRD method can be obtained from the actual stereotomy, beyond using a clever partition where any kind of potential crack lines are allowed, the C^0 method could be used for selecting the rigid macroblock discretization to be fed into the PRD method.

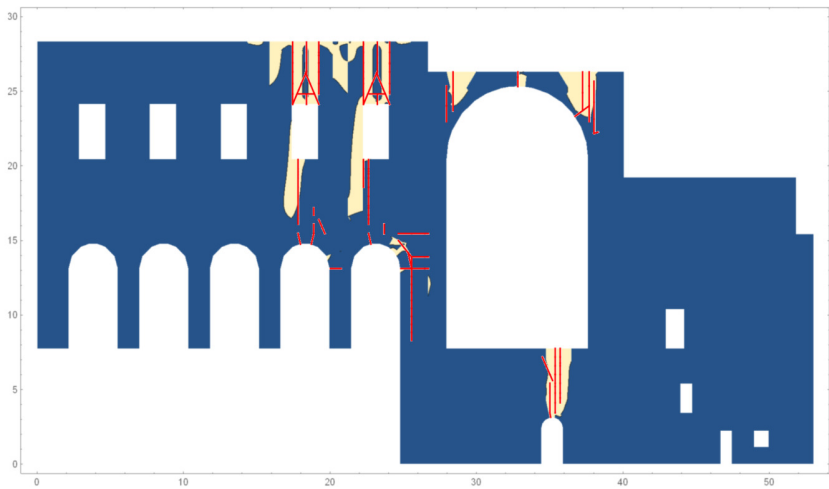


Figure 13. Overlapping of the solutions obtained with the two methods: in red the solution obtained in terms of cracks with the PRD method and in white the zones of smeared cracks.

6. Conclusions

In practical applications to real structures, one of the main issues is to identify the optimal profile of foundation displacements, that is, the settlements giving the best qualitative fit with the detected crack pattern. With this in mind, a study concerning the “Chiesa di Santa Maria Incoronatella della Pietà dei Turchini” is here proposed. The church is modelled as composed by NRNT material and two numerical methods, that is PRD and C^0 methods, are applied. With both the methods the solution of the BVP is represented by the minimizer of the potential energy of the loads, and it is obtained by discretizing the problem in two different suitable functional spaces: with the PRD method the energy is minimized within the set of piecewise rigid displacements whilst with the C^0 method the search of the minimum is restricted to continuous displacement fields.

By using small displacements, the optimization problem becomes linear and can be solved with standard algorithms used for linear programming optimization, such as interior-point method (here adopted) allowing to reach solutions in a few seconds.

The optimal profile of foundation displacements was found with the PRD method in an iterative procedure. The detected crack pattern drove the discretization, in the sense that the partition is much more refined in those areas where the cracks were observed and it is further cut by diagonal lines for reproducing other potential crack lines. This is due to a shortcoming of the PRD method: when the stereotomy of the structure does not suggest any particular partition (e.g., for arched structures), the best way to tackle the problem is to allow cleverly many kinds of potential crack lines but avoiding any a priori choice.

Once the optimal profile of foundation displacements was found through the PRD method, the C^0 has been applied by using this profile as boundary condition. The results in terms of displacements and fractures show an impressive concordance among these two different numerical approximations. In particular, the main result of the C^0 method is that, even if continuous functions are considered, the solution returns an approximate partition of the whole structure into rigid blocks, confirming the validity of the PR method approach.

Furthermore, these results suggest that the C^0 method, being more time consuming, is more appropriate in the analysis of simple structures or as a preliminary tool for defining the rigid macroblock partition to be implemented in the PRD method.

References

- [Addressi and Sacco 2018] D. Addressi and E. Sacco, “Homogenization of heterogeneous masonry beams”, *Meccanica (Milano)* **53**:7 (2018), 1699–1717.
- [Angelillo 1993] M. Angelillo, “Constitutive relations for no-tension materials”, *Meccanica (Milano)* **28**:3 (1993), 195–202.
- [Angelillo 2014] M. Angelillo, “Practical applications of unilateral models to masonry equilibrium”, pp. 109–210 in *Mechanics of masonry structures*, edited by M. Angelillo, Springer, Vienna, 2014.
- [Angelillo 2019] M. Angelillo, “The model of Heyman and the statical and kinematical problems for masonry structures”, *Int. J. Masonry Res. Innov.* **4**:1-2 (2019), 14–31.
- [Angelillo and Fortunato 2004] M. Angelillo and A. Fortunato, “Equilibrium of masonry vaults”, pp. 105–111 in *Novel approaches in civil engineering*, edited by M. Frémond and F. Maceri, Springer, Berlin, Heidelberg, 2004.
- [Angelillo and Rosso 1995] M. Angelillo and F. Rosso, “On statically admissible stress fields for a plane masonry-like structure”, *Quart. Appl. Math.* **53**:4 (1995), 731–751.

- [Angelillo et al. 2010] M. Angelillo, L. Cardamone, and A. Fortunato, “A numerical model for masonry-like structures”, *J. Mech. Mater. Struct.* **5**:4 (2010), 583–615.
- [Angelillo et al. 2012] M. Angelillo, E. Babilio, and A. Fortunato, “Numerical solutions for crack growth based on the variational theory of fracture”, *Comput. Mech.* **50**:3 (2012), 285–301.
- [Angelillo et al. 2014] M. Angelillo, A. Fortunato, A. Montanino, and M. Lippiello, “Singular stress fields in masonry structures: Derand was right”, *Meccanica (Milano)* **49**:5 (2014), 1243–1262.
- [Angelillo et al. 2016] M. Angelillo, E. Babilio, A. Fortunato, M. Lippiello, and A. Montanino, “Analytic solutions for the stress field in static sandpiles”, *Mech. Mater.* **95** (2016), 192–203.
- [Angelillo et al. 2018] M. Angelillo, A. Fortunato, A. Gesualdo, A. Iannuzzo, and G. Zuccaro, “Rigid block models for masonry structures”, *Int. J. Masonry Res. Innov.* **3**:4 (2018), 349–368.
- [Bagi 2014] K. Bagi, “When Heyman’s Safe Theorem of rigid block systems fails: non-Heymanian collapse modes of masonry structures”, *Int. J. Solids Struct.* **51**:14 (2014), 2696–2705.
- [Bathe and Wilson 1976] K.-J. Bathe and E. L. Wilson, *Numerical methods in finite element analysis*, Prentice-Hall, 1976.
- [Block 2009] P. Block, *Thrust network analysis: exploring three-dimensional equilibrium*, Ph. D. thesis, Massachusetts Institute of Technology. Dept. of Architecture., 2009, Available at <https://dspace.mit.edu/handle/1721.1/49539>.
- [Block and Lachauer 2013] P. Block and L. Lachauer, “Three-dimensional (3D) equilibrium analysis of gothic masonry vaults”, *Int. J. Archit. Herit.* **8**:3 (2013), 312–335.
- [Block and Lachauer 2014] P. Block and L. Lachauer, “Three-dimensional funicular analysis of masonry vaults”, *Mech. Res. Commun.* **56** (2014), 53–60.
- [Block et al. 2006] P. Block, M. De Jong, and J. Ochsendorf, “As hangs the flexible line: equilibrium of masonry arches”, *Nexus Netw. J.* **8**:2 (2006), 13–24.
- [Brandonisio et al. 2015] G. Brandonisio, E. Mele, and A. De Luca, “Closed form solution for predicting the horizontal capacity of masonry portal frames through limit analysis and comparison with experimental test results”, *Eng. Fail. Anal.* **55** (2015), 246–270.
- [Brandonisio et al. 2017] G. Brandonisio, E. Mele, and A. De Luca, “Limit analysis of masonry circular buttressed arches under horizontal loads”, *Meccanica (Milano)* **52**:11-12 (2017), 2547–2565.
- [Castellano 1988] G. Castellano, “Un modello cinematico per i materiali non resistenti a trazione”, in *Cinquantenario della Facoltà di Architettura di Napoli: Franco Jossa e la sua opera*, Napoli, 1988.
- [Cennamo et al. 2018] C. Cennamo, C. Cusano, A. Fortunato, and M. Angelillo, “A study on form and seismic vulnerability of the dome of San Francesco di Paola in Naples”, *Ing. Sismica* **35**:1 (2018), 88–108.
- [Chambolle et al. 2007] A. Chambolle, A. Giacomini, and M. Ponsiglione, “Piecewise rigidity”, *J. Funct. Anal.* **244**:1 (2007), 134–153.
- [Como 1992] M. Como, “Equilibrium and collapse analysis of masonry bodies”, *Meccanica (Milano)* **27**:3 (1992), 185–194.
- [Coulomb 1776] C. A. Coulomb, “Essai sur une application des règles de maximis & minimis à quelques problèmes de statique: relatifs à l’architecture”, *Mémoires de mathématique & de physique, présentés à l’Académie Royale des Sciences par divers savans* **7** (1776), 343–382.
- [Couplet 1729] P. Couplet, “De la poussée des voûtes”, *Mémoires de l’Académie Royale des Sciences* (1729), 79–117.
- [Couplet 1730] P. Couplet, “Seconde partie de l’examen de la poussée des voûtes”, *Mémoires de l’Académie Royale des Sciences* (1730), 117–141.
- [Dantzig 1963] G. Dantzig, *Linear programming and extensions*, Princeton university press, 1963.
- [Danyzy 1732/1778] A. A. H. Danyzy, “Méthode générale pour déterminer la résistance qu’il faut opposer à la poussée des voûtes”, *Histoire de la Société Royale des Sciences établie à Montpellier* **2**:1718-1745 (1732/1778), 40–56.
- [De Serio et al. 2018] F. De Serio, M. Angelillo, A. Gesualdo, A. Iannuzzo, G. Zuccaro, and M. Pasquino, “Masonry structures made of monolithic blocks with an application to spiral stairs”, *Meccanica (Milano)* **53**:8 (2018), 2171–2191.
- [Del Piero 1998] G. Del Piero, “Limit analysis and no-tension materials”, *Int. J. Plast.* **14**:1-3 (1998), 259–271.

- [Di Pasquale 1984] S. Di Pasquale, *Statica dei solidi murari: teoria ed esperienze*, Università di Firenze: Atti Dipartimento Costruzioni, 1984.
- [Fortunato et al. 2014] A. Fortunato, F. Fraternali, and M. Angelillo, “Structural capacity of masonry walls under horizontal loads”, *Ing. Sismica* **31**:1 (2014), 41–49.
- [Fortunato et al. 2016] A. Fortunato, E. Babilio, M. Lippiello, A. Gesualdo, and M. Angelillo, “Limit analysis for unilateral masonry-like structures”, *Open Construct. Build. Technol. J.* **10**:Suppl 2: M12 (2016), 346–362.
- [Fortunato et al. 2018] A. Fortunato, F. Fabbrocino, M. Angelillo, and F. Fraternali, “Limit analysis of masonry structures with free discontinuities”, *Meccanica (Milano)* **53**:7 (2018), 1793–1802.
- [Fraddosio et al. 2019] A. Fraddosio, N. Lepore, and M. D. Piccioni, “Lower bound limit analysis of masonry vaults under general load conditions”, pp. 1090–1098 in *Structural analysis of historical constructions*, edited by R. Aguilar et al., Springer, Cham, 2019.
- [Gesualdo and Monaco 2015] A. Gesualdo and M. Monaco, “Constitutive behaviour of quasi-brittle materials with anisotropic friction”, *Lat. Am. J. Solids Struct.* **12**:4 (2015), 695–710.
- [Gesualdo et al. 2017] A. Gesualdo, C. Cennamo, A. Fortunato, G. Frunzio, M. Monaco, and M. Angelillo, “Equilibrium formulation of masonry helical stairs”, *Meccanica (Milano)* **52**:8 (2017), 1963–1974.
- [Gesualdo et al. 2018] A. Gesualdo, A. Iannuzzo, M. Monaco, and F. Penta, “Rocking of a rigid block freestanding on a flat pedestal”, *J. Zhejiang Univ. Sci. A* **19**:5 (2018), 3310–345.
- [Giaquinta and Giusti 1985] M. Giaquinta and E. Giusti, “Researches on the equilibrium of masonry structures”, *Arch. Ration. Mech. Anal.* **88**:4 (1985), 359–392.
- [Giuffrè 1991] A. Giuffrè, *Letture sulla Meccanica delle Murature Storiche*, Edizioni Kappa, 1991.
- [Gregory 1695] D. Gregory, “Catenaria”, *Philos. Trans. Royal Soc.* **19**:231 (1695), 637–652.
- [Heyman 1966] J. Heyman, “The stone skeleton”, *Int. J. Solids Struct.* **2**:2 (1966), 249–279.
- [Heyman 1998] J. Heyman, *Structural analysis: a historical approach*, Cambridge University Press, Cambridge, 1998.
- [Hooke 1676] R. Hooke, *A description of helioscopes and some other instruments made by Robert Hooke, fellow of the Royal Society*, T.R. for John Martyn, London, 1676.
- [Huerta 2006] S. Huerta, “Galileo was wrong: the geometrical design of masonry arches”, *Nexus Netw. J.* **8**:2 (2006), 25–52.
- [Huerta 2008] S. Huerta, “The analysis of masonry architecture: a historical approach: to the memory of professor Henry J. Cowan”, *Architect. Sci. Rev.* **51**:4 (2008), 297–328.
- [Iannuzzo 2017] A. Iannuzzo, *A new rigid block model for masonry structures*, Ph. D. dissertation, Department of Structures for Engineering and Architecture, Università degli Studi di Napoli Federico II, 2017, Available at http://www.fedoa.unina.it/11732/1/Iannuzzo_Antonino_29.pdf.
- [Iannuzzo et al. 2018a] A. Iannuzzo, M. Angelillo, E. De Chiara, F. De Guglielmo, F. De Serio, F. Ribera, and A. Gesualdo, “Modelling the cracks produced by settlements in masonry structures”, *Meccanica (Milano)* **53**:7 (2018), 1857–1873.
- [Iannuzzo et al. 2018b] A. Iannuzzo, A. De Luca, A. Fortunato, A. Gesualdo, and M. Angelillo, “Fractures detection in masonry constructions under horizontal seismic forces”, *Ing. Sismica* **35**:3 (2018), 87–103.
- [Iannuzzo et al. 2018c] A. Iannuzzo, F. De Serio, A. Gesualdo, G. Zuccaro, A. Fortunato, and M. Angelillo, “Crack patterns identification in masonry structures with a C° displacement energy method”, *Int. J. Masonry Res. Innov.* **3**:3 (2018), 295–323.
- [Kooharian 1952] A. Kooharian, “Limit analysis of voussoir (segmental) and concrete arches”, *J. Am. Concrete Ins.* **49**:24 (1952), 317–328.
- [Kurrer 2008] K.-E. Kurrer, “The history of the theory of structures: from arch analysis to computational mechanics”, *Int. J. Space Struct.* **23**:3 (2008), 193–197.
- [Le Seur et al. 1742] T. Le Seur, F. Jacquier, and R. G. Boscovich, *Parere di tre matematici sopra i danni che si sono trovati nella cupola di S. Pietro sul fine dell’anno 1742*, Roma, 1742.
- [Livesley 1978] R. K. Livesley, “Limit analysis of structures formed from rigid blocks”, *Int. J. Numer. Methods Eng.* **12**:12 (1978), 1853–1871.

- [Marmo and Rosati 2017] F. Marmo and L. Rosati, “Reformulation and extension of the thrust network analysis”, *Comput. Struct.* **182** (2017), 104–118.
- [Marmo et al. 2018] F. Marmo, D. Masi, and L. Rosati, “Thrust network analysis of masonry helical staircases”, *Int. J. Archit. Herit.* **12**:5 (2018), 828–848.
- [Mehrotra 1992] S. Mehrotra, “On the implementation of a primal-dual interior point method”, *SIAM J. Optim.* **2**:4 (1992), 575–601.
- [Milani 2011] G. Milani, “Simple lower bound limit analysis homogenization model for in- and out-of-plane loaded masonry walls”, *Constr. Build. Mater.* **25**:12 (2011), 4426–4443.
- [Monaco et al. 2014] M. Monaco, M. Guadagnuolo, and A. Gesualdo, “The role of friction in the seismic risk mitigation of freestanding art objects”, *Nat. Hazards* **73**:2 (2014), 389–402.
- [Ochsendorf 2006] J. Ochsendorf, “The masonry arch on spreading supports”, *Struct. Eng.* **84**:2 (2006), 29–34.
- [Poleni 1748] G. Poleni, *Memorie storiche della gran cupola del tempio Vaticano e de’ danni di essa e detristoramenti loro, divisi in libri cinque*, Nella stamperia del seminario, Padova, 1748.
- [Portioli et al. 2014] F. Portioli, C. Casapulla, M. Gilbert, and L. Cascini, “Limit analysis of 3D masonry block structures with non-associative frictional joints using cone programming”, *Comput. Struct.* **143** (2014), 108–121.
- [Romano and Romano 1979] G. Romano and M. Romano, “Sulla soluzione di problemi strutturali in presenza di legami costitutivi unilaterali”, *Atti della Accademia Nazionale dei Lincei. Classe di Scienze Fisiche, Matematiche e Naturali. Rendiconti* **67**:1-2 (1979), 104–113.
- [Sacco 2014] E. Sacco, “Micro, multiscale and macro models for masonry structures”, pp. 241–291 in *Mechanics of masonry structures*, edited by M. Angelillo, Springer, Vienna, 2014.
- [Shin et al. 2016] H. V. Shin, C. F. Porst, E. Vouga, J. Ochsendorf, and F. Durand, “Reconciling elastic and equilibrium methods for static analysis”, *ACM Trans. Graph.* **35**:2 (2016), article 13.
- [Van Mele et al. 2012] T. Van Mele, J. McInerney, M. DeJong, and P. Block, “Physical and computational discrete modeling of masonry vault collapse”, pp. 2252–2560 in *Proceedings of the 8th International Conference on Structural Analysis of Historical Constructions Wroclaw* (Wroclaw, Poland), 2012.
- [Šilhavý 2014] M. Šilhavý, “Mathematics of the masonry-like model and limit analysis”, pp. 29–69 in *Mechanics of masonry structures*, edited by M. Angelillo, Springer, Vienna, 2014.
- [Yvon Villarceau 1853] A. Yvon Villarceau, *Sur l’établissement des arches de pont, envisagé au point de vue de la plus grande stabilité: mémoire accompagné de tables pour faciliter les applications numériques*, Imprimerie impériale, 1853.
- [Yvon Villarceau 1854] A. Yvon Villarceau, *L’établissement des arches de pont*, Institut de France, Académie des Sciences, 1854.
- [Zuccaro et al. 2017] G. Zuccaro, F. Dato, F. Cacace, D. De Gregorio, and S. Sessa, “Seismic collapse mechanisms analyses and masonry structures typologies: a possible correlation”, *Ing. Sismica* **34**:4 (2017), 121–149.

Received 14 Dec 2018. Revised 9 Sep 2019. Accepted 28 Sep 2019.

ANTONINO IANNUZZO: iannuzzo@arch.ethz.ch

Institute of Technology in Architecture, Block Research Group, ETH Zurich, Stefano-Franscini-Platz 1, 8093 Zurich, Switzerland

DISPLACEMENT CAPACITY OF MASONRY STRUCTURES UNDER HORIZONTAL ACTIONS VIA PRD METHOD

ANTONINO IANNUZZO, CARLO OLIVIERI AND ANTONIO FORTUNATO

The displacement capacity of masonry structures, investigated through the piecewise rigid displacement (PRD) method, is the principal focus of the present study. Since a masonry construction exhibits a rigid block mechanism when shaken by severe earthquakes, by adopting the Heyman material restrictions, the PRD method can be used to look for the global collapse mechanism of the structure under horizontal actions and the static load multiplier. As a result of this investigation, a one-degree of freedom mechanism is detected. In the moving part of the collapsing structure, the field of relative displacement among the blocks allows to identify the fracture distribution. The paper examines the stability of masonry constructions analysing the displacement capacity curves which is obtained by a kinematical incremental analysis via PRD method, operating in the framework of limit analysis. The displacement capacity of the structure is defined as the maximum displacement in which the potential energy assumes a local maximum. Consequently, the moving part of the structure in this configuration is unstable. Finally, two examples are exposed in detail to show the performance of the PRD method.

1. Introduction

In many technical regulations, it is requested to assess the displacement capacity of masonry structures under seismic loads. This represents one of the recent and current critical issues (see [Ochsendorf 2006]) in the analysis of unreinforced masonry structures, and many numerical codes, with more or less success, were recently developed in order to answer to this request. Most of them are implemented in Finite Element (FE) environment and take into account geometric and mechanical nonlinearities, but, in most of the cases, without considering unilateral contacts between elements. Although there is a possibility to use FE codes implementing a finite number of unilateral contacts the results are often not satisfactory as shown in [Shin et al. 2016]. The phenomenological behaviour involving the unilaterality of masonry structures is better taken in account by discrete element methods (DEM) [Cundall 1971] with commercial software such as 3DEC (see [Drei et al. 2016; Forgács et al. 2017; Simon and Bagi 2016; Sarhosis et al. 2016; Tóth et al. 2009]). DEM codes model the unilateral contact among blocks by considering special friction laws at interfaces. The solutions obtained depend crucially on the initial configuration and on the load history. Our aim is to explore the stability of masonry structures and then to evaluate their displacement capacity curves in the framework of limit analysis by using the piecewise rigid displacement (PRD) method. Heyman [1966] fixed in a rigorous and a clear way the theoretical basis for the application of limit analysis to generic masonry structures through the formulation of three simple basic

Iannuzzo is the corresponding author.

Keywords: masonry, unilateral materials, stability, piecewise rigid displacements, concentrated cracks, displacement capacity.

material restrictions: (i) masonry has no tensile strength, (ii) masonry has infinite compressive strength, (iii) sliding does not occur.

These three hypotheses represent sufficient assumptions for the application of the two basic theorems of limit analysis to masonry structures. For the discussion and the application of limit analysis to masonry-like structures the reader can examine the works in [Livesley 1978; Como 1992; Angelillo 2014; 2015; 2019; Block 2009; Huerta 2008; Sacco 2014; Brandonisio et al. 2013; 2015; 2017; Cennamo and Di Fiore 2013; Cennamo et al. 2018; Chiozzi et al. 2017; Gesualdo et al. 2017; Angelillo et al. 2014; 2018; Block et al. 2006b; Block and Lachauer 2013; Fortunato et al. 2015; 2018; Fraddosio et al. 2019; Iannuzzo et al. 2018c; Portioli et al. 2014].

On adopting for the material Heyman's restrictions, the stability of some masonry structures under finite displacement is implemented parametrically by solving the equilibrium problem via thrust line in [Block et al. 2006a; Zampieri et al. 2018]. On the other hand, the displacement capacity can be explored dynamically by using DEM as in [McInerney and DeJong 2015] or comparing DEM results with laboratory tests (see [Rossi et al. 2017; Misseri et al. 2018; Van Mele et al. 2012]). Portioli and Cascini [2016] assess the stability of some simple structures by using rigid block limit analysis.

2. Material restrictions, BVP and the energy criterion for NRNT materials

NRNT materials. Heyman's constraints (i), (ii), (iii) can be extended to 2D continua on introducing unilateral material restrictions on the stress and on strain. A 2D masonry structure is modelled as a continuum occupying the region Ω of the Euclidean space \mathbb{E}^2 . Within the small displacement assumption, we denote \mathbf{T} the stress inside Ω , \mathbf{u} the displacement of material points \mathbf{x} belonging to Ω and adopt the infinitesimal strain \mathbf{E} as the strain measure.

A normal rigid no-tension (NRNT) material is one that satisfies the following restrictions:

$$\mathbf{T} \in \text{Sym}^-, \quad \mathbf{E} \in \text{Sym}^+, \quad \mathbf{T} \cdot \mathbf{E} = 0, \quad (1)$$

where Sym^- , Sym^+ are the mutually polar cones of negative and positive semidefinite symmetric tensors. The restrictions (1) are equivalent to the so-called normality conditions

$$\mathbf{T} \in \text{Sym}^-, \quad (\mathbf{T} - \mathbf{T}^*) \cdot \mathbf{E} \geq 0, \quad \forall \mathbf{T}^* \in \text{Sym}^-, \quad (2)$$

and to the *dual normality conditions*:

$$\mathbf{E} \in \text{Sym}^+, \quad (\mathbf{E} - \mathbf{E}^*) \cdot \mathbf{T} \geq 0, \quad \forall \mathbf{E}^* \in \text{Sym}^+. \quad (3)$$

The restrictions defining an NRNT material in the particular form (2) are the essential ingredients for the application of the theorems of limit analysis (see [Kooharian 1952; Giaquinta and Giusti 1985; Fortunato et al. 2014; 2016]).

The boundary value problem. The equilibrium of a 2D masonry structure, modelled as a continuum made of an NRNT material subject to given loads and settlements, can be formulated as a boundary value problem (BVP), in the following form: “Find a displacement field \mathbf{u} and the allied strain \mathbf{E} , and a

stress field \mathbf{T} such that

$$\mathbf{E} = \frac{1}{2}(\nabla \mathbf{u} + \nabla \mathbf{u}^T), \quad \mathbf{E} \in \text{Sym}^+, \quad \mathbf{u} = \bar{\mathbf{u}} \text{ on } \partial\Omega_D, \quad (4)$$

$$\text{div} \mathbf{T} + \mathbf{b} = 0, \quad \mathbf{T} \in \text{Sym}^-, \quad \mathbf{T} \mathbf{n} = \bar{\mathbf{s}} \text{ on } \partial\Omega_N, \quad (5)$$

$$\mathbf{T} \cdot \mathbf{E} = 0, \quad (6)$$

where \mathbf{n} is the unit outward normal to the boundary $\partial\Omega$, and $\partial\Omega_D, \partial\Omega_N$ is a fixed partition of the boundary into constrained and loaded parts [Angelillo and Fortunato 2004].

Concentrated strain and stress. For NRNT materials, it's well known that the strain and stress are bounded measures and can be decomposed into the sum of two parts

$$\mathbf{E} = \mathbf{E}^r + \mathbf{E}^s, \quad \mathbf{T} = \mathbf{T}^r + \mathbf{T}^s, \quad (7)$$

where $(\cdot)^r$ is the regular part (i.e., the part which is absolutely continuous with respect to the area measure) and $(\cdot)^s$ is the singular part.

A nonzero singular part of the strain or also of the stress substantiates the possibility of admitting discontinuities of the displacement vector and of the stress vector across certain curves. For a more detailed review about jump discontinuities of stress or of displacement the reader could look at [Angelillo and Rosso 1995; Angelillo et al. 2005; 2010; 2012; 2016].

Displacement approach. With respect to a given structure under given loads and distortions, a solution of the BVP through the *displacement approach* consists in the search of a displacement field $\mathbf{u} \in \mathcal{K}$ for which there exist a stress field $\mathbf{T} \in \mathcal{H}$ such that $\mathbf{T} \cdot \mathbf{E}(\mathbf{u}) = 0$, where \mathcal{K} and \mathcal{H} are the sets of kinematically admissible displacements and stresses, defined by

$$\mathcal{K} = \{\mathbf{u} \in S / \mathbf{E} = \frac{1}{2}(\nabla \mathbf{u} + \nabla \mathbf{u}^T) \in \text{Sym}^+ \text{ and } \mathbf{u} = \bar{\mathbf{u}} \text{ on } \partial\Omega_D\}, \quad (8)$$

$$\mathcal{H} = \{\mathbf{T} \in S' / \text{div} \mathbf{T} + \mathbf{b} = 0, \quad \mathbf{T} \in \text{Sym}^-, \quad \mathbf{T} \mathbf{n} = \bar{\mathbf{s}} \text{ on } \partial\Omega_N\}, \quad (9)$$

where S, S' are two suitable function spaces.

Energy criterion. The energy $\mathcal{P}(\mathbf{u})$ for Heyman's materials is just the potential energy of the loads [De Serio et al. 2018], namely

$$\mathcal{P}(\mathbf{u}) = - \int_{\partial\Omega_N} \bar{\mathbf{s}} \cdot \mathbf{u} \, ds - \int_{\Omega} \mathbf{b} \cdot \mathbf{u} \, da. \quad (10)$$

The search of a solution of the BVP through a displacement approach could be performed by looking for the minimizer \mathbf{u}^0 of $\mathcal{P}(\mathbf{u})$:

$$\mathcal{P}(\mathbf{u}^0) = \min_{\mathbf{u} \in \mathcal{K}} \mathcal{P}(\mathbf{u}) \quad \text{with } \mathbf{u} \in \mathcal{K}. \quad (11)$$

The search of an approximate solution: PRD Method. The idea at the base of the PRD Method is to approximate the solution of the BVP by restricting the search of the minimizer to a proper subset of \mathcal{K} , that is by minimizing the energy function in the set $\mathcal{K}_{\text{pr}} \subset \mathcal{K}$ of piecewise rigid displacements (PRD) verifying Heyman's material restrictions, that is

$$\mathcal{K}_{\text{pr}} = \{\mathbf{u} \in \mathcal{S}_{\text{PR}} / \mathbf{E} \in \text{Sym}^+ \text{ and } \mathbf{u} = \bar{\mathbf{u}} \text{ on } \partial\Omega_D\} \subset \mathcal{K}, \quad (12)$$

where \mathcal{H}_{pr} is an infinite dimensional space and can be discretized by fixing a proper finite subset, called $\mathcal{H}_{\text{pr}}^M$, generated by a finite polygonal partition of the structural domain Ω into rigid parts Ω_i , say

$$(\Omega_i)_{i \in \{1, 2, \dots, M\}}. \quad (13)$$

The minimizer $\mathbf{u}_{\text{PR}}^0 \in \mathcal{H}_{\text{pr}}^M$ of the potential energy, namely

$$\mathcal{P}(\mathbf{u}_{\text{PR}}^0) = \min_{\mathbf{u} \in \mathcal{H}_{\text{pr}}^M} \mathcal{P}(\mathbf{u}), \quad (14)$$

represents an approximation of the solution \mathbf{u}^0 of the exact problem (11) in the subset $\mathcal{H}_{\text{pr}}^M$ and, in this sense, represents the solution of the BVP by using the PRD Method. The way used to numerically implement the problem (14) is treated in deep in other papers, e.g., [Angelillo et al. 2018; Iannuzzo 2017; 2018c; 2018b]. For completeness, here the main steps needed to numerically implement problem (14) in order to transform it in a typical linear programming problem are reported. \mathcal{H}_{pr} is assumed as the discretized kinematical admissible displacements set generated by the partition of the domain Ω into M rigid polygons Ω_i , whose boundary $\partial\Omega_i$ is the union of straight *interfaces* $\partial\Omega_i^j$ with unit normal \mathbf{n}_{ij} and tangent vector \mathbf{t}_{ij} . By restricting to PRD displacements, the strain \mathbf{E} coincides with its singular part \mathbf{E}^s and can be written with reference to the partition (13) as

$$\mathbf{E} = \mathbf{E}^s = \sum_{ij} v_{ij} \delta(\partial\Omega_i^j) \mathbf{u}_{ij} \otimes \mathbf{n}_{ij} + \frac{1}{2} \sum_{ij} w_{ij} \delta(\partial\Omega_i^j) (\mathbf{t}_{ij} \otimes \mathbf{n}_{ij} + \mathbf{n}_{ij} \otimes \mathbf{t}_{ij}), \quad (15)$$

where $\delta(\partial\Omega_i^j)$ is the unit line Dirac delta with support on the interfaces $\partial\Omega_i^j$ belonging to the skeleton of the mesh. The Heyman's restrictions are taken into account by enforcing the normality conditions (2) on the strain, that is by writing, for each interface $\partial\Omega_i$, the two following conditions:

$$v_{ij} = [\mathbf{u}] \cdot \mathbf{n}_{ij} \geq 0, \quad (16)$$

$$w_{ij} = [\mathbf{u}] \cdot \mathbf{t}_{ij} = 0, \quad (17)$$

where $[\mathbf{u}]$ denotes the displacement jump associated to the generic piecewise rigid displacement $\mathbf{u} \in \mathcal{H}_{\text{pr}}^M$. It is worth to note that conditions [(16), (17)] enforce unilateral contact with no sliding on the interface $\partial\Omega_i$. Since $\mathbf{u} \in \mathcal{H}_{\text{pr}}^M$ is in one to one correspondence with a vector $\mathbf{U} \in \mathbb{R}^{3M}$ whose components represent the $3M$ degree of freedom of the element Ω_i , both the energy function $\mathcal{P}(\mathbf{u})$ and the restrictions [(16), (17)] can be expressed in terms of \mathbf{U} ; in particular relations [(16), (17)], written at each interface, can be transformed into matrix forms:

$$\mathbf{A}\mathbf{U} \geq \mathbf{0}, \quad (18)$$

$$\mathbf{B}\mathbf{U} = \mathbf{0}. \quad (19)$$

Finally, the minimum problem (14) which approximates the minimum problem (11) can be transformed into

$$\mathcal{P}(\mathbf{U}^0) = \min_{\mathbf{U} \in \mathbb{K}^M} \mathcal{P}(\mathbf{U}), \quad (20)$$

where \mathbb{K}^M is the set

$$\mathbb{K}^M = \{\mathbf{U} \in \mathbb{R}^{3M} / \mathbf{A}\mathbf{U} \geq \mathbf{0}, \quad \mathbf{B}\mathbf{U} = \mathbf{0}\}. \quad (21)$$

Problem (20) is a standard linear finite dimensional minimization problem, since the function $\mathcal{P}(\hat{\mathbf{U}})$ is a linear functional of the $3M$ -vector $\hat{\mathbf{U}}$ and all the constraints are represented by linear conditions. Furthermore, it is worth to note that problem (20) transforms the original minimization problem (11) for a continuum, into a minimization problem for a multibody structure subject to unilateral contact conditions along the interfaces. The solution can be searched with the simplex method [Dantzig et al. 1955] or, if the number of variables is large, one can resort to the interior point algorithm (see [Mehrotra 1992; Vanderbei 2015; Dantzig 1963]).

Seismic analysis. The object of the present study is to assess the bearing capacity of masonry structures under seismic actions. Horizontal seismic actions, modelled as static, are gradually increased by considering forces proportional to the mass through the scalar parameter λ (for reference see [Iannuzzo 2017; Iannuzzo et al. 2018b]).

In order to solve this problem and to evaluate the horizontal collapse multiplier λ_c , with our approach, we proceed as follows. Denoting λ the scale factor of the horizontal actions we can find an interval $[\lambda_s, \lambda_m]$ to which the collapse multiplier λ_c has to belong. In particular, λ_s represents an approximation of the supremum of the multipliers for which the initial configuration is still safe (i.e., $\hat{\mathbf{U}}^0 = \mathbf{0}$) whilst λ_m represents an approximation of the infimum of the multipliers for which the structure becomes a mechanism (i.e., $\hat{\mathbf{U}}^0 \rightarrow \infty$).

3. Capacity curves with PRD method: two examples

In this section two trivial examples concerning the evaluation of the static displacement capacity of two masonry structures are reported: the first one concerns a circular arch whilst the second refers to a simple portal.

First, via the PRD method (see [Iannuzzo et al. 2018a]), the horizontal static multiplier λ_m and the relative one-degree of freedom mechanism is detected. Then, beginning from this last mechanism, an incremental kinematic procedure is undertaken. In particular, the mechanism corresponding to λ_m is used to start a step-by-step kinematical procedure in order to assess the maximum horizontal displacement. To preserve linearity, the macroblocks are considered rigid and the incremental kinematical analysis is conducted by considering the superposition of small rigid displacements: the geometry of the structure at the generic step is obtained by upgrading, in an incremental step-by-step process, the previous configuration. In this incremental analysis, the governing Lagrangian parameter increases with fixed value δq at each step j , so that the evolution of the configuration of the structure depends on the step j . At the same time, by evaluating the infinitesimal incremental work made by the external gravitational forces, a curve describing the upgraded total potential energy is obtained. The displacement capacity of the structure is assumed as the displacement for which the total potential energy admits a local maximum with respect to λ . Such a state represents an unstable equilibrium configuration. Moreover, this approach can allow to extend rocking analyses (see [Gesualdo et al. 2018]) to masonry structures.

Two numerical analyses, presented below, are developed in Mathematica [Wolfram 2003] through a numerical procedure based on the following main steps:

- (1) definition of the structural geometry and its discretization;
- (2) representation of the piecewise rigid displacement field over the given support (discretized partition);

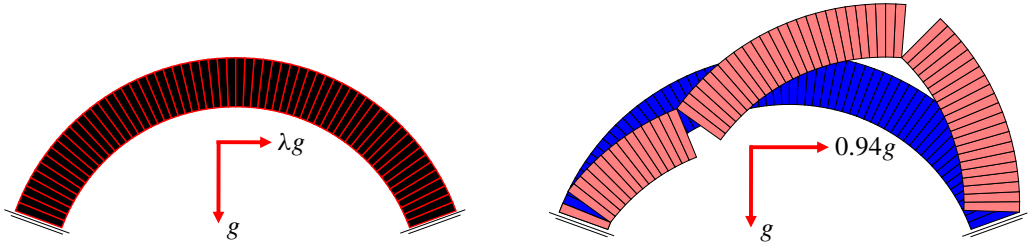


Figure 1. Left: the circular arch, discretized into 62 rigid elements, is subjected to the self-weight and to horizontal incremental action represented by forces proportional to the mass through the scale parameter λ . Right: a representation of the solution U^0 corresponding to $\lambda = 0.94$ and obtained through the simplex method.

- (3) formalization of the minimum problem (20) in terms of the displacement parameters;
- (4) numerical solution of the problem: determination of the static multiplier and the allied global mechanism;
- (5) identification of the macroblocks moving rigidly constituting the one-degree of freedom mechanism;
- (6) step-by-step linear superposition upgrading of the initial geometry;
- (7) evaluation of the curve describing the total potential energy evolution;
- (8) identification of the maximum displacement corresponding to a local maximum of the total potential energy.

3.1. Circular arch. The example reported here regards a circular arch subjected to horizontal forces, simulating a seismic action. The only loads considered are the self-weight and the horizontal incremental action. The horizontal forces are proportional to the mass through the scale parameter λ , and act at the centroids of each block. The circular arch we considered has a springing angle $\beta = 20^\circ$ (total angle of embrace 140°), an internal radius $r = 1.50$ m and a thickness $s = 0.40$ m. We discretize it into 62 prismatic rigid elements as shown in Figure 1 (left).

By applying the PRD method the collapse multiplier λ_c is found to belong to the interval $[0.932, 0.941]$. The mechanism corresponding to $\lambda = 0.94$ reached through the simplex method in 0.04 s (with an Intel Core i7-6700HQ) is depicted in Figure 1 (right): the four hinges form and the arch becomes a one-degree of freedom mechanism whose moving part involves three rigid macroblocks.

With respect to the obtained mechanism (see Figure 2, left) a linearized kinematical incremental analysis is performed. Assuming the rotation φ_3 of the block 3 as the Lagrangian parameter governing the mechanism and by fixing a constant incremental step, namely $\delta\varphi_3 = 0.0001$ rad, the geometry of the structure at the step j is obtained by upgrading the geometry of step $(j - 1)$. At each step the incremental work made by the external gravitational actions is evaluated and by summing up each increment the curve describing the total potential energy (TPE) of the load is obtained (see Figure 2, right). In this figure, the maximum static displacement corresponds to the statically unstable configuration.

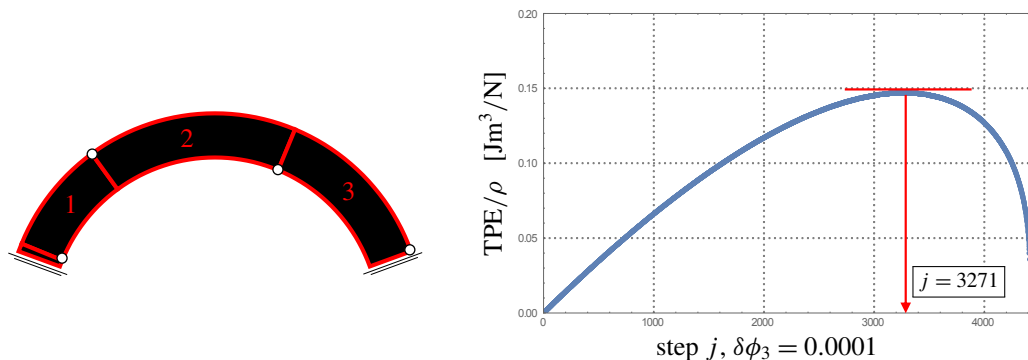


Figure 2. Partition of the arch domain obtained through the PRD method: the moving part of the structure involves 3 rigid macroblocks hinged at four points (left) and the curve describing the TPE (right), relative to the evolution of the mechanism and dimensionless with respect to the material density ρ .

The local maximum of this curve, corresponding to an unstable configuration, is reached at step 3271 for which the rotation of the block 3 is 0.3271 rad. The need of using a step-by-step superposition procedure in order to preserve the linearity has, as counterpart, the error due to small displacement fields rather than finite ones. In particular, the effect of finite displacements are reached as the summation of the effects of many small displacements controlled by a given parameter: the incremental scalar step, in this case, a constant increment $\delta\varphi_3$ of the rotation φ_3 of block 3 is assumed as a controlled parameter (e.g., Lagrangian parameter). Indeed, for small displacements, the rotation is a skew-symmetric matrix and this means that the area of a given size increases and the amount of this increment depends on the “size of the rotation”. Then, to simulate finite displacements, particularly the finite rotations, a small size step can be chosen. Thus the ratio between the area in a given step and the initial area is a reasonable measure of the error committed. Definitely, the smaller is the value of the scalar controlled parameter the better is the approximation. As shown in Figure 3 (top left), the ratio between the area of each block at step j and the initial area is assumed as a measure of the error committed: the magnitude of the error is approximately of the order 10^{-5} . The rotation and the horizontal and vertical displacements of the centroid of the three moving blocks are reported in Figure 3 (top right, and bottom).

In Figure 4 four configurations of the structure are depicted: the maximum static displacement corresponding to the step $j = 3271$ is shown in Figure 4 (bottom right).

3.2. Simple portal under horizontal action. The second example regards a simple NRNT portal subjected at the top edge to a vertical uniformly distributed load q and to an external horizontal action represented by a force λQ applied at the upper left corner. Here Q is the resultant of the acting vertical loads and λ is the load scalar factor (see Figure 5, left). The NRNT portal is discretized into 528 rigid polygonal elements defining a nontrivial partition of the structural domain. Indeed, in the previous example, the arch is trivially discretized by using radial cuts and the PRD method is used only to define the location of the hinges when the mechanism forms. This is why one knows in advance that the common fractures in an arch subjected to horizontal actions are represented by radial cuts.

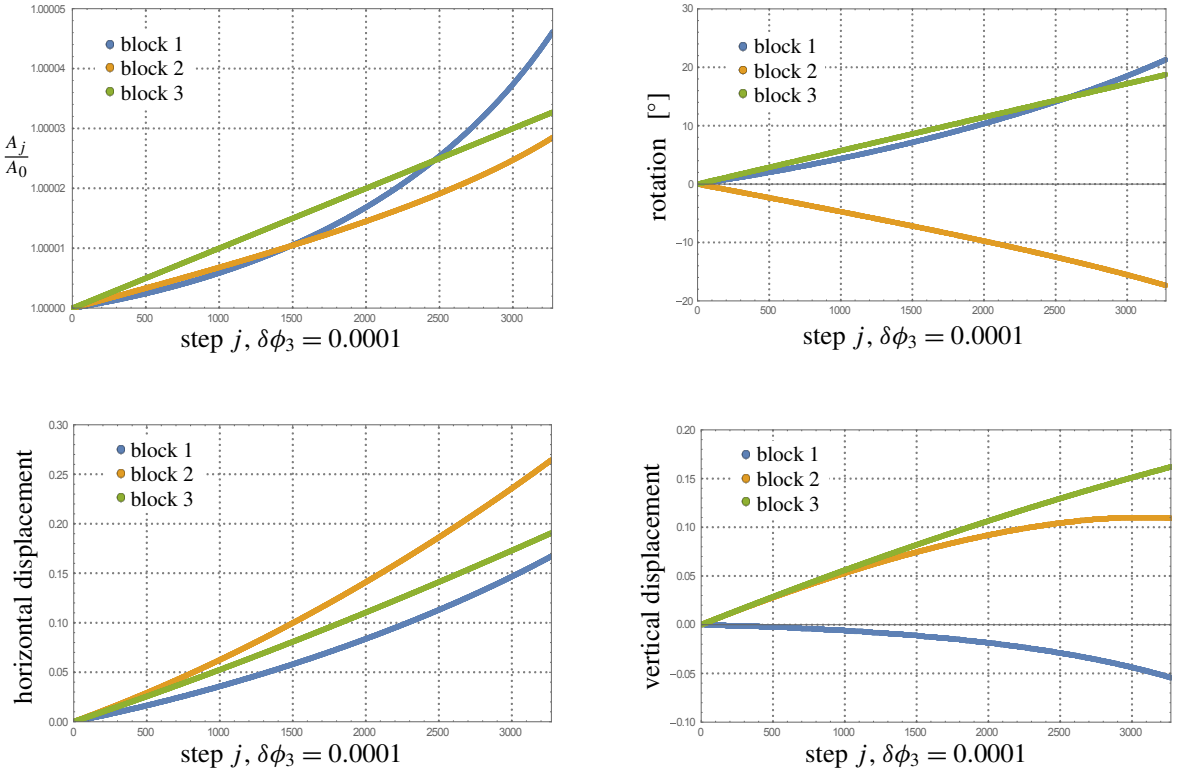


Figure 3. Top left: a measure of the error is reported by plotting the ratio between the area at the step j , namely A_j , and the initial area A_0 of each block. The number of iterations versus rotation (top right), horizontal displacement (bottom left) and vertical displacement (bottom right) of the centroid of each block.

On the contrary, in this example, it is hard to define in advance which the best discretization is: portals are characterised by vertical fractures as well as diagonal ones. One can choose to discretize this structure by using rectangular blocks, triangular blocks or another kind of discretization, but, one of the PRD method's strengths is to handle any kind of polygonal elements. With this in mind, the best way to tackle this problem is to allow for any typology of cracks, namely: vertical, horizontal and diagonal cracks. PRD method will choose the location of cracks and consequently the best rigid macroblocks partition of the domain as the one solving the minim problem (20).

Here the portal is discretised first with triangular elements, and then this discretization is further refined by allowing many other kinds of diagonal cracks for each panel. The dimension of the set of kinematical admissible mechanisms is 1584.

By applying the PRD method the collapse multiplier λ_c is found to belong to the interval $[0.406, 0.412]$. The mechanism corresponding to $\lambda = 0.41$ and reached through the interior point method in 0.28 s (with an Intel Core i7-6700HQ) is depicted in Figure 5 (right). In this case the structure transforms into a one-degree of freedom mechanism involving three rigid macroblocks hinged to each other at four points.

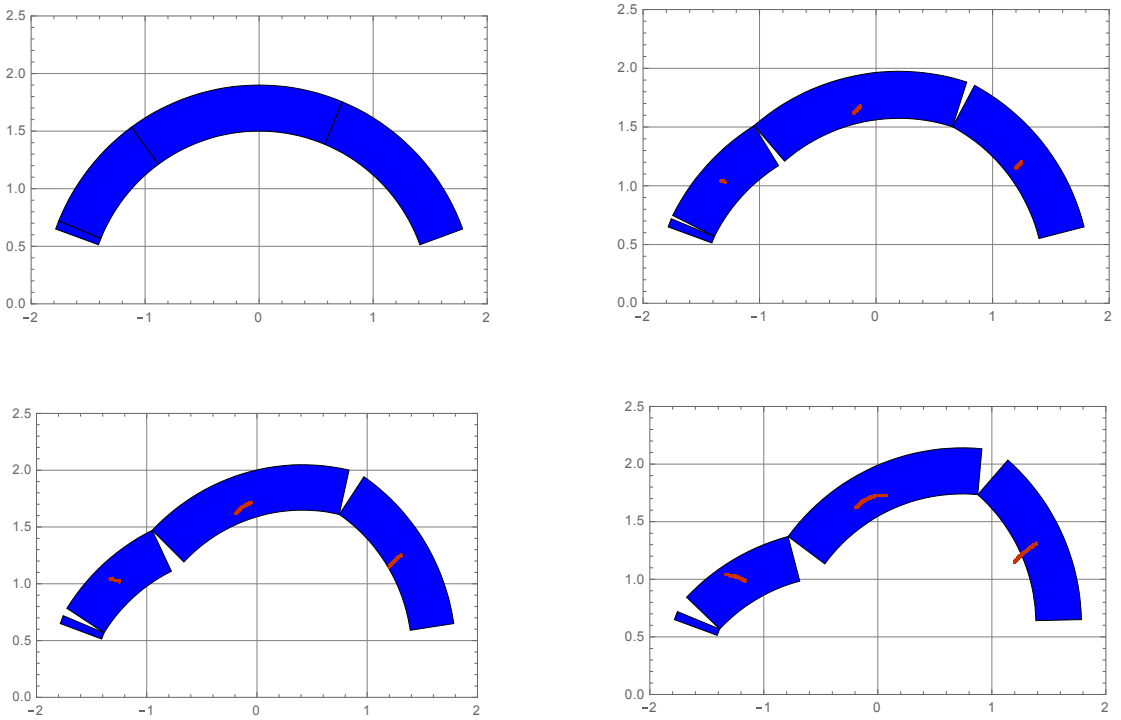


Figure 4. Configurations of the structures at four different steps: $j = 0$ (top left), $j = 1000$ (top right), $j = 2000$ (bottom left), $j = 3271$ (bottom right). The configuration at $j = 3271$ (bottom right) is unstable and represents the maximum admissible static displacement. The red line represents the paths of the centroids of each block.

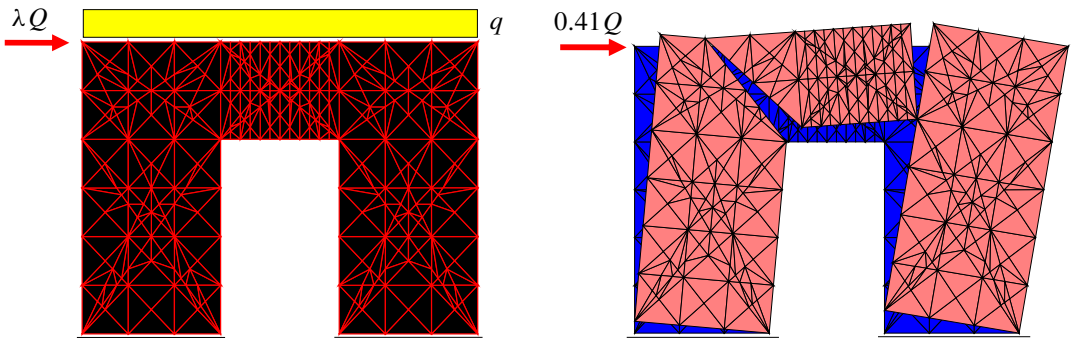


Figure 5. Left: the NRNT portal, discretized with 528 rigid polygonal elements, is subjected to a uniformly distributed load q and to the horizontal force λQ . Right: a representation of the solution U^0 corresponding to $\lambda = 0.41$ and obtained through the interior point method.

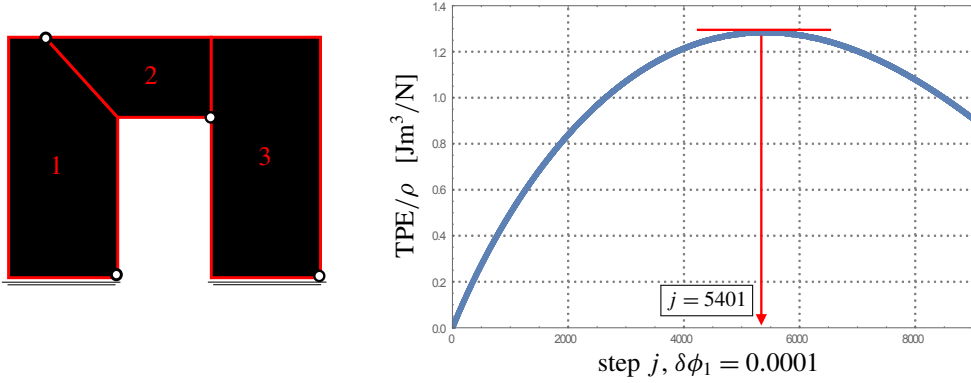


Figure 6. Left: the total potential energy (TPE), dimensionless with respect to the material density ρ , is reported: the maximum static displacement corresponds to the local maximum representing an unstable configuration. Right: a measure of the error is reported by plotting the ratio between the area at the step j and the initial area.

With respect to the mechanism shown in [Figure 6](#) (left), a kinematical incremental analysis assuming small rigid displacements and by considering the rotation φ_1 of the block 1 as the Lagrangian parameter governing the mechanism and by fixing a constant incremental step, namely $\delta\varphi_1 = 0.0001$ rad, the geometry of the structure at step j is obtained by upgrading the geometry of step $(j - 1)$ through the infinitesimal displacement field valued via the kinematical analysis. In each step the incremental work made by the external gravitational actions is evaluated. By summing each increment it is possible to obtain, as shown in previous examples, the curve describing the total potential energy of the load (see [Figure 6](#), right).

The local maximum of this curve, corresponding to an unstable configuration, is reached at step 5401 for which the rotation of the block 1 is 0.5401 rad. In [Figure 7](#) (left) a measure of the error committed considering small rigid displacements is reported showing the ratio between the area of each block at step j and the initial area. The rotation, the horizontal and the vertical displacement of the centroid of each block are reported in [Figure 7](#) (top right, bottom left and right, respectively). In [Figure 8](#) four configurations of the structure are depicted: the maximum static displacement corresponding to the step $j = 5401$ is shown in [Figure 8](#) (bottom right).

By looking at the configuration depicted in [Figure 8](#) (bottom right) it can be seen that the unilateral restrictions among blocks have been violated; that is, tensile forces are needed to be in equilibrium in this configuration. Indeed, to have an intuitive understanding of this phenomenon it is possible to imagine the structure as forced to lie in the configuration (see [Figure 8](#), bottom right): just after it is left free it does not come back to the starting configuration ([Figure 8](#), top left) but it falls down. To assess and explore this phenomenon analytically it is sufficient to evaluate the internal forces acting on the interfaces depicted in [Figure 9](#) (right). This can be done by evaluating at each step the transpose of the kinematical matrix, namely the static matrix. In particular, once the inverse problem is solved it is possible to evaluate the axial forces acting along the interfaces during all superposition processes as shown in [Figure 9](#) (left). As it is expected starting from the step $j = 2924$ (see [Figure 8](#), bottom left) there is traction at the *interface 2*.

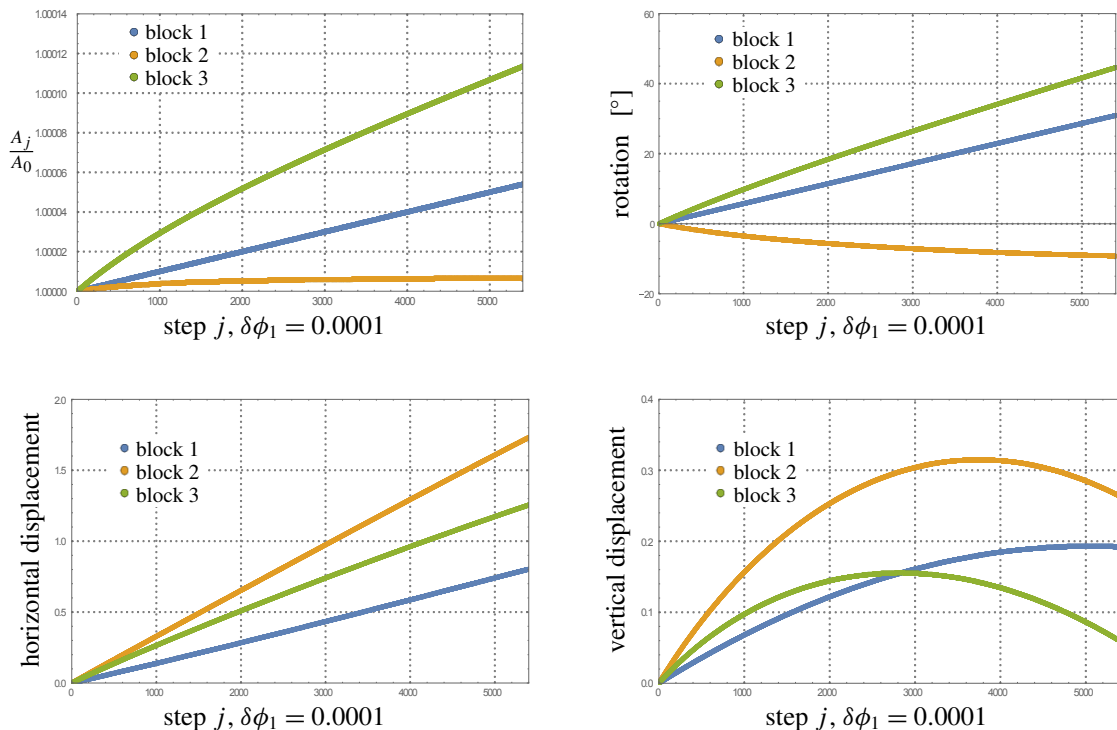


Figure 7. Top left: a measure of the error connected with the assumption of small rigid displacements is reported by plotting the ratio between the area at the step j , namely A_j , and initial area A_0 of each block. The number of iterations versus rotation (top right), horizontal displacement (bottom left) and vertical displacement (bottom right) of the centroid of each block.

4. Conclusions

In the present work, to perform a stability analysis of masonry structures under the effect of horizontal loads simulating a severe earthquake, a PRD method has been developed. The masonry has been modelled as an NRNT material on the base of Heyman's hypotheses, by which the theorems of limit analysis still hold true.

It is worth noting that the PRD mechanisms analysis arise naturally in the solution of equilibrium problem for structures made of NRNT materials. Both crack patterns and horizontal load multipliers, formulating the BVP as an energy minimum search in the space of piecewise rigid displacement, have been identified.

Due to linear contact relations between two adjacent blocks of the structural domain partition, the PRD method transforms a continuum minimum problem (11) in a linear programming one (20) in which the minimization function is the potential energy of the loads and the constraints are linearly formulated, see (21). In this context, the PRD method gives the possibility to investigate the behaviour of a generic 2D planar masonry structure subjected to settlements and load as, for example, horizontal seismic actions.

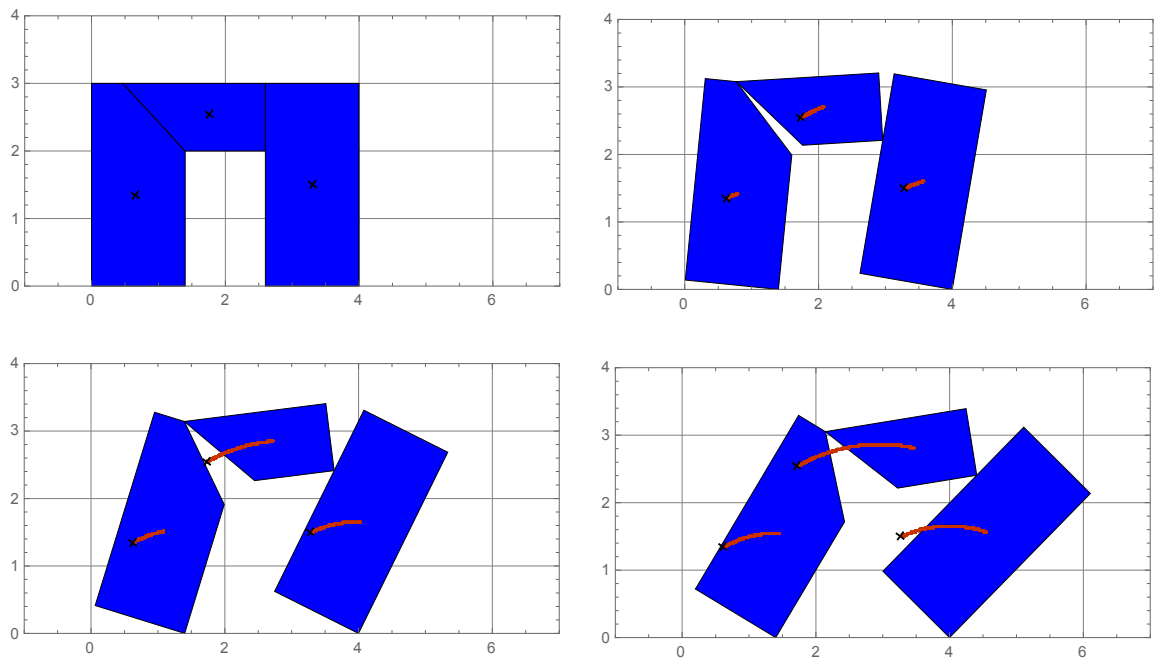


Figure 8. Configurations of the structures in different steps: $j = 0$ (top left), $j = 1000$ (top right), $j = 2924$ (bottom left), $j = 5401$ (bottom right). The configuration at $j = 5401$ (bottom right) is unstable and represents the maximum admissible static displacement. The red line represents the paths of the centroids of each block.

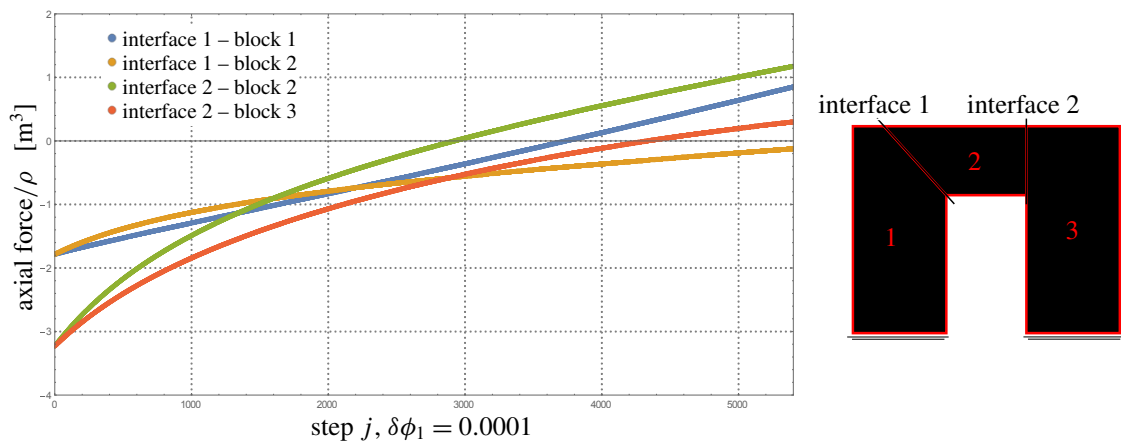


Figure 9. Axial forces (dimensionless with respect to the material density ρ) versus the number of iterations (left) acting on the interfaces (right): starting from the step $j = 2924$ the axial force acting on the interface 2 of block 2 is no longer in compression.

With PRD method both the horizontal static load multiplier and the corresponding one-degree of freedom mechanism are identified. This mechanism is employed to start a step-by-step kinematical procedure, based on small rigid displacement at each step, in order to assess the maximum horizontal displacement of the structure and to build the displacement capacity curve in finite displacement conditions. With reference to this last consideration, it is noted that the incremental PRD kinematical approach preserves the linearity of the problem and consequently it is solved in few seconds for a wide range of masonry structures.

In order to point out the potentiality of the PRD method, a circular arch and a simple portal, have been finally examined. In both cases, maximum static displacements are founded as local maximum of potential energy. As shown in the examples, a masonry structure can exhibit a large displacement before taking an unstable configuration (see [Mauro et al. 2015]).

References

- [Angelillo 2014] M. Angelillo, “[Practical applications of unilateral models to masonry equilibrium](#)”, pp. 109–210 in *Mechanics of masonry structures*, edited by M. Angelillo, Springer, Vienna, 2014.
- [Angelillo 2015] M. Angelillo, “[Static analysis of a Guastavino helical stair as a layered masonry shell](#)”, *Compos. Struct.* **119** (2015), 298–304.
- [Angelillo 2019] M. Angelillo, “[The model of Heyman and the statical and kinematical problems for masonry structures](#)”, *Int. J. Masonry Res. Innov.* **4**:1-2 (2019), 14–31.
- [Angelillo and Fortunato 2004] M. Angelillo and A. Fortunato, “[Equilibrium of masonry vaults](#)”, pp. 105–111 in *Novel approaches in civil engineering*, vol. 14, edited by M. Frémond and F. Maceri, Springer, Berlin, Heidelberg, 2004.
- [Angelillo and Rosso 1995] M. Angelillo and F. Rosso, “[On statically admissible stress fields for a plane masonry-like structure](#)”, *Quart. Appl. Math.* **53**:4 (1995), 731–751.
- [Angelillo et al. 2005] M. Angelillo, E. Babilio, and A. Fortunato, “[A numerical method for fracture of rods](#)”, pp. 277–292 in *Mechanical modelling and computational issues in civil engineering*, vol. 23, edited by M. Frémond and F. Maceri, Springer, Berlin, Heidelberg, 2005.
- [Angelillo et al. 2010] M. Angelillo, L. Cardamone, and A. Fortunato, “[A numerical model for masonry-like structures](#)”, *J. Mech. Mater. Struct.* **5**:4 (2010), 583–615.
- [Angelillo et al. 2012] M. Angelillo, E. Babilio, and A. Fortunato, “[Numerical solutions for crack growth based on the variational theory of fracture](#)”, *Comput. Mech.* **50**:3 (2012), 285–301.
- [Angelillo et al. 2014] M. Angelillo, A. Fortunato, A. Montanino, and M. Lippiello, “[Singular stress fields in masonry structures: Derand was right](#)”, *Meccanica (Milano)* **49**:5 (2014), 1243–1262.
- [Angelillo et al. 2016] M. Angelillo, E. Babilio, A. Fortunato, M. Lippiello, and A. Montanino, “[Analytic solutions for the stress field in static sandpiles](#)”, *Mech. Mater.* **95** (2016), 192–203.
- [Angelillo et al. 2018] M. Angelillo, A. Fortunato, A. Gesualdo, I. A., and G. Zuccaro, “[Rigid block models for masonry structures](#)”, *Int. J. Masonry Res. Innov.* **3**:4 (2018), 349–368.
- [Block 2009] P. Block, *Thrust network analysis: exploring three-dimensional equilibrium*, Ph. D. thesis, Massachusetts Institute of Technology. Dept. of Architecture., 2009, Available at <https://dspace.mit.edu/handle/1721.1/49539>.
- [Block and Lachauer 2013] P. Block and L. Lachauer, “[Three-dimensional \(3D\) equilibrium analysis of gothic masonry vaults](#)”, *Int. J. Archit. Herit.* **8**:3 (2013), 312–335.
- [Block et al. 2006a] P. Block, T. Ciblac, and J. Ochsendorf, “[Real-time limit analysis of vaulted masonry buildings](#)”, *Comput. Struct.* **84**:29-30 (2006), 1841–1852.
- [Block et al. 2006b] P. Block, M. De Jong, and J. Ochsendorf, “[As hangs the flexible line: equilibrium of masonry arches](#)”, *Nexus Netw. J.* **8**:2 (2006), 13–24.

- [Brandonisio et al. 2013] G. Brandonisio, G. Lucibello, E. Mele, and A. De Luca, “Damage and performance evaluation of masonry churches in the 2009 L’Aquila earthquake”, *Eng. Fail. Anal.* **34** (2013), 693–714.
- [Brandonisio et al. 2015] G. Brandonisio, E. Mele, and A. De Luca, “Closed form solution for predicting the horizontal capacity of masonry portal frames through limit analysis and comparison with experimental test results”, *Eng. Fail. Anal.* **55** (2015), 246–270.
- [Brandonisio et al. 2017] G. Brandonisio, E. Mele, and A. De Luca, “Limit analysis of masonry circular buttressed arches under horizontal loads”, *Meccanica (Milano)* **52**:11-12 (2017), 2547–2565.
- [Cennamo and Di Fiore 2013] C. Cennamo and M. Di Fiore, “Structural, seismic and geotechnical analysis of the Sant’ Agostino church in L’Aquila”, *Rev. Ing. Constr.* **28**:1 (2013), 7–20.
- [Cennamo et al. 2018] C. Cennamo, C. Cusano, A. Fortunato, and M. Angelillo, “A study on form and seismic vulnerability of the dome of San Francesco di Paola in Naples”, *Ing. Sismica* **35**:1 (2018), 88–108.
- [Chiozzi et al. 2017] A. Chiozzi, G. Milani, and A. Tralli, “A Genetic Algorithm NURBS-based new approach for fast kinematic limit analysis of masonry vaults”, *Comput. Struct.* **182** (2017), 187–204.
- [Como 1992] M. Como, “Equilibrium and collapse analysis of masonry bodies”, *Meccanica (Milano)* **27**:3 (1992), 185–194.
- [Cundall 1971] P. A. Cundall, “A computer model for simulating progressive large scale movements in blocky rock systems”, in *Proceedings of the Symposium of the International Society of Rock Mechanics* (Nancy, France), 1971.
- [Dantzig 1963] G. Dantzig, *Linear programming and extensions*, Princeton University Press, 1963.
- [Dantzig et al. 1955] G. B. Dantzig, A. Orden, and P. Wolfe, “The generalized simplex method for minimizing a linear form under linear inequality restraints”, *Pac. J. Math.* **5**:2 (1955), 183–195.
- [De Serio et al. 2018] F. De Serio, M. Angelillo, A. Gesualdo, A. Iannuzzo, G. Zuccaro, and M. Pasquino, “Masonry structures made of monolithic blocks with an application to spiral stairs”, *Meccanica (Milano)* **53**:8 (2018), 2171–2191.
- [Drei et al. 2016] A. Drei, G. Milani, and G. Sincraian, “Application of DEM to historic masonries, two case-studies in Portugal and Italy: Aguas Livres Aqueduct and Arch-Tympana of a church”, pp. 326–366 in *Computational modeling of masonry structures using the discrete element method*, IGI Global, 2016.
- [Forgács et al. 2017] T. Forgács, V. Sarhosis, and K. Bagi, “Minimum thickness of semi-circular skewed masonry arches”, *Eng. Struct.* **140** (2017), 317–336.
- [Fortunato et al. 2014] A. Fortunato, F. Fraternali, and M. Angelillo, “Structural capacity of masonry walls under horizontal loads”, *Ing. Sismica* **31**:1 (2014), 41–49.
- [Fortunato et al. 2015] A. Fortunato, E. De Chiara, F. Fraternali, and M. Angelillo, “Advanced models for the limit analysis of masonry structures”, pp. 3716–3725 in *5th International conference on computational methods in structural dynamics and earthquake engineering* (Crete Island, Greece), 2015.
- [Fortunato et al. 2016] A. Fortunato, E. Babilio, M. Lippiello, A. Gesualdo, and M. Angelillo, “Limit analysis for unilateral masonry-like structures”, *Open Construct. Build. Technol. J.* **10**:Suppl 2: M12 (2016), 346–362.
- [Fortunato et al. 2018] A. Fortunato, F. Fabbrocino, M. Angelillo, and F. Fraternali, “Limit analysis of masonry structures with free discontinuities”, *Meccanica (Milano)* **53**:7 (2018), 1793–1802.
- [Fraddosio et al. 2019] A. Fraddosio, N. Lepore, and M. D. Piccioni, “Lower bound limit analysis of masonry vaults under general load conditions”, pp. 1090–1098 in *Structural analysis of historical constructions*, edited by R. Aguilar et al., Springer, Cham, 2019.
- [Gesualdo et al. 2017] A. Gesualdo, C. Cennamo, A. Fortunato, G. Frunzio, M. Monaco, and M. Angelillo, “Equilibrium formulation of masonry helical stairs”, *Meccanica (Milano)* **52**:8 (2017), 1963–1974.
- [Gesualdo et al. 2018] A. Gesualdo, A. Iannuzzo, V. Minutolo, and M. Monaco, “Rocking of freestanding objects: theoretical and experimental comparisons”, *J. Theor. Appl. Mech. (Warsaw)* **56**:4 (2018), 977–991.
- [Giaquinta and Giusti 1985] M. Giaquinta and E. Giusti, “Researches on the equilibrium of masonry structures”, *Arch. Ration. Mech. Anal.* **88**:4 (1985), 359–392.
- [Heyman 1966] J. Heyman, “The stone skeleton”, *Int. J. Solids Struct.* **2**:2 (1966), 249–279.
- [Huerta 2008] S. Huerta, “The analysis of masonry architecture: a historical approach: to the memory of professor Henry J. Cowan”, *Architect. Sci. Rev.* **51**:4 (2008), 297–328.

- [Iannuzzo 2017] A. Iannuzzo, *A new rigid block model for masonry structures*, Ph. D. dissertation, Department of Structures for Engineering and Architecture, Università degli Studi di Napoli Federico II, 2017, Available at http://www.fedoa.unina.it/11732/1/Iannuzzo_Antonino_29.pdf.
- [Iannuzzo et al. 2018a] A. Iannuzzo, E. Angelillo, M. De Chiara, F. De Guglielmo, F. De Serio, F. Ribera, and A. Gesualdo, “Modelling the cracks produced by settlements in masonry structures”, *Meccanica (Milano)* **53**:7 (2018), 1857–1873.
- [Iannuzzo et al. 2018b] A. Iannuzzo, A. De Luca, A. Fortunato, A. Gesualdo, and M. Angelillo, “Fractures detection in masonry constructions under horizontal seismic forces”, *Ing. Sismica* **35**:3 (2018), 87–103.
- [Iannuzzo et al. 2018c] A. Iannuzzo, F. De Serio, A. Gesualdo, G. Zuccaro, A. Fortunato, and M. Angelillo, “Crack patterns identification in masonry structures with a C° displacement energy method”, *Int. J. Masonry Res. Innov.* **3**:3 (2018), 295–323.
- [Koocharian 1952] A. Koocharian, “Limit analysis of voussoir (segmental) and concrete arches”, *J. Am. Concrete Ins.* **49**:24 (1952), 317–328.
- [Livesley 1978] R. K. Livesley, “Limit analysis of structures formed from rigid blocks”, *Int. J. Numer. Methods Eng.* **12**:12 (1978), 1853–1871.
- [Mauro et al. 2015] A. Mauro, G. de Felice, and M. J. DeJong, “The relative dynamic resilience of masonry collapse mechanisms”, *Eng. Struct.* **85** (2015), 182–194.
- [McInerney and DeJong 2015] J. McInerney and M. J. DeJong, “Discrete element modeling of groin vault displacement capacity”, *Int. J. Archit. Herit.* **9**:8 (2015), 1037–1049.
- [Mehrotra 1992] S. Mehrotra, “On the implementation of a primal-dual interior point method”, *SIAM J. Optim.* **2**:4 (1992), 575–601.
- [Misseri et al. 2018] G. Misseri, M. J. DeJong, and L. Rovero, “Experimental and numerical investigation of the collapse of pointed masonry arches under quasi-static horizontal loading”, *Eng. Struct.* **173** (2018), 180–190.
- [Ochsendorf 2006] J. Ochsendorf, “The masonry arch on spreading supports”, *Struct. Eng.* **84**:2 (2006), 29–34.
- [Portioli and Cascini 2016] F. Portioli and L. Cascini, “Assessment of masonry structures subjected to foundation settlements using rigid block limit analysis”, *Eng. Struct.* **113** (2016), 347–361.
- [Portioli et al. 2014] F. Portioli, C. Casapulla, M. Gilbert, and L. Cascini, “Limit analysis of 3D masonry block structures with non-associative frictional joints using cone programming”, *Comput. Struct.* **143** (2014), 108–121.
- [Rossi et al. 2017] M. Rossi, C. Calvo Barentin, T. Van Mele, and P. Block, “Collapse analysis of unreinforced masonry vaults using 3D-printed scale-model testing”, pp. 327–345 in *Proceedings of the 7th International Conference on Advances in Experimental Structural Engineering* (Pavia, Italy), 2017.
- [Sacco 2014] E. Sacco, “Micro, multiscale and macro models for masonry structures”, pp. 241–291 in *Mechanics of masonry structures*, edited by M. Angelillo, Springer, Vienna, 2014.
- [Sarhosis et al. 2016] V. Sarhosis, K. Bagi, J. V. Lemos, and G. Milani (editors), *Computational modeling of masonry structures using the discrete element method*, IGI Global, 2016.
- [Shin et al. 2016] H. V. Shin, C. F. Porst, E. Vouga, J. Ochsendorf, and F. Durand, “Reconciling elastic and equilibrium methods for static analysis”, *ACM Trans. Graph.* **35**:2 (2016), article 13.
- [Simon and Bagi 2016] J. Simon and K. Bagi, “Discrete element analysis of the minimum thickness of oval masonry domes”, *Int. J. Archit. Herit.* **10**:4 (2016), 457–475.
- [Tóth et al. 2009] A. R. Tóth, Z. Orbán, and K. Bagi, “Discrete element analysis of a stone masonry arch”, *Mech. Res. Commun.* **36**:4 (2009), 469–480.
- [Van Mele et al. 2012] T. Van Mele, J. McInerney, M. DeJong, and P. Block, “Physical and computational discrete modeling of masonry vault collapse”, pp. 2252–2560 in *Proceedings of the 8th International Conference on Structural Analysis of Historical Constructions Wroclaw* (Wroclaw, Poland), 2012.
- [Vanderbei 2015] R. J. Vanderbei, *Linear programming: foundations and extensions*, Springer, 2015.
- [Wolfram 2003] S. Wolfram, *The Mathematica book*, fifth ed., Wolfram Media, 2003.
- [Zampieri et al. 2018] P. Zampieri, F. Faleschini, M. A. Zanini, and N. Simoncello, “Collapse mechanisms of masonry arches with settled springing”, *Eng. Struct.* **156** (2018), 363–374.

Received 11 Apr 2019. Revised 12 Sep 2019. Accepted 28 Sep 2019.

ANTONINO IANNUZZO: iannuzzo@arch.ethz.ch

Institute of Technology in Architecture, Block Research Group, ETH Zurich, Stefano-Frascini-Platz 1, 8093 Zurich, Switzerland

CARLO OLIVIERI: colivieri@unisa.it

Department of Civil Engineering, University of Salerno, 84084 Fisciano, Italy

ANTONIO FORTUNATO: a.fortunato@unisa.it

Department of Civil Engineering, University of Salerno, 84084 Fisciano, Italy

AUTOMATIC GENERATION OF STATICALLY ADMISSIBLE STRESS FIELDS IN MASONRY VAULTS

ELENA DE CHIARA, CLAUDIA CENNAMO, ANTONIO GESUALDO,
ANDREA MONTANINO, CARLO OLIVIERI AND ANTONIO FORTUNATO

The objective of the present work is to develop an automated numerical method for the analysis of thin masonry shells. The material model for masonry that we adopt is the so-called “normal rigid no-tension” (NRNT) material; and for such a material, the kinematical and the safe theorems of limit analysis are valid. The present study focuses on the application of the second theorem to masonry vaults and domes, being devoted to the determination of a class of purely compressive stress regimes, which are balanced with the load. The mere existence of such a class is a proof that the structure is safe, and members of this class may be used to assess the geometric degree of safety of the structure and to estimate bounds on the thrust forces exerted by the structure on its boundary. The problem is reduced to the equilibrium of a membrane S and can be formulated in terms of projected stresses defined on the planform Ω of S . The search of the stress reduces to the solution of a second-order pde, in terms of the stress potential F . In order that the membrane stress on S be compressive, the potential F must be concave. As for the thrust line in an arch, the surface S is not fixed and may be changed, given that it remains inside the masonry. Under these simplifying assumptions, the whole class of equilibrated stress regimes for a masonry shell is obtained by moving and deforming S inside the masonry, and also, for any fixed shape, by changing the boundary data for F , that is the distribution of thrust forces along the boundary. The search for a feasible stress state on a convenient membrane surface, to be chosen with a trial and error procedure, requires a substantial effort and may be unrewarded. Then, the main object of the present work, is to produce a computer code that can handle numerically the interplay of the shape controlled by a function f , and of the stress potential F , by developing a convergent optimization scheme able to give a safe state under the given material and geometrical constraints, namely the concavity of F and the inclusion of f within the masonry. Two simple cases, are exposed in detail to illustrate the method.

1. Introduction

A particularly simple and efficient way to approach the structural analysis of masonry is to adopt for the material the model of Heyman [1966]. This model is based on three strong simplifying assumptions: the material is unilateral (no-tension), it cannot slide, and is infinitely rigid and resistant in compression. In this context there are a number of themes that are still at cutting edge of research, namely: doing unilateral with a computer (see [Angelillo et al. 2010; Bruggi and Taliercio 2015]), studying the effects of settlements [Cennamo et al. 2017], predicting fracture patterns produced by settlements in masonry structures and, vice versa, identifying the causes of a given fracture pattern (see [Iannuzzo et al. 2018]), assessing the equilibrium of masonry vaults under vertical and horizontal forces [Angelillo and Fortunato 2004;

Keywords: masonry vaults, no-tension materials, Airy’s stress function, Pucher equilibrium.

Block et al. 2006], studying dynamical effects as in [DeJong and Dimitrakopoulos 2014] or in [Monaco et al. 2014; Gesualdo et al. 2014; 2018a; 2018b]. The formulation of the boundary value problem for unilateral masonry materials (that is, the NRNT materials for which the latent strains, known as fractures, satisfy a normality condition with respect to the admissible stresses) can be found in [Angelillo 2014]. For such a material, the kinematical and the safe theorems of limit analysis are valid and can be applied to different structures as can be seen in [Heyman 1966; Kooharian 1952; Livesley 1978] as well as in [Como 1992; Angelillo 2014; 2015; Brandonisio et al. 2015; Gesualdo et al. 2017; Angelillo et al. 2014; 2016; Fortunato et al. 2014; 2016; 2018; Iannuzzo et al. 2018].

Indeed, the more efficient tool that can be introduced for applying the unilateral no-tension model to masonry structures is the systematic use of singular stress and strain fields, within the framework defined by the two theorems of limit analysis (see [Angelillo et al. 2014], for applications of the safe theorem and [Fortunato et al. 2014], for applications of the kinematic theorem to walls).

The objective of the present work is to develop an automated numerical method for the analysis of thin masonry shells made of NRNT materials.

The more recent literature on masonry-like vaults is rather vast; apart from the production of the school of Salerno, originated by the paper on the lumped stress method [Fraternali et al. 2002a], and applied to vaults in [Fraternali et al. 2002b; Block et al. 2006; Fraternali 2010], and recently in [Angelillo et al. 2013; Marmo and Rosati 2017; Marmo et al. 2018], we recall the pioneering work by O'Dwyer [1999], and the works in [Block 2009; Block et al. 2006; Vouga et al. 2012; De Goes et al. 2013; Block and Lachauer 2014; Miki et al. 2015]. The case of spiral stairs, treated with a classical elastic membrane model by Calladine [2005], was also considered with the unilateral model in [Block 2009; Angelillo 2015; 2016; De Serio et al. 2018; Gesualdo et al. 2017].

In the spirit of the safe theorem, the vault structure is stable if a statically admissible stress field can be constructed. On allowing for singular stresses, here we consider statically admissible stress fields concentrated on surfaces or lines lying inside the masonry vault. Such structures are unilateral membranes/arches, whose geometry is described as Monge, and the equilibrium of them is formulated in Pucher form, that is, in terms of the so-called projected stresses over the planform Ω .

In particular, the method we propose is devoted to the determination of a class of purely compressive stress regimes, which are balanced with the load. The mere existence of such a class is a proof that the structure is safe, and members of this class may be used to assess the geometric degree of safety of the structure and to estimate bounds on the thrust forces exerted by the structure on its boundary.

The main simplifications we make to conduct our analysis concern the load and the type of internal stress that we consider: (i) the main part of the internal stress is a membrane stress concentrated on a surface S located inside the masonry, and (ii) the external load is lumped in such a way that it can be transferred to the surface S as a distributed load per unit area.

Under these simplifying assumptions, the equilibrium problem for the membrane S can be formulated in Pucher form (see [Angelillo and Fortunato 2004; Angelillo et al. 2013; Pucher 1934; Heyman 2012]), in terms of projected stresses defined on the planform Ω of S . The search for the stress reduces to the solution of a second-order pde, in terms of the stress potential F . In order that the membrane stress on S be compressive, the potential F must be concave [Angelillo et al. 2010; Fraternali et al. 2002a].

As for the thrust line in an arch, the surface S is not fixed and may be changed, given that it remains inside the masonry. Under these simplifying assumptions, the whole class of equilibrated stress regimes

for a masonry shell, is obtained by moving and deforming S inside the masonry, and also, for any fixed shape, by changing the boundary data for F , that is, the distribution of thrust forces along the boundary.

A masonry shell is a 3D structure which is somehow thin, the usual slenderness (span/thickness ratio) ranging between 20 and 50. Despite this relative slenderness, given that the shape enters the second-order pde with its Hessian, even small changes of the shape of S in a neighbourhood of the middle surface, may alter sensibly the solution in terms of F , that is, of the resulting stresses.

2. Outline of the method

The unilateral restrictions require that the membrane surface lies in between the extrados and intrados surfaces of the vault and that the stress function be concave. Such last constraint is, in general, not satisfied on a given shape for given loads: in such a case, the shape has to be modified to fit the constraint. In a sense, the unilateral assumption renders the membrane an underdetermined structure that must adapt its shape in order to satisfy the unilateral restrictions. The search for a feasible stress state on a convenient membrane surface has been conducted so far iteratively by trial and error; this sort of manual procedure, based on a skillful ansatz either on the initial shape (that is, on the function f describing S) or on the initial projected stress (that is, on F), requires a substantial effort and may be unrewarded. Therefore, the main object of the present work is to produce a computer code that can handle numerically the interplay of the shape f and the stress potential F by developing a convergent optimization scheme capable of producing a safe state under the given material and geometrical constraints, namely the concavity of F and the inclusion of f within the masonry.

The way we propose here for constructing a convergent iterative scheme, stems from the variational approximation of the transverse equilibrium equation, obtained by discretizing both the shape f and the stress potential F on the same grid. On adopting a simplicial representation of both surfaces, the curvature of these surfaces is singular, and an efficient method of approximating the Hessian is required; we adopt a lumped stress method (LSM) type approximation (see [Fraternali et al. 2002a]). One may start the iterative procedure by giving either an initial tentative simplicial shape f^0 or a tentative simplicial stress potential F^0 . If f^0 is assigned and the boundary values F^* of F are prescribed, the solution of the approximate variational equation will give a corresponding potential $F(f^0, F^*)$, balanced with the transverse loads. Since the problem at hand is linear, it can be formalized as

$$A(f^0)F = b(F^*), \quad (1)$$

$A(f^0)$ being a linear operator. By solving for F one obtains

$$F(f^0, F^*) = A^{-1}(f^0) b(F^*). \quad (2)$$

An objective function $\text{Conc}(F)$, measuring the degree of concavity of the stress potential $F(f^0, F^*)$ over the domain, can be introduced. By assuming that the shape f^0 is fixed and the boundary data F^* are unknown, if one makes explicit $\text{Conc}(F)$ in terms of F^* , say $C(F^*) = \text{Conc}(A^{-1}(f^0) b(F^*))$, the optimum problem for the objective function $C(F^*)$, can be formulated, and the best choice for the datum F^* for the given discretization and the given shape f^0 can be determined. If the resulting solution F_{opt} is concave, the iterative procedure stops, otherwise, the stress potential F_{opt} is concavified into a new concave stress potential F^0 with a convex hull type technique; the resulting stress potential F^0 is

used as the starting point for a second step in which the roles of f and F are interchanged. In this second step, the objective function to be optimized in terms of the boundary state f^* is changed into a norm of the distance of the form f from the mean surface.

3. Equilibrium formulation

3.1. Geometry. The geometry of a vault can be described by its intrados and extrados surfaces and by the geometry of the filling. With our model, it is assumed that the load applied to the vault is carried by a membrane structure S of thickness s . The geometry of the membrane S is not fixed, in the sense that it can be displaced and distorted, provided that it lays inside the masonry. The surface S that we consider, is continuous but not necessarily smooth, and to describe it we can adopt Monge representation.

The unit vectors associated to the fixed Cartesian reference system are denoted as $\{\hat{e}_1, \hat{e}_2, \hat{e}_3\}$. The position vector \mathbf{x} of a point of the surface is given by

$$\mathbf{x} = x_1 \hat{e}_1 + x_2 \hat{e}_2 + f(x_1, x_2) \hat{e}_3, \quad \{x_1, x_2\} \in \Omega, \quad (3)$$

where Ω is a plane two-dimensional connected domain, called the planform of S , whose boundary $\partial\Omega$ is composed of a finite number of closed curves, of outer normal \mathbf{n} ; $\{x_1, x_2\}$ are the Cartesian coordinates of S in the planform Ω , and the curvilinear coordinates on S ; $x_3 = f(x_1, x_2)$ is the rise of the membrane with $f \in C^0(\Omega)$.

A three-dimensional view of S is shown in Figure 1 (left). A couple of coordinate lines x_1 and x_2 are depicted in Figure 1, along with a magnified view of a differential element of the shell bounded by arcs of coordinate lines (Figure 1, right). The membrane is loaded by the external forces \mathbf{q} per unit area of S and held in equilibrium by the membrane stresses \mathbf{T} (for the components of \mathbf{T} see Figure 1, right). The natural or covariant base vectors \mathbf{a}_i tangent to S are represented in Figure 1 (middle). With \mathbf{a}_i we denote the dual bases.

3.2. Membrane equilibrium in Pucher form. Here we follow essentially the developments contained in [Fortunato et al. 2014], repeating the essential ingredients of the analysis only for completeness. The generalized membrane stress on S is defined by the surface stress tensor \mathbf{T} , represented in the covariant base as

$$\mathbf{T} = T^{\alpha\beta} \mathbf{a}_\alpha \otimes \mathbf{a}_\beta. \quad (4)$$

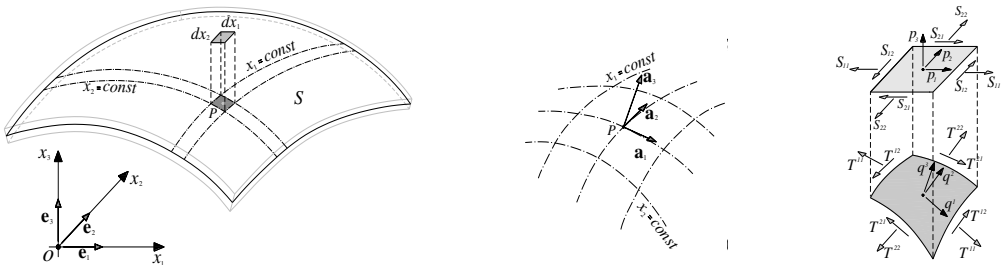


Figure 1. Membrane and surface stresses (left), covariant basis (middle), shell element and stresses (right).

In (4), $T^{\alpha\beta}$ are the contravariant components of \mathbf{T} and the summation convention over repeated Greek indices: $\alpha, \beta, \gamma, \dots = 1, 2$, has been adopted. Contravariant components of stress are convenient but are nonphysical, and we will need to transform them into Cartesian ones in order to read more easily the results of the analysis.

In the equilibrium equations, the divergence of the generalized surface stress \mathbf{T} balances the load $\mathbf{q} = \{q_1, q_2, q_3\}$, defined per unit surface area on S :

$$\frac{\partial}{\partial x_\gamma} (T^{\alpha\beta} a_\alpha \otimes a_\beta) a^\gamma + \mathbf{q} = \mathbf{0}. \quad (5)$$

The most efficient way to describe membrane equilibrium of a thin shell under a load \mathbf{q} is due essentially to Pucher [1934]. The generalized contravariant stress components $T^{\alpha\beta}$ on the membrane surface are transformed into projected stress components $S_{\alpha\beta} = J T^{\alpha\beta}$ in the planform, being $J = \sqrt{1 + f_{,1}^2 + f_{,2}^2}$ the *Jacobian* determinant, that is, the ratio between the differential surface area on S and its projection on the planform Ω . Denoting $\mathbf{p} = J\mathbf{q}$ the load per unit projected area. In the case of pure vertical loading $\mathbf{p} = \{0, 0, -p\}$, and the problem may be solved by introducing the *Airy stress function* $F(x_1, x_2)$ (here we assume only continuous surfaces) in the form

$$S_{11} = F_{,22}, \quad S_{22} = F_{,11}, \quad S_{12} = S_{21} = -F_{,12}. \quad (6)$$

The first two equilibrium equations are identically solved by (6), and we are left with a single equation in the transverse direction as reported with more details in [Gesualdo et al. 2014; Angelillo et al. 2013].

The transverse equilibrium equation corresponds to the balance of the vertical component of the force $p_3 = -p$ with the scalar product of the Pucher stress matrix times the Hessian of the function f in its covariant form. In terms of the Airy's stress function, it can be written as

$$F_{,22} f_{,11} + F_{,11} f_{,22} - 2F_{,12} f_{,12} = p. \quad (7)$$

3.3. Singular stress and the equilibrium of unilateral membranes. We describe the masonry as a continuum made of NRNT materials in the sense of Heyman, therefore the following material restrictions are imposed: the generalized stress \mathbf{T} is a negative semidefinite and does no work for the corresponding strain \mathbf{E} , that is, a positive semidefinite:

$$\mathbf{T} \in \text{Sym}^-, \quad \mathbf{E} \in \text{Sym}^+, \quad \mathbf{T} \cdot \mathbf{E} = 0. \quad (8)$$

The first application of Pucher's transformation for NT masonry vaults can be found in [Angelillo and Fortunato 2004], where it is shown that, due to the NT constraint, both the surface stress tensor and the matrix of the projected stresses must be negative semidefinite. In terms of the stress function F , this condition can be written as

$$F_{,11} + F_{,22} \leq 0, \quad F_{,11} F_{,22} - F_{,12}^2 \geq 0, \quad (9)$$

hence $F(x_1, x_2)$ is concave.

If F is only continuous, it may exhibit folds; if so, the projected stress is a line Dirac delta with support along the projection Γ of the fold on Ω . The *Hessian* \mathbf{H} of F is singular transversely to Γ , namely a uniaxial singular part parallel to the unit vector \mathbf{h} normal to Γ . Correspondingly the directional derivative

of F in the direction of \mathbf{h} , denoted F_h , presents a jump. Therefore, the singular part of the Hessian \mathbf{H} of F can be written as

$$\mathbf{H}_s = \delta(\Gamma) \Delta F_h \mathbf{h} \otimes \mathbf{h}, \quad (10)$$

$\delta(\Gamma)$ being the unit line Dirac delta on Γ and ΔF_h the jump of slope along the direction \mathbf{h} . Due to the relation (6), the singular part of the projected stress, corresponding to F , is a line Dirac delta on Γ of the form

$$\mathbf{S}_s = \delta(\Gamma) \Delta F_h \mathbf{k} \otimes \mathbf{k}, \quad (11)$$

where \mathbf{k} is the unit vector tangent to Γ . The concavity of F implies the concavity of the fold Γ . Then ΔF_h is negative and the corresponding projected singular stress concentrated on Γ is compressive.

As a consequence of the previous analysis, the equilibrium problem for the unilateral membrane S , under pure vertical loading, consists in finding a concave stress function $F(x_1, x_2)$ satisfying equation (7), with boundary conditions of Dirichlet or Neumann type, namely

$$F(x_1(s), x_2(s)) = g(s), \quad \text{or} \quad \frac{dF}{dn}(x_1(s), x_2(s)) = h(s), \quad \text{on } \partial\Omega, \quad (12)$$

s being the parametrization of the boundary $\partial\Omega$ with the arc length, and $g(s)$, $h(s)$ the contact internal moment and axial force produced by the allied tractions, on a 1D beam structure having the shape of the curve $\partial\Omega$. We also notice that the normal and shear components σ , τ of the tractions applied along the boundary, can be defined in terms of the boundary data g , h , as

$$\sigma(s) = g_{/ss}(s), \quad \tau(s) = h_{/n}(s), \quad (13)$$

where $/$ denotes the covariant derivative with respect to s , n along the boundary.

4. Computational scheme

4.1. Simplicial approximation of f^0 . To illustrate the procedure, we consider two examples: a cloister vault and a domical vault, both based on a rectangular planform Ω . As initial shape function f^0 , an approximation of the middle surface of the vault, obtained by discretizing the Monge description of this surface over a triangular grid (described below), is considered (Figure 2).

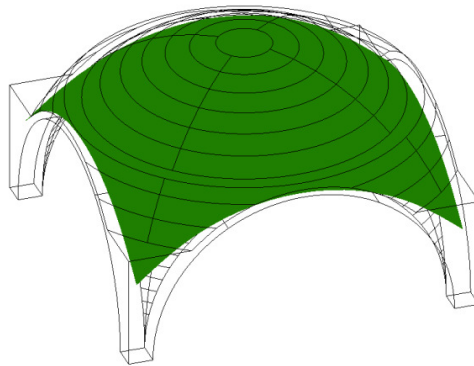


Figure 2. Initial choice for the shape function.

4.2. Variational formulation of the equilibrium. For approximating the solution of the equilibrium problem, we refer to the variational formulation of equation (7). As can be seen in [Giaquinta and Giusti 1985] and more specifically for vaults in [Angelillo and Fortunato 2004] and [Fraternali 2010], we impose the stationarity of the functional:

$$E(F) = \frac{1}{2} \int_{\Omega} a_{\alpha\beta} F_{,\alpha} F_{,\beta} da + \int_{\Omega} p F da, \quad (14)$$

where the matrix $\{a_{\alpha\beta}\}$ is the $\pi/2$ rotation of the Hessian \mathbf{H} of f^0 .

Indeed, it is easy to show that equation (8)₃ can be obtained as the Euler equation associated to the condition

$$\delta E(F) = 0, \quad (15)$$

if Dirichlet type boundary conditions are considered.

4.3. Definition of the meshes. The region Ω is discretized considering two complementary and overlapping meshes, the primal mesh: $\Pi_M = \{\Omega_i, i \in 1, \dots, M\}$, M being the number of triangular elements of the mesh (Figure 3, left), and the dual mesh: $\Pi_N = \{\Omega_i, i \in 1, \dots, N\}$, N being the number of elements of the dual mesh, that is, the number of nodes of the primal mesh (Figure 3, right). In our examples, the primal mesh is a regular triangular mesh, the dual mesh is formed by equal hexagons whose centroids are the nodes of the primal mesh. The skeleton of the primal mesh is used to approximate the stress field through uniaxial singular stresses while the dual mesh is used to average such singularities in the neighborhood of each primal node with an LSM-type approximation (see [Fraternali et al. 2002a]). In this way the final description of the stress field is a piecewise constant field over the dual mesh.

In order to allow the calculation of both the Hessian \mathbf{H} of f and F on the boundary of the vault, we enlarge the domain for the two meshes with respect to the actual planform. To this end, a one element strip of fictitious elements is added all around the original domain. Therefore, we have an additional mesh: $\Pi'_{M'} = \{\Omega_i, i \in 1, \dots, M'\}$, M' being the number of triangular elements of the fictitious part of the mesh.

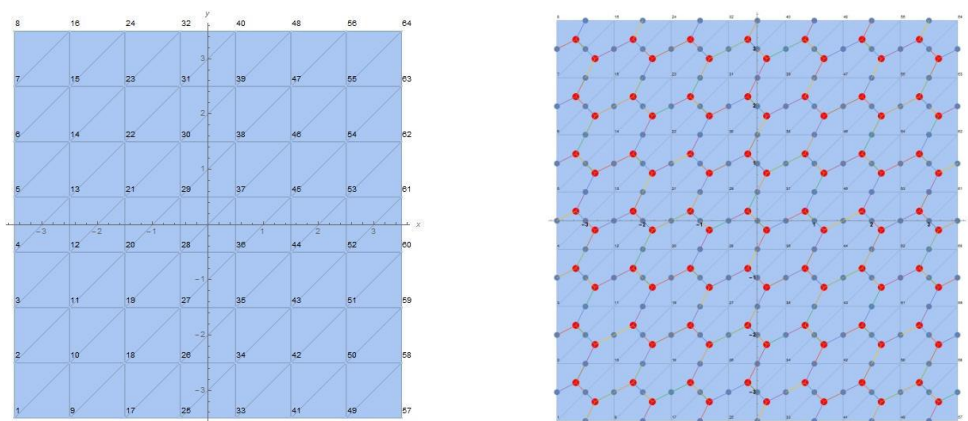


Figure 3. Primal mesh (left) and dual mesh (right) for the mesh 1.

4.4. Approximation of the curvature of f^0 . Once the initial shape f^0 is chosen and approximated over the given triangular grid, we use the same mesh to discretize problem (15). The surface S^0 (and any other surface S obtained during the iteration process) is piecewise linear, the simplicial surface being generated by the list as the values that f^0 takes at the nodes of the primal mesh:

$$\hat{S}^0 = \{x_1(i), x_2(i), f^0(i)\}, \quad i \in \{1, 2, \dots, N\}. \quad (16)$$

We also introduce the list of nodal values:

$$\hat{f}^0 = \begin{Bmatrix} f^0(1) \\ f^0(2) \\ \dots \\ f^0(N) \end{Bmatrix}. \quad (17)$$

The Hessian of f^0 is singular, being represented by line Dirac deltas $\delta(\Gamma)$, applied along the skeleton of the mesh. Such singular field is transformed into a piecewise constant field over the dual mesh through a LSM type approximation scheme as

$$H(\hat{f}^0)_j = \frac{\sum_i \Delta f^0(i) l(i) \hat{\mathbf{h}}(i) \otimes \hat{\mathbf{h}}(i)}{\text{area}(\hat{\Omega}_j)}, \quad j \in \{1, 2, \dots, N\}, \quad i \in \{1, 2, \dots, m_j\}, \quad (18)$$

$\Delta f^0(i)$ being the jump of the gradient of f across the edge i , in the direction orthogonal to the edge, and $l(i)$ the length of the edge i , $\hat{\mathbf{h}}(i)$ the unit normal vector of the edge i , m_j the number of the edges of the dual element at the generic node j (in our case, $m_j = 6$ for the inner nodes).

To reduce the apparent anisotropy effect introduced by the mesh, especially for rough discretizations, we consider two different primal meshes (mesh 1, mesh 2) characterized by opposite diagonals. The final solution, reached at the end of each step of the iteration, will then be averaged by combining linearly the results obtained by employing mesh 1 and mesh 2. To completely formulate the discretized problem, we have to impose the boundary conditions for the stress function F .

4.5. Variational approximation of ∇F . The gradient list associated to the primary mesh is defined by

$$\nabla F = \begin{Bmatrix} \begin{bmatrix} F_{,1} \\ F_{,2} \end{bmatrix}_1 \\ \begin{bmatrix} F_{,1} \\ F_{,2} \end{bmatrix}_2 \\ \dots \\ \begin{bmatrix} F_{,1} \\ F_{,2} \end{bmatrix}_M \end{Bmatrix}, \quad (19)$$

denoting 1, 2, 3 the nodes of a generic primal element, for each triangle the gradient is calculated as

$$\text{fun } F = F(1) + \alpha(F(2) - F(1)) + \beta(F(3) - F(1)), \quad \nabla F = \frac{\partial \text{fun } F}{\partial \alpha} \mathbf{b}^1 + \frac{\partial \text{fun } F}{\partial \beta} \mathbf{b}^2, \quad (20)$$

where $\mathbf{b}^1, \mathbf{b}^2$ are the base vector dual to the vectors $\mathbf{b}_1, \mathbf{b}_2$ shown in Figure 4 and $F(i)$ the values that the stress function assumes at the nodes of the considered triangle (see Figure 4).

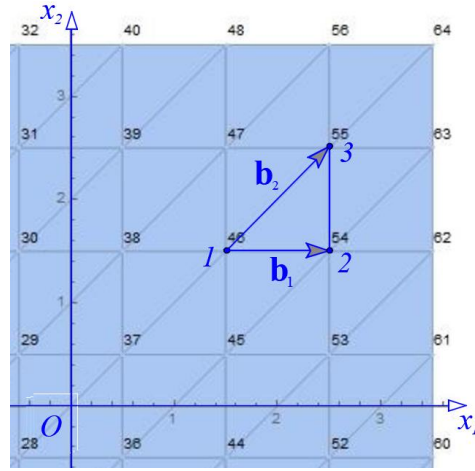


Figure 4. Natural element base.

4.6. Dirichlet data. We choose Dirichlet type boundary conditions considering the value of F at the boundary. In particular, we approximate σ (see (16)₁) with a polynomial expression:

$$\sigma = a_0 + c_1 x_1^2 + c_1 x_2^2 + c_2 x_1^4 + c_2 x_2^4 + c_3 x_1^6 + c_3 x_2^6, \quad (21)$$

from which F^* can be obtained by integrating (13).

4.7. Energy in discrete form. From (14) we obtain a linear problem for F in the form (1) as described below. Considering the discretization on the mesh, equation (14) can be transformed into

$$E(F) = \frac{1}{2} \sum_{n=1}^N a_{\alpha\beta}(n) F_{,\alpha}(n) F_{,\beta}(n) + \sum_{n=1}^N p(n) F(n). \quad (22)$$

4.8. Stationarity in discrete form. Considering condition (15), we obtain

$$\sum_{n=1}^N a_{\alpha\beta}(n) F_{,\beta}(n) + p(n) = 0. \quad (23)$$

A system of the form (1) can be obtained from (23) considering that the matrix A is the coefficient matrix of F for the internal part of the mesh, that is the part where the values of F are unknown, and the vector b is the coefficient vector of $F^* = F/\partial\Omega$ to which the load p is subtracted.

For the evaluation of the term $\sum_{n=1}^N a_{\alpha\beta}(n) F_{,\beta}(n)$ in (23), we considered for each node:

$$a_{\alpha\beta} F_{,\alpha} F_{,\beta} = \frac{\hat{f}^0_{,22} \sum_m F_{,1} F_{,1} + \hat{f}^0_{,11} \sum_m F_{,2} F_{,2} + 2\hat{f}^0_{,12} \sum_m F_{,1} F_{,2}}{\text{area}(\Omega_j)}, \quad j \in \{1, 2, \dots, n\}, \quad (24)$$

where $\hat{f}^0_{,ij}$ is the Hessian matrix at the node, and $F_{,\alpha}$, $F_{,\beta}$ are the covariant component of the gradient of F evaluated in the triangular element of the mesh that are partially included in the dual element of the node (Figure 5).

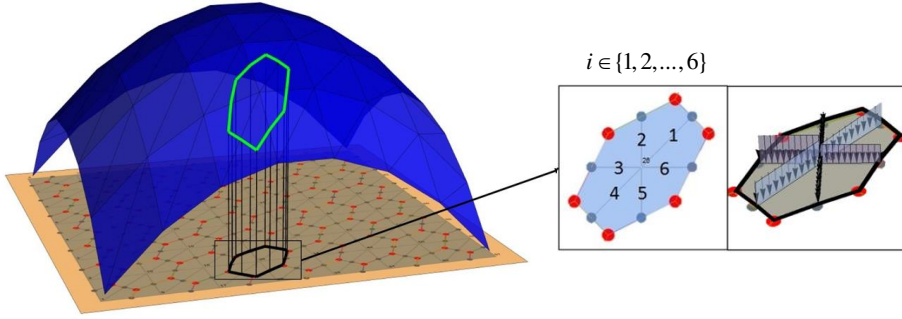


Figure 5. Curvature approximation.

4.9. Stress optimization. To find the best equilibrium solution, the boundary values will be selected by an optimization procedure. The optimization function density we select, encouraging the concavity of the stress function, is (see [Figure 6](#))

$$\Psi(x_1, x_2) = \begin{cases} 0 & x_1 \leq 0, x_2 \leq 0 \\ x_1^2 & x_1 > 0, x_2 < 0 \\ x_2^2 & x_1 < 0, x_2 > 0 \\ x_1^2 + x_2^2 & x_1 > 0, x_2 > 0, \end{cases} \quad (25)$$

with

$$x_1 = \frac{H_{11} + H_{22}}{2} + \sqrt{\left(\frac{H_{11} + H_{22}}{2}\right)^2 + H_{12}^2}, \quad x_2 = \frac{H_{11} + H_{22}}{2} - \sqrt{\left(\frac{H_{11} + H_{22}}{2}\right)^2 + H_{12}^2}, \quad (26)$$

where H_{ij} are the components of the Hessian of the stress function F .

The objective function to minimize is

$$\Phi_F = \int_{\Omega} \Psi(x_1, x_2) d\Omega. \quad (27)$$

The smaller the value found during the optimization process, the more the Hessian matrix will be closer to being a negative semidefinite matrix. In [Figure 6](#) the objective function is depicted.

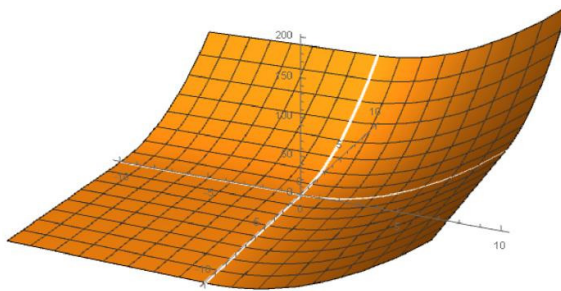


Figure 6. Density $\Psi(x_1, x_2)$ of the objective function Φ_F .

By means of equation (2) we can evaluate the stress function F . Having adopted two different meshes, two stress functions are obtained. Therefore, F will be evaluated by superimposing these two functions. If the deducted stress function is concave, then the vault is purely compressed and the current solution is accepted. Otherwise, we start a new iteration process considering the form function as the unknown. With a similar procedure as described above by changing the role of the form and of the stress function, a new form is obtained. In this case, the objective function to be optimized is

$$\Phi_f = \int_{\Omega} (f - f^0)^2 d\Omega, \quad (28)$$

that is, the mean squared deviation from the middle surface.

5. Examples

To illustrate the method, we consider two simple examples: a cloister vault and a cross vault.

5.1. Cloister vault. The optimization procedure exposed in Section 4 is adapted for the cloister vault starting with an initial form, that is, the middle surface of the vault structure in Figure 7 (see [Angelillo et al. 2013]):

$$f^0 = \begin{cases} \frac{L}{R} \sqrt{R^2 - x_1^2}, & |x_1| \geq |x_2|, \\ \frac{L}{R} \sqrt{R^2 - x_2^2}, & |x_1| < |x_2|, \end{cases} \quad (29)$$

taking the geometrical parameters $L = 5$ and $R = 5.5$ as the dimensions of the square planform and the apical rise of the cloister vault.

Two primal meshes of the form (see Figure 3) are introduced on the planform with $e = 0.5$. The domain of the vault and the meshes are extended with a strip of elements of width 0.5 on all sides. The applied transverse load is uniform with $p = -1$. By using the objective function (25), the optimization process at the first iteration gives $\Phi_F = 236$. By means of equation (2) we obtain the stress functions associated to the two primal meshes (Figure 8).

Superimposing linearly the two stress functions, we have the resulting stress function (Figure 9, left). By taking the convex hull, we transform this surface into a concave function (Figure 9, right).

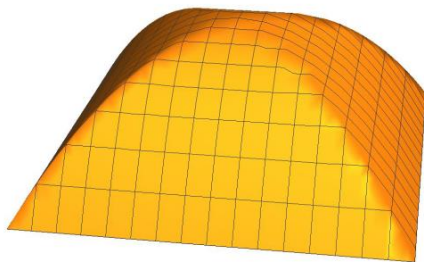


Figure 7. Starting form function f^0 .



Figure 8. Stress functions due to mesh 1 and mesh 2.

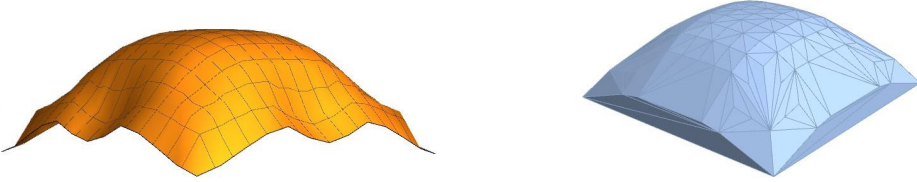


Figure 9. Optimized stress function F^0 related to f^0 (left) and its convex hull result (right).

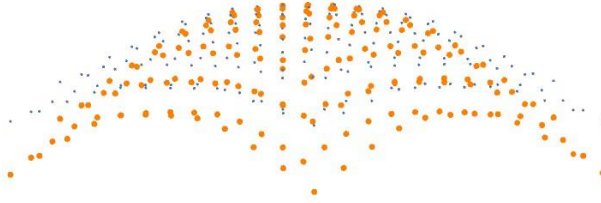


Figure 10. Initial convexified stress function (light blue points), and final stress function considering the uniform load superposition (orange points).

To avoid flat areas, where the curvature vanishes (giving possible numerical problems in the subsequent evaluations) we increase the stress function by a uniform pressure tuned by coefficient β :

$$F_{\text{new}} = F - \left[\frac{1}{2} \beta F_{\text{med}} (x_1^2 + x_2^2) \right]. \quad (30)$$

In particular, we take $\beta = 0.1$.

In [Figure 10](#), the stress function obtained after the convex hull and the uniform load superposition, is compared with the one corresponding to the convex hull procedure. In [Figure 11](#) (left) the final stress function is depicted.

In the second step, this stress function F is considered as assigned and the form function f as the unknown. In this phase, the optimization function (28) is considered. As a result of the optimization we have, in this case, $\Phi_f = 18$. The results for the optimized form function are displayed in [Figure 11](#) (right). In [Figure 12](#) (left) such surface is compared with the starting shape f .

To improve the result, a new optimization cycle is performed. The new optimization cycle on the stress functional (27) gives $\Phi_F = 186$ and after the convex hull, the final stress function of [Figure 12](#) (right) that we use for the evaluation of the form function is obtained.

Therefore, a new iteration adopting the optimization functional (28), whose unknown is the form function, is executed. Performing the optimization, we get $\Phi_f = 2$. As a result, [Figure 13](#) (left) shows

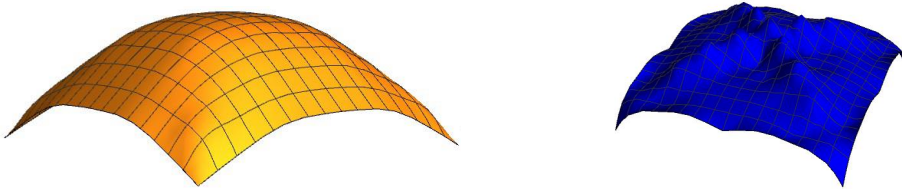


Figure 11. Left: final stress function at step 1. Right: optimized form function.

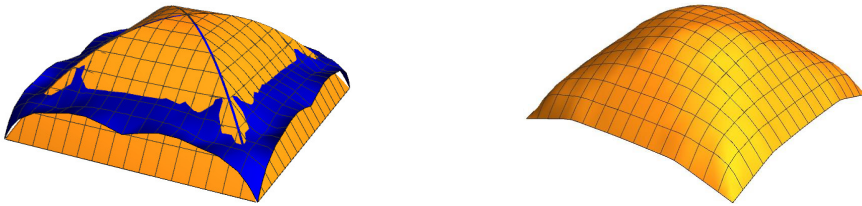


Figure 12. Left: comparison between the new form function (blue) and the starting form f^0 . Right: final stress function after at step 2.

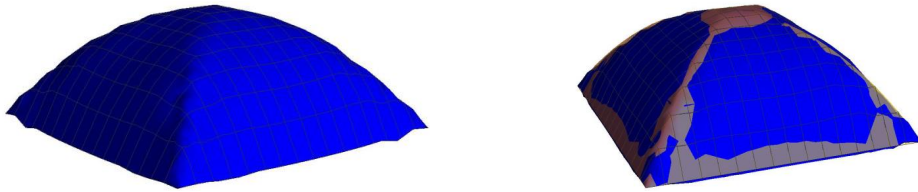


Figure 13. Left: final form function. Right: comparison between the final form function (blue) and the starting form f^0 .

the final optimized form, while in [Figure 13](#) (right) this surface is compared with the starting surface. We can observe that the form function is very close to the surface of the vault and that a tolerance value of less than 0.1 is verified at each point. Finally, [Figure 14](#) shows the envelope field of the principal direction of stress corresponding to the final stress function represented in [Figure 12](#) (right).

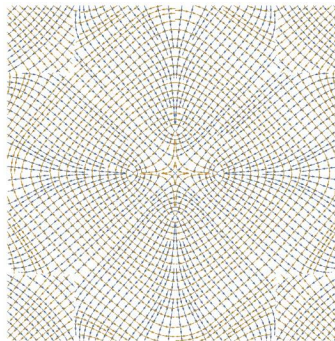


Figure 14. Principal stress lines.

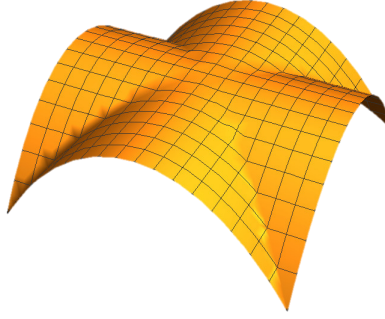


Figure 15. Starting form function f^0 for the cloister vault.

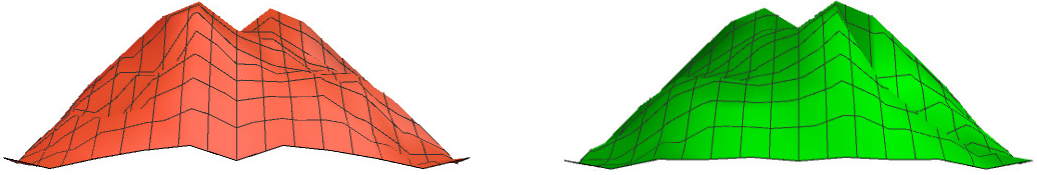


Figure 16. Stress functions due to mesh 1 and mesh 2.

5.2. Cross vault. As in the previous case, for the cross vault we choose the middle surface of the same vault as the initial shape from which starting the optimization process as in Figure 15, as exposed in [Angelillo et al. 2013]:

$$f^0 = \begin{cases} \frac{L}{R} \sqrt{R^2 - x_1^2}, & |x_1| < |x_2|, \\ \frac{L}{R} \sqrt{R^2 - x_2^2}, & |x_1| \geq |x_2|. \end{cases} \quad (31)$$

for the side and the radius of the vault we put $L = 5$ and $R = 7$.

The procedure for this example is similar to the previous one, therefore the main features and results will be summarized briefly in the following. We have two primal meshes with element size $e = 0.5$ and a transverse load $p = -1$. The optimization at the first step gives $\Phi_F = 291$. By using (2), the two stress functions corresponding to the two primal meshes are depicted in Figure 16. Superimposing them we obtain the stress function of Figure 17 (left). In Figure 17 (right) the stress function obtained through the convex hull procedure is shown.

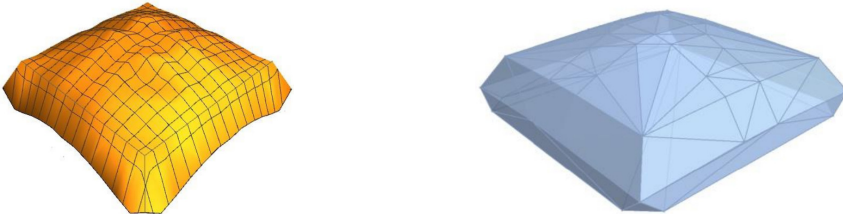


Figure 17. Left: optimized stress function F^0 associate to f^0 . Right: convex hull result of the stress function.

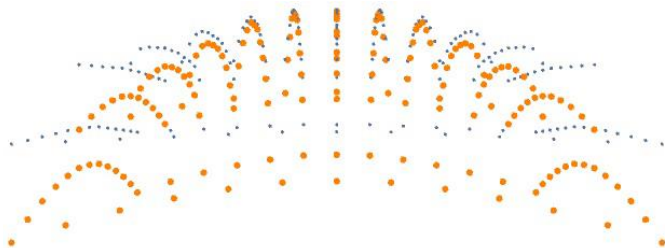


Figure 18. Initial convexified stress function (points in light blue), and final stress function considering the uniform load superposition (points in orange).

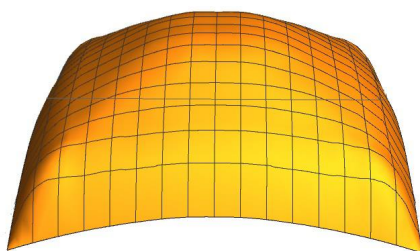


Figure 19. Final stress function at step 1.

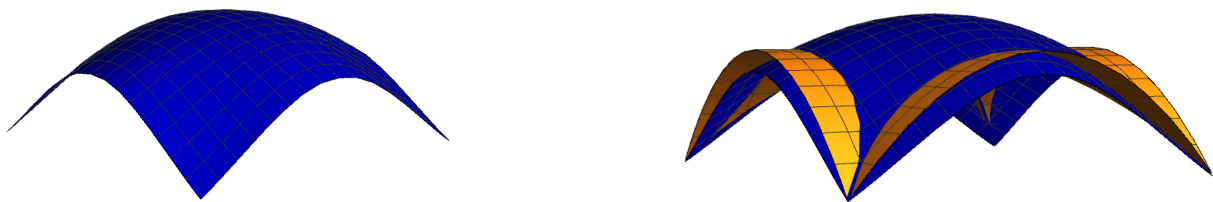


Figure 20. Left: optimized form function. Right: comparison between the new form function (in blue) and the initial one.

The flat areas are eliminated adding to the stress function a uniform pressure (see (30)) and taking $\beta = 0.1$. In Figure 18 the stress function obtained with the superposition is compared with the one derived through the convex hull. In Figure 19 the final stress function is depicted.

In the second step, the optimization of the function (28) gives $\Phi_f = 8$. The results obtained for the optimized form function are reported in Figure 20 (left); in Figure 20 (right), such form is compared with the starting shape f^0 .

The new optimization of the objective function (27) with respect to the stress function gives $\Phi_F = 256$, to which corresponds the stress function depicted in Figure 21.

The new optimization of the form function with respect to the objective function (28) gives $\Phi_f = 1$. The final optimized form is displayed in Figure 22 (left); the two forms are compared in Figure 22 (right). The isostatic stress lines corresponding to the final stress function are reported in Figure 23.

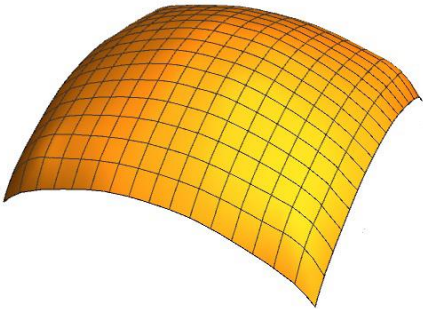


Figure 21. Final stress function at step 2 after concavification.

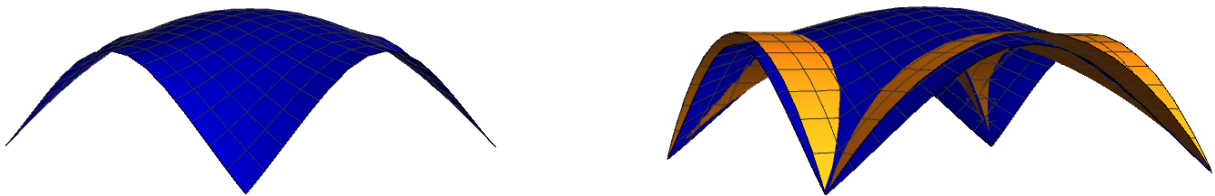


Figure 22. Left: final form function (left). Right: comparison between the final form function (blue) and the starting form f^0 .

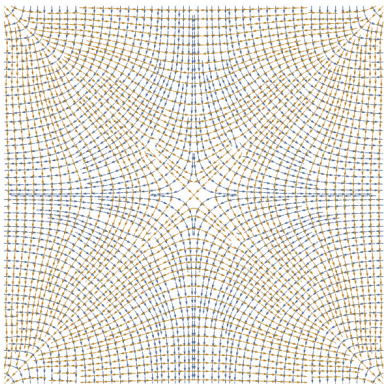


Figure 23. Principal stress lines.

6. Conclusions

The present work develops an automated numerical method for the analysis of thin masonry shells. The model of material adopted for masonry is the NRNT, for which the limit analysis theorems are still valid. Accordingly, the study focuses on the application of the static theorem to masonry vaults.

In detail, the proposed method is devoted to the automatic generation of a class of purely compressive stress regimes, which are balanced with the load. As a consequence, the structure is safe and members of this statically admissible stresses may be used to assess the geometric degree of safety of the structure and to estimate bounds on the thrust forces exerted by the structure on its boundary.

By taking up the simplified model of Heyman, the equilibrium problem for the membrane has been formulated in terms of projected stresses defined on the planform of the vault. The search for the stresses reduces to the solution of a second-order pde, in terms of the stress potential F . In order that the membrane stress on S be compressive, the potential F must be concave. As for the thrust line in an arch, the surface S is not fixed and may be changed, given that it remains inside the masonry.

Under these assumptions, the whole class of equilibrated stress regimes for a masonry shell, is obtained by moving and deforming S inside the masonry, and also, for any fixed shape, by changing the boundary data for F , that is the distribution of thrust forces along the boundary. The unilateral NT condition require that F lies in between the extrados and intrados surfaces of the vault and that be moreover concave. Such last constraint is, in general, not satisfied on a given shape for given loads. In such a case, the shape has been modified to fit the constraint.

The search for a feasible stress state on a convenient membrane surface, has been conducted so far iteratively, by trial and error; this sort of manual procedure, based on a skillful ansatz either on the initial shape (that is, on f) or on the initial projected stress (that is, on F), requires a substantial effort and may be unrewarded.

Thus, the development of a computer code capable of handling numerically the interplay of the shape f and the stress potential F , has been the main object of the present work.

In particular, in the present work, the cases of cloister and cross vaults are considered as examples of application of the method. For such a special case, easy and efficient methods to evaluate the equilibrium do not exist, and the simplified slicing technique gives rather inaccurate estimates of the geometrical factor of safety. The proposed method, in these simple cases, appears to be rather efficient.

References

- [Angelillo 2014] M. Angelillo, “Practical applications of unilateral models to Masonry equilibrium”, pp. 109–210 in *Mechanics of masonry structures*, vol. 551, edited by M. Angelillo, Springer, Vienna, 2014.
- [Angelillo 2015] M. Angelillo, “Static analysis of a Guastavino helical stair as a layered masonry shell”, *Compos. Struct.* **119** (2015), 298–304.
- [Angelillo 2016] M. Angelillo, “The equilibrium of helical stairs made of monolithic steps”, *Int. J. Archit. Herit.* **10**:6 (2016), 675–687.
- [Angelillo and Fortunato 2004] M. Angelillo and A. Fortunato, “Equilibrium of masonry vaults”, pp. 105–111 in *Novel approaches in civil engineering: lecture notes in applied and computational mechanics*, vol. 14, edited by M. Frémond and F. Maceri, Springer, Berlin, Heidelberg, 2004.
- [Angelillo et al. 2010] M. Angelillo, L. Cardamone, and A. Fortunato, “A numerical model for masonry-like structures”, *J. Mech. Mater. Struct.* **5**:4 (2010), 583–615.
- [Angelillo et al. 2013] M. Angelillo, E. Babilio, and A. Fortunato, “Singular stress fields for masonry-like vaults”, *Contin. Mech. Therm.* **25**:2-4 (2013), 423–441.
- [Angelillo et al. 2014] M. Angelillo, A. Fortunato, A. Montanino, and M. Lippiello, “Singular stress fields in masonry structures: Derand was right”, *Meccanica (Milano)* **49**:5 (2014), 1243–1262.
- [Angelillo et al. 2016] M. Angelillo, E. Babilio, A. Fortunato, M. Lippiello, and A. Montanino, “Analytic solutions for the stress field in static sandpiles”, *Mech. Mater.* **95** (2016), 192–203.
- [Block 2009] P. Block, *Thrust network analysis: exploring three-dimensional equilibrium*, PhD dissertation, Dept. of Architecture, Massachusetts Institute of Technology, Cambridge, USA, 2009, Available at <https://dspace.mit.edu/handle/1721.1/49539>.

- [Block and Lachauer 2014] P. Block and L. Lachauer, “Three-dimensional funicular analysis of masonry vaults”, *Mech. Res. Commun.* **56** (2014), 53–60.
- [Block et al. 2006] P. Block, T. Ciblac, and J. Ochsendorf, “Real-time limit analysis of vaulted masonry buildings”, *Comput. Struct.* **84**:29-30 (2006), 1841–1852.
- [Brandonisio et al. 2015] G. Brandonisio, E. Mele, and A. De Luca, “Closed form solution for predicting the horizontal capacity of masonry portal frames through limit analysis and comparison with experimental test results”, *Eng. Fail. Anal.* **55** (2015), 246–270.
- [Bruggi and Taliercio 2015] M. Bruggi and A. Taliercio, “Analysis of no-tension structures under monotonic loading through an energy-based method”, *Comput. Struct.* **159** (2015), 14–25.
- [Calladine 2005] C. R. Calladine, “Preliminary structural analysis of a Guastavino spiral staircase shell”, in *Essays in the history of the theory of structures, in honour of Jacques Heyman*, Instituto Juan de Herrera, Madrid, 2005.
- [Cennamo et al. 2017] C. Cennamo, M. Angelillo, and C. Cusano, “Structural failures due to anthropogenic sinkholes in the urban area of Naples and the effect of a FRP retrofitting”, *Compos. B Eng.* **108** (2017), 190–199.
- [Como 1992] M. Como, “Equilibrium and collapse analysis of masonry bodies”, *Meccanica (Milano)* **27**:3 (1992), 185–194.
- [De Goes et al. 2013] F. De Goes, P. Alliez, H. Owahdi, and M. Desbrun, “On the equilibrium of simplicial masonry structures”, *ACM Trans. Graph.* **32**:4 (2013), article 93.
- [De Serio et al. 2018] F. De Serio, M. Angelillo, A. Gesualdo, A. Iannuzzo, G. Zuccaro, and M. Pasquino, “Masonry structures made of monolithic blocks with an application to spiral stairs”, *Meccanica (Milano)* **53**:8 (2018), 2171–2191.
- [DeJong and Dimitrakopoulos 2014] M. J. DeJong and E. G. Dimitrakopoulos, “Dynamically equivalent rocking structures”, *Earthq. Eng. Struct. Dyn.* **43**:10 (2014), 1543–1563.
- [Fortunato et al. 2014] A. Fortunato, F. Fraternali, and M. Angelillo, “Structural capacity of masonry walls under horizontal loads”, *Ing. Sismica* **31**:1 (2014), 41–49.
- [Fortunato et al. 2016] A. Fortunato, E. Babilio, M. Lippiello, A. Gesualdo, and M. Angelillo, “Limit analysis for unilateral masonry-like structures”, *Open Construct. Build. Technol. J.* **10**:Suppl 2: M12 (2016), 346–362.
- [Fortunato et al. 2018] A. Fortunato, F. Fabbrocino, M. Angelillo, and F. Fraternali, “Limit analysis of masonry structures with free discontinuities”, *Meccanica (Milano)* **53**:7 (2018), 1793–1802.
- [Fraternali 2010] F. Fraternali, “A thrust network approach to the equilibrium problem of unreinforced masonry vaults via polyhedral stress functions”, *Mech. Res. Commun.* **37**:2 (2010), 198–204.
- [Fraternali et al. 2002a] F. Fraternali, M. Angelillo, and A. Fortunato, “A lumped stress method for plane elastic problems and the discrete-continuum approximation”, *Int. J. Solids Struct.* **39**:25 (2002), 6211–6240.
- [Fraternali et al. 2002b] F. Fraternali, M. Angelillo, and G. Rocchetta, “On the stress skeleton of masonry vaults and domes”, in *Proceedings of the Seventh Pan American Congress of Applied Mechanics (PACAM VII)* (Temuco, Chile), 2002.
- [Gesualdo et al. 2014] A. Gesualdo, A. Iannuzzo, M. Monaco, and M. T. Savino, “Dynamic analysis of freestanding rigid blocks”, in *The Twelfth International Conference on Computational Structures Technology* (Naples, Italy), vol. 106, 2014.
- [Gesualdo et al. 2017] A. Gesualdo, C. Cennamo, A. Fortunato, G. Frunzio, M. Monaco, and M. Angelillo, “Equilibrium formulation of masonry helical stairs”, *Meccanica (Milano)* **52**:8 (2017), 1963–1974.
- [Gesualdo et al. 2018a] A. Gesualdo, A. Iannuzzo, V. Minutolo, and M. Monaco, “Rocking of freestanding objects: theoretical and experimental comparisons”, *J. Theor. Appl. Mech. (Warsaw)* **56**:4 (2018), 977–991.
- [Gesualdo et al. 2018b] A. Gesualdo, A. Iannuzzo, M. Monaco, and F. Penta, “Rocking of a rigid block freestanding on a flat pedestal”, *J. Zhejiang Univ. Sci. A* **19**:5 (2018), 331–345.
- [Giaquinta and Giusti 1985] M. Giaquinta and E. Giusti, “Researches on the equilibrium of masonry structures”, *Arch. Ration. Mech. Anal.* **88**:4 (1985), 359–392.
- [Heyman 1966] J. Heyman, “The stone skeleton”, *Int. J. Solids Struct.* **2**:2 (1966), 249–279.
- [Heyman 2012] J. Heyman, “The membrane analysis of thin masonry shells”, *Nuts Bolts Construct. Hist.* **1** (2012), 281–283.
- [Iannuzzo et al. 2018] A. Iannuzzo, M. Angelillo, E. De Chiara, F. De Guglielmo, F. De Serio, F. Ribera, and A. Gesualdo, “Modelling the cracks produced by settlements in masonry structures”, *Meccanica (Milano)* **53**:7 (2018), 1857–1873.

- [Kooharian 1952] A. Kooharian, “Limit analysis of voussoir (segmental) and concrete arches”, *J. Am. Concr. Inst.* **24**:4 (1952), 317–328.
- [Livesley 1978] R. K. Livesley, “Limit analysis of structures formed from rigid blocks”, *Int. J. Numer. Methods Eng.* **12**:12 (1978), 1853–1871.
- [Marmo and Rosati 2017] F. Marmo and L. Rosati, “Reformulation and extension of the thrust network analysis”, *Comput. Struct.* **182** (2017), 104–118.
- [Marmo et al. 2018] F. Marmo, D. Masi, and L. Rosati, “Thrust network analysis of masonry helical staircases”, *Int. J. Archit. Herit.* **12**:5 (2018), 828–848.
- [Miki et al. 2015] M. Miki, T. Igarashi, and P. Block, “Parametric self-supporting surfaces via direct computation of airy stress functions”, *ACM Trans. Graph.* **34**:4 (2015), article 89.
- [Monaco et al. 2014] M. Monaco, M. Guadagnuolo, and A. Gesualdo, “The role of friction in the seismic risk mitigation of freestanding art objects”, *Nat. Hazards* **73**:2 (2014), 389–402.
- [O’Dwyer 1999] D. W. O’Dwyer, “Funicular analysis of masonry vaults”, *Comput. Struct.* **73**:1-5 (1999), 187–197.
- [Pucher 1934] A. Pucher, “Über der spannungszustand in gekrümmten flächen”, *Beton u Eisen* **33** (1934), 298–304.
- [Vouga et al. 2012] E. Vouga, M. Höbinger, J. Wallner, and H. Pottmann, “Design of self-supporting surfaces”, *ACM Trans. Graph.* **31**:4 (2012), article 87.

Received 24 Mar 2019. Revised 3 Oct 2019. Accepted 18 Oct 2019.

ELENA DE CHIARA: elenadechiara@gmail.com

Department of Civil Engineering, University of Salerno, Via Giovanni Paolo II, 132, 84084 Fisciano, Italy

CLAUDIA CENNAO: claudia.cennamo@unicampania.it

Department of Architecture and Industrial Design, University of Campania “Luigi Vanvitelli”, 81031 Aversa, Italy

ANTONIO GESUALDO: gesualdo@unina.it

Department of Structures for Engineering and Architecture, University of Naples Federico II, Via Claudio 21 (buildings 6-7), 80125 Naples, Italy

ANDREA MONTANINO: andrea.montanino@polimi.it

Department of Structures for Engineering and Architecture, University of Naples Federico II, Via Claudio 21 (buildings 6-7), 80125 Naples, Italy

CARLO OLIVIERI: colivieri@unisa.it

Department of Civil Engineering, University of Salerno, Via Giovanni Paolo II, 132, 84084 Fisciano, Italy

ANTONIO FORTUNATO: a.fortunato@unisa.it

Dipartimento di Ingegneria Civile, University of Salerno, Via Giovanni Paolo II, 132, 84084 Fisciano, Italy

LIMIT ANALYSIS OF CLOISTER VAULTS: THE CASE STUDY OF PALAZZO CARACCILO DI AVELLINO

ANTONIO GESUALDO, GIUSEPPE BRANDONISIO, ANTONELLO DE LUCA,
ANTONINO IANNUZZO, ANDREA MONTANINO AND CARLO OLIVIERI

The equilibrium of cloister masonry vaults, treated as composed of unilateral material in the sense of Heyman, is the topic of the present work. For such a material, the safe and the kinematic theorems of limit analysis can be employed to detect equilibrium and nonequilibrium. In the spirit of the safe theorem, the structure is stable if a statically admissible stress field can be detected. On allowing for singular stresses, here we consider statically admissible stress fields concentrated on surfaces or lines lying inside the masonry vault. Such structures are unilateral membranes, whose geometry is described *a la Monge*, and the equilibrium of them is formulated in Pucher form, that is, in terms of the so-called projected stresses over the planform Ω . The problem, under purely parallel loads, is reduced to a single partial differential equation of the second-order, in two space variables, where the shape function f and the stress function F appear symmetrically. The unilateral restrictions require that the membrane surface S lies in between the extrados and intrados surfaces of the vault and that the stress function be concave. In the present work, by starting with a sensible choice of a concave stress function F , the transverse equilibrium equation is solved for f by imposing suitable boundary conditions. A cloister vault of *Palazzo Caracciolo di Avellino*, a XIV century building located along *via dell'Anticaglia* in Naples, is the case study. For two load conditions, membrane surfaces and geometrical safety factors are identified.

1. Introduction

The present work is concerned with the equilibrium of cloister masonry vaults, treated as composed of no-tension material in the sense of Heyman [1966]. For such a material the safe and the kinematic theorems of limit analysis can be employed to detect equilibrium and nonequilibrium, as originally shown in [Heyman 1966; Kooharian 1952; Livesley 1978] and most recently in [Como 1992; Angelillo 2015; 2019; Gesualdo et al. 2017; 2019; Angelillo et al. 2010; 2014; 2016; 2018; Fortunato et al. 2014; 2016; 2018; Brandonisio et al. 2013; 2015; Iannuzzo et al. 2018a; 2018c; 2018b].

The method that we apply here is the so-called membrane equilibrium analysis (MEA), originated in the papers on vaults [Angelillo and Fortunato 2004; Fraternali 2010; Fraternali et al. 2002; Angelillo et al. 2013]. The MEA can be seen as the continuous counterpart of the method called thrust network analysis, first proposed in a pioneering work by O'Dwyer [1999], and then developed in subsequent works in [Block et al. 2006; Block and Lachauer 2014; Vouga et al. 2012; De Goes et al. 2013; Miki et al. 2015; Marmo and Rosati 2017].

Keywords: limit analysis, vaults, masonry-like materials, Airy's stress function.

The classical Heyman hypotheses of null tensile strength, infinite compressive strength and no-sliding are the basis of the present approach, together with the static theorem of limit analysis. Statically admissible singular stress fields, in the form of surface and line Dirac deltas applied on material surfaces and lines are involved. The support lines Γ and surfaces S of these Dirac deltas can be interpreted as arches and membranes enclosed inside the vault thickness.

The unilateral assumption implies that the generalized stress on S be compressive, and restrict S to be located in between the extrados and intrados surfaces of the vault. Then, as in the case of the thrust line Γ that we can devise inside a plane arch, the ideal structure S is not fixed, but forms inside the masonry, in order to balance and transmit the external loads.

In the present paper, we essentially use the ideas put forward in [Angelillo and Fortunato 2004; Angelillo et al. 2013; Heyman 2012], by applying the method to cloister vaults of different geometry. The geometry of the membrane is described by means of a Monge representation and the equilibrium is expressed in Pucher form (see [Pucher 1934]). In this paper, by starting with a sensible choice of a restricted class of concave stress functions, the transverse equilibrium equation is solved for the shape by imposing suitable boundary conditions. In the flat part of the cloister vault, for example, the stress function F is considered quadratic because the projected stress is assumed constant. The case study of the cloister vaults of Palazzo Caracciolo di Avellino (an historical palace of Naples, whose basal part was built in the XIV century) is considered. Geometrical safety factors are computed for different cases of loading.

2. Mathematical preliminaries: Pucher stress

We study the equilibrium, under the action of given loads, of a membrane surface S contained inside the thickness of the shell.

The formulation of membrane equilibrium that we consider is essentially the one proposed by Pucher in his seminal paper [Pucher 1934], though here a more modern and straightforward formalism is adopted. The symmetry of the problem with respect to the two numeric functions of two variables controlling the shape and the stress is exploited by interchanging the role of data and unknowns with the aim of generating shapes for given stresses.

2.1. Geometry. The particular geometry of typical shells and domes allows for the representation, in Monge form, of a membrane surface S contained inside the structure, that is (see Figure 1)

$$\mathbf{x} = x_1 \hat{\mathbf{e}}_1 + x_2 \hat{\mathbf{e}}_2 + f(x_1, x_2) \hat{\mathbf{e}}_3, \quad (1)$$

where \mathbf{x} is the position vector of points of S , $\{\hat{\mathbf{e}}_1, \hat{\mathbf{e}}_2, \hat{\mathbf{e}}_3\}$ is the orthonormal triad coherent with a given Cartesian frame $\{O; x_1, x_2, x_3\}$, the couple (x_1, x_2) belongs to a region Ω of the plane $\{O; x_1, x_2\}$ called planform of S , and $f = f(x_1, x_2)$ is a smooth function of its arguments. Summation convention over repeated indices will be used throughout these notes, implying that Greek indices range over 1, 2 and Latin indices over 1, 2, 3.

2.2. Forces and equilibrium. We consider the equilibrium of S subject to a given, possibly nonuniform, load \mathbf{p} per unit projected area of S :

$$\mathbf{p} = -p \hat{\mathbf{e}}_3. \quad (2)$$

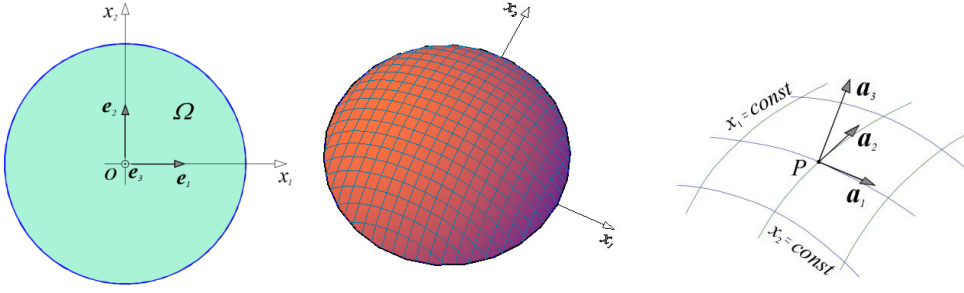


Figure 1. Monge representation of the membrane surface S of a spherical dome. Plan-form Ω (left), 3D view with curvilinear coordinates (x_1, x_2) (middle), and base vectors on S (right).

Calling \mathbf{T} the generalized surface stress (that is, the stress per unit length on S), that is, the membrane stress on S , we can express it in the form

$$\mathbf{T} = T^{\alpha\beta} \mathbf{a}_\alpha \otimes \mathbf{a}_\beta, \quad (3)$$

$T^{\alpha\beta}$ being the contravariant components of \mathbf{T} in the covariant base $\{\mathbf{a}_1, \mathbf{a}_2\}$ associated to the curvilinear coordinates (x_1, x_2) (see Figure 1). The pseudostresses $S_{\alpha\beta}$ (Pucher-stresses) can be introduced:

$$S_{\alpha\beta} = J T^{\alpha\beta}, \quad (4)$$

J being the ratio between the area on S and the corresponding projected area.

On introducing the stress potential F :

$$S^{11} = F_{,22}, \quad S^{22} = F_{,11}, \quad S^{12} = S^{21} = -F_{,12}, \quad (5)$$

the equilibrium problem is reduced to a single scalar equation in the unknown stress potential function F :

$$F_{,22} f_{,11} + F_{,11} f_{,22} - 2F_{,12} f_{,12} - p = 0. \quad (6)$$

The boundary condition for this partial differential equation can be either of the Dirichlet or of the Neumann type, that is,

$$F|_{\partial\Omega} = m, \quad \text{or} \quad \left. \frac{dF}{dn} \right|_{\partial\Omega} = -n, \quad (7)$$

or of any combination of the two on a partition of the boundary $\partial\Omega$.

2.3. Unilateral membranes and singular stresses. In the present study, we consider shells that are purely compressed under the effect of the loads. Then we assume that the generalized stress \mathbf{T} is negative semidefinite: $\mathbf{T} \in \text{Sym}^-$.

The first application of Pucher's transformation for compressed masonry vaults can be found in [Angelillo and Fortunato 2004], where it is shown that, due to the compression constraint, the matrix of the projected stress components $S^{\alpha\beta} = J T^{\alpha\beta}$ must be also negative semidefinite. In terms of the stress

function F , this condition transforms into

$$F_{,11} + F_{,22} \leq 0, \quad F_{,11} F_{,22} - F_{,12} F_{,12} \geq 0, \quad (8)$$

hence, the surface described by $F(x_1, x_2)$ must be concave.

We admit that $F(x_1, x_2)$ be only continuous, that is, F may be folded. In this case the projected stress is a line Dirac delta with support along the projection Γ of the fold. The *Hessian* \mathbf{H} of F is singular transversely to Γ , that is, it has a uniaxial singular part parallel to the unit vector \mathbf{h} normal to Γ . Correspondingly the directional derivative of F in the direction of \mathbf{h} , called F_h , presents a jump. Therefore, the singular part of the Hessian \mathbf{H} of F can be written as

$$\mathbf{H}_s = \delta(\Gamma) F_h \mathbf{h} \otimes \mathbf{h}, \quad (9)$$

$\delta(\Gamma)$ being the unit line Dirac delta on Γ . Analogously, the singular part of the corresponding projected stress (2) is a Dirac delta on Γ :

$$\mathbf{T}_s = \delta(T) F_h \mathbf{k} \otimes \mathbf{k}, \quad (10)$$

\mathbf{k} being the unit vector tangent to Γ . The concavity of F implies the concavity of the fold, then F_h is negative and the corresponding projected singular stress concentrated on Γ is compressive.

3. Equilibrium of cross and cloister vaults

The simplified equilibrium solution of a cross vault can be easily devised through the so-called slicing technique (see [Heyman 1995]). The vault is sliced into strips parallel to the boundary arches and meeting along the cross diagonals; such strips carry the load per unit area and transfer it as a load per unit length to two diagonal cross arches discharging it as a vertical and horizontal load thrust to the four columns (see Figure 2, left). The analytical MEA version of this simplified geometrical approach can be found in [Angelillo and Fortunato 2004; Contestabile et al. 2016].

The slicing technique, that is, a method to reduce a 3D problem to a plane analysis, is applied to cloister vault (for a discussion on the slicing method, see [Angelillo et al. 2013; Bloch and Ochsendorf 2007; Como 2013; Fang et al. 2019]). A schematic view of the planform of a typical cloister vault is depicted in Figure 2 (right). Indeed, in this case, the slices should be taken orthogonally to the flat boundary, but if these elementary arches are interrupted along the cross diagonals, they transfer to them a load that pushes these cross arches upward, which means the concentrated force along them must be tensile. If instead these parallel arches are not interrupted and are allowed to cross each other, they must be fitted, in their central part, within two flat parallel boundaries (see Figure 2, right), a condition that, to be satisfied, requires a large thickness in the upper 1/3 of the vault.

In order to optimize the equilibrium solution, we propose to slice the vault with nonparallel arches in the lower 2/3 of the vault, making the arches cross each other in the upper central part (see Figure 3, left). The mathematical construction through MEA of such equilibrium state is described in the following paragraphs.

3.1. Equilibrium on the planform. To generate an equilibrium state of compression into the vault, we start from the assumption of a particular equilibrated stress regime in the planform, corresponding to the partition of the planform into zones of uniaxial and biaxial stress fields (see Figure 3, left). Referring

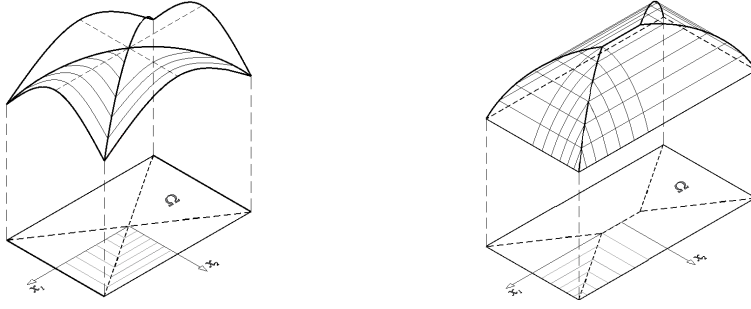


Figure 2. Slicing technique for simplified equilibrium solutions for cross vaults (left) and cloister vaults (right).

to this last figure for notations, Ω_2 is the uniaxial zone and Ω_1 is the zone where the projected stress is an uniaxial stress field along the directions of the segments reported pictorially in the figure. By calling $\pi/2 - \alpha$ the angle that each ray forms with the straight external boundary, in each of the four wedges forming the region Ω_2 the fan of these rays of uniaxial compression can be given, as a one-parameter family of directions in terms of an abscissa x specified along the boundary, as

$$\tan \alpha = g(x), \quad (11)$$

the function $g(x)$ being fixed in advance and x is the length along the boundary.

We introduce, in the wedge Ω_{21} (see Figure 3, right), and similarly in the other outer lower regions Ω_{2j} , a curvilinear reference system $\{\vartheta^1 = x, \vartheta^2 = y\}$ with the curvilinear lines (that are actually straight lines) directed as the rays:

$$x_1 = x + y g(x), \quad x_2 = y, \quad (12)$$

where x_1, x_2 are the coordinates in Ω_{21} .

The natural base vectors \mathbf{b}_1 and \mathbf{b}_2 tangent to the $\{\vartheta^1, \vartheta^2\}$ curvilinear lines, denoting with a prime differentiation of numeric functions with respect to their argument, in Cartesian components in the reference (see Figure 3, right), are

$$\mathbf{b}_1 = (1 + y g'(x)) \hat{\mathbf{e}}_1, \quad \mathbf{b}_2 = g(x) \hat{\mathbf{e}}_1 + \hat{\mathbf{e}}_2, \quad (13)$$

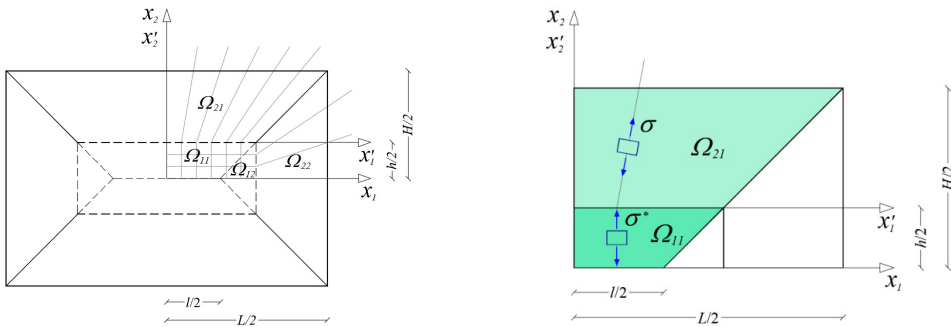


Figure 3. Partition of the planform into uniaxial and biaxial stress zones (left) and axial stress along the rays (right).

$\{\hat{e}_1, \hat{e}_2\}$ being the orthonormal pair coherent with the given Cartesian frame. We also consider the dual base vectors

$$\mathbf{b}^1 = \frac{1}{1 + y g'(x)} \hat{e}_1 - \frac{g(x)}{1 + y g'(x)} \hat{e}_2, \quad \mathbf{b}^2 = \hat{e}_2. \quad (14)$$

The uniaxial projected stress in the fan zone can be written as

$$\mathbf{S} = s \mathbf{b}_2 \otimes \mathbf{b}_2, \quad (15)$$

s being the sole nonvanishing contravariant component of the projected stress in the curvilinear reference $\{\vartheta^1, \vartheta^2\}$. For the two equilibrium equations (12) to be satisfied, it must be

$$s = \frac{q(x)}{1 + y g'(x)}, \quad (16)$$

$q(x)$ being an arbitrary function of x , to be specified through the boundary conditions.

Calling $\hat{\mathbf{k}}$ the unit vector directed as \mathbf{b}_2 , the physical stress component σ of this uniaxial stress field can be obtained as

$$\sigma = \mathbf{S} \cdot \hat{\mathbf{k}} \otimes \hat{\mathbf{k}}, \quad (17)$$

that is,

$$\sigma = -\frac{q(x)}{1 + y g'(x)} (1 + g^2(x)). \quad (18)$$

The emerging stress vector at the interface is then

$$\mathbf{t} = (\sigma \hat{\mathbf{k}} \otimes \mathbf{k})(-\hat{e}_2) = q(x) g(x) \hat{e}_1 + q(x) \hat{e}_2. \quad (19)$$

The biaxial state in the central zone Ω_1 is produced by the superposition of two orthogonal uniaxial stress fields directed as the Cartesian axes. The kink of the compression rays at the straight interface ($y = 0$) corresponds to a jump of the tangential component of stress producing a concentrated uniaxial stress of the form (21) along such interface.

The axial force $F_h(x)$ along the interface can be obtained by writing the equilibrium equation

$$F'_h(x) - q(x) g(x) = 0. \quad (20)$$

Instead, the normal component of the stress vector emerging at the interface is transmitted to the part Ω_{11} as a vertical uniaxial stress state of the form

$$s = q(x) \hat{e}_2 \otimes \hat{e}_2. \quad (21)$$

3.2. Membrane form. The form of the surface S carrying the compressive membrane stress \mathbf{T} can be obtained by studying the transverse equilibrium equation (6). We rewrite such equation in the curvilinear reference (θ^1, θ^2) in the form

$$S^{\alpha\beta} f_{/\alpha\beta} = 0, \quad (22)$$

where $S^{\alpha\beta}$ are the contravariant component of the projected stress in the covariant base $\{\mathbf{b}_1, \mathbf{b}_2\}$ and the symbol “/” followed by an index, say α , denotes the covariant derivative with respect to the coordinate θ^α .

Differentiating the base vectors and after some algebra, the equation (22) reduces to

$$\frac{q(x)}{1+y g'(x)} f_{,22} - p(x, y) = 0, \quad (x, y) \in \Omega_{21}. \quad (23)$$

In the part Ω_{11} the equilibrium equation (23) simplifies to

$$q(x) f_{,22}(x, y) - p(x, y) = 0, \quad (x, y) \in \Omega_{11}. \quad (24)$$

This equation can be easily integrated to obtain the shape $f(x, y)$, once $q(x)$ and $p(x, y)$ are given.

3.3. Case study: Palazzo Caracciolo di Avellino in Naples. The *Palazzo Caracciolo di Avellino*, one of the most ancient monumental buildings of Naples, is located in the Avellino Square and develops along via dell'Anticaglia. It was built at the end of XIV century by the architect Giacomo de Santis, adapting an existent convent as a residence of Gambacorta family. In the late Renaissance, it was inherited by the great poet Torquato Tasso and by the prince Caracciolo di Avellino. The Palace was saved by the destructions of the noble buildings in the revolt of Masaniello against the Spanish viceroyalty. In the XIX century, the edifice was restored and used as condominium. Despite the historical vicissitudes and the changes that have occurred over centuries, the palace is a fine example of Renaissance and Baroque architecture within the historic city of Naples. The Palazzo Caracciolo di Avellino, constituted by two levels with a central courtyard, has recently been undergone to an extensive restoration involving external facades and ground and first floors (see Figure 5).

The form of the surface S carrying the compressive membrane stress T can be obtained by studying the transverse equilibrium equation (24).

In particular, we study the vault 5 (see Figure 5, bottom left). The part of the vault that we analyze is reported in a longitudinal section in Figure 5 (bottom right). The plan of the vault and the partition of the planform into the zones Ω_{21} , Ω_{11} , Ω_{22} and Ω_{12} , are depicted in Figure 6, to which we refer for notations.



Figure 4. *Palazzo Caracciolo di Avellino*: view of the main facade.

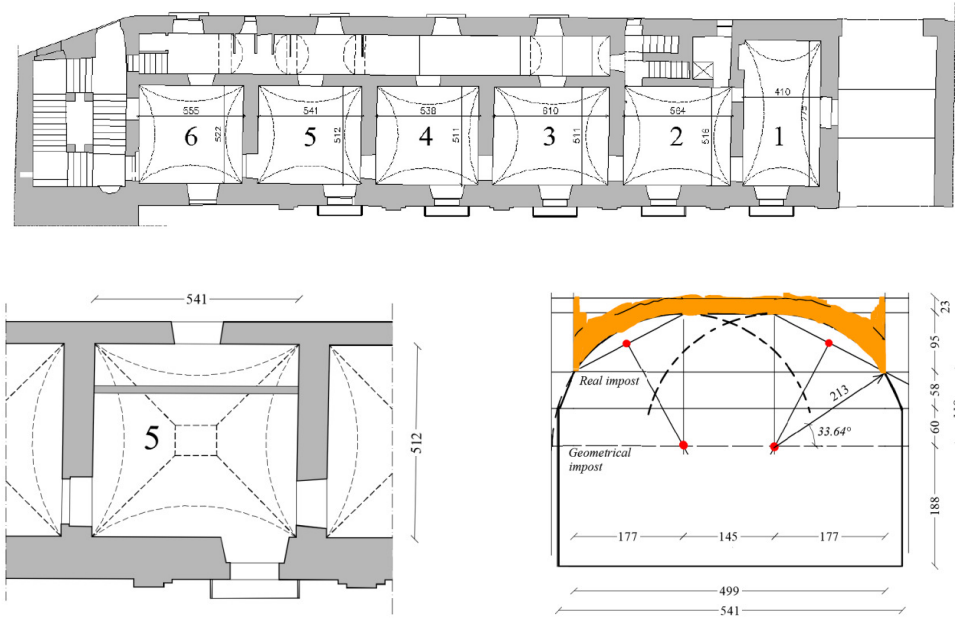


Figure 5. Main facade of the ground floor plan with vaulted structures (top), particular of analyzed cloister vault plan (bottom left) and its longitudinal section (bottom right).

We fix the orientation of the compression rays of Figure 3 (left) by giving (see Figure 7):

$$g(x) = 3 \frac{\bar{g}}{l} \left(1 - \frac{4}{3} \frac{x^2}{l^2} \right) x. \quad (25)$$

We consider two types of load. Load 1 is the effect of the dead load in uniform force per unit area $p_0 = 8 \text{ kN/m}^2$, and of the weight w of the wall whose position in the plan is sketched in Figure 5 (top).

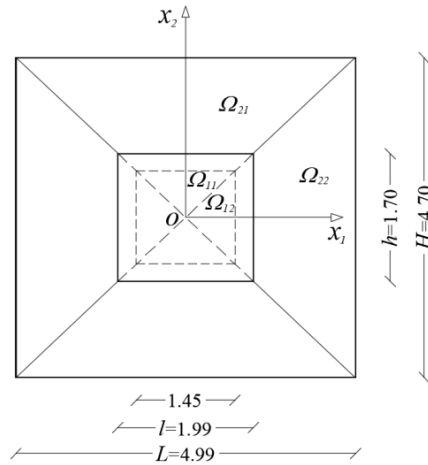


Figure 6. Cloister vault 5: plan dimensions and planform partition zones.

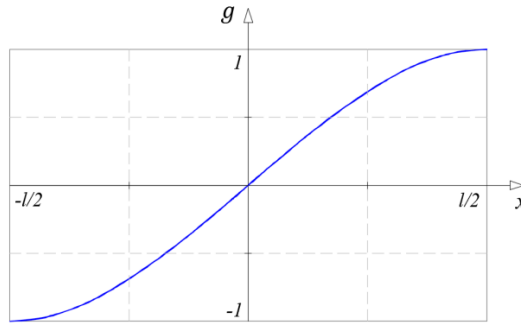


Figure 7. Orientation function (25) of the compressive rays of Figure 3.

As the load w , considering the smearing effect of the filling, we assume the following regularized form:

$$w(x, y) = p_1 e^{-\frac{1}{2c}(x-\Delta x)^2} e^{-\frac{1}{2d}(y-\Delta y)^2}, \quad (26)$$

represented in Figure 8 (left).

By solving (23) and (24), the form $f(x, y)$ depicted in Figure 8 (right) is obtained in such a shape contained inside the masonry vault.

Load 2 is the sum of the dead load p_0 and of the load p_{var} representing the effect of a live load. The live load we consider is the weight of a box of water which is 1 m wide, 1 m deep and 0.76 m high. Taking into account the smearing effect of the filling, this load 2 can be sketched as in Figure 9 (left).

As in the previous load case, the shape $f(x, y)$ associated to load 2 and contained inside the masonry vault, is still deducted as solution of equations (26) and (27).

The Heyman geometrical safety factor (see [Heyman 1995; Huerta 2006]), can be assessed by the ratio between the thickness of the real vault and the minimal thickness of a homothetic fictitious vault containing the equilibrium membrane structure S . For both cases of figures 8 (right) and 9 (right), the geometrical safety factor assumes a value near the following:

$$s_H = s/s_{\min} = 20/11 = 1.82. \quad (27)$$

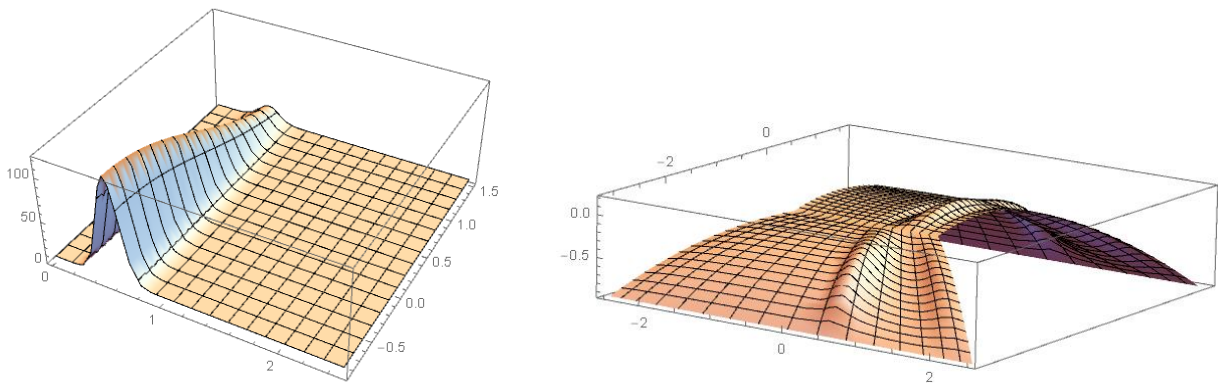


Figure 8. Representation of the load 1 (left) and the form function associated to this load (right).

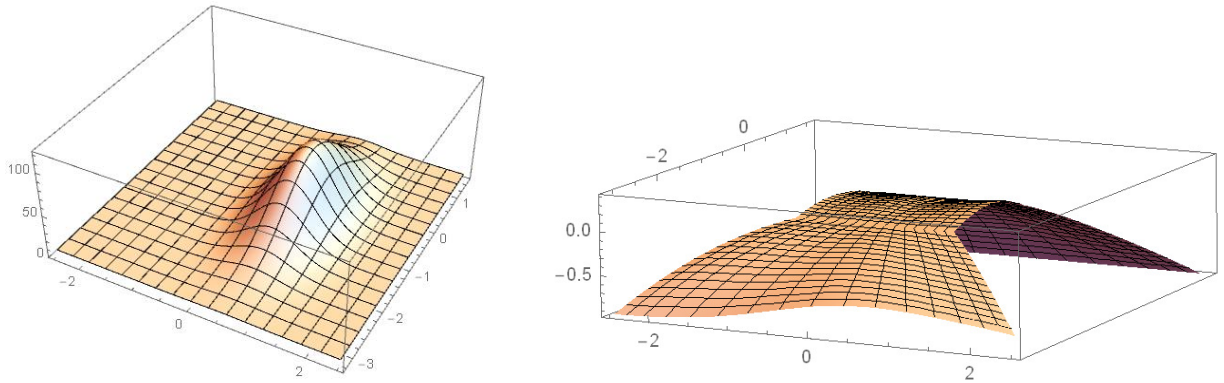


Figure 9. Representation of the load 2 (left) and the form function associated to this load (right).

An upper bound of the collapse load multiplier can be found using the kinematic theorem of limit analysis considering an efficient approach based on the piecewise rigid displacement (PRD) method (see [Iannuzzo et al. 2018c; Iannuzzo et al. 2018b; De Serio et al. 2018]) to adapt at the cloister vault geometry.

4. Concluding remarks

The paper has dealt with the equilibrium of cloister masonry vaults composed of no-tension Heyman material for which the theorems of limit analysis can be still applied. The equilibrium has been expressed as an extension of the Pucher's method, so that convenient systems of coordinates for the formulation of the stress problem and a concave stress function has been assumed. The problem, under purely vertical loads, has turned into a single partial differential equation of the second-order where the shape function f and the stress function F play symmetrical role. The unilateral restrictions have requested that the membrane surface S lies in between the extrados and intrados surfaces of the vault and that the stress function be concave. Making a sensible choice of a concave stress function F , the transverse equilibrium equation has been solved with the unknown function f by imposing suitable boundary conditions. As example, a cloister vault of the *Palazzo Caracciolo di Avellino* has been analyzed, whose membrane surfaces and geometrical safety factors for two load conditions have been assessed.

References

- [Angelillo 2015] M. Angelillo, “Static analysis of a Guastavino helical stair as a layered masonry shell”, *Compos. Struct.* **119** (2015), 298–304.
- [Angelillo 2019] M. Angelillo, “The model of Heyman and the statical and kinematical problems for masonry structures”, *Int. J. Masonry Res. Innov.* **4**:1-2 (2019), 14–31.
- [Angelillo and Fortunato 2004] M. Angelillo and A. Fortunato, “Equilibrium of masonry vaults”, pp. 105–111 in *Novel approaches in civil engineering: lecture notes in applied and computational mechanics*, vol. 14, edited by M. Frémond and F. Maceri, Springer, Berlin, Heidelberg, 2004.
- [Angelillo et al. 2010] M. Angelillo, L. Cardamone, and A. Fortunato, “A numerical model for masonry-like structures”, *J. Mech. Mater. Struct.* **5**:4 (2010), 583–615.

- [Angelillo et al. 2013] M. Angelillo, E. Babilio, and A. Fortunato, “Singular stress fields for masonry-like vaults”, *Contin. Mech. Therm.* **25**:2-4 (2013), 423–441.
- [Angelillo et al. 2014] M. Angelillo, A. Fortunato, A. Montanino, and M. Lippiello, “Singular stress fields in masonry structures: Derand was right”, *Meccanica (Milano)* **49**:5 (2014), 1243–1262.
- [Angelillo et al. 2016] M. Angelillo, E. Babilio, A. Fortunato, M. Lippiello, and A. Montanino, “Analytic solutions for the stress field in static sandpiles”, *Mech. Mater.* **95** (2016), 192–203.
- [Angelillo et al. 2018] M. Angelillo, A. Fortunato, A. Gesualdo, A. Iannuzzo, and G. Zuccaro, “Rigid block models for masonry structures”, *Int. J. Masonry Res. Innov.* **3**:4 (2018), 349–368.
- [Bloch and Ochsendorf 2007] P. Bloch and J. Ochsendorf, “Thrust network analysis: a new methodology for three-dimensional equilibrium”, *J. IASS* **48**:3 (2007), 167–173.
- [Block and Lachauer 2014] P. Block and L. Lachauer, “Three-dimensional funicular analysis of masonry vaults”, *Mech. Res. Commun.* **56** (2014), 53–60.
- [Block et al. 2006] P. Block, T. Ciblac, and J. Ochsendorf, “Real-time limit analysis of vaulted masonry buildings”, *Comput. Struct.* **84**:29-30 (2006), 1841–1852.
- [Brandonisio et al. 2013] G. Brandonisio, G. Lucibello, and A. Mele, E. De Luca, “Damage and performance evaluation of masonry churches in the 2009 L’Aquila earthquake”, *Eng. Fail. Anal.* **34** (2013), 693–714.
- [Brandonisio et al. 2015] G. Brandonisio, E. Mele, and A. De Luca, “Closed form solution for predicting the horizontal capacity of masonry portal frames through limit analysis and comparison with experimental test results”, *Eng. Fail. Anal.* **55** (2015), 246–270.
- [Como 1992] M. Como, “Equilibrium and collapse analysis of masonry bodies”, *Meccanica (Milano)* **27**:3 (1992), 185–194.
- [Como 2013] M. Como, *Statics of historic masonry constructions*, Springer, Berlin, 2013.
- [Contestabile et al. 2016] M. Contestabile, E. Babilio, A. Fortunato, L. Guerriero, M. Lippiello, M. Pasquino, and M. Angelillo, “Static analysis of cross vaults: the case of the cathedral of Casertavecchia”, *Open Construct. Build. Technol. J.* **10**:Suppl 2: M11 (2016), 329–345.
- [De Goes et al. 2013] F. De Goes, P. Alliez, H. Owahdi, and M. Desbrun, “On the equilibrium of simplicial masonry structures”, *ACM Trans. Graph.* **32**:4 (2013), article 93.
- [De Serio et al. 2018] F. De Serio, M. Angelillo, A. Gesualdo, A. Iannuzzo, G. Zuccaro, and M. Pasquino, “Masonry structures made of monolithic blocks with an application to spiral stairs”, *Meccanica (Milano)* **53**:8 (2018), 2171–2191.
- [Fang et al. 2019] D. L. Fang, R. K. Napolitano, T. L. Michiels, and S. M. Adriaenssens, “Assessing the stability of unreinforced masonry arches and vaults: a comparison of analytical and numerical strategies”, *Int. J. Archit. Herit.* **13**:5 (2019), 648–662.
- [Fortunato et al. 2014] A. Fortunato, F. Fraternali, and M. Angelillo, “Structural capacity of masonry walls under horizontal loads”, *Ing. Sismica* **31**:1 (2014), 41–49.
- [Fortunato et al. 2016] A. Fortunato, E. Babilio, M. Lippiello, A. Gesualdo, and M. Angelillo, “Limit analysis for unilateral masonry-like structures”, *Open Construct. Build. Technol. J.* **10**:Suppl 2: M12 (2016), 346–362.
- [Fortunato et al. 2018] A. Fortunato, F. Fabbrocino, M. Angelillo, and F. Fraternali, “Limit analysis of masonry structures with free discontinuities”, *Meccanica (Milano)* **53**:7 (2018), 1793–1802.
- [Fraternali 2010] F. Fraternali, “A thrust network approach to the equilibrium problem of unreinforced masonry vaults via polyhedral stress functions”, *Mech. Res. Commun.* **37**:2 (2010), 198–204.
- [Fraternali et al. 2002] F. Fraternali, M. Angelillo, and G. Rocchetta, “On the stress skeleton of masonry vaults and domes”, in *Proceedings of the Seventh Pan American Congress of Applied Mechanics (PACAM VII)* (Temuco, Chile), 2002.
- [Gesualdo et al. 2017] A. Gesualdo, C. Cennamo, A. Fortunato, G. Frunzio, M. Monaco, and M. Angelillo, “Equilibrium formulation of masonry helical stairs”, *Meccanica (Milano)* **52**:8 (2017), 1963–1974.
- [Gesualdo et al. 2019] A. Gesualdo, B. Calderoni, A. Sandoli, and M. Monaco, “Minimum energy approach for the in-plane shear resistance of masonry panels”, *Ing. Sismica* **36**:1 (2019), 42–53.
- [Heyman 1966] J. Heyman, “The stone skeleton”, *Int. J. Solids Struct.* **2**:2 (1966), 249–279.
- [Heyman 1995] J. Heyman, *The stone skeleton: structural engineering of masonry architecture*, Cambridge University Press, Cambridge, UK, 1995.

- [Heyman 2012] J. Heyman, “The membrane analysis of thin masonry shells”, *Nuts Bolts Construct. Hist.* **1** (2012), 281–283.
- [Huerta 2006] S. Huerta, “Galileo was wrong: the geometrical design of masonry arches”, *Nexus Netw. J.* **8**:2 (2006), 25–52.
- [Iannuzzo et al. 2018a] A. Iannuzzo, M. Angelillo, E. De Chiara, F. De Guglielmo, F. De Serio, F. Ribera, and A. Gesualdo, “Modelling the cracks produced by settlements in masonry structures”, *Meccanica (Milano)* **53**:7 (2018), 1857–1873.
- [Iannuzzo et al. 2018b] A. Iannuzzo, A. De Luca, A. Fortunato, A. Gesualdo, and M. Angelillo, “Fractures detection in masonry constructions under horizontal seismic forces”, *Ing. Sismica* **35**:3 (2018), 87–103.
- [Iannuzzo et al. 2018c] A. Iannuzzo, F. De Serio, A. Gesualdo, G. Zuccaro, and M. Fortunato, A. Angelillo, “Crack patterns identification in masonry structures with a C^0 displacement energy method”, *Int. J. Masonry Res. Innov.* **3**:3 (2018), 295–323.
- [Kooharian 1952] A. Kooharian, “Limit analysis of voussoir (segmental) and concrete arches”, *J. Am. Concr. Inst.* **24**:4 (1952), 317–328.
- [Livesley 1978] R. K. Livesley, “Limit analysis of structures formed from rigid blocks”, *Int. J. Numer. Methods Eng.* **12**:12 (1978), 1853–1871.
- [Marmo and Rosati 2017] F. Marmo and L. Rosati, “Reformulation and extension of the thrust network analysis”, *Comput. Struct.* **182** (2017), 104–118.
- [Miki et al. 2015] M. Miki, T. Igarashi, and P. Block, “Parametric self-supporting surfaces via direct computation of airy stress functions”, *ACM Trans. Graph.* **34**:4 (2015), article 89.
- [O’Dwyer 1999] D. W. O’Dwyer, “Funicular analysis of masonry vaults”, *Comput. Struct.* **73**:1-5 (1999), 187–197.
- [Pucher 1934] A. Pucher, “Über der spannungszustand in gekrümmten flächen”, *Beton u Eisen* **33** (1934), 298–304.
- [Vouga et al. 2012] E. Vouga, M. Höbinger, J. Wallner, and H. Pottmann, “Design of self-supporting Surfaces”, *ACM Trans. Graph.* **31**:4 (2012), article 87.

Received 11 Apr 2019. Revised 11 Oct 2019. Accepted 28 Oct 2019.

ANTONIO GESUALDO: gesualdo@unina.it

Department of Structures for Engineering and Architecture, University of Naples Federico II, Via Claudio 21 (buildings 6-7), 80125 Naples, Italy

GIUSEPPE BRANDONISIO: giuseppe.brandonisio@unina.it

Department of Structures for Engineering and Architecture (Di.St.), University of Naples “Federico II”, P.le Tecchio, 80, 80125 Naples, Italy

ANTONELLO DE LUCA: antonio.deluca@unina.it

Department of Structures for Engineering and Architecture (Di.St.), University of Naples “Federico II”, P.le Tecchio, 80, 80125 Naples, Italy

ANTONINO IANNUZZO: iannuzzo@arch.ethz.ch

Institute of Technology in Architecture, Block Research Group, ETH Zurich, Stefano-Franscini-Platz 1, 8093 Zurich, Switzerland

ANDREA MONTANINO: andrea.montanino@polimi.it

Dipartimento di Strutture per L’Ingegneria e l’Architettura, Università degli studi di Napoli “Federico II”, Via Toledo, 902, 80132 Napoli, Italy

CARLO OLIVIERI: colivieri@unisa.it

Department of Civil Engineering, University of Salerno, Via Giovanni Paolo II, 132, 84084 Fisciano, Italy

THE ROCKING: A RESOURCE FOR THE SIDE STRENGTH OF MASONRY STRUCTURES

MARIO COMO

Masonry constructions activate rocking motions endeavouring to elude the action of horizontal impulse accelerations, typical of seismic actions. They can reach the dynamical collapse under acceleration impulse with intensity much higher than the one that causes the static collapse. Sudden changes of mechanisms take place during the rocking with the occurrence of impacts and consequent energy losses. Research on the topic has been generally carried out examining various schemes of structural components, as a rule considered or as a solid block or subdivided in a sequence of blocks connected by hinges. Innovative aspect of the paper, on the contrary, that collects also some results of the author, is the analysis of the influence on the rocking motion at the onset of oblique cracks that sway diagonally during the rocking of masonry walls.

1. Introduction

Masonry constructions behave under seismic actions very differently from reinforced concrete and steel structures. Masonry constructions endeavour to elude the seismic action activating a rocking motion rather than deforming with doubtful dissipating mechanisms.

Rocking is a direct consequence of the no-tension behavior of the masonry material. A masonry pier or a masonry wall, hit by a sudden horizontal impulse, moves sideways and detaches from its bases and, if does not overturn, once reached its maximum side displacement inverts its motion going back to the initial position, and so on. The pier continues to move with oscillations of reducing amplitudes and periods, until the stop of the motion.

The study of the rocking and the discovery of its importance in the seismic strength assessment of masonry buildings started with a fundamental paper of Housner [1963], in which he studied the rocking motion of a stone column resting on a rigid base. The Housner's paper showed the reasons for which tall and slender columns were able to survive severe ground shaking whereas more stable appearing reinforced concrete structures were severely damaged.

Only more recently interest in the study of rocking increased noteworthy and many contributions, involving the dynamical behavior of some simple masonry structures under various types of dynamical actions, have been given [Yim et al. 1980; Hogan 1992; Giannini and Masiani 1996; Liberatore et al. 2002; Sorrentino et al. 2006; 2008; Peña et al. 2007; Di Carlo 2014; Coccia et al. 2016], generally analysing models composed by rigid blocks.

Innovative aspect of the paper, on the contrary, that collects also some results of the author and others [Coccia et al. 2016; Di Carlo et al. 2017], is the analysis of the influence of the onset of oblique cracks swaying diagonally during the rocking of masonry piers and walls. In this context the present paper

Keywords: masonry piers and walls, rocking, cracking, acceleration pulse.

points out more clearly the differences existing between the rocking response of the solid column and that of a masonry pier or of a masonry wall, composed by two piers and one spandrel, whose piers crack diagonally during the motion.

Analysis of rocking requires the study of the impacts, that take place during the motion, to estimate the corresponding energy losses. Still more exhaustively is here studied the problem of the localization of points where impacts take place, as between piers and basement, and as between piers and spandrel.

The paper assumes, as dynamical action, the impulse of a constant horizontal acceleration A and duration t , particularly advantageous to deal with the response of structures to seismic actions via analytical approach. This loading is the dynamical extension of the common pushover statical action. Thus, if the magnitude of the acceleration impulse is higher than the limit value A_L , obtained by limit analysis, the cracked pier or the wall with openings, starts to move, overturning at base corner. By further increasing the acceleration level A_0 the pier, at a definite time t_0 , reaches a configuration at which the opposing action of the weight vanishes and dynamically fails.

The research of the dependence of the ratio A_0/A_L upon the limit duration t_0 is crucial to define the seismic strength capacity of the masonry wall. This ratio A_0/A_L represents the strength reduction factor q that has great importance in the assessment of the seismic strength of masonry constructions [Peña et al. 2007; Sorrentino et al. 2008; Di Carlo 2014; Coccia et al. 2016; Di Carlo et al. 2017; ≥ 2019; Heyman 1992; Ochserdorf 2002; Como 2016].

2. Recalls of the rocking of the solid column

The discovery of the importance of studying rocking in seismic strength assessments of masonry buildings started with a fundamental paper of Housner [1963] in which he studied the rocking motion of a stone column resting on a rigid frictional base. We will reassume and comment the main results of Housner analysis.

A constant horizontal acceleration impulse of magnitude A_1 has been chosen here to represent schematically the perturbing action that hits the column at its initial vertical position: varying the duration t_1 of the impulse, this condition can give a simple qualitative representation of the seismic action (Figure 1, left).

Let us make reference to the Figure 1 (right) that shows the column in its rocking motion. The friction coefficient between the column and its basement is sufficiently large to prevent sliding. The column, at the position (1) (Figure 1, right), is falling down rotating around the base right corner O . When the column reaches the vertical position (2), its left base corner impacts against the basement rigid plane and an impulsive force suddenly takes place at the impact point O' and a change of motion suddenly occurs.



Figure 1. Constant horizontal acceleration impulse.

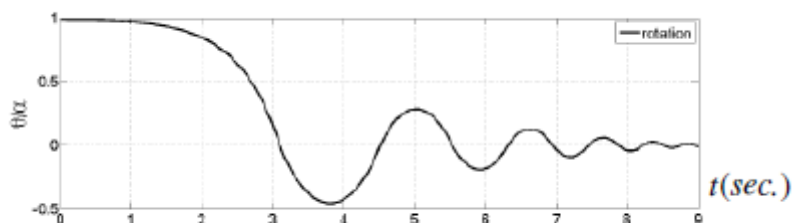


Figure 2. Damped oscillations of the column with gradually reducing amplitudes [Di Carlo 2014].

Just after the impact, the column begins to rotate now around the left base corner, the new point O' , the pivot of the new motion of the column. Dissipations of energy occur each time the column impacts on its base.

The column develops its swaying rocking motion oscillating around O and O' . Figure 2 shows this motion, with reducing amplitudes and shorter periods: it is of the inverted pendulum type, not harmonic but oscillatory, damped, in consequence of impacts. Rocking motion starts only if

$$A_1 \geq A_L = g \cdot t g \alpha, \quad (1)$$

where $t g \alpha = b/h$ defines the slenderness of the column having width b and height h .

Condition (1) shows that only if the magnitude A of the horizontal acceleration pulse A_1 is larger than $A_L = g \cdot t g \alpha$ — the magnitude of the acceleration that leads the pier to the limit equilibrium condition — the column puts itself in motion. At this point the resultant of all vertical and horizontal forces passes through the external edge O of the base section of the column, as shown in the left scheme of Figure 3.

The equation of the column motion hit by a constant horizontal acceleration impulse was firstly formulated in Housner [1963] as

$$I_0 \frac{d^2 \theta}{dt^2} = -W R (\alpha - \theta) + \frac{W A}{g} R. \quad (2)$$

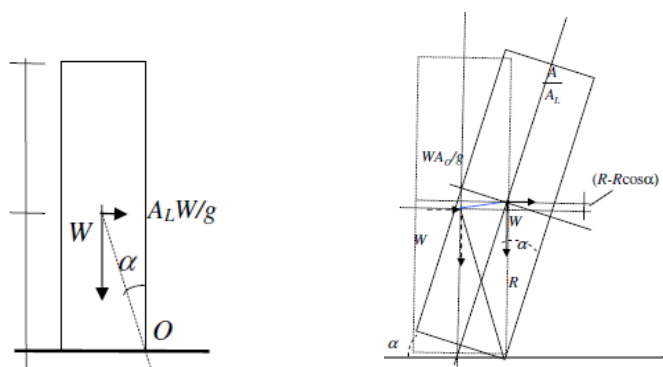


Figure 3. The solid column at the static failure and at the dynamical failure.

That, solved, gives

$$\theta(t) = \alpha \left(\frac{A}{A_L} - 1 \right) (\cosh pt - 1), \quad \frac{A}{A_L} > 1, \quad (3)$$

with

$$p = \sqrt{\frac{WR}{I_o}} = \sqrt{\frac{3g}{4h\sqrt{1+tg^2\alpha}}}. \quad (4)$$

The column, forced by an acceleration impulse A_0 , larger than A_L and of adequate duration t_0 , will continue to move sideways until to the inversion of the motion or, on the contrary, if the impulse acceleration and its duration are sufficiently high, until reaches the *critical* overturning configuration. This last state is defined by inclination (α) of the column at which any increment of the opposing action of the weight vanishes (Figure 3, right scheme).

The equation defining the intensity A_0 of this impulse, together with the corresponding duration t_0 , is obtained equating the work done by inertial force along the motion and during the whole time t_0 to the work required to raise the weight W of the column as far as to the limit position α :

$$\int_0^{t_1} \frac{W}{g} A_0 \frac{ds}{dt} dt = \frac{W}{g} A_0 R \int_0^{t_1} \dot{\theta}(t) dt = WR(1 - \cos \alpha). \quad (5)$$

Solution of condition (5) gives the relation occurring between the intensity A_0 of the acceleration impulse and its duration t_0 required to reach the critical dynamical overturning state [Housner 1963]

$$t_0 = \sqrt{\frac{4h\sqrt{1+tg^2\alpha}}{3g}} \cosh^{-1} \left(1 + \frac{1}{(2A_0/A_L)(A_0/A_L - 1)} \right). \quad (6)$$

A scale effect is present in (6) because two columns have the same ratio b/h , the higher requires a larger time duration t_0 to reach the failure under the same acceleration intensity A_0 . From the inspection of condition (6) we have

$$\frac{A_1}{A_L} \rightarrow \infty, \quad t_1 \rightarrow 0, \quad \frac{A_1}{A_L} \rightarrow 1, \quad t_1 \rightarrow \infty. \quad (7)$$

3. The masonry wall pier

3.1. Rocking with diagonal cracking. The wall pier is the vertical element of masonry walls with openings, the main resistant structural components of masonry buildings. Oblique cracking occurs in the masonry hit by horizontal actions and influence rocking.

On the wake of the above study of the Housner's solid column, let us examine the rocking motion of a wall pier (Figure 4, left) hit by a short horizontal acceleration pulse. Figure 4 (right) shows the wall pier at a generic cracked configuration, loaded by vertical forces — due to the self-weight of the element as to the weight of spandrels — and by the corresponding horizontal inertia forces.

The wall pier behaves quite differently from the solid column. This last can in fact only detach from its base while the masonry pier suffers from diagonal cracks.

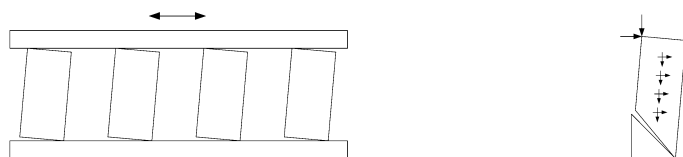


Figure 4. Generic configuration under alternate horizontal actions: masonry wall (left) and cracked wall pier (right).



Figure 5. The typical X-shaped cracking pattern occurring in a wall pier.

Rocking of the cracked pier, on the other hand, can effectively occur only if the inactive detached wedge of the block, represented by the dotted triangle in Figure 4 (right), does not crumble at the impacts with the pier tag-end, coming back during the inverted oscillation.

Answer to this question can be obtained by inspecting Figure 5 that shows the typical X-shaped cracking pattern occurred in a vertical pier, after the in-plane rocking of the wall. Analysis of the sequence of the cracking geometries occurring during the shaking movement that affects the scheme of a wall pier (see Figure 6) can better clarify the reasons of the development of these X-shaped cracks.

The first scheme (Figure 6) represents the undeformed configuration of the element. The second scheme shows the compressed right pier wedge, at the onset of the wall rotation. It moves along the first mechanism u^- in the clockwise direction and detaches from the left wedge, that remains ineffective. The third scheme shows the counter-clockwise rotation of the wedge that returns towards the vertical position still following the first mechanism u^- ; the fourth scheme refers to the contact occurring between the two wedges and to subsequent impact occurring at the left corner of the pier base. In the fifth scheme, the left wedge, following the subsequent returning mechanism u^+ , is detaching from the right one, thereby producing the other diagonal crack that, crossing with the first one, determines the detected X-shaped cracking, observed at the stop of the motion.

A prospective masonry destruction at the contact of the inactive wedge could not permit the occurrence of rocking. The presence of the X-shaped cracking, commonly detected in damaged walls of masonry buildings, proves that inactive masonry wedges are generally able to sustain, during the rocking, contacts with the other ones. At this contact the compression forces are, in fact, immediately conveyed as far as to the opposite corner of the pier base. Impact occurs just at this corner, the new pivot of the subsequent rotation mechanism u^+ . We remark that in both the Housner column and the masonry pier impact occurs at the hinge of the returning mechanism.

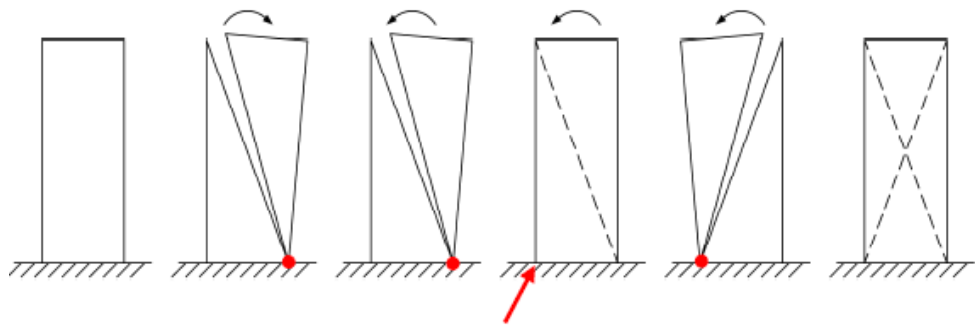


Figure 6. Sequence of the wall pier configurations during the formation of the X-shaped cracks.

3.2. Incipient rocking acceleration. As to the solid column, the rocking motion starts only if the magnitude A of the horizontal acceleration pulse is larger than A_L , the acceleration that leads the pier to the limit static equilibrium condition. At this state, in fact, the resultant of all vertical and horizontal forces passes exactly through the external edge O of the base section of the pier (Figure 7).

The value of the limit acceleration A_L equals the failure multiplier λ_0 of the horizontal inertia forces W/g , that can be obtained as application of the limit analysis approach.

As shown in Figure 7, a fracture KO , approximately assumed straight, starts at the section $K-K'$, at a distance ξ from the top of the element and reaches the toe O of the pier. This fracture splits the masonry block between the compressed portion and the ineffective one. The compressed region is composed by the upper uncracked rectangular parallelepiped of weight W_1 and by the lower triangular wedge of weight W_2 . The other triangular lower region located at the left side of the element is ineffective.

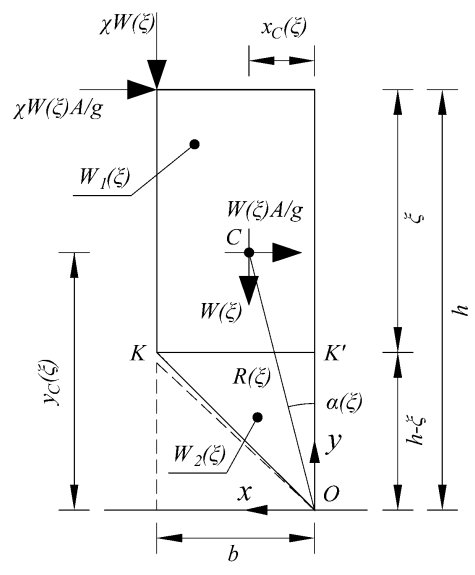


Figure 7. Forces acting during the rocking of the cracked wall pier.

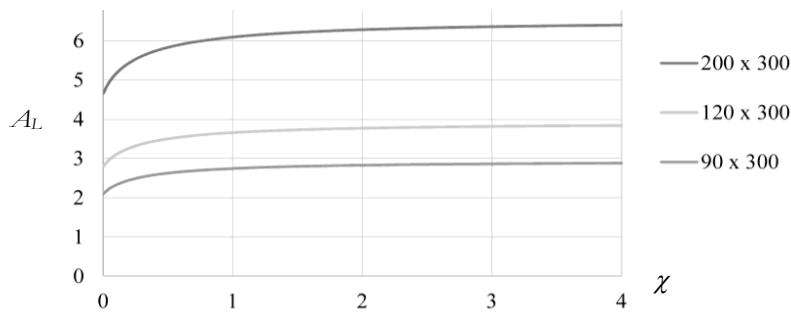


Figure 8. Incipient rocking acceleration A_L versus the factor χ varying the pier wall geometry.

A vertical force χW is applied at the head of the pier, being W the weight of the whole pier and χ a coefficient higher or equal to zero. The corresponding horizontal force is $\chi W A/g$, where A is the acceleration that hits the wall and g the gravity acceleration.

The magnitudes of the weights W_1 and W_2 depend on the distance ξ and, with reference to Figure 7, can be expressed as

$$W_1(\xi) = \gamma b \xi, \quad W_2(\xi) = \gamma \frac{b}{2} (h - \xi). \quad (8)$$

The weight W of all masses taking part in the mechanism is

$$W(\xi) = W_1(\xi) + W_2(\xi). \quad (9)$$

Defining the location of the gravity center C of all moving masses, the cracked configuration of the masonry pier at the incipient overturning is defined by the distance ξ and the limit acceleration A_L , which can be obtained by solving the following system of two equations:

$$\begin{aligned} W_1(\xi) \frac{A_L}{g} \frac{\xi}{2} + \chi W(\xi) \frac{A_L}{g} \xi &= W_1(\xi) \frac{b}{6} + \chi W(\xi) \frac{2}{3} b, \\ W_1(\xi) \frac{A_L}{g} \left(h - \frac{\xi}{2} \right) + W_2(\xi) \frac{A_L}{g} \frac{2}{3} (h - \xi) + \chi W(\xi) \frac{A_L}{g} h &= W_1(\xi) \frac{b}{2} + W_2(\xi) \frac{b}{3} + \chi W(\xi) b, \end{aligned} \quad (10)$$

respectively defining as the incipient cracking occurring at the section $K-K'$, as the incipient failure of the whole pier. The rocking of the pier, hit by a constant acceleration pulse of magnitude A , can actually start if $A > A_L$.

Figure 8 plots the incipient rocking acceleration A_L versus the ratio χ — i.e., the ratio between the load applied at the head and the whole weight of the pier — for the three considered geometries of the wall pier: a pier of 3 m height and a width variable between 0.9 m, 1.2 m and 2 m [Di Carlo et al. 2017].

3.3. Overturning caused by a constant acceleration pulse of finite duration. As in the Housner column, let us value the relation occurring at the dynamical collapse between the constant overturning acceleration A_0 and the corresponding critical duration t_0 .

The pier, hit by the horizontal acceleration pulse A , starts its motion in the cracked configuration, defined by the distance ξ : this last, together with the limit acceleration A_L , obtained by solving the system of (10).

Let I_0 be the moment of inertia around the point O of all the masses involved in the overturning of the pier. Making reference to the motion of the center C of all masses engaged, the equation of motion of the pier can be written as

$$I_0(\xi)\ddot{\theta} = -W(\xi)R(\xi)[\alpha(\xi) - \theta] + W(\xi)R(\xi)\frac{A}{g}, \quad (11)$$

that, with the position

$$p(\xi)^2 = \frac{W(\xi)R(\xi)}{I_0(\xi)},$$

has the solution

$$\theta(t) = [A/g - \alpha(\xi)][\cosh p(\xi)t - 1]. \quad (12)$$

The magnitude A_0 of an acceleration pulse having duration t_0 , required to overturn the block, is then given, likewise (5), by the condition

$$\frac{W(\xi)}{g}A_0 \int_0^{t_0} \frac{ds}{dt} dt = W(\xi)R(\xi)[1 - \cos \alpha(\xi)], \quad (13)$$

and we obtain

$$t_0 = \frac{1}{p(\xi)} \cosh^{-1} \left[1 + \frac{1}{\frac{2A_0}{A_L(\xi)} \left(\frac{A_0}{A_L(\xi)} - 1 \right)} \right], \quad (14)$$

that defines the dependence of the duration time t_0 from the impulse acceleration A_0 required to overturn the block. As it can be noted, equation (14) is characterized by the existence of vertical and horizontal asymptotes, being

$$\lim_{\frac{A_0}{A_L(\xi)} \rightarrow 1} t_0 = \infty, \quad \lim_{\frac{A_0}{A_L(\xi)} \rightarrow \infty} t_0 = 0. \quad (15)$$

With reference, for instance, to a 3 meters high and 0.9 meters wide pier, Figure 9 shows the trend of the overturning time t_0 varying the magnitude A_0 of the acceleration pulse, for different values of the coefficient χ varying in the range from 0 to 4 [Di Carlo et al. 2017]. The intercepts of the vertical asymptotes of the curves given by (14) with the horizontal axis give the corresponding magnitudes of the limit accelerations $A_L(\chi)$. The case $\chi = 0$ corresponds to the pier without masses applied at its top. This case is significant because is in direct correlation with the behavior of the Housner column.

Compared with the solid column, cracking occurring in the masonry pier implies either smaller duration t_0 of pulses with a given acceleration A_0 or, keeping fixed the duration t_0 , smaller magnitude of the overturning acceleration A_0 .

It is worth to note that the duration of the impulse required to overturn the pier wall increases with the increasing of the factor χ , i.e., of the magnitude of the mass applied at the pier top corner. It means that the presence of a mass applied at the pier head has thus a stabilizing effect, in spite of the corresponding increase in magnitude of the inertia horizontal force.

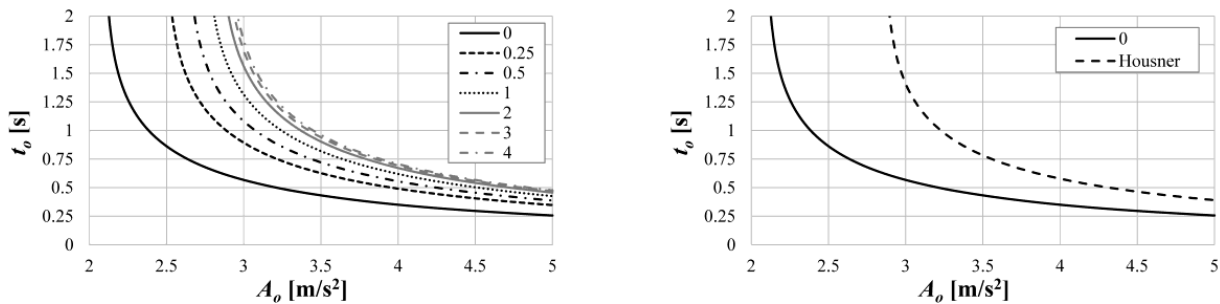


Figure 9. Plot of t_0 versus A_0 : varying the factor χ (left) and comparison with Housner's model (right).

4. Rocking of a masonry wall with opening and a steel tie

4.1. The limit static acceleration impulse. We will consider the scheme in Figure 10 as a simple wall composed by two masonry piers and a spandrel, connected by a top steel tie, in the oscillating motion activated by a sudden action of a constant horizontal impulse acceleration. It represents the simplest model of the multistorey walls with openings, composed by piers and spandrels, the main resistant structural components of the masonry building.

The acceleration impulse A induces on the wall a distribution of inertial horizontal loads. If the magnitude of the impulse is sufficiently high, the wall will reach the limit state and will deform according to the sideways swaying mechanism from the left to the right (Figure 11, left scheme). Cracking will occur at the bases of piers and the determination of the cracked layout of the piers, together with the limit horizontal acceleration A_L , can be achieved by the limit analysis approach [Di Carlo et al. \geq 2019].

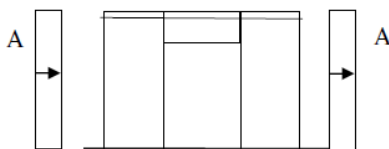


Figure 10

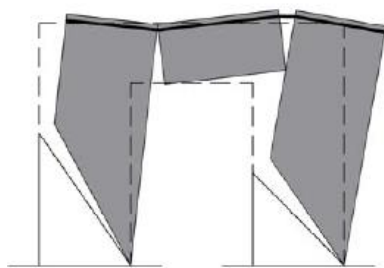


Figure 11. The rocking of the wall.

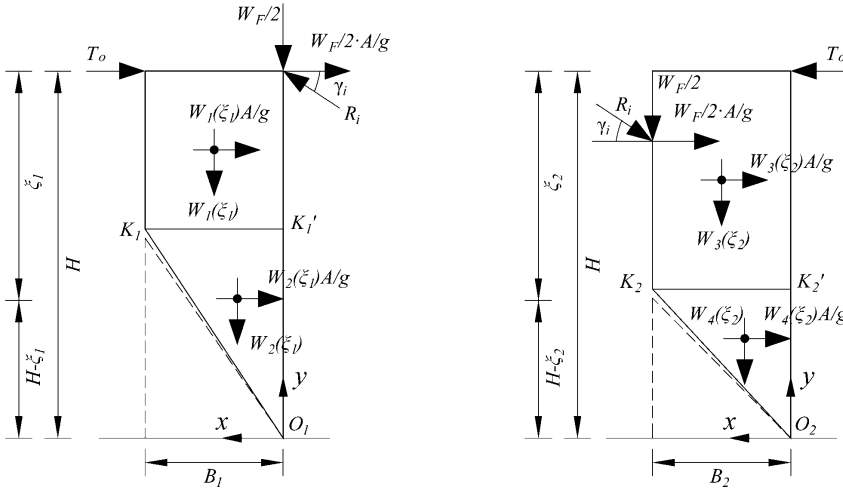


Figure 12. Forces on the cracked wall piers.

As shown in Figure 12, a fracture K_1C_1 (K_2C_2), assumed to be approximately straight, starts at the section $K_1-K'_1$ ($K_2-K'_2$), at a distance ξ_1 (ξ_2) from the top of the element and reaches the toe C_1 (C_2) of the pier. This fracture splits the masonry block into a compressed portion and in an ineffective part. The compressed region is composed by the upper uncracked rectangular parallelepiped of weight W_1 (W_3) and by the lower triangular wedge of weight W_2 (W_4). The other triangular lower region located at the left side of the element is ineffective. The semi-weights of the spandrel $W_F/2$ and the corresponding horizontal force $W_F/2 \cdot A/g$ are applied at hinges sections between piers and spandrel. The loading pattern on each of the piers is completed by the inclined compressive reaction R_i of the central panel. The magnitudes of the weights W_1 (W_3) and W_2 (W_4) depend on the distance ξ_1 (ξ_2) and, with reference to Figure 12, can be expressed as

$$W_1(\xi_1) = \gamma B_1 \xi_1, \quad W_2(\xi_1) = \gamma \frac{B_1}{2} (H - \xi_1), \quad (16)$$

and

$$W_3(\xi_2) = \gamma B_2 \xi_2, \quad W_4(\xi_2) = \gamma \frac{B_2}{2} (H - \xi_2). \quad (17)$$

The problem to define the cracked configuration of the masonry pier at the incipient overturning is a function of four unknowns: the two distances ξ_1 and ξ_2 , the reaction of the central panel R_i and the limit acceleration A_L . Two equations define the incipient cracking occurring at sections $K_1-K'_1$ and $K_2-K'_2$, respectively and another equation defines the limit equilibrium of the first pier.

For a given value of the limit acceleration A_L , let $\bar{\xi}_1$, $\bar{\xi}_2$ and \bar{R}_i be the solutions of these three equations that define the cracked zones of the piers and

$$W_1 = W_1(\bar{\xi}_1), \quad W_2 = W_2(\bar{\xi}_1), \quad W_3 = W_3(\bar{\xi}_2), \quad W_4 = W_4(\bar{\xi}_2), \quad (18)$$

are the weights of the four parts of the wall divided by cracks.

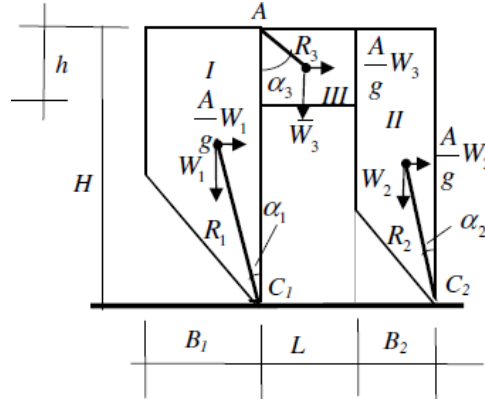


Figure 13. Geometry of the cracked swaying wall.

We can lump the weights W_1 and W_2 of the parts corresponding to the same pier at the corresponding centers G_1 and G_2 of the uncracked parts I and II. At the same time G_3 will represent the center of the spandrel where its weight W_3 is applied. At the cracked state, the essential wall geometry is described in Figure 13. Here the radii R_1 , R_2 and R_3 of vectors with their corresponding angles α_1 , α_2 and α_3 along the vertical axis can be easily determined.

The condition of the static global failure of the wall at the admissible cracking state is due to the action of a constant horizontal acceleration, acting so slowly on the wall to be represented by a static force. Thus applying the virtual work principle at limit equilibrium of the cracked state of the wall at the starting of the motion we get

$$\langle g, d\mathbf{u} \rangle + \delta L_{\text{tie}} + \langle \rho \mathbf{A}, d\mathbf{u} \rangle = 0, \quad t > 0, \quad (19)$$

where, with reference to the cracked configuration of the wall:

$$\langle g, \delta \mathbf{u} \rangle = - \sum_{i=1}^3 W_i R_i \sin \alpha_i d\theta_i, \quad (20)$$

is the resisting work of the dead loads g and $d\theta_1$, $d\theta_2$ and $d\theta_3$ are the small rotation increments of the three parts I, II, and III of the wall divided by cracks:

$$\delta L_{\text{tie}} = -T_0 H d\theta_1 (k_{21} - 1), \quad (21)$$

is the resisting plastic work in the steel tie:

$$\delta L_A = \frac{A_L}{g} \sum_{i=1}^3 W_i R_i d\theta_i \cos \alpha_i, \quad (22)$$

is the work of pushing inertial forces AW_i/g acting on the walls masses.

With the positions

$$\mu_{21} = \frac{W_2}{W_1}, \quad \mu_{31} = \frac{W_3}{W_1}, \quad \rho_{21} = \frac{R_2}{R_1}, \quad \rho_{31} = \frac{R_3}{R_1}, \quad (23)$$

we obtain the limit acceleration A_L :

$$A_L = g \frac{\sigma_{AL}}{\chi_{AL}}, \quad (24)$$

with

$$\sigma_{AL} = (\sin \alpha_1 + \mu_{21} \rho_{21} k_{21} \sin \alpha_2 + \mu_{31} \rho_{31} k_{31} \sin \alpha_3) + (T_0 H / W_1 R_1)(k_{21} - 1), \quad (25)$$

$$\chi_{AL} = (\cos \alpha_1 + \mu_{21} \rho_{21} k_{21} \cos \alpha_2 + \mu_{31} \rho_{31} k_{31} \cos \alpha_3). \quad (26)$$

It is worth to remark, on the other hand, that this result is valid if the stress state in the wall is statically admissible. To satisfy this condition, some local reinforcements can be placed at the top of piers in order to avoid local failures due to interactions between piers and spandrel.

4.2. Free rocking of the wall. Let us examine now the motion of the wall when, released at a sideways deformed configuration, it puts itself in motion going back to its initial position (Figure 14). In this stage, the motion is a fall and all the weights come down. The wall moves from the right to the left along the failure mechanism \mathbf{u}^- before it is determined by means of the limit analysis approach. This motion ends at the instant when simultaneous impacts occur between the piers with their basement as well as between piers and the central spandrel.

The second step goes from the instant of the inversion of motion, along the subsequent mechanism \mathbf{u}^+ , the *reverse* of the previous mechanism \mathbf{u}^- , i.e., having a mirrored hinges layout. Piers continue to rotate in clockwise direction while the spandrel, on the contrary, counter-clockwise. Impacts, between piers and the spandrel as well as between piers and the basement, take place at the positions of the new hinge of the mechanism \mathbf{u}^+ (Figure 14). Then the motion of the wall continues until the instant when the wall reaches the maximum side deformation, before to go back again and so on.

Let us consider the dynamical equilibrium of the wall in the first phase of this motion. Piers I and II are rotated of the angles θ_1 and θ_2 around their absolute centers C_1 and C_2 , while the central panel III is rotated of θ_3 around C_3 , all quantities connected by means of suitable kinematical conditions. This analysis is achieved by applying the principle of virtual displacements, evaluating, along a small deformation increment δu of the wall, the works done by the various engaged forces, *at the generic deformed configuration of the wall*, attained at the time t of the motion.

Application of the virtual work equation thus gives

$$\langle g, \delta \mathbf{u} \rangle + \delta L_{\text{tie}} - \langle \rho \ddot{\mathbf{u}}(t), \delta \mathbf{u} \rangle = 0, \quad t > 0, \quad (27)$$

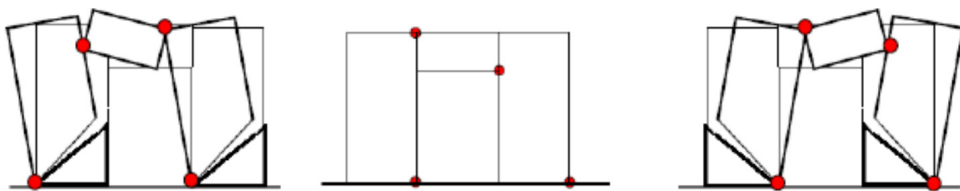


Figure 14. The motion of the wall at the instants just before and just after the impacts and the position of impact points.

where the work of the dead loads (g) is

$$\langle g, \delta u \rangle = \sum_{i=1}^3 W_i R_i \sin(\alpha_i - \theta_i) d\theta_i, \quad (28)$$

and the work of the inertial loads is

$$-\langle \rho \ddot{u}(t), \delta u \rangle = \sum_{i=1}^3 I_{C_i}^{(i)} \ddot{\theta}_i d\theta_i, \quad (29)$$

with $I_{C_1}^{(1)}$, $I_{C_2}^{(2)}$, $I_{C_3}^{(3)}$ being the moments of inertia for the centers C_1 , C_2 , C_3 . The latter is the work of the stretch force T_0 in the steel tie. There is no release of energy in the steel tie with the assumed perfectly rigid plastic constitutive law (Figure 16) and $\delta L_{\text{tie}} = 0$. These works are all positive because all the weights W_1 , W_2 and W_3 move down as the wall falls along the mechanism with the outcome of the rotation increments $d\theta_1$, $d\theta_2$ and $d\theta_3$.

Continuing the analysis, whose development has been given in [Como 2016] we will reach the same conclusions about the features of the free rocking motion as in the case of the Housner solid column even if, in this case, the motion is influenced by cracking. These oscillations, that, due to the energy losses occurring at the impacts, become step by step faster and present gradually smaller amplitudes, are distinctive of the rocking motion.

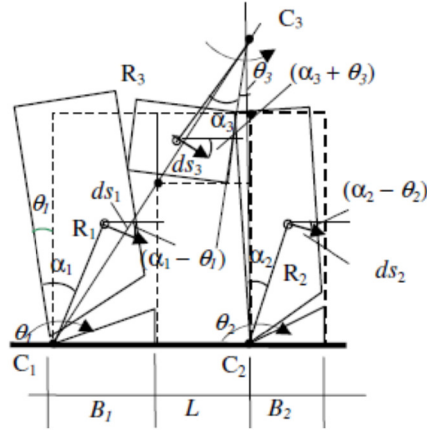


Figure 15. Geometry of the falling down mechanism of the first stage of motion.

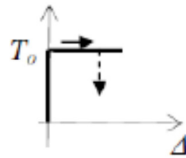


Figure 16. No release of energy in the steel tie at the unloading stage.

4.3. Impacts. As in the case of the column, the falling motion of the wall that moves along the mechanism (Figure 17, first scheme), stops at the instant $T/4$ when the wall reaches the undeformed “zero” configuration, a bit early than impacts will occur. At this instant all the hinges of the mechanism are closed and the motion cannot proceed along the same mechanism. At the “zero” configuration, contact will occur along the inclined fractures in the piers and along the connection sections piers/spandrel.

A compression flow thus immediately takes place along the ineffective masonry wedges and along the side sections of the spandrel. Inertial forces push the wall to continue its side motion, from the left to the right, so that it will activate a new mechanism with the formation of new hinges, placed in the “mirror” position with respect to the hinges of the previous mechanism.

At the reaching of the “zero” configuration, impacts will thus occur at the right corners of the base sections of the piers and at corners of the spandrel. In brief, impact points are thus spotted at the positions of the new mechanism (Figure 17). The velocities of the wall masses immediately before the impact — i.e., the rotational velocity $\dot{\theta}_1(T/4 - \varepsilon)$ of the pier I around C_1 and the velocities $\dot{\theta}_2$ and $\dot{\theta}_3$ — are known. Unknown, on the contrary, is the velocity $\dot{\theta}_{1p}(T/4 + \varepsilon)$ immediately after the impact. The knowledge of this velocity is on the other hand required to determine the second phase of the motion and the energy loss due to the impact. The determination of this velocity can be performed by applying the principles of impulse and angular momentum.

This application involves other unknown quantities, i.e., the impulses $F_1 dt$, $F_2 dt$, acting at the impact points between the piers I and II and their base sections. It is thus necessary to consider suitable applications in sequence of the above principles. First, from the principle of the impulse applied to the whole system of Figure 18, immediately before and immediately after the impact, in the coordinate directions x and y , we have

$$mv_x(T/4 - \varepsilon) + IMP_x = mv_x(T/4 + \varepsilon), \quad (30)$$

$$mv_y(T/4 - \varepsilon) + IMP_y = mv_y(T/4 + \varepsilon). \quad (31)$$

Likewise, from the principle of the angular momentum applied to the whole system around the impact point A of the first pier with the basement (Figure 18), we have

$$\Lambda_A(T/4 - \varepsilon) + \mathcal{M}_A dt = \Lambda_A(T/4 + \varepsilon). \quad (32)$$

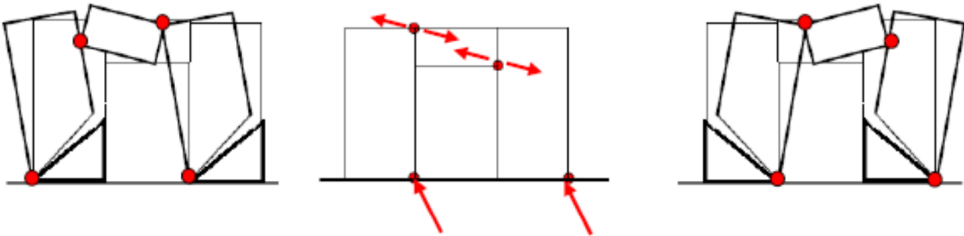


Figure 17. wall configuration just before impacts, impacts, wall configuration subsequent impacts.

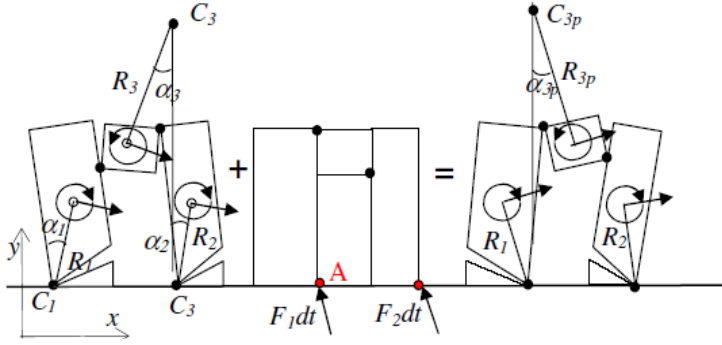


Figure 18. Application of the impulse principle to the whole system.

Similarly, applying to the first pier the principle of the angular momentum around the impact point B with the central panel (Figure 19, left), we have

$$\Lambda_B^{(1)}(T/4 - \varepsilon) + \mathcal{M}_B^{(1)} dt = \Lambda_B^{(1)}(T/4 + \varepsilon). \quad (33)$$

Finally, applying to the second pier the principle of the angular momentum around the impact point C with the central panel (Figure 19, right), we have

$$\Lambda_C^{(2)}(T/4 - \varepsilon) + \mathcal{M}_C^{(2)} dt = \Lambda_C^{(2)}(T/4 + \varepsilon). \quad (34)$$

Taking into account that

$$\dot{\theta}_2 = k_{21} \dot{\theta}_1, \quad \dot{\theta}_3 = k_{31} \dot{\theta}_1, \quad \dot{\theta}_{2p} = k_{21p} \dot{\theta}_{1p}, \quad \dot{\theta}_{3p} = k_{31p} \dot{\theta}_{1p}, \quad (35)$$

with the suitable connection factors k_{21} , k_{31} , k_{21p} and k_{31p} , the five equations (30), (31), (32), (33) and (34) can be solved, determining the five unknowns F_{1x} , F_{1y} , F_{2x} , F_{2y} and $\dot{\theta}_{1p}(T/4 + \varepsilon)$. A numerical application has been performed considering a simple masonry wall composed by 2 m wide piers and one spandrel, having a length of 2 m and a height of 1.2 m.

Two values of the height of the piers have been considered, 4 m and 6 m, respectively. The ratio between the rotational velocities immediately after and immediately before the impact results to be 0.181 and 0.413, respectively.

As in the Housner column [Housner 1963], the coefficient of restitution increases with the increasing of the slenderness of the system.

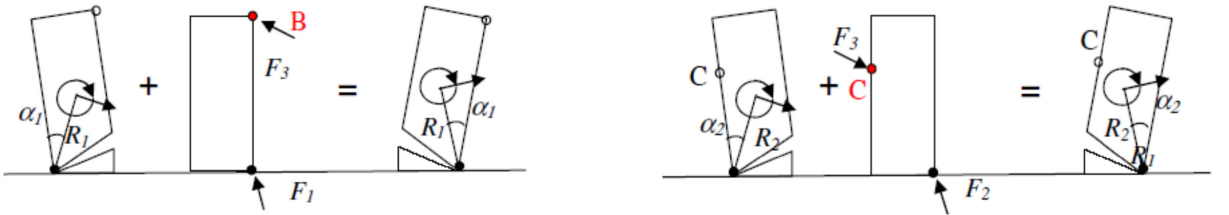


Figure 19. The principle of angular momentum: on the first pier around the impact point B (left) and on the second pier around the impact point C (right).

4.4. Forced motion of the wall hit by an acceleration impulse of given duration. Let us consider now a generic deformed configuration of the wall while it is pushed by a constant horizontal acceleration impulse A of given duration t . The corresponding motion of the wall is achieved as an application of the principle of virtual displacements, evaluating, along a small deformation increment δu , the works done by the various engaged forces, *at the generic deformed configuration of the wall*—defined by the rotation angles $\theta_1, \theta_2, \theta_3$, occurring around the absolute centers of the three panels in which the wall is subdivided—attained at time t of the motion (Figure 20). We get

$$\langle \mathbf{g}, \delta \mathbf{u} \rangle + \delta L_{\text{tie}} - \langle \rho \ddot{\mathbf{u}}(t) + \rho \mathbf{A}, \delta \mathbf{u} \rangle = 0, \quad t > 0, \quad (36)$$

where the work of the dead loads is

$$\langle \mathbf{g}, \delta \mathbf{u} \rangle = -W_1 ds_1 \sin(\alpha_1 - \theta_1) - W_2 ds_2 \sin(\alpha_2 - \theta_2) - W_3 ds_3 \sin(\alpha_3 + \theta_3), \quad (37)$$

where, with reference to Figure 20 $ds_1 = R_1 d\theta_1$, $ds_2 = R_2 d\theta_2$, $ds_3 = R_3 d\theta_3$ and

$$\langle \mathbf{g}, \delta \mathbf{u} \rangle = -W_1 R_1 d\theta_1 \sin(\alpha_1 - \theta) - W_2 R_2 d\theta_2 \sin(\alpha_2 - \theta_2) - W_3 R_3 d\theta_3 \sin(\alpha_3 + \theta_3). \quad (36')$$

During the increasing wall sideways displacement, the steel tie stretches at the yielding state. We have

$$\delta L_{pl} = -T_0(k_{21} - 1)H \delta \theta_1. \quad (38)$$

Summing up all the works, with the positions

$$\lambda_A = (\cos \alpha_1 + \mu_{21}\rho_{21}k_{21} \cos \alpha_2 + \mu_{31}\rho_{31}k_{31} \cos \alpha_3) = \chi_{AL}, \quad (39)$$

$$\sigma_A = \sin \alpha_1 + \mu_{21}\rho_{21}k_{21}^2 \sin \alpha_2 - \mu_{31}\rho_{31}k_{31}^2 \sin \alpha_3, \quad (40)$$

$$\sigma_{Aasc} = \sin \alpha_1 + \mu_{21}\rho_{21}k_{21} \sin \alpha_2 + \mu_{31}\rho_{31}k_{31} \sin \alpha_3 + T_0 H(k_{21} - 1)/W_1 R_1 = \sigma_{AL}, \quad (41)$$

$$\chi_{Aasc} = (\cos \alpha_1 + \mu_{21}\rho_{21}k_{21}^2 \cos \alpha_2 - \mu_{31}\rho_{31}k_{31}^2 \cos \alpha_3), \quad (42)$$

$$p_*^2 = \frac{W_1 R_1}{I_C^*} \chi_{Aasc}, \quad (43)$$

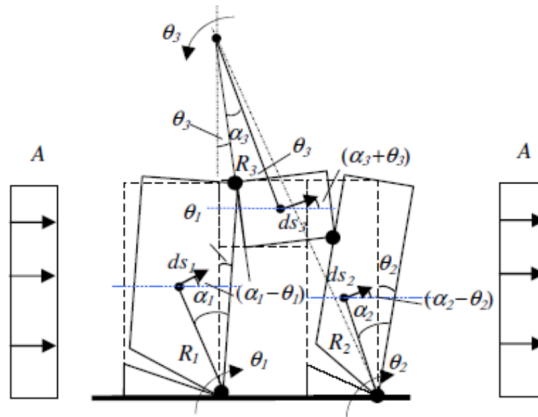


Figure 20. The wall in an ascending motion dragged by the horizontal acceleration impulse A .

the equation of the forced motion of the wall simplifies and becomes

$$\ddot{\theta}_1 - p_*^2 \theta_1 = -\frac{p_*^2}{\chi_{Aasc}} \left(\sigma_{AL} - \frac{A}{g} \chi_{AL} \right), \quad (44)$$

whose solution, satisfying the initial conditions $\theta_1(0) = \dot{\theta}_1(0) = 0$, is

$$\theta_1(t) = \Phi(\cosh p_* t - 1), \quad (45)$$

where

$$\Phi = \frac{1}{\chi_{Aasc}} \left(\frac{A}{g} \chi_{AL} - \sigma_{AL} \right). \quad (46)$$

4.5. Dynamical collapse. There is a configuration C_0 of the wall along the side motion $\theta = \theta_1(t)$ at which the potential energy of all the weights acting on the wall reaches its maximum. When the wall reaches this configuration, weights no longer oppose any displacement increment starting from C_0 . The dynamical collapse of the wall is thus attained if the acceleration impulse has sufficient intensity A_1 and sufficient duration t_0 so that the inertial forces, induced by A_1 , move, just in the time t_0 , the wall along motion $\theta = \theta_1(t)$ as far as the configuration C_0 has been reached. Hence, taking into account that

$$\dot{\theta}_1(t) = \Phi p_* \sinh p_* t, \quad \dot{\theta}_2(t) = k_{21} \dot{\theta}_1(t), \quad \dot{\theta}_3(t) = k_{31} \dot{\theta}_1(t), \quad (47)$$

and with reference, for the sake of simplicity, to [Figure 21](#), that shows the raising of the weight W_1 , we get that the difference in potential energy between the deformed and the initial configurations of the wall, can be evaluated as

$$\Delta E = \sum_{i=1}^3 W_i R_i [\cos(\alpha_i - \theta_i) - \cos \alpha_i]. \quad (48)$$

At the same time the work done along the motion by the horizontal push due to the acceleration impulse, making reference to [Figure 20](#), is

$$L_{IMP} = \frac{A_0}{g} \sum_{i=1}^3 W_i R_i \int_0^{t_0} \frac{ds_i}{dt} \cos(\alpha_i - \theta_i) dt. \quad (49)$$

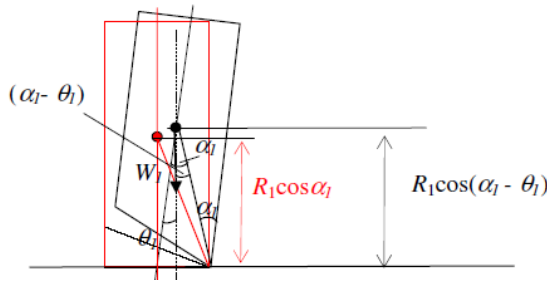


Figure 21. The raising of the weight W_1 of the pier I.

Finally, the balance between the work of the inertial forces and the potential energy increment, gives

$$L_{\text{IMP}} = \frac{A_0}{g} \sum_{i=1}^3 W_i R_i \int_0^{t_0} \frac{ds_i}{dt} \cos(\alpha_i - \theta_i) dt = \Delta E = \sum_{i=1}^3 W_i R_i [\cos(\alpha_i - \theta_i) - \cos \alpha_i]. \quad (50)$$

Evaluating the integrals up to the time t_0 , the dynamical failure condition is

$$\begin{aligned} L_{\text{IMP}} &= \Phi \frac{A_0}{g} \frac{1}{p_*} \left(\{w_1 R_1 \cos \alpha_1 + w_2 R_2 k_{21} \cos \alpha_2 + w_3 R_3 k_{31} \cos \alpha_3\} (\cosh p_* t_0 - 1) \right. \\ &\quad \left. + \{w_1 R_1 \sin \alpha_1 + w_2 R_2 k_{21}^2 \sin \alpha_2 - w_3 R_3 k_{31}^2 \sin \alpha_3\} \left[\frac{\sinh^2 p_* t_0}{2} - \cosh p_* t_0 + 1 \right] \right) \\ &= MAX W_1 R_1 [\cos(\alpha_1 - \theta_1) - \cos \alpha_1] + W_2 R_2 [\cos(\alpha_2 - \theta_2) - \cos \alpha_2] \\ &\quad + W_3 R_3 [\cos \alpha_3 - \cos(\alpha_3 + \theta_3)], \end{aligned} \quad (51)$$

correlating the magnitude of the acceleration impulse A_0 with its duration t_0 .

We point out that when $t_0 \rightarrow \infty$, $\Phi \rightarrow 0$. In this case the value of the acceleration impulse A_0 coincides with the value of the acceleration impulse A_L , determining the static failure of the wall. We have in fact, with (51)

$$\Phi \rightarrow 0 \Leftrightarrow \frac{1}{\chi_{\text{Aasc}}} \left(\frac{A}{g} \chi_{AL} - \sigma_{AL} \right) \rightarrow 0 \Leftrightarrow \frac{A}{g} \chi_{AL} \rightarrow \sigma_{AL} \Leftrightarrow \frac{A}{g} \rightarrow \frac{\sigma_{AL}}{\chi_{AL}} = A_L, \quad (52)$$

matching (24). A numerical investigation is carried out in order to clarify the described procedure and to practically show how to evaluate the incipient rocking and collapse accelerations. For the sake of simplicity, a simple geometry of the wall, characterized by two piers and one storey, is considered in the following.

The side view of the active wall is shown in Figure 22 (left), together with the indication of the main geometrical parameters. Both piers and the spandrel have the same thickness. In particular, the widths of the two piers are equal to 2 m and 2.5 m, while their height is equal to 6 m. The spandrel is 2 m wide and 1.5 m high.

The specific weight of the masonry material is taken to be equal to 16 kN/m^3 . The incipient rocking acceleration value A_L is evaluated and it is equal to 3 m/s^2 . The cracked configuration is defined by the distances ξ_1 and ξ_2 of the sections in which the cracks start from the top of the piers, equal to 2.73 m and 3.47 m, respectively. The fourth unknown is the diagonal reaction of the spandrel, equal to 16.8 kN.

The dynamical failure condition of the wall, pushed by a constant horizontal acceleration impulse of given duration, is obtained by solving (51). By varying the duration t_0 of the impulse, it is thus possible to evaluate the magnitude of the collapse acceleration A_0 .

In this way, we can define a failure domain of the masonry wall, numerically solving (51), finding different combinations of values of pulse magnitude and duration, which lead the system to the achievement of a failure condition. Figure 22 (right) shows the failure domain of the considered scheme of masonry wall, in terms of the ratio between collapse and activation accelerations. The domain located below the curve corresponds to an equilibrium condition, while the upper part of the graph refers to the attainment of a failure state.

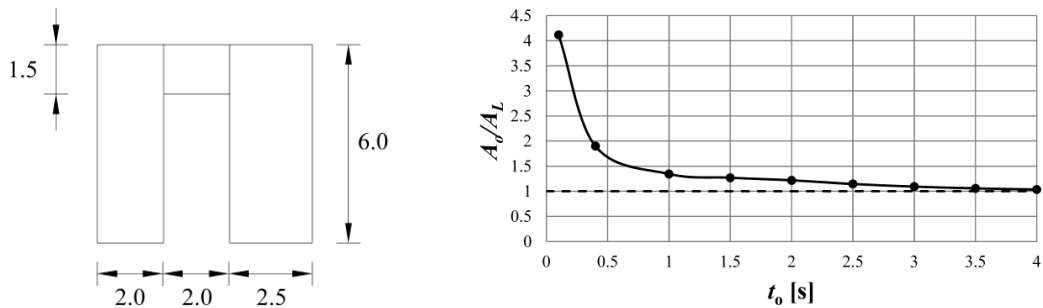


Figure 22. Left: geometry of the masonry wall. Right: failure domain of the examined masonry wall.

The horizontal dashed line (Figure 22, right) indicates the load multiplier value required for the activation of the motion, evaluated through the equivalent static analysis: it represents a horizontal asymptote of the failure domain, attainable for infinite values of the pulse duration. The zone of the graph located under this value represents a rest condition of the system. Figure 22 (right) shows the trend of the ratio A_0/A_L between the dynamical constant acceleration impulse A_0 and the static limit acceleration A_L versus its duration time t_0 . It is recognized from this graph that for a duration time $t_0 = 0.25$ s — a value corresponding to a strong seismic shock — the ratio $A_0/A_L = 2.5$. It means that in this case the intensity of the acceleration impulse determining the dynamic failure of the wall is 2.5 times larger than the static limit acceleration usually considered to evaluate the seismic strength of the wall.

If we consider the peak ground acceleration a_{PGa} representative of the seismic shock of the given site, equating A_0 to a_{PGa} , we can assume static limit acceleration A_L 2.5 lower than a_{PGa} . The ratio $A_0(t_0)/A_L$ can thus be considered as the reduction factor q to assume checking the seismic strength of the wall, rather than values obtained by assumptions founded on a doubtful masonry ductility.

5. Conclusions

The paper has examined the rocking of some important structural schemes by using an analytical approach, starting from the solid column to the masonry pier, and then to a simple model of a masonry wall, composed by two piers and a spandrel, connected by a steel chain. The dynamic action applied to these models is a horizontal acceleration impulse at given intensity and duration.

The rocking capacity of these models has been thoroughly examined under these dynamic loadings, firstly to obtain useful information concerning the maximum acceleration intensity, corresponding to a given duration, able to produce the dynamic failure of the structure. Impacts occurring during the rocking motion have been analyzed to determine the corresponding dynamical energy losses able to give information on the dissipation of energy occurring during the motion, dissipation at a first sight unexpected in masonry structures that, deform with mechanisms with hinges that open without any material opposition.

The intensity of the dynamic acceleration impulse able to produce the dynamical collapse can be much larger than the limit static acceleration; this last is the representative of the seismic side strength of the structure.

These results, in some points innovative, recall some issues of the author and others [Coccia et al. 2016; Di Carlo et al. 2017] and point out the usefulness of dynamical approaches to obtain sound evaluations of the strength reduction factor q , fundamental in checking the seismic strength of constructions.

References

- [Coccia et al. 2016] S. Coccia, F. Di Carlo, and S. Imperatore, “Force reduction factor for out-of-plane simple mechanisms of masonry structures”, *Bull. Earthq. Eng.* **15**:3 (2016), 1241–1259.
- [Como 2016] M. Como, *Statics of historic masonry constructions*, 2nd ed., Springer, Switzerland, 2016.
- [Di Carlo 2014] F. Di Carlo, *Strength reduction factor, for rocking masonry structures*, Ph.D. dissertation, Department of Civil Engineering and Computer Science Engineering, University of Rome Tor Vergata, 2014.
- [Di Carlo et al. 2017] F. Di Carlo, S. Coccia, and M. Como, “Rocking in presence of cracking of masonry wall piers”, *Key Eng. Mater.* **747** (2017), 678–685.
- [Di Carlo et al. ≥ 2019] F. Di Carlo, S. Coccia, and M. Como, “Rocking of cracked masonry walls loaded by constant impulse acceleration”, to appear in *Meccanica (Milano)*.
- [Giannini and Masiani 1996] R. Giannini and R. Masiani, “Non-Gaussian solution for random rocking of slender rigid block”, *Probab. Eng. Mech.* **11**:2 (1996), 87–96.
- [Heyman 1992] J. Heyman, “Leaning towers”, *Meccanica (Milano)* **27**:3 (1992), 153–159.
- [Hogan 1992] S. J. Hogan, “On the motion of a rigid block, tethered at one corner, under harmonic forcing”, *Proc. R. Soc. Lond. A* **439**:1905 (1992), 35–45.
- [Housner 1963] G. W. Housner, “The behaviour of inverted pendulum structures during earthquakes”, *Bull. Seismol. Soc. Am.* **53**:2 (1963), 403–417.
- [Liberatore et al. 2002] D. Liberatore, G. Spera, G. D’Alessandro, and D. Nigro, “Rocking of slender blocks subjected to seismic motion of the base”, in *Twelfth European Conference on Earthquake Engineering* (London), 2002.
- [Ochserdorf 2002] J. A. Ochserdorf, *Collapse of masonry structures*, Doctoral thesis, Department of Engineering, University of Cambridge, 2002, Available at <https://www.repository.cam.ac.uk/handle/1810/244820>.
- [Peña et al. 2007] F. Peña, F. Prieto, P. B. Lourenço, A. Campos Costa, and J. V. Lemos, “On the dynamics of rocking motion of single rigid-block structures”, *Earthq. Eng. Struct. Dyn.* **36**:15 (2007), 2383–2399.
- [Sorrentino et al. 2006] L. Sorrentino, R. Masiani, and L. D. Decanini, “Overturning of rocking rigid bodies under transient ground motions”, *Struct. Eng. Mech.* **22**:3 (2006), 293–310.
- [Sorrentino et al. 2008] L. Sorrentino, R. Masiani, and M. C. Griffith, “The vertical spanning strip wall as a coupled rocking rigid body assembly”, *Struct. Eng. Mech.* **29**:4 (2008), 433–453.
- [Yim et al. 1980] C.-S. Yim, A. K. Chopra, and J. Penzien, “Rocking response of rigid blocks to earthquakes”, *Earthq. Eng. Struct. Dyn.* **8**:6 (1980), 565–587.

Received 27 May 2018. Revised 27 Sep 2019. Accepted 18 Oct 2019.

MARIO COMO: como@ing.uniroma2.it

Department of Civil Engineering and Computer Science Engineering (DICII), University of Rome Tor Vergata,
Via del Politecnico 1, 00133 Rome, Italy

SUBMISSION GUIDELINES

ORIGINALITY

Authors may submit manuscripts in PDF format online at the Submissions page. Submission of a manuscript acknowledges that the manuscript is original and has neither previously, nor simultaneously, in whole or in part, been submitted elsewhere. Information regarding the preparation of manuscripts is provided below. Correspondence by email is requested for convenience and speed. For further information, write to contact@msp.org.

LANGUAGE

Manuscripts must be in English. A brief abstract of about 150 words or less must be included. The abstract should be self-contained and not make any reference to the bibliography. Also required are keywords and subject classification for the article, and, for each author, postal address, affiliation (if appropriate), and email address if available. A home-page URL is optional.

FORMAT

Authors can use their preferred manuscript-preparation software, including for example Microsoft Word or any variant of \LaTeX . The journal itself is produced in \LaTeX , so accepted articles prepared using other software will be converted to \LaTeX at production time. Authors wishing to prepare their document in \LaTeX can follow the example file at www.jomms.net (but the use of other class files is acceptable). At submission time only a PDF file is required. After acceptance, authors must submit all source material (see especially Figures below).

REFERENCES

Bibliographical references should be complete, including article titles and page ranges. All references in the bibliography should be cited in the text. The use of Bib \TeX is preferred but not required. Tags will be converted to the house format (see a current issue for examples); however, for submission you may use the format of your choice. Links will be provided to all literature with known web locations; authors can supply their own links in addition to those provided by the editorial process.

FIGURES

Figures must be of publication quality. After acceptance, you will need to submit the original source files in vector format for all diagrams and graphs in your manuscript: vector EPS or vector PDF files are the most useful. (EPS stands for Encapsulated PostScript.)

Most drawing and graphing packages—Mathematica, Adobe Illustrator, Corel Draw, MATLAB, etc.—allow the user to save files in one of these formats. Make sure that what you’re saving is vector graphics and not a bitmap. If you need help, please write to graphics@msp.org with as many details as you can about how your graphics were generated.

Please also include the original data for any plots. This is particularly important if you are unable to save Excel-generated plots in vector format. Saving them as bitmaps is not useful; please send the Excel (.xls) spreadsheets instead. Bundle your figure files into a single archive (using zip, tar, rar or other format of your choice) and upload on the link you been given at acceptance time.

Each figure should be captioned and numbered so that it can float. Small figures occupying no more than three lines of vertical space can be kept in the text (“the curve looks like this:”). It is acceptable to submit a manuscript with all figures at the end, if their placement is specified in the text by means of comments such as “Place Figure 1 here”. The same considerations apply to tables.

WHITE SPACE

Forced line breaks or page breaks should not be inserted in the document. There is no point in your trying to optimize line and page breaks in the original manuscript. The manuscript will be reformatted to use the journal’s preferred fonts and layout.

PROOFS

Page proofs will be made available to authors (or to the designated corresponding author) at a Web site in PDF format. Failure to acknowledge the receipt of proofs or to return corrections within the requested deadline may cause publication to be postponed.

Preface	MAURIZIO ANGELILLO and SANTIAGO HUERTA FERNÁNDEZ	601
Studying the dome of Pisa cathedral via a modern reinterpretation of Durand-Claye's method	DANILO AITA, RICCARDO BARSOTTI and STEFANO BENNATI	603
Experimental and numerical study of the dynamic behaviour of masonry circular arches with non-negligible tensile capacity	ALEJANDRA ALBUERNE, ATHANASIOS PAPPAS, MARTIN WILLIAMS and DINA D'AYALA	621
Influence of geometry on seismic capacity of circular buttressed arches	GIUSEPPE BRANDONISIO and ANTONELLO DE LUCA	645
Failure pattern prediction in masonry	GIANMARCO DE FELICE and MARIALAURA MALENA	663
Energy based fracture identification in masonry structures: the case study of the church of "Pietà dei Turchini"	ANTONINO IANNUZZO	683
Displacement capacity of masonry structures under horizontal actions via PRD method	ANTONINO IANNUZZO, CARLO OLIVIERI and ANTONIO FORTUNATO	703
Automatic generation of statically admissible stress fields in masonry vaults	ELENA DE CHIARA, CLAUDIA CENNAMO, ANTONIO GESUALDO, ANDREA MONTANINO, CARLO OLIVIERI and ANTONIO FORTUNATO	719
Limit analysis of cloister vaults: the case study of Palazzo Caracciolo di Avellino	ANTONIO GESUALDO, GIUSEPPE BRANDONISIO, ANTONELLO DE LUCA, ANTONINO IANNUZZO, ANDREA MONTANINO and CARLO OLIVIERI	739
The rocking: a resource for the side strength of masonry structures	MARIO COMO	751